uOttawa

L'Université canadienne
Canada's university

FACULTÉ DES ÉTUDES SUPÉRIEURES ET POSTOCTORALES

u Ottawa

L'Université canadienne
Canada's university

FACULTY OF GRADUATE AND POSDOCTORAL STUDIES

Amre Kamal Deif

AUTEUR DE LA THÈSE / AUTHOR OF THESIS

Ph.D. (Civil Engineering)

GRADE / DEGREE

Department of Civil Engineering

FACULTÉ, ÉCOLE, DÉPARTEMENT / FACULTY, SCHOOL, DEPARTMENT

Chloride Ingress into Reinforced Concrete Sustaining In-Service Loads

TITRE DE LA THÈSE / TITLE OF THESIS

Beatriz Martin-Perez

DIRECTEUR (DIRECTRICE) DE LA THÈSE / THESIS SUPERVISOR

CO-DIRECTEUR (CO-DIRECTRICE) DE LA THÈSE / THESIS CO-SUPERVISOR

James Beaudoin

Mamadou Fall

Burkan Isgor

Michelle Nokken (Concordia U.)

Gary W. Slater

Le Doyen de la Faculté des études supérieures et postdoctorales / Dean of the Faculty of Graduate and Postdoctoral Studies

CHLORIDE INGRESS INTO REINFORCED CONCRETE SUSTAINING IN-SERVICE LOADS

By

Amre Kamal Deif

Thesis submitted to the Faculty of Graduate and Postdoctoral Studies in partial fulfillment of the requirements for the degree of

Doctor of Philosophy in Civil Engineering

Department of Civil Engineering
University of Ottawa
Ottawa, Ontario, Canada
K1N 6N5

The Ph.D. in Civil Engineering is a joint program with Carleton University administered by the Ottawa-Carleton Institute for Civil Engineering

Your file Votre référence
ISBN: 978-0-494-69123-6
Our file Notre référence
ISBN: 978-0-494-69123-6

Abstract

The service life of a reinforced concrete (RC) bridge deck in cold climates is often limited by chloride-induced corrosion of the reinforcement due to exposure to de-icing salts routinely applied in the winter. Although there has been an extensive research effort on chloride ingress into concrete in the last three decades, research conducted on structural concrete members carrying in-service loads is limited. The objectives of this study were to investigate the effect of sustained load on chloride ingress into concrete and to examine the reliability of spraying a $AgNO_3$ solution onto concrete as a quick method to determine chloride penetration.

To achieve these objectives, an experimental program was carried out, in which a small-scale RC slab was subjected to wet and dry cycles with a saturated chloride solution while sustaining static service loads. The concrete slab was cast with three strips of different water-to-cement ratios to represent different field conditions. Supports were located to create both positive and negative moment regions in the top mat reinforcement of the slab. Concrete cores were taken at several sections along the RC deck, which were stressed to different levels, and at three time intervals, each of them after a wet/dry cycle of 90 days. Concrete cores were sprayed with a $AgNO_3$ solution to determine an average chloride penetration front, and chloride profiles along the concrete cover for each core were measured by potentiometric titration.

Chloride diffusion coefficients were obtained from the data obtained from spraying $AgNO_3$ and titration, the latter by curve-fitting to Fick's 2^{nd} law. The comparison between both sets of data reveals that the differences diminish as the time of exposure increases. The chloride diffusivity along the span of the slab, relative to that of an unstressed section, was related to the applied bending moment. The experimental results also indicate that there is a dependence of chloride ingress properties on the type and level of sustained load. An analysis of the data to study the effect of exposure time and water-to-cement ratio using colourimetric and potentiometric titration methods was also carried out.

To: O He Who is in the Heaven !

Acknowledgments

First of all, wholeheartedly, I would like to dedicate my deep thanks to my Lord "Allah" for his great endless sustenance, giving me the power and patience to fulfil this research. From my deep belief in Allah, I am nothing without the blessing of him.

I would also like to express my sincere appreciation to my supervisor, Dr. Beatriz Martín-Pérez, who was a source of assistance and booster. Besides the knowledge I gained from her, her invaluable insights and skilled supervisory guidance made me write and complete this dissertation. Her patience in listening and hearing my arguments, however incorrect they were sometimes, had a great effect in finishing this thesis. Her painstaking criticisms, editorial details, and the discussions that I had with her, made my writing of this dissertation a much more pleasurable experience. Her understanding and down-to-earth nature cannot, in addition, go without being acknowledged. I thank her, most sincerely, for all her generous acts and deeds and for being the wonderful human being that she is.

I am also grateful to Dr. Bruno Cousin, Université Montpellier, France, for his support and extremely valuable comments during the preparation of this project. In fact, the fruitful discussions I had with Dr. Beatriz and Dr. Bruno have played a significant role in my intellectual development and make it imperative for me to feel indebted to them.

Thanks are also due to Dr. Murat Saatcioglu for his advice and the discussions I had with him on loading the deck, Dr. John Gardner for his valuable advice, Dr. Roberto Narbaitz for his help in giving me easy access to the environmental lab to accomplish the titration work, Francisco Aposaga from the environmental lab of the Faculty of Engineering, for his support, Dr. Burkan Isgor, Carleton University, for his help in lending me some of his equipment to finish some of the related works, and Dr. Jim Beaudoin for teaching me "Advanced Concrete Technology," which opened my mind to the world of concrete.

Thanks are also due to Mr. Rene Matte at the Quality Control Department of the National Capital Region, Lafarge Company for his help in providing me with the ready mix-design and facilitating casting. Special thanks are due to all the staff in Financial Aid and Awards Office at the University of Ottawa.

Finally, unconditional love, appreciation and respect are acknowledged to Mr. John Perrins, from the machine shop of the Faculty of Engineering, for his valuable assistance to this work.

Contents

List of Tables

List of Figures

Notations

The following symbols are used in this thesis:

A = empirical constant;

A = cross-sectional area of concrete (m^2);

A_c = the total area perpendicular to the diffusion flux of cracked material (m^2);

A_{cr} = crack area (m^2);

A_m = total area perpendicular to the diffusion flux of uncracked material (m^2);

A_s = area of tensile reinforcement (m^2);

A_s' = area of comressive reinforcement (m^2);

a = depth of equivalent compression rectangular stress block for flexural member;

b = width of a flexural member (m);

C = chloride mass per unit volume or concentration of chlorides dissolved in the pore solution (kg/m^3 of pore solution);

C_0 = chloride concentration at the surface x = 0 (kg/m^3);

C_r =compressive force in concrete (N);

C_r' = compressive force in compression reinforcement (N);

$C(x, t)$ = total chlorides at depth x after time t (kg/m^3);

c = position of neutral axis (m);

D = apparent diffusion coefficient of the cracked material (m^2/s);

D_{ao} = apparent diffusion coefficient for the unloaded specimen (m^2/s);

$D_a(\sigma_s)$ = apparent diffusion coefficient at the given load level as expressed by (m^2/s);

D_{cr} = diffusion coefficient through the crack (m^2/s);

D_0 = diffusion coefficient of the species in the homogeneous (uncracked) material (m^2/s);

D_l = diffusion coefficient of a given ionic (or molecular) species in free solution (m^2/s);

d = crack depth;

d = effective depth of a section measured from extreme compression fibre to centroid of tensile reinforcement (m);

d' = distance from extreme compression fibre to centroid of compression reinforcement (m);

E = Young's modulus for the reinforcing steel bar (N/m^2);

E_c = elastic modulus of concrete (MPa);

erf = error function;

f'_c = cylinder compressive strength of concrete (MPa);

f_s = flexural stress in tensile steel at service load (MPa);

f_y = yield strength of steel (MPa);

f_r = modulus of rupture (MPa);

h = total thickness of member (m);

I_g = moment of inertia of the uncracked transformed section (m^4);

L_1 = mean crack spacing;

L_4 = mean aperture of the cracks;

$L(\sigma_s)$ = load function (N/m^2);

M = internal bending moment (N.m);

N = exact normality of 0.05 N $AgNO_3$ solution;

n = modular ratio (ratio of modulus of elasticity of steel to that of concrete;

Q = seepage flow rate (l/s);

Q_s = spray flow rate (l/h);

q = flux of chloride ions due to diffusion per unit area of solution in the x direction ($kg/m^2.s$);

V_1 = volume of consumed 0.05 N $AgNO_3$ solution for concrete at the equivalence point (mL);

V_2 = volume of consumed 0.05 N $AgNO_3$ solution for blank titration at the equivalence point (mL);

W = weight of concrete sample (g);

w = crack width;

w/c = water-to-cement ratio;

x = depth at which C is calculated measured normal to the exposure surface (m);

y = distance from the neutral axis to the beam fibre where σ_c is calculated (m);

y_t = distance from the neutral axis to the extreme tension fibre (m);

α_1 = ratio of the average compressive stress in the compression zone to the cylinder strength, f'_c ;

γ_{CL} = crack influence factor for chloride penetration;

ε_{cmax} = maximum strain in concrete;

ε_s = maximum strain in tensile reinforcement;

ε_s' = maximum strain in compressive reinforcement;

σ_s = the maximum stress in the rebar when the concrete is cracked (N/m^2);

ϕ_c = concrete resistance factor;

ϕ_s = steel resistance factor.

Chapter 1

Introduction

1.1. Background

The cost to repair and rehabilitate damaged concrete infrastructure is very high. In the United States, bridges in need of intervention amount to more than a quarter of the total country's inventory; this deficiency is on the rise in urban areas (ASCE, 2009). The majority of the durability-related problems in concrete are due to the movement of aggressive species into concrete by ground water, sea-water, runoff and splash. Chloride penetration is one of the major problems that affect the durability of reinforced concrete structures as it causes the corrosion of embedded steel bars. Bridges and parking garages that are routinely exposed to deicing salt spread in the winter are among the structures most affected in Canada.

The alkaline environment (pH>13) provided by the hydration of cement in concrete protects the steel reinforcement against corrosion by forming an iron oxide micro-film passive layer on the steel surface. Good quality concrete cover also protects the reinforcing steel by preventing or slowing down the movement of chloride towards the reinforcement. But if sufficient chloride ions move through this cover and reach the reinforcement, then the iron oxide passive film is broken down and the process of corrosion is initiated.

Corrosion products have a volume that can be greater than six times that of the original material (see Figure 1.1); as corrosion products accumulate around the reinforcement, they exert an outward pressure that eventually leads to cover cracking, spalling and/or delamination of the concrete cover when its tensile capacity is reached. Other consequences of reinforcement corrosion are the reduction in cross-sectional area of the reinforcement, which leads to a reduction of the load carrying capacity, and the loss of bond between the steel and the concrete. This process is more critical for prestressed reinforced concrete than ordinary reinforced concrete structures.

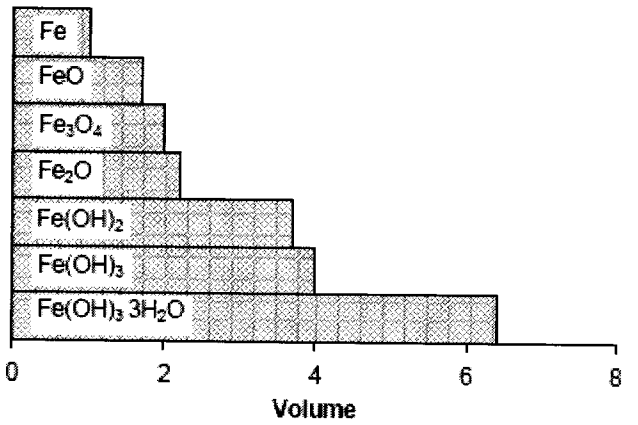

Figure 1.1: Relative volume for various corrosion products (adapted from Rosenberg et al., 1989).

The mechanism of corrosion has been often idealized by the model first proposed by Tuutti (1982), in which the corrosion timeline is divided into an initiation and a propagation period. The time from the initial exposure to chlorides until they accumulate in sufficient quantities (called the threshold concentration) on the reinforcing steel is defined as the initiation period. According to CSA A23.1-04, the amount of water-soluble chlorides coming from the mix ingredients is to be limited to 0.06% and 0.15% by mass of cementing material for prestressed concrete and reinforced concrete, respectively. ACI 222 imposes these limitations on acid-soluble chlorides as 0.08% and 0.20% by mass of cementing material for prestressed concrete and reinforced concrete, respectively (ACI Committee 222, 2001). The time from onset of corrosion until an unacceptable damage level is reached is defined as the propagation period. There are several stages included in the propagation phase: longitudinal cracking, spalling/delamination and finally structural collapse (see Figure 1.2). The length of the initiation period leading to steel depassivation (t_D in Figure 1.2) depends on: the surface chloride concentration, the rate of ingress of chlorides into concrete, the thickness and quality of the concrete cover, and the chloride threshold.

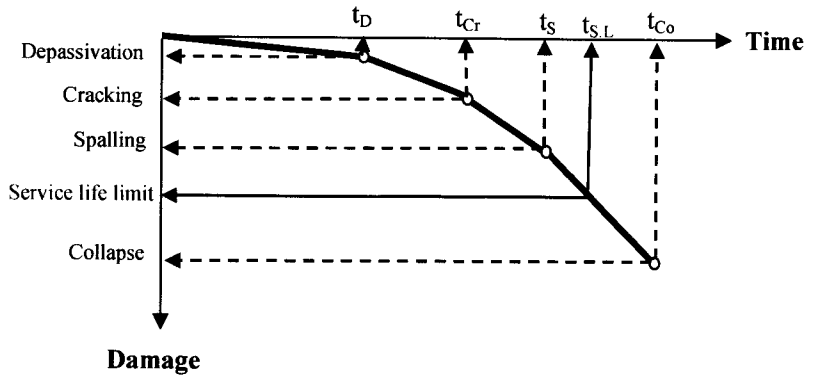

Figure 1.2: Events related to the service life, detailing of the propagation phase (adapted from Rostam, 2005).

Most published models attempting to estimate the duration of the initiation period assume concrete to be free of cracks (Maruyama et al., 2006), which is not the case in real reinforced concrete structures. Reinforced concrete structures under service loads are accepted to have some level of cracking; however, in this case the process of chloride ingress through the concrete cover will be completely different and more complex. Cracks in concrete are an easy access path for chloride ions to reach the reinforcement. Instead of chloride ions taking years to reach the mentioned threshold levels, chlorides could take a very short period of time to reach the reinforcement in the presence of cracks (Lindquist et al., 2006). Yet, there is still no clear model available that can predict the rate of chloride ingress in concrete with cracks or sustaining stresses.

According to Konin et al. (1998), although there are few studies on the effect of cracks on chloride ingress in concrete under sustained loads, there are discrepancies among the different obtained results. Most of the specimens used in the experimental tests were pre-cracked prior to chloride exposure, by either artificially creating a notch before casting or loading and unloading the specimens prior to exposure. The patterns of load-induced cracks are completely different from those of artificial cracks, the former being more representative of real life conditions. Furthermore, the surfaces of artificial cracks have more cement paste on them and the concrete next to these surfaces is not damaged. As a result, there will be differences in the ingress of chloride ingress along

cracks corresponding to the two cases. There will also be differences in the cases when the specimen is subjected to compressive, tensile and/or environmental loads.

1.2. Objective and scope

The main objective of the present work is to study the effect of mechanical loading on chloride ingress into concrete by relating chloride transport properties to parameters describing the mechanical state of the structure. To achieve this objective, a small-scale reinforced concrete (RC) bridge deck made of different water-to-cement (w/c) ratios was exposed to de-icing salt (through three wetting and drying cycles with a saturated chloride solution) while sustaining in-service loads. Concrete core samples were obtained from the slab after each wetting and drying cycle and analyzed for chloride content by both spraying a silver nitrate solution and conducting potentiometric titrations.

1.3. Research significance

Current standards dealing with durability of concrete only require a minimum concrete cover quality and thickness to protect a reinforced concrete structure for potential chloride-induced corrosion of the reinforcement. Although an enormous amount of research has been conducted in the last three decades in the field of concrete durability, there are still difficulties in "codifying" this knowledge, so that this information can be used as guidelines for practicing engineers (Lee and Christholm, 2000). According to Lounis et al. (2001), the experience, expert decisions and some simple models of limited reliability are considered to be guidelines to predict the service life and maintenance of RC bridge structures. Yet, more attention needs to be paid to the effect of cracking and stress on chloride ingress in concrete and reflect it in the durability and structural design standards (Lee and Christholm, 2000).

The work presented in this thesis is expected to shed some light on the effect of mechanical loading on chloride transport in concrete. The aim in establishing this relation is to forecast the possible movement and accumulation of chloride ions in the concrete by estimating the diffusion coefficients at different applied load levels. It is believed that the expected results will be useful to verify/modify numerical models on chloride ingress in

concrete, especially where the concrete is sustaining loads and is cracked, so that better predictions of the onset of chloride-induced steel corrosion and thus of service life and time for rehabilitation can be made.

1.4. Outline of the thesis

Chapter 2 presents a literature survey of research related to chloride penetration into concrete in general and in cracked concrete in particular. The review focuses on published experimental studies dealing with the effect of concrete cracking on transport properties.

Chapter 3 presents the detailed experimental program on which this thesis work is based. It includes a description of the test specimen and related specifications, the materials used, and the casting and curing processes. In addition, the chloride exposure regime and mechanical loading system used are explained. Both data collection of chloride concentration and strains are described.

A detailed discussion on the experimental results is presented in Chapter 4. Assessment of chloride ingress properties are presented in Chapter 5. Finally, conclusions gained from this research as well as recommended future work are discussed in Chapter 6.

Chapter 2

Literature Review

2.1. Chloride transport mechanisms in concrete

The main mechanisms of chloride transport in concrete as described by Poulsen and Mejlbro (2006) are:

(1) Diffusion: in which the driving force responsible for chloride ions movement is the difference in ion concentration between two points, known as concentration gradient. Chloride ions migrate from zones of high concentrations to zones of low concentrations, provided that the medium is saturated; this process reaches equilibrium once the concentration is the same between the two points.

(2) Permeation: in which the driving force responsible for chloride ions movement is the hydraulic pressure difference between two points. Chloride ions will move from zones of high hydraulic pressure to zones of low hydraulic pressure. Foundations exposed to water contaminated with chloride ions are an example of concrete structures subjected to chloride permeation.

(3) Migration: also known as electro-migration, in which the driving force is the difference in electrical potential between two points.

(4) Convection: in which the driving force is capillary absorption of chloride-laden water by dry concrete. Chloride ions move from zones of high moisture content to zones of low moisture content due to water flow. This transport mechanism occurs at a much faster pace than pure diffusion, as chloride ions move with the water flow. A good example where this mechanism is observed is in concrete structures subjected to wetting and drying cycles. In the drying cycle, the concrete surface gets dry due to moisture evaporation; however, once the surface gets wet, chloride ions move in as water is absorbed resulting in an accumulation of chlorides.

Diffusion is regarded as the main transport mechanism governing chloride ingress in concrete (Poulsen and Mejlbro, 2006). The diffusion process is well described by Fick's laws. Fick's 1st law of diffusion states that the chloride flux q (i.e., the rate of transport of chloride ions perpendicular to a unit area of concrete per unit time) is proportional to the concentration gradient, i.e.,

$$q = -D\frac{\partial C}{\partial x} \tag{2.1}$$

where

q = flux of chloride ions due to diffusion per unit area of solution in the x direction ($kg/m^2 \cdot s$);

D = diffusion coefficient (m^2/s), which depends on the concrete characteristics and exposure time. The value of the diffusion coefficient changes as different units are used;

C = chloride mass per unit volume or concentration of chlorides dissolved in the pore solution (kg/m^3 of pore solution); and,

x = depth at which C is calculated measured normal to the exposure surface (m).

The negative sign in Eq. (2.1) means diffusion occurs in a direction opposite to that of increased concentration. The assumptions underlying Eq. (2.1) are: steady–state regime, pure diffusion, and isotropic medium. A representation of Fick's first general law of diffusion is shown in Figure 2.1.

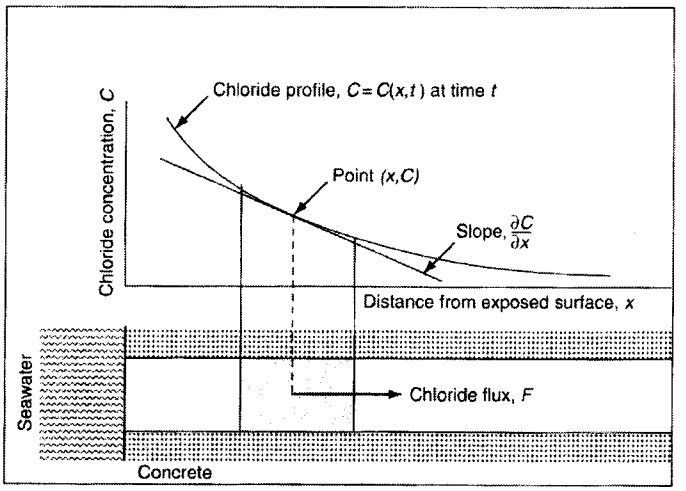

Figure 2.1: Fick's first general law of diffusion expresses that the flux of chloride ions is proportional to the chloride concentration gradient normal to the section (reproduced from Poulsen and Mejlbro, 2006).

Chloride mass balance requires that the change in chloride content per unit time is equal to the difference in chloride flux per unit time as illustrated in Figure 2.2, i.e.,

$$\frac{\partial C}{\partial t}dx = q - \left(q + \frac{\partial q}{\partial x}dx\right) = -\frac{\partial q}{\partial x}dx \qquad [\text{kg/m}^3\cdot\text{s}] \qquad (2.2)$$

which leads to:

$$\frac{\partial C}{\partial t} = -\frac{\partial q}{\partial x} \qquad [\text{kg/m}^3\cdot\text{s}] \qquad (2.3)$$

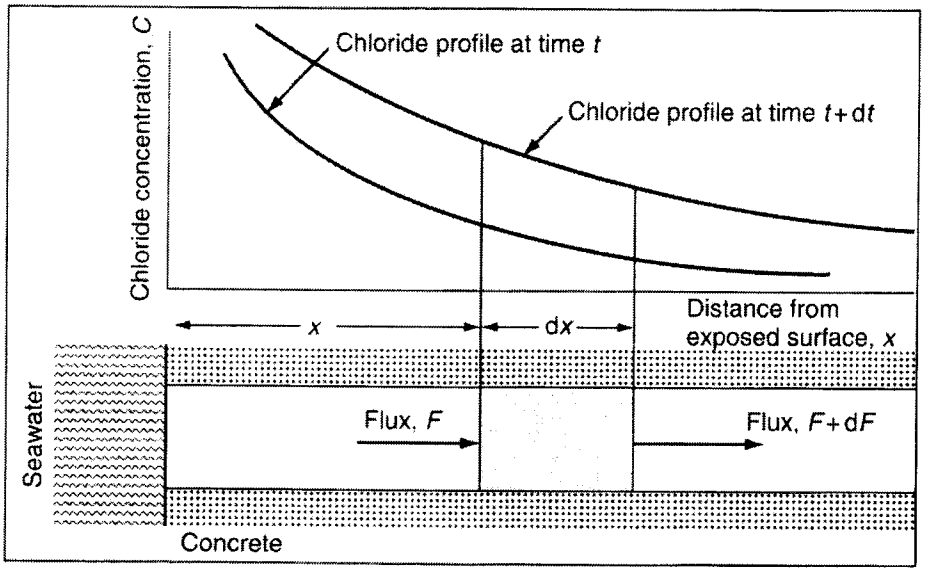

Figure 2.2: Fick's second general law of diffusion expresses that changes in chlorides per unit time (on the *t*-axis) is equal to the change of flux per unit length (on the *x*-axis) (reproduced from Poulsen and Mejlbro, 2006).

By substituting q from Eq. (2.1) into Eq. (2.3), the following expression results:

$$\frac{\partial C}{\partial t} = \frac{\partial}{\partial x}\left(D\frac{\partial C}{\partial x}\right) \qquad [\text{kg/m}^3\cdot\text{s}] \qquad (2.4)$$

Equation (2.4) is Fick's second law of diffusion in one dimension. An analytical solution to Eq. (2.4) for a semi-infinite medium with initial condition $C(x > 0, t = 0) = 0$ and boundary condition $C(x = 0, t > 0) = C_0$, where C_0 is the chloride concentration at the surface $x = 0$, is given by Crank (1975) as:

$$C(x,t) = C_0\left[1 - erf\left(\frac{x}{\sqrt{4Dt}}\right)\right] \qquad [kg/m^3] \qquad (2.5)$$

where

$C\ (x,\ t)$ = total chlorides at depth x after time t (kg/m^3);

C_0 = chloride concentration at the surface x = 0 (kg/m^3), assumed to be constant in time and space;

D = diffusion coefficient; and,

erf = error function.

Equation (2.5) is used to find chloride concentrations at any depth for a given period of time assuming that the concrete is homogenous and that D and C_o are constant. According to Atkins et al. (2001), the existence of cracks in the field in addition to the heterogeneity of concrete make chloride ingress in concrete a more complex process than that mathematically expressed in Eq. (2.5).

2.2. Cracking in reinforced concrete structures

Reinforced concrete structures, unless they are prestressed, are designed to experience some degree of cracking under service loads. In fact, the stresses that develop in the reinforcement for an efficient composite action are usually higher than the tensile capacity of the concrete. Furthermore, concrete might experience additional cracking under in-service conditions due to (ACI 224, 2007):

(1) moisture or thermal gradients;

(2) differential settlement of foundations;

(3) chemical reactions;

(4) weathering;

(5) reinforcement corrosion;

(6) poor construction practices;

(7) construction or accidental overloads;

(8) errors in design and detailing.

CSA A23.3-04 does not specifically limit crack width in the design of RC members; however, it does provide provisions for minimum reinforcement amount and maximum reinforcement spacing to ensure those widths are kept to a minimum value and cracks are adequately distributed.

Cracking of concrete in RC members is controlled by: (1) the relative displacement between the reinforcing steel and the concrete through bond action, and (2) the carrying of tensile stresses by the reinforcement across a crack. Whereas the first mechanism sets off concrete micro-cracking in the vicinity of the reinforcement (Goto, 1971), the second mechanism delays the opening of a macro-crack through the bridging effect of the reinforcing steel. Damage build-up in concrete as a result of the first mechanism develops in three stages as illustrated in Figure 2.3 (Ben Romdhane and Ulm, 2002). As bond is activated, inclined micro-cracks start to grow from the reinforcement to approximately one-bar diameter thick zone around the rebars. As the tensile load in the reinforcement increases, these micro-cracks start to coalesce into radially propagating macrocracks, with the final stage corresponding to the propagation of these macro-cracks through the concrete cover. While the first stage mainly depends on the bond behaviour between the concrete and the steel (Goto 1971), the last stage largely depends on the cover depth and confinement conditions. According to Ben Romdhane and Ulm (2002), the characteristic length of the micro-cracked zone next to the reinforcement corresponds to eight reinforcing steel ribs along the reinforcing bar (see Figure 2.3). Hence, in most cases, the entire length between cracks is damaged, as experimentally observed by Goto (1971). From the previous description of damage build-up between cracks in the tensile zone of an RC beam, one can draw the following conclusions: (i) concrete surrounding the reinforcement is damaged in-between macro-cracks, with this damage being non homogeneous and non isotropic; and, (ii) the damage state at the interface between the steel and concrete plays an important role in the chloride transfer properties of the concrete, since this interface constitutes a preferential pathway for chloride ions coming from a crack surface. Therefore, research on the chloride transfer properties of concrete in the vicinity of a crack should account for the coupling between the opening of a crack and the simultaneous damage build-up of the concrete next to it. For a given crack width,

the damage that results in the concrete adjacent to the crack and reinforcing steel is different if plain bars rather than deformed bars are used for reinforcement.

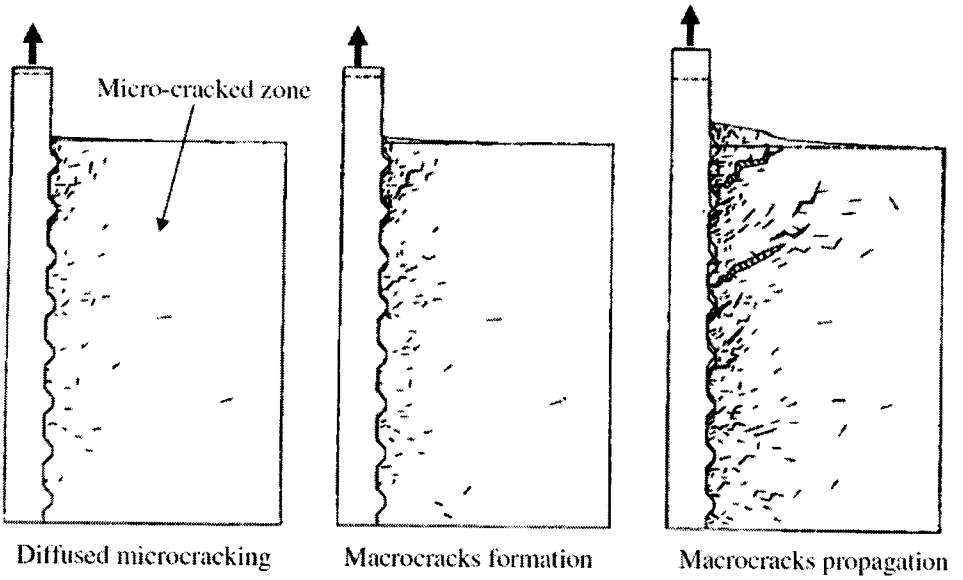

Figure 2.3: Damage build-up in concrete in the vicinity of a tensile reinforcing bar (reproduced from Ben Romdhane and Ulm, 2002).

At a certain stress level in the reinforcing steel, the width of a crack on the surface of the concrete increases with the cover thickness (Chen, 1998). This means that the ratio of crack width to concrete cover W_{cr}/C changes for RC members with different concrete covers. Therefore, this ratio can be used as a suitable parameter to consider in the durability performance of cracked reinforced concrete. For design of sea concrete structures, some standards suggest this ratio W_{cr}/C to be between 0.0025 and 0.0075 (Chen, 1998). ACI specifies an allowable crack width of 0.15 mm and minimum covers of 50-60 mm, resulting in W_{cr}/C of 0.0025-0.003. It is important to note that W_{cr} is usually specified or measured at the outer surface of the concrete cover, and this width does not necessarily correspond to the crack width near the reinforcement (see Figure 2.4).

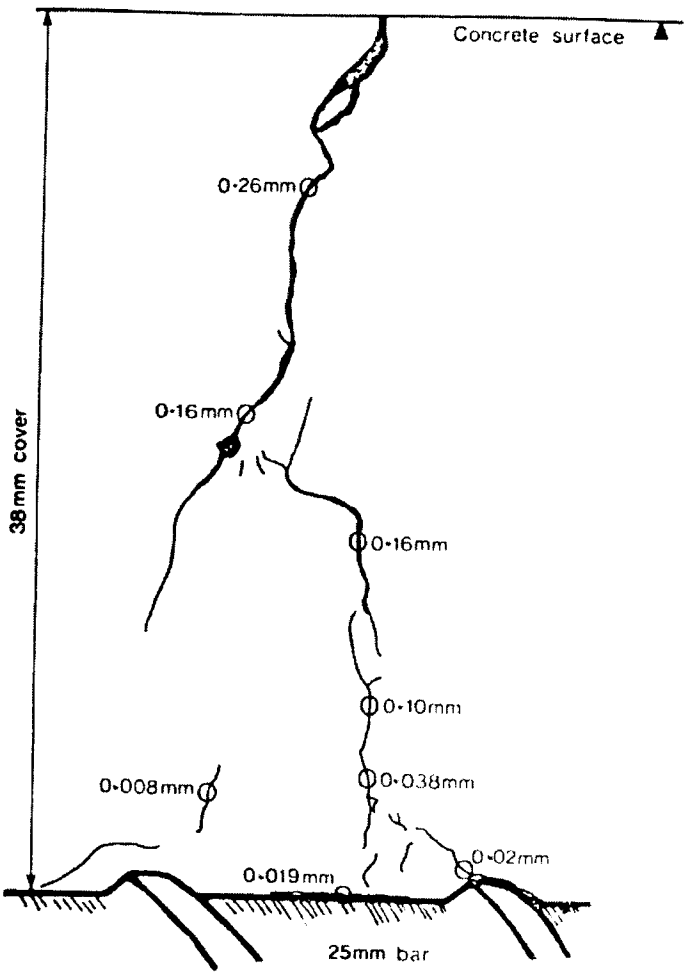

Figure 2.4: Cracking pattern and widths along the cover of a RC member observed by optical microscopy (reproduced from Diamond and Bentur, 1984).

Since it is clear that cracks offer a pathway for chloride ingress into concrete, and that some extent of cracking is expected in reinforced concrete under service conditions, then the effect of cracking on the transfer properties of chloride ions in concrete should be considered. This interaction will have an impact in the estimation of service life based on chloride-induced corrosion (see Figure 2.5).

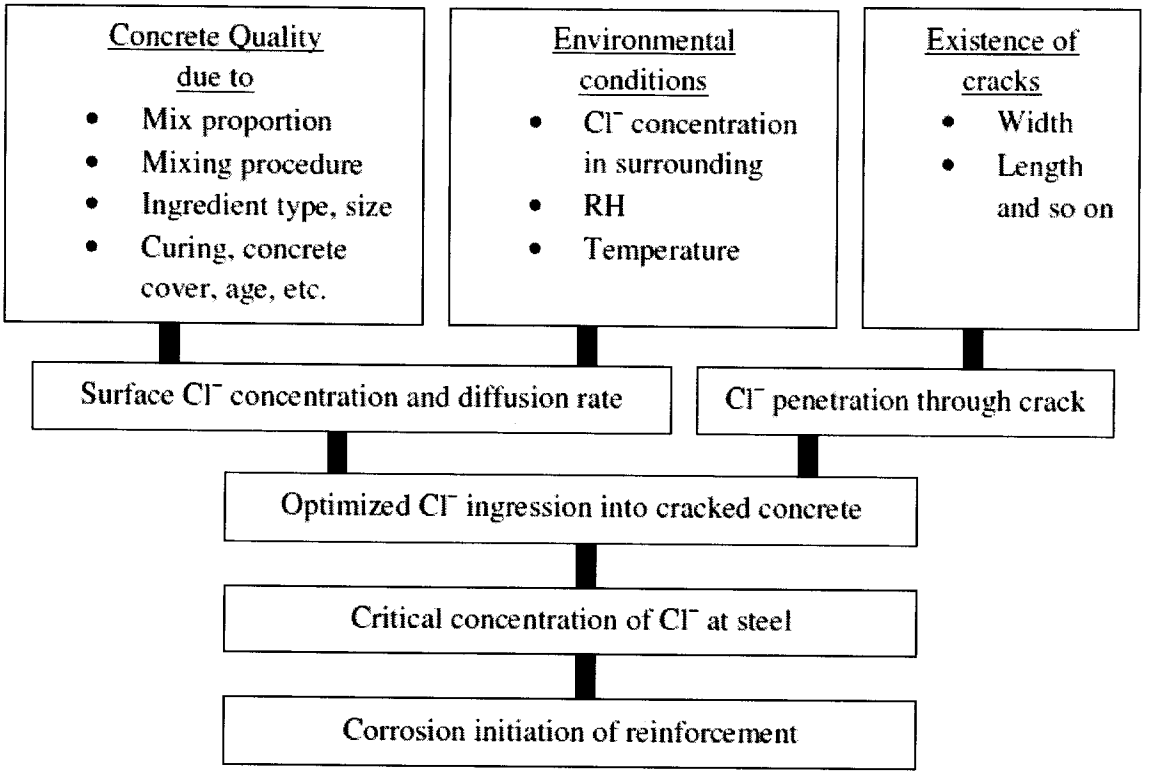

Figure 2.5: Chloride-induced corrosion in cracked RC structures (reproduced from Win et al., 2004).

2.3. Effect of cracking on transport properties

A review of experimental studies done on the effect of concrete cracking and sustained loading on chloride ingress in concrete is presented in the following two sections.

2.3.1. Experimental studies on mortar/concrete samples

Selvarajah and Johnston (1995) carried out an experimental program to study water permeation through cracked masonry blocks. In fact, cracks were artificially positioned by means of metal spacers between the masonry blocks, i.e., in the cement mortar that holds them together, as illustrated in Figure 2.6. The simulated crack widths were 0.7 mm, 1.00 mm and 2.00 mm. From their results, they observed that the water seepage rate through cracks mainly depends on the crack width as well as crack direction. For the same crack width, the seepage rates measured through vertical cracks were lower than through horizontal ones.

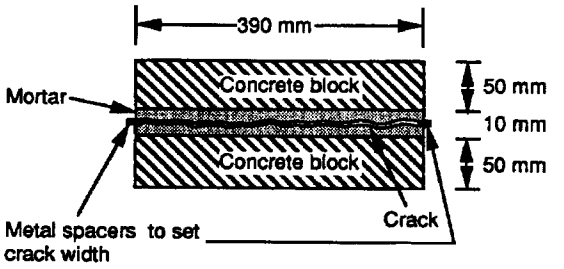

Figure 2.6: An artificial crack in the test specimen (reproduced from Selvarajah and Johnston, 1995).

Their experimental results, which relate the effects of cracks on water seepage, are summarized in the following equation:

$$Q = AQ_s \tag{2.6}$$

where

Q = seepage flow rate (l/s);

Q_s = spray flow rate (l/h); and,

A = empirical constant that varies according to crack width and orientation according to Table 2.1.

Table 2.1: Values of "A" in Eq. (2.6)

Crack width (mm)		Horizontal crack	Vertical crack
0.70	A	0.3049	0.0036
	R^2	0.95	0.04
1.00	A	0.3267	0.0267
	R^2	0.97	0.65
2.00	A	0.3327	0.0380
	R^2	0.99	0.82

R^2 = coefficient of determination

Jacobsen et al. (1996) studied the effect of cracking and healing on chloride migration transport in OPC concrete of w/c of 0.4. Cylindrical samples were subjected to chloride migration after exposing them to rapid freeze/thaw cycles. The findings revealed that due

to the internal micro-cracking caused by rapid freeze/thaw exposure, the compressive strength was reduced by 40–68%, whereas the chloride migration rate was increased by a factor of 2.5 to 7.9. Also, the migration time was reduced from 64 to 0 hours in the case of damaged samples. After the freezing/thawing cyclic regime, the samples were immersed in lime saturated water at 20°C for a period of three months. The healing process led to an increase in compressive strength up to 10% of the initial value and a decrease in chloride migration rates by 28–35%. It was observed that for air-entrained concrete with the same w/c ratio, chloride migration rates were not influenced by freeze/thaw cycles.

De Schutter (1999) tested six small-scale prisms of different mortar composition (all with w/c = 0.5), subjected to five different environmental conditions, in which both carbonation and chloride ingress were evaluated. The specimens' size was 40×40×160 mm^3. Artificial cracks were created by placing a thin copper sheet during casting, creating notches with widths of 0.2, 0.3, and 0.5 mm, and depths of 5 and 10 mm. Chloride penetration depths X were measured by spraying the samples with silver nitrate and were assumed to follow the equation below:

$$X = A_{CL}\sqrt{t} \tag{2.7}$$

where A_{CL} (mm/√year) is a constant affected by the chloride ion diffusion resistance of the material. The influence of crack width and depth was found by defining the crack influence factor (γ_{CL}), which is the ratio between the "A_{CL}" values of the cracked sample to the uncracked sample, i.e.,

$$\gamma_{CL}(w,d) = \frac{A_{CL}(w,d)}{A_{CL}(w=0,d=0)} \tag{2.8}$$

where:

γ_{CL} = the crack influence factor for chloride penetration;

w = the crack width; and,

d = the crack depth.

From regression analysis of the experimental data, Eq. (2.8) was re-written as:

$$\gamma_{CL} = \exp\left[0.2541\left(\frac{d}{d_0}\right)^{0.5202}\left(\frac{w}{w_0}\right)^{0.2652}\right] \tag{2.9}$$

A graphical representation of Eq. (2.9) is shown in Figure 2.7 for different crack influence factors.

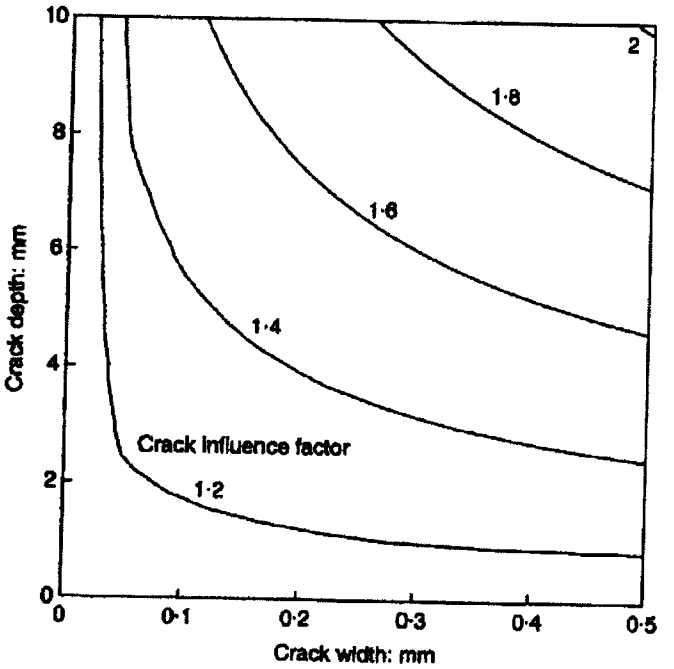

Figure 2.7: Crack influence factor for chloride penetration (reproduced from De Schutter, 1999).

A shortcoming from studies such as the one carried out by De Schutter (1999) is the fact that the surface of artificial notches contain more cement than that of a real crack; the chloride transfer properties thus obtained might differ from concrete structures in actual field conditions.

Gérard and Marchand (2000) also studied the influence of cracking on the diffusion properties of cement-based materials by exposing concrete cylinders of 0.45 w/c to freezing and thawing cycles. The samples had a cement content of 433 kg/m^3 and were subjected to 31, 61, and 95 freezing and thawing cycles. Migration experiments were carried out on slices of 15-mm thickness. By assuming that cracks were uniform in size and uniformly distributed on a one- or two-dimensional grid (see Figure 2.8), the authors

proposed a model to account for the effect of cracking on the concrete chloride diffusivity:

$$\frac{D}{D_0} = \frac{\frac{D_1}{D_0} + S}{1 + S} \tag{2.10}$$

where

D = the apparent diffusion coefficient of the cracked material (m^2/s);

D_0 = the diffusion coefficient of the species in the homogeneous (uncracked) material (m^2/s);

D_1= the diffusion coefficient of a given ionic (or molecular) species in free solution (m^2/s);

$$S = \begin{cases} A_m / A_c & \text{for an isotropic, 2-D crack network} \\ (L_1 - L_4)/L_4 & \text{for an anisotropic, 1-D crack network} \end{cases}$$

A_m = the total area perpendicular to the diffusion flux of uncracked material (m^2);

A_c= the total area perpendicular to the diffusion flux of cracked material (m^2);

L_1 = the mean crack spacing; and,

L_4 = the mean aperture of the cracks.

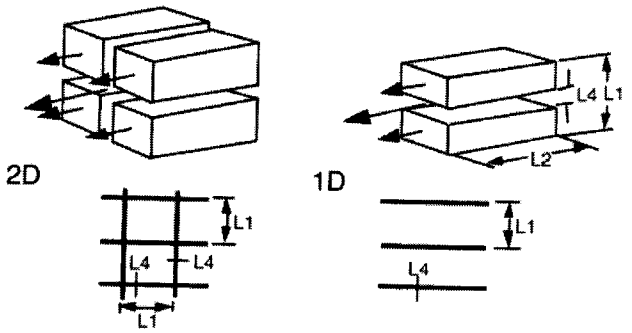

Figure 2.8: Schematic representations of the crack patterns considered: (a) isotropic (2-D) cracking; (b) anisotropic (1-D) cracking (reproduced from Gérard and Marchand, 2000).

Garces Rodriguez and Hooton (2003) studied the influence of cracks on chloride ingress into concrete by varying crack widths as well as the roughness of the crack

surface. Cracks were artificially created by either saw-cutting (smooth surface) or splitting (rough surface) concrete cylindrical specimens, and cracks widths ranged from 0.08 to 0.68 mm. Two different concrete mixtures, with the same w/c of 0.40, were used: OPC and OPC with 25% of slag replacement. The samples were immersed in a chloride solution with 2.82 mol/L concentration for 40 days. Their findings, shown in Figure 2.9, revealed that for the range of values studied, there was no effect of the crack width or surface roughness on the penetration rate of chlorides in concrete. However, the diffusion coefficient for the mixture with 25% slag replacement was lower than that of the OPC mixture.

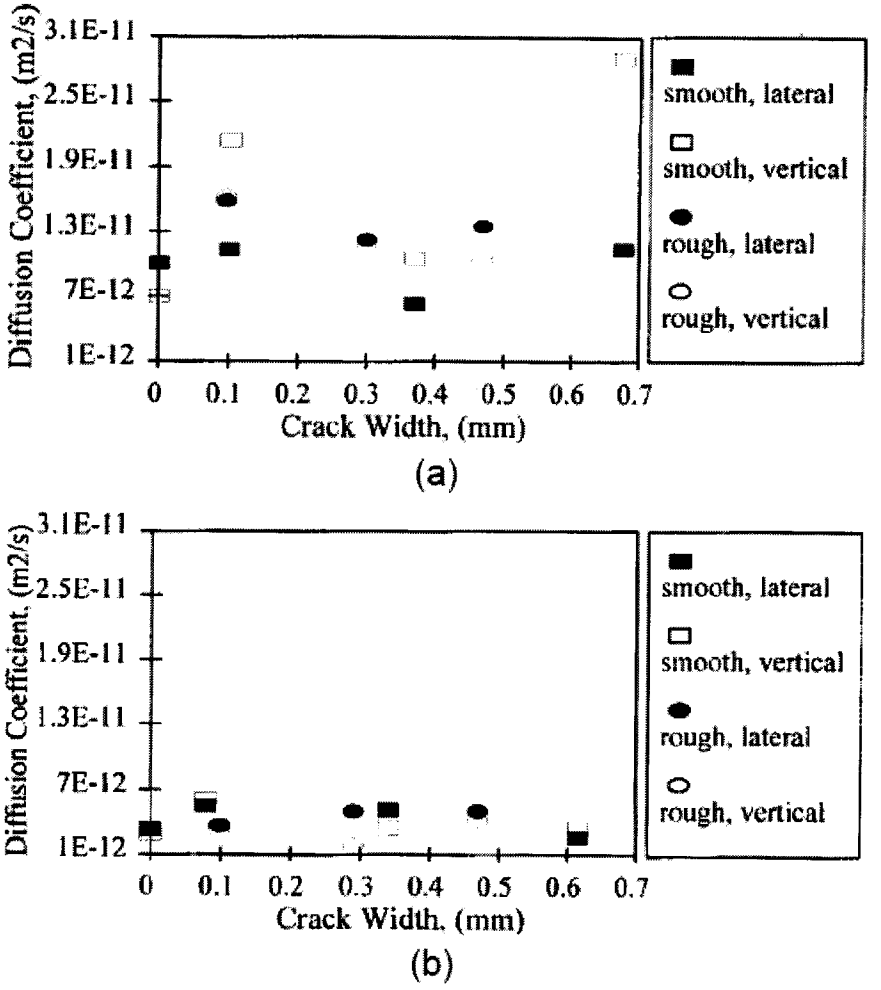

Figure 2.9: Chloride diffusion coefficient versus crack width: (a) 0.40 w/cm, 100% OPC concrete; and (b) 0.40 w/cm, 25% slag replacement (reproduced from Garces Rodriguez and Hooton, 2003).

The effects of transverse cracks (ranging from 30 to 250 μm in width) on chloride diffusion was also studied by Djerbi et al. (2008). Steady state migration tests were used instead of diffusion experiments to shorten the testing time. In this experimental program, three concrete mixes of w/c of 0.5 (ordinary concrete), 0.32 (high-performance concrete), and 0.38 (high-performance concrete with 6% of silica fume) were tested. For each mix, twenty cylinders of 110×220 mm^2 dimensions were prepared. Discs of diameter of 110 mm and thickness of 50 mm were sawed and pre-cracked by a controlled splitting test, as illustrated in Figure 2.10.

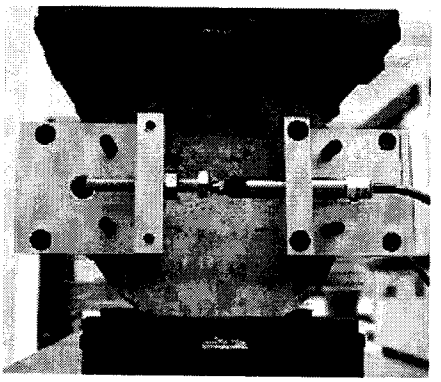

Figure 2.10: Controlled splitting test (reproduced from Djerbi et al., 2008).

From the analysis of their experimental results, the authors modelled the chloride diffusion coefficient of a cracked sample by superimposing the chloride diffusion fluxes in un-cracked and cracked specimens (see Figure 2.11), leading to Eq. (2.11) for the diffusion coefficient through a crack:

$$D_{cr} = \frac{A(D - D_o) + A_{cr} D}{A_{cr}} \tag{2.11}$$

where

D_{cr} = the diffusion coefficient through the crack (m^2/s);

A = the cross-sectional area of concrete (m^2);

D = the diffusion coefficient in a cracked specimen (m^2/s);

D_o = the diffusion coefficient in an un-cracked specimen (m^2/s); and,

A_{cr} = crack area (m^2).

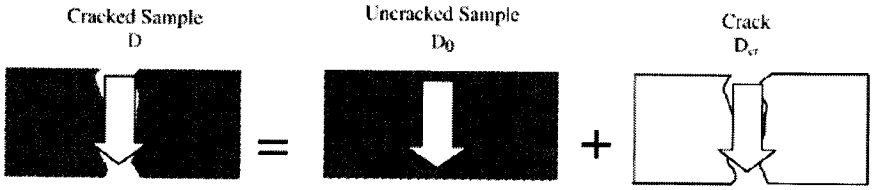

Figure 2.11: Superposition hypothesis of chloride diffusion through cracked concrete (reproduced from Djerbi et al., 2008).

The relationship of crack width versus the chloride diffusion coefficient through the crack D_{cr} calculated according to Eq. (2.11) is shown in Figure 2.12. It is observed from this figure that there is a linear relation between the crack width w and D_{cr} for crack widths up to 0.08 mm, beyond which D_{cr} remains constant. A mathematical expression of the relation plotted in Figure 2.12 is expressed in Eq. (2.12):

$$\begin{aligned} D_{cr} &= 2\times10^{-11}w - 4\times10^{-10} \quad [\mathrm{m^2/s}] \quad \text{for} \quad 30\mu\mathrm{m} \le w \le 80\mu\mathrm{m} \\ D_{cr} &\approx 14\times10^{-10} \qquad\qquad\quad [\mathrm{m^2/s}] \quad \text{for} \quad w \ge 80\mu\mathrm{m} \end{aligned} \tag{2.12}$$

The results illustrated in Figure 2.12 agree with those obtained by Garces Rodriguez and Hooton (2003), who also observed that the chloride diffusivity was not affected by crack widths in the range of 0.08 to 0.68 mm.

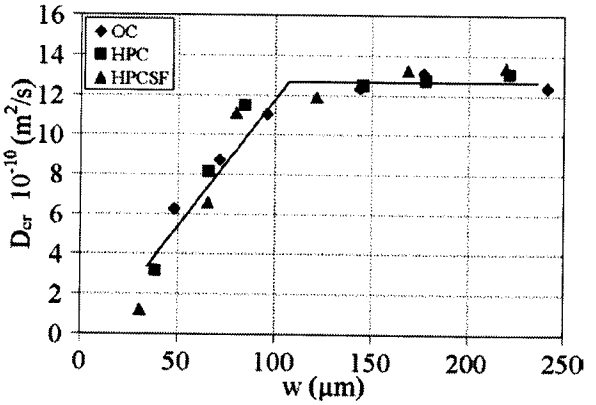

Figure 2.12: Effect of crack width on the diffusion coefficient through a crack (reproduced from Djerbi et al., 2008).

Ismail et al. (2008) also studied chloride penetration through cracked mortar discs (150-mm diameter and 50-mm thickness) with a w/c of 0.48. Crack widths, which ranged

from 6 to 325 μm, were created by applying an internal pressure through the centre of the disc (see Figure 2.13). The sample was then fitted into a chloride penetration cell (Figure 2.14). From their measurements, the authors observed that there is no chloride diffusion for samples with crack widths ≤ 60 μm created at 28 days compared to those samples whose cracks were created after 2 years. This phenomenon was attributed to the self-healing of cracks at early ages. They also studied the effect of crack roughness by cutting smooth cracks of 81 and 225-μm width with a circular saw. Their results showed that chloride diffusion normal to the crack surface was not affected by cracks greater than 205-μm width, which means that the crack tortuosity has no effect on chloride ingress for higher crack widths. This observation was also reported by Garces Rodriguez and Hooton (2003). The chloride profiles experimentally obtained by Ismail et al. (2008) are plotted in Figure 2.15. The effect of crack widths on chloride ingress is clearly seen when comparing the profiles for samples with narrow cracks (84 μm) created after 28 days and 2 years, wider cracks (>205 μm) created after 28 days and 2 years, and samples made with an inert material in order to highlight the effect of self-healing.

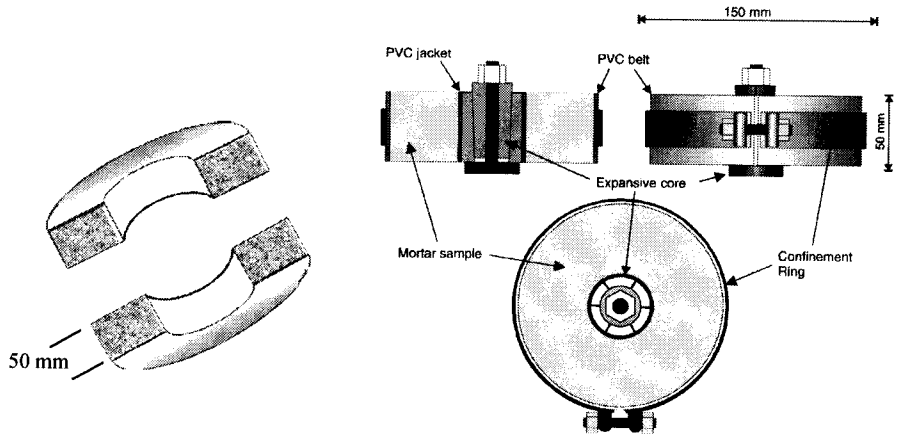

Figure 2.13: Sample dimensions and schematic view of the procedure used to produce simulated cracks (reproduced from Ismail et al., 2008).

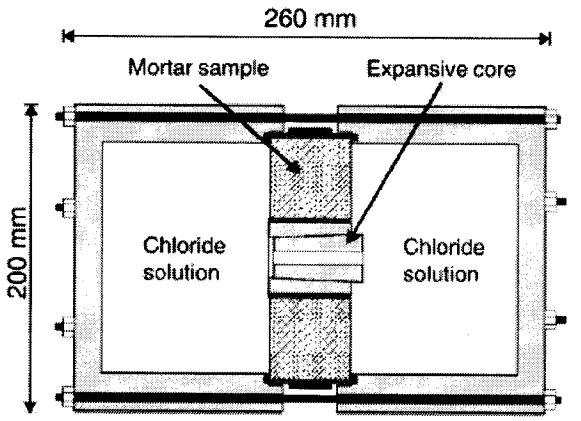

Figure 2.14: Chloride penetration cell (reproduced from Ismail et al., 2008).

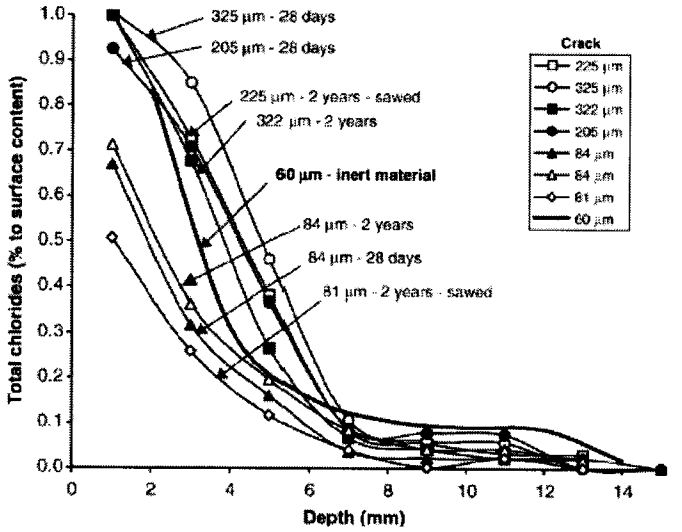

Figure 2.15: Selected chlorides penetration profiles obtained from mortars discs at 28 days and 2 years (reproduced from Ismail et al., 2008).

2.3.2. Experimental studies on structural concrete samples

Heideman and Sundström (1995) studied the effect of stress on chloride penetration into concrete by testing concrete specimens in both compression and flexural tension. Specimens subjected to compression were cubes of dimensions of 100×100×100 mm^3, whereas those subjected to flexural tension were RC beams of dimensions of 100×150×800 mm^3. The applied loading levels were 50% and 75% of f'_c. The specimens were immersed in a 3% chloride solution for 5 weeks while sustaining the load. The

specimens had a water-to-cement ratio of 0.45 and 0.65. A third set of specimens had micro silica added with a w/c ratio of 0.35. For specimens subjected to axial compression, the effect of compressive stress level sustained was only detectable in the concrete specimens with a w/c of 0.65. Likewise, for the RC beams under flexural loading, the stress level was slightly significant in the concrete with the highest w/c. The authors concluded that the lack of a strong effect between applied load level and chloride penetration depth might have been due to the heterogeneity of the concrete materials, the limited number of tested specimens, and incomplete experimental procedures.

Konin et al. (1998) carried out an experimental program on structural concrete samples in order to relate chloride profiles and diffusion coefficients to the applied loading. They tested nine prisms of 10×10×50 cm^3 dimensions and different compressive strengths (45, 80 and 100 MPa) with a centered rebar of 16-mm diameter, as illustrated in Figure 2.16. The samples were preloaded and exposed to a salt fog, which was applied every two weeks for a period of 6, 9 and 12 months. The chloride concentration in the fog was 35 g/1, and the fog was applied by four sprays fixed at the four upper corners of a closed chamber. The findings showed that there is a linear relationship between the apparent chloride diffusion coefficient D_a and the concrete compressive strength. The authors also established a relationship between D_a and the applied load level, given as:

$$D_a(\sigma_s) = D_{ao}\left[1 + L(\sigma_s)\right] \tag{2.13}$$

where

$D_a(\sigma_s)$ = the apparent diffusion coefficient at the given load level as expressed by σ_s;

D_{ao} = the apparent diffusion coefficient for the unloaded specimen;

$L(\sigma_s)$ = load function, given by $L(\sigma_s) = 598(E) - 8(\sigma_s)^3$;

E = Young's modulus for the reinforcing steel bar; and,

σ_s = the maximum stress in the rebar when the concrete is cracked.

The relationship as expressed in Eq. (2.13) was obtained from regression analysis of the experimental values after 9 months of exposure, as illustrated in Figure 2.17.

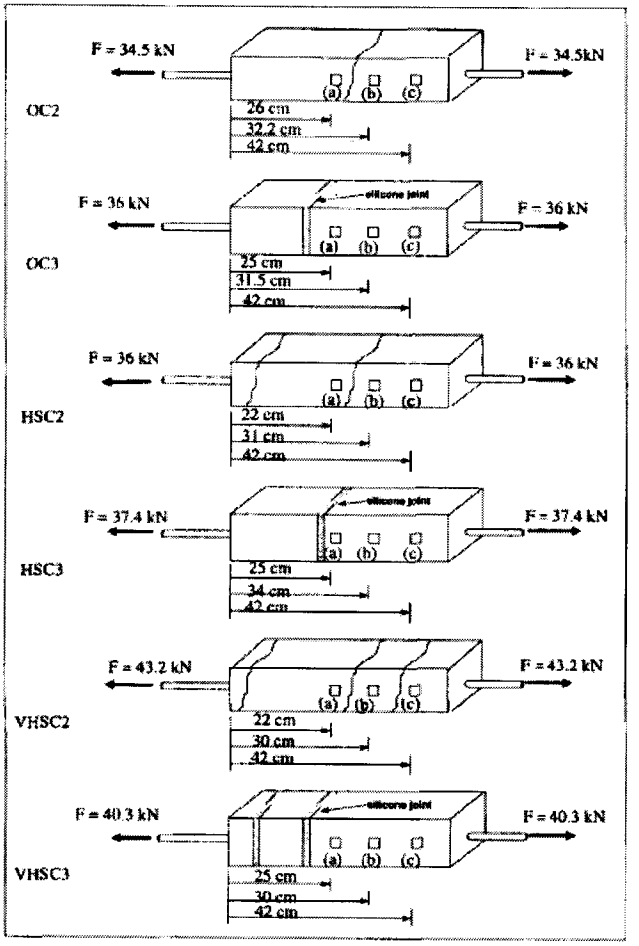

Figure 2.16: Specimens at different loading conditions and locations of powder samples (reproduced from Konin et al., 1998).

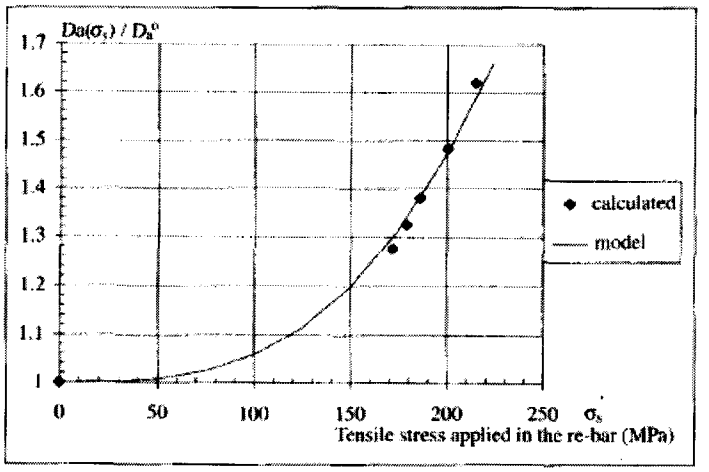

Fig. 2.17: Evolution of D_a/D_{ao} ratio in relation to the loading level after 9 months of exposure (reproduced from Konin et al., 1998).

Gowripalan et al. (2000) suggested that the crack width/cover ratio (W_{cr}/C) can be considered as a good indication for durability performance of cracked reinforced concrete members. In this study, 90×100×650 mm^3 concrete prisms with concrete cover equal to 30 mm were pre-cracked by means of flexural loading, with crack widths up to 0.3 mm (see Figure 2.18).

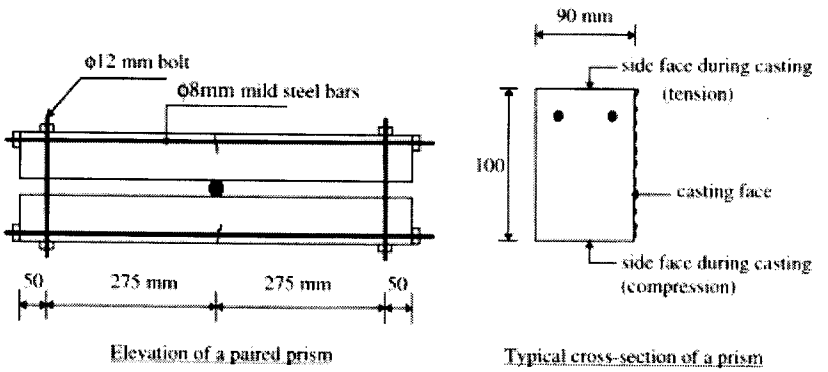

Figure 2.18: Experimental set-up (reproduced from Gowripalan et al., 2000).

In order to avoid wall effects due to casting, the specimens were casted sideways as illustrated in Figure 2.18. The specimens were immersed in a 3% NaCl solution for 300 days. From their results, the crack width/cover ratio (W_{cr} /C) and the chloride threshold level were related according to a hyperbolic relationship. Furthermore, the authors found that the apparent chloride diffusion coefficient was higher in the tensile zones of the beams than in the compression zones. The authors attributed the lower diffusion coefficient in the compression zone to the reduction in porosity due to compressive stresses.

Chloride ion profiles through and around cracks in reinforced concrete flexural members were also studied by Win et al. (2004). In order to determine the presence of chloride ions in the concrete, both colorimetric tests and electron probe microanalysis (EPMA) were used. The samples were 400×100×100 mm^3 in dimension and were reinforced with 2-10 mm diameter reinforcing bars at the tension side (see Figure 2.19): plain bars for single-crack specimens and deformed bars for multi-crack specimens. The cracks were created prior to exposure through three-point and four-point loading configurations. The obtained crack widths ranged from 0.1 to 0.2 mm. Specimens were

immersed in a sodium chloride solution for a test period that varied up to two months. The findings revealed that the existence of cracks not only facilitates chloride penetration towards the reinforcement, but it also promotes chloride ingress along the reinforcing bars (with the exception of the specimen with the lowest w/c of 0.25). The effect of cracking on chloride profiles in concretes with w/c of 0.45 and 0.65 is observed in Figure 2.20.

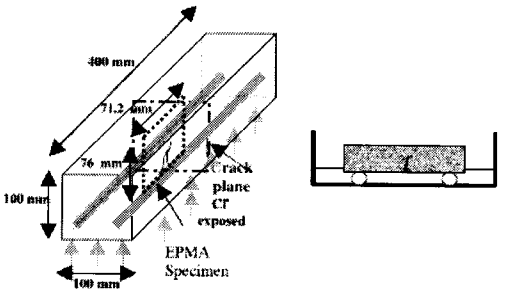

Figure 2.19: Beam specimens used (reproduced from Win et al., 2004).

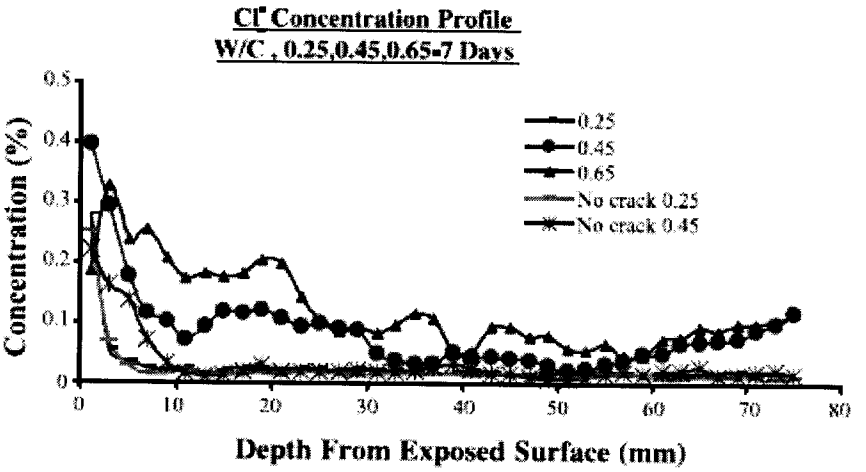

Figure 2.20: Chloride concentration profiles for different w/c (reproduced from Win et al., 2004)

Maruyama et al. (2006) studied the effect of cracking on chloride ingress into concrete samples subjected to wet-dry cycles by applying rain of salty water with a 3% NaCl solution (each cycle consisted of 7 days: 1 day of wetting and 6 days of drying). According to the authors, these exposure conditions represent the most aggressive environment with respect to reinforcement corrosion. Twelve reinforced concrete

specimens of 150×200×900 mm^3 dimensions and w/c of 0.40 were pre-cracked prior to exposure by creating two grooves in the mould before casting, in order to force the crack location at the centre of each specimen. The prisms were loaded in tension to achieve crack width targets, in the range of 0.25 to 0.30 mm, and non-shrink mortar was injected afterwards through the grooves, in order to maintain the achieved crack widths (see illustration in Figure 2.21). Applied loads were removed prior to exposure. Different waterproofing coating configurations were applied to the samples prior to immersion to represent all possible exposure situations in actual field conditions, as shown in Figure 2.22.

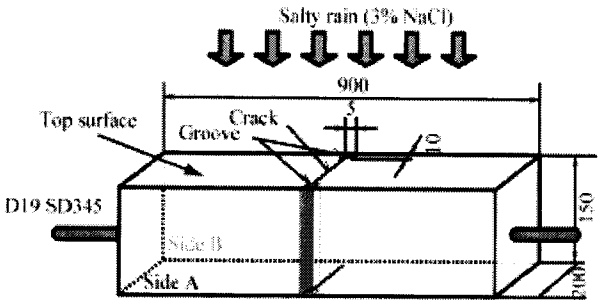

Figure 2.21: Specimen geometry (reproduced from Maruyama et al., 2006).

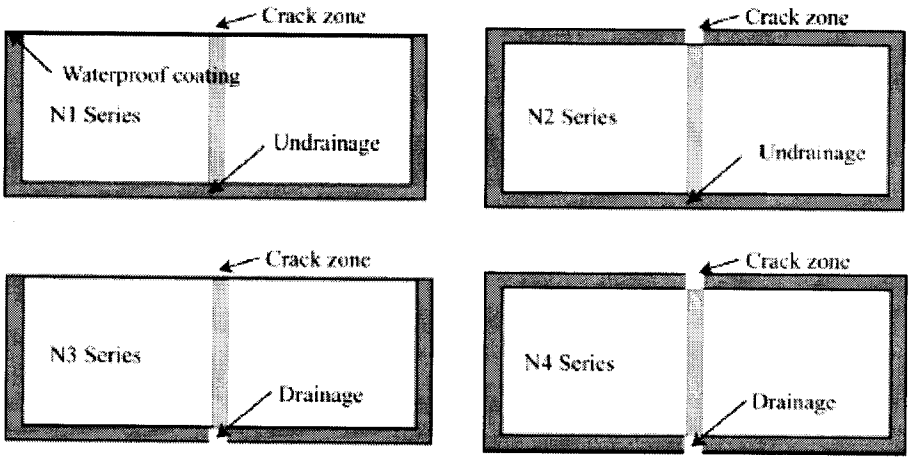

Figure 2.22: Specimen coating conditions (reproduced from Maruyama et al., 2006).

The measured chloride profiles after several wet/dry cycles are shown in Figure 2.23. These results reveal that the chloride content along the crack for the different

waterproofing configurations was indeed increased with the number of wetting and drying cycles, and the damaged concrete near cracks and along the reinforcing bars promoted this ingress (see Figure 2.24), as already observed by Win et al. (2004). The increase in chloride concentration due to wetting and drying cycles was also evident in those specimens where drainage was allowed, as illustrated in cases N3 and N4 in Figure 2.23.

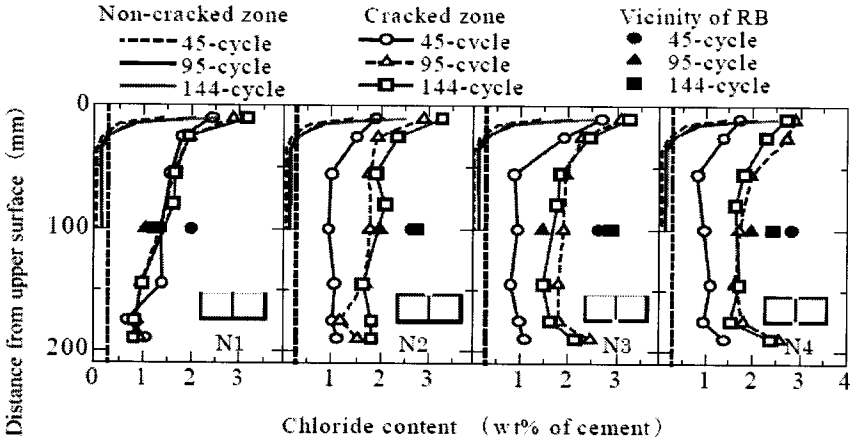

Figure 2.23: Profiles of chloride content after 45, 95, and 144 wet/dry cycles (reproduced from Maruyama et al., 2006).

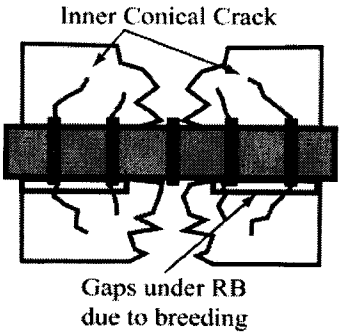

Figure 2.24: Concrete conditions in cracked zone (reproduced from Maruyama et al., 2006).

2.4. Experimental methods

A review of experimental methods that are commonly used for determination of chloride content in concrete and have been used in this research follows.

2.4.1. Silver nitrate solution spray

The average chloride penetration depth in concrete can be determined by spraying a silver nitrate ($AgNO_3$) solution of 0.1 mole/l on freshly split concrete samples. When free chlorides are present in the concrete, they react with the silver nitrate to form a white/gray precipitate (silver chloride). The chemical reaction that takes place is given by:

$$AgNO_3(aq) + NaCl(aq) \rightarrow AgCl\downarrow + NaNO_3(aq) \qquad (2.14)$$

This method, sometimes referred to as a colourimetric method, provides a quick and inexpensive way of estimating chloride contamination by measuring the depth of the colour change boundary (Otsuki et al. 1992, De Schutter 1999, Win et al. 2004, Marsavina et al. 2008). Figure 2.25 shows a concrete sample on which a $AgNO_3$ solution was sprayed to determine the chloride penetration front. However, this depth represents the average penetration front of free chlorides, i.e., chlorides dissolved in the concrete pore solution. The colourimetric method is a simple and fast technique to indicate whether or not free chlorides are present in the concrete. Some of the advantages of this technique are (Baroghel-Bouny and Maultzsch, 2007):

- simple and quick method;
- the potential to be carried out either in the field or laboratory;
- applicable to all kinds of concrete; and,
- not as expensive and time consuming as other methods.

It is important to note that spraying a concrete sample with a silver nitrate solution does not provide the value of chloride concentration at the boundary of colour change in the concrete. However, Otsuki et al. (1992) and Meck and Sirivivatnanon (2003) argue

that spraying a solution of $AgNO_3$ of 0.1 N concentration on fresh concrete is very useful in the risk assessment of steel reinforcement corrosion.

Figure 2.25: Local penetration of chlorides in a weak zone (around a reinforcing bar and cracks) detected by $AgNO_3$ spray (reproduced from Baroghel-Bouny and Maultzsch, 2007).

2.2.1. Titration

Titration is a quantitative method in which the actual chloride concentration at different penetration depths is estimated. The most well known procedure to carry out titration is described in the ASTM C 1152/C 1152M-04 standard. Although there is a general agreement among researchers that chlorides dissolved in the concrete pore solution are responsible for the initiation of reinforcing steel corrosion, the acid soluble test, which determines the concentration of total chlorides, is usually preferred over the water soluble test (to find free chlorides), since the results of the latter can be affected by a change in temperature, pH or pressure (Tritthart and Cavlek, 2000; Claisse, 2005; Poulsen and Mejlbro, 2006; Baroghel-Bouny and Maultzsch, 2007).

The procedure as outlined in the standard states that after adding nitric acid to the concrete sample, the titration process is carried to the filtered solution. However,

according to Climent et al. (1999, 2004) and Tritthart and Cavlek (2000), there is not a significant difference in the results if the samples are titrated without filtration. These authors argue that if there is any ionic effect from the existing suspended residue resulting from using the acid, then this effect will be positive near the end point where there is low chloride and silver concentrations. Furthermore, by eliminating the filtration step, common errors associated to this step due to solution losses are also eliminated (Climent et al., 2004).

2.5. Concluding remarks

With the exception of the studies carried out by Heideman and Sundström (1995) and Konin et al. (1998), there has not been a prior attempt to relate chloride ingress or chloride transfer properties to the actual level of loads sustained by reinforced concrete structures, regardless of the existence, characteristics and complexity of the resulting cracks. Konin et al. (1998) related the effective diffusion coefficient to the maximum tensile stress developed in the reinforcement. If the samples were considered small enough, the resulting stress distribution along the reinforcement could be considered uniform across the member section. However, since these were samples subjected to pure axial tension, the actual stresses were maximum at the reinforcing steel in-between cracks and minimum at the outer concrete surface, resulting in a maximum crack width at the rebar surface and minimum at the concrete surface. This loading condition does not actually reflect the actual stress and crack width distribution along the concrete cover of many practical and real conditions (see Figure 2.4). The main objective of this work is therefore to relate chloride ingress to parameters indicative of the mechanical state of the RC member.

Chapter 3

Experimental Program

3.1. Overview

The objective of this research is to study the effect of sustained mechanical loads on the rate of chloride penetration into concrete. To achieve this objective, a small-scale RC bridge deck was exposed to chloride de-icing salts while sustaining in-service loads. The RC slab was also subjected to three wetting/drying cycles in order to simulate conditions found in the field. This chapter presents a detailed description of the test specimen built for this research, the characteristics of the materials used as well as the instrumentation employed in the experimental set-up for data collection.

3.2. Test specimen

3.2.1. Specifications

To simulate an RC bridge deck, a 4.35-m long by 2.73-m wide RC slab was chosen as the test specimen. The slab was cast with three 0.91-m width strips of different w/c: 0.35, 0.40 and 0.50, which respectively meet the requirements for exposure classes C-XL (structurally RC exposed to chlorides with high durability performance expectations), C-1 (structurally RC exposed to chlorides), and C-3 (continuously submerged concrete exposed to chlorides) as defined in the standard CSA A23.1-04 (2004). Each concrete strip, of 155-mm depth, was reinforced with eight top and eight bottom deformed steel bars of 11.3-mm nominal diameter. Clear concrete covers to top and bottom reinforcements were respectively 50 mm and 45 mm. The yield strength of the reinforcing steel was 400 MPa. A cross section of a single strip of the RC slab is illustrated in Figure 3.1.

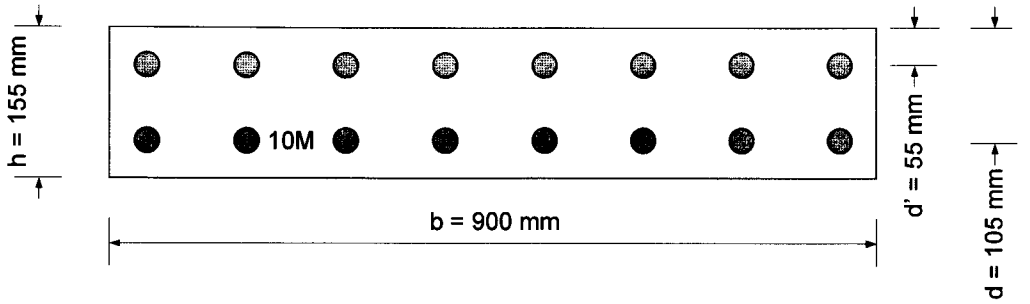

Figure 3.1: Details of the 0.9-m strip's cross section.

Each RC strip was simply supported at the one end and at 1260 mm from the other end, as illustrated in Figure 3.2. Supports were located to create both positive and negative moment regions in the slab. The span between supports was 2.73 m. A plan and elevation views of the bridge deck under study is shown in Figure 3.2. The slab dimensions as well as the location of supports and points of load application were determined by the distance between holes in the strong floor of the Structures Lab, which is 910 mm as shown in Figure 3.2. For safety purposes, the simple support at the right end was achieved by connecting the slab to the support with threaded bars with un-tightened nuts (see detail in Figure 3.3). This system was provided to avoid unexpected accidents during the loading process and test.

Because of the large width of each strip (910 mm), four transverse reinforcement bars were provided in two layers; two in each layer, at sections where the concentrated load was applied, in order to ensure the distribution of the axial load across the whole width of the strip (see detail in Figure 3.4). Reinforcement details for the left support and the simple support provided at that section are respectively shown in Figures 3.5 and 3.6. Note that at sections where the load is applied as well as at the two supports, steel chairs were provided in order to maintain the concrete cover design (see Figure 3.5). Section (E) in Figure 3.2 is shown in Figure 3.7. Concrete blocks of $165\times165\times100$ mm^3 dimensions were cast at locations where the concentrated load is applied, as illustrated in Figure 3.7. These blocks were confined by bottom and top square FRP stirrups of 9×9 mm^2 cross section and 160×160 mm^2 overall dimensions. The reason behind building these concrete blocks at these locations was to prevent chloride solution from filtrating through the holes. The completed bridge deck is shown in Figure 3.8.

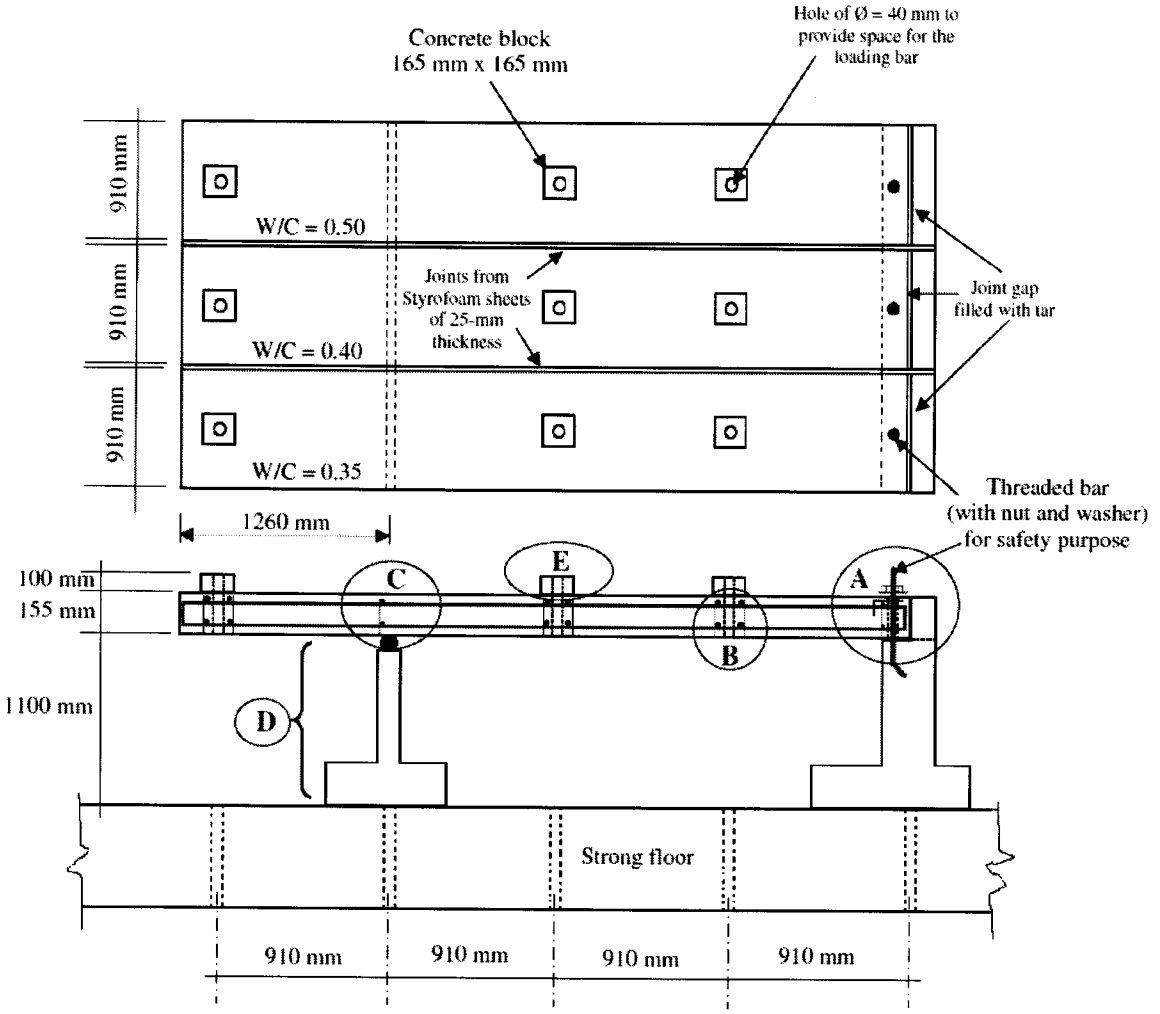

Figure 3.2: Plan and elevation views of the bridge deck (dimensions not to scale).

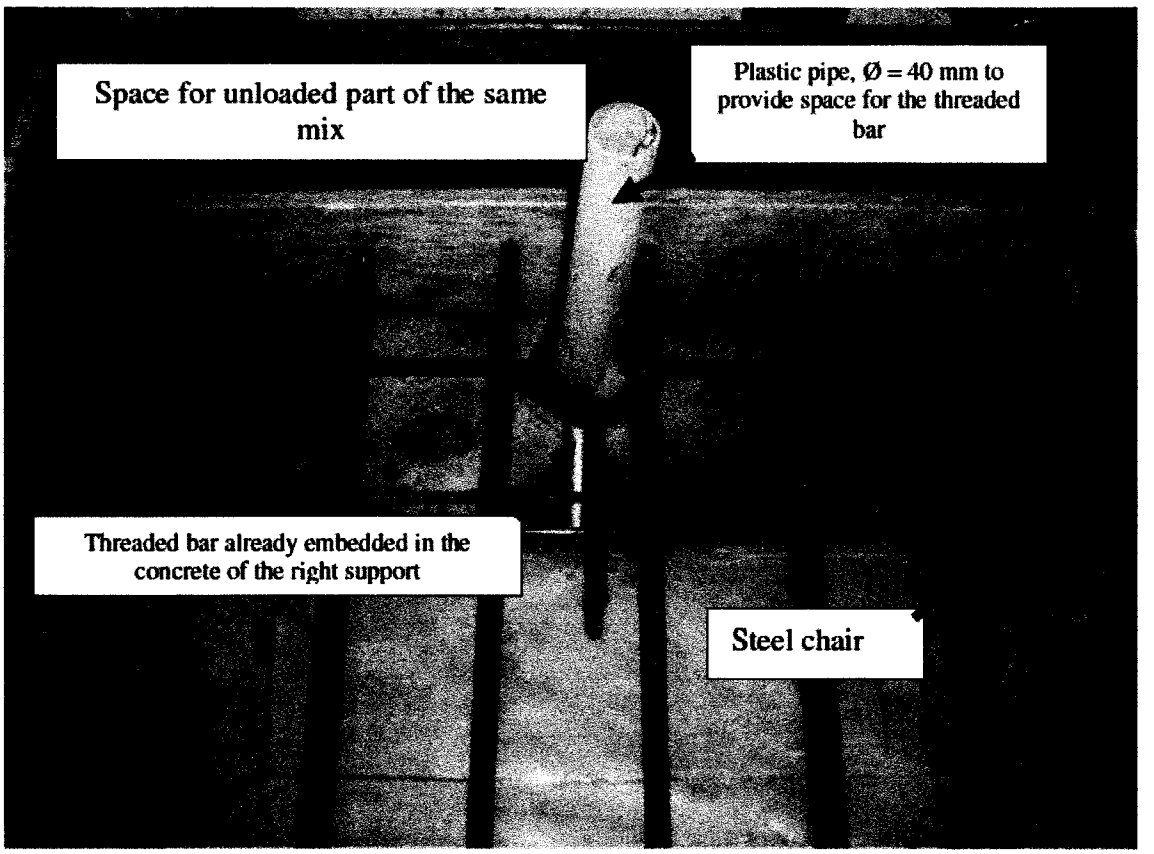

Figure 3.3: Details of simple support at right end (part (A) in Figure 3.2).

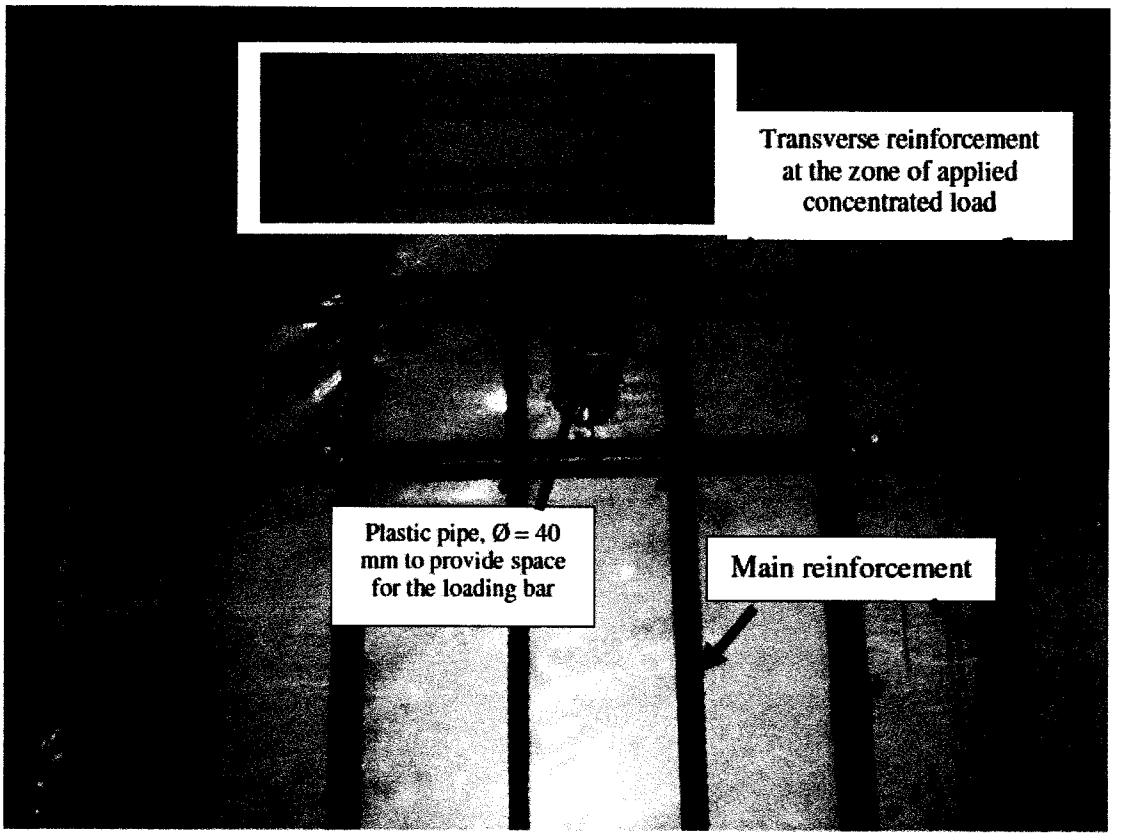

Figure 3.4: Transverse reinforcement at section (B) in Figure 3.2.

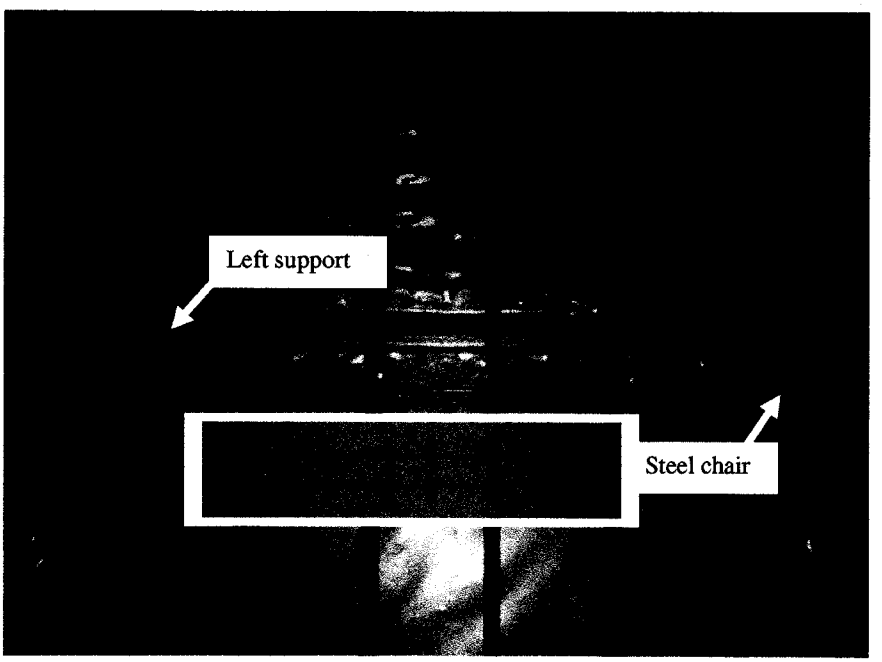

Figure 3.5: Reinforcement details at section (C) in Figure 3.2.

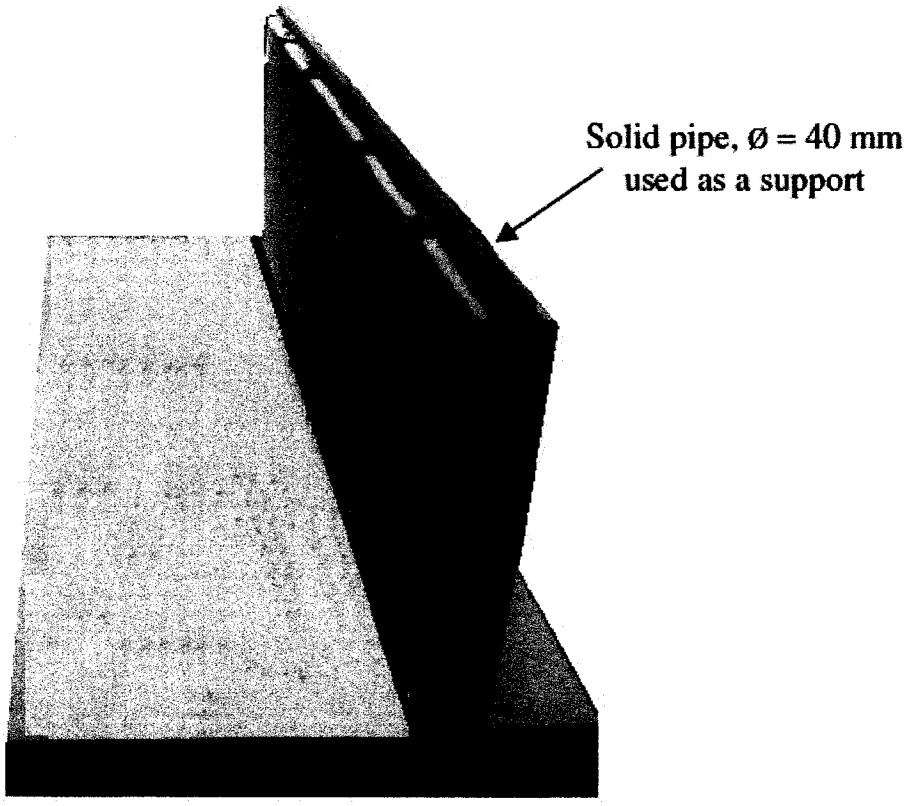

Figure 3.6: Simple support provided at section (D) in Figure 3.2.

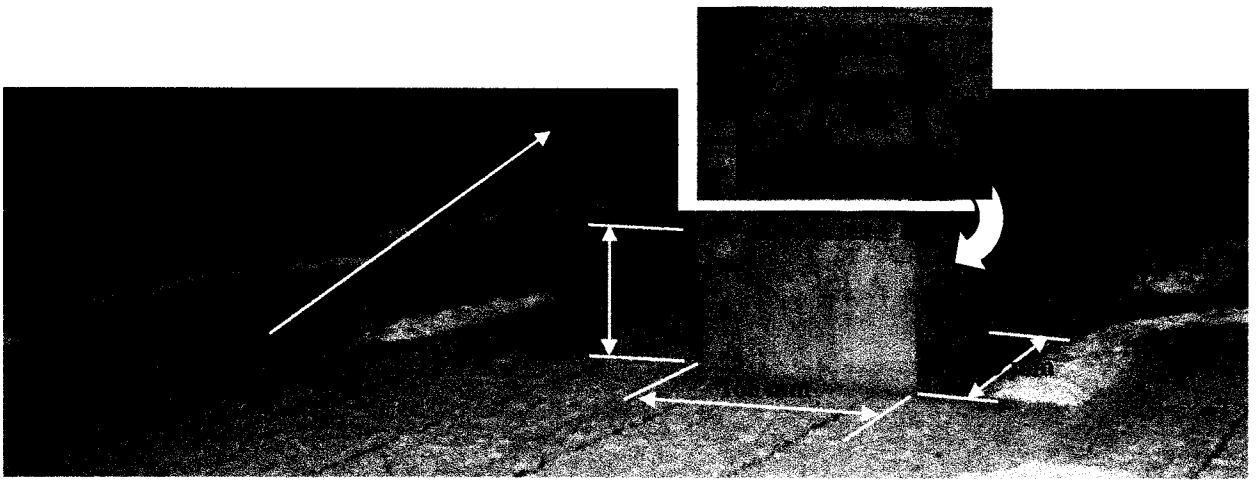

Figure 3.7: Geometric details at section where loads are applied (section (E) inFigure 3.2).

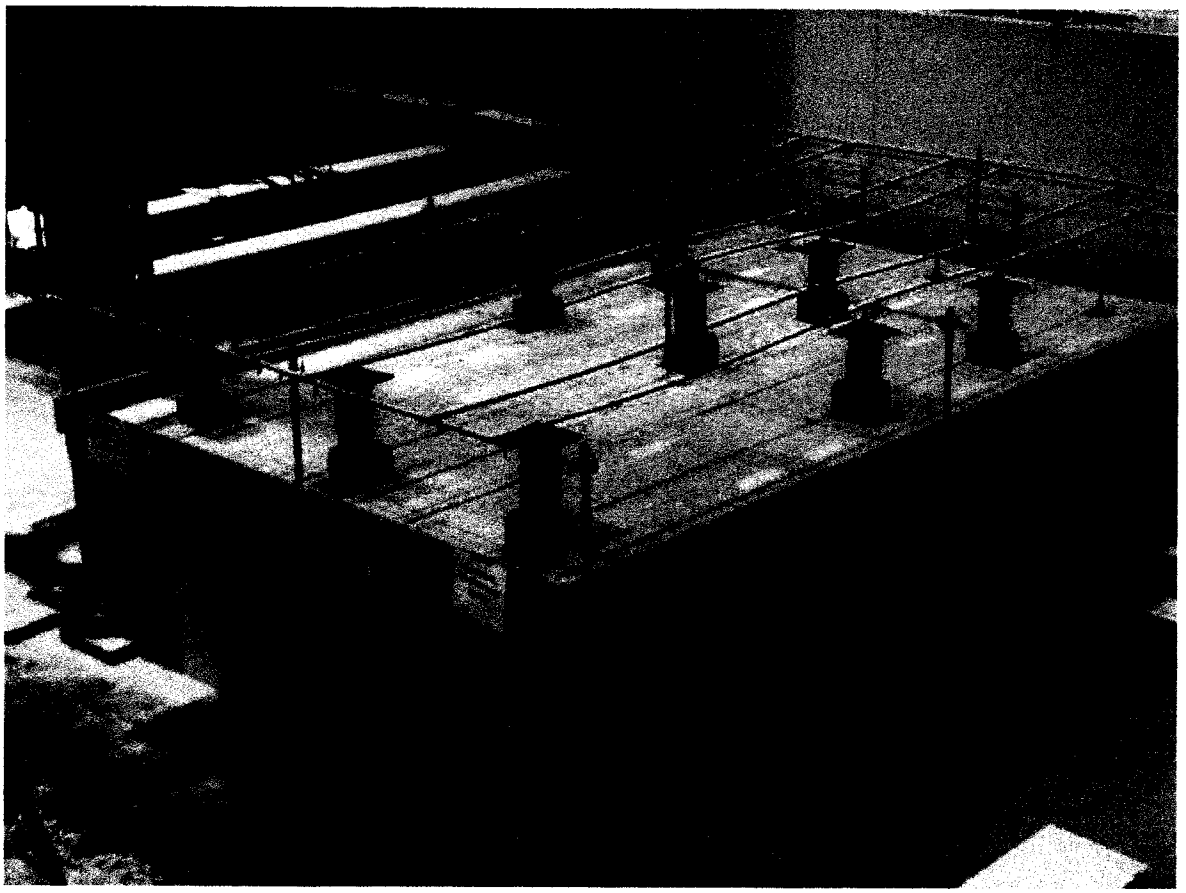

Figure 3.8: The completed bridge deck.

3.2.2. Materials

The slab was cast in three strips of different w/c to represent different concrete qualities found in the field. Ready-mix concrete provided by Lafarge was used to build the slab. The proportions of the mix ingredients used for each concrete strip are tabulated in Table 3.1. Portland cement GU was used. A water reducing admixture was added to the mix of w/c = 0.5 at a dosage of 600 ml/m^3, whereas super-plasticizer was added to the mixes of w/c = 0.35 and 0.4 at a dosage of 300 ml/m^3. Note that the mixes were ordered to Lafarge according to the required w/c ratios. The cement composition is given in Table 3.2. Both fine and coarse aggregates were well graded according to CSA A23.1-04 specifications. Gradation curves for the coarse and fine aggregates are illustrated in Figures 3.9 and 3.10, respectively.

Table 3.1: Concrete mix proportions (per m^3).

Material	w/c			Source
	0.35	0.40	0.50	
Cement (kg)	400	400	400	Lafarge
Coarse agg. –20 mm (kg)	1055	1048	1020	Tomlinson Moodie
Fine agg. (kg)	852	815	760	Burnside Moodie
Water (kg)	140	160	200	Well
Water reducer (ml)	-	-	600	Pozzolith210
Plasticizer (ml)	3000	1000	-	1466
Retarder (ml)	300	300	-	Pozzolith 100XR

Table 3.2: Physical and chemical data of the cement used (as provided by manufacturer).

Physical data		**Chemical data**	**Percent**
Blaine Surface Area (m^2/kg)	380	Aluminum Oxide (Al_2O_3)	4.6
Percent Retained 325 Mesh	3	Ferric Oxide (Fe_2O_3)	2.8
Compressive Strength (MPa) Mortar Cubes	3 day 25.2 7 day 31.6 28 day 42.1	Calcium Oxide (CaO)	62.7
Vicat Time Of Set (min.)	105	Magnesium Oxide (MgO)	2.6
Autoclave Expansion (%)	(Previous) 0.0	Sulfur Trioxide (SO_3)	3.2
Sulfate Expansion (%) 0.010	(Previous)	Loss on Ignition	1.9
		Insoluble Residue	(Previous) 0.4
		Free Lime	1.1
		Tricalcium Silicate (C_3S)	55
		Tricalcium Aluminate (C_3A)	7
		Equivalent Alkalis (as Sodium Oxide)	0.66

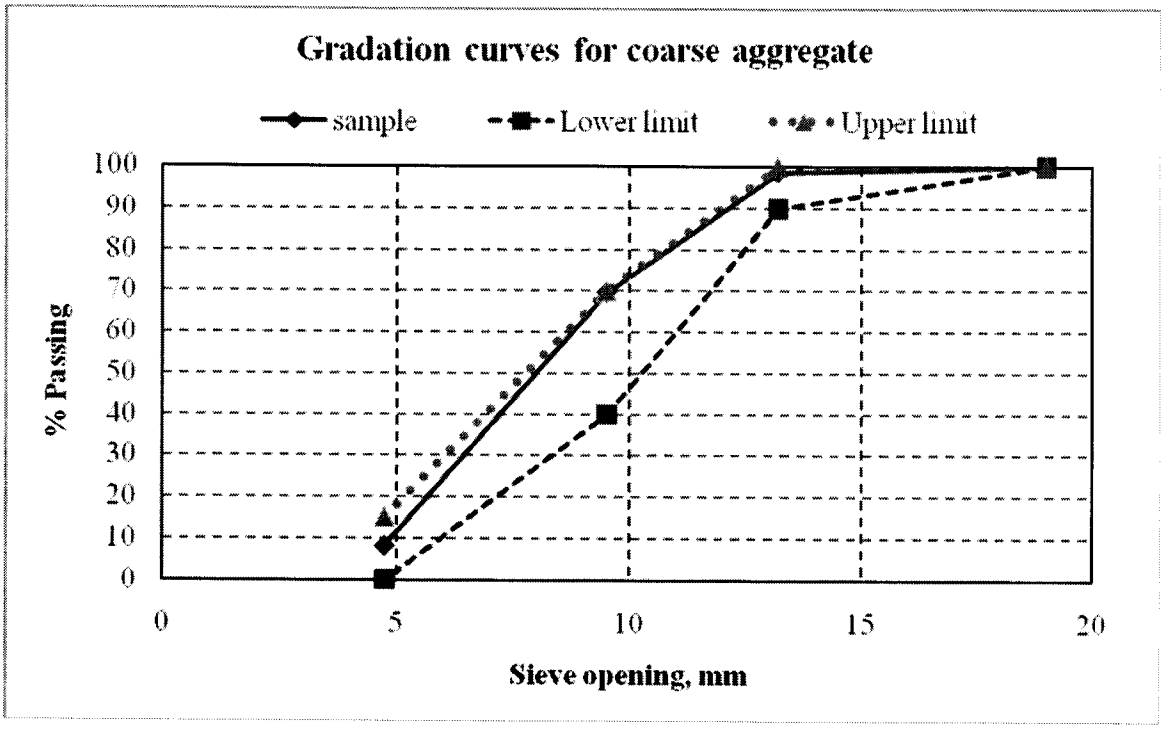

Figure 3.9: Gradation curves for coarse aggregate.

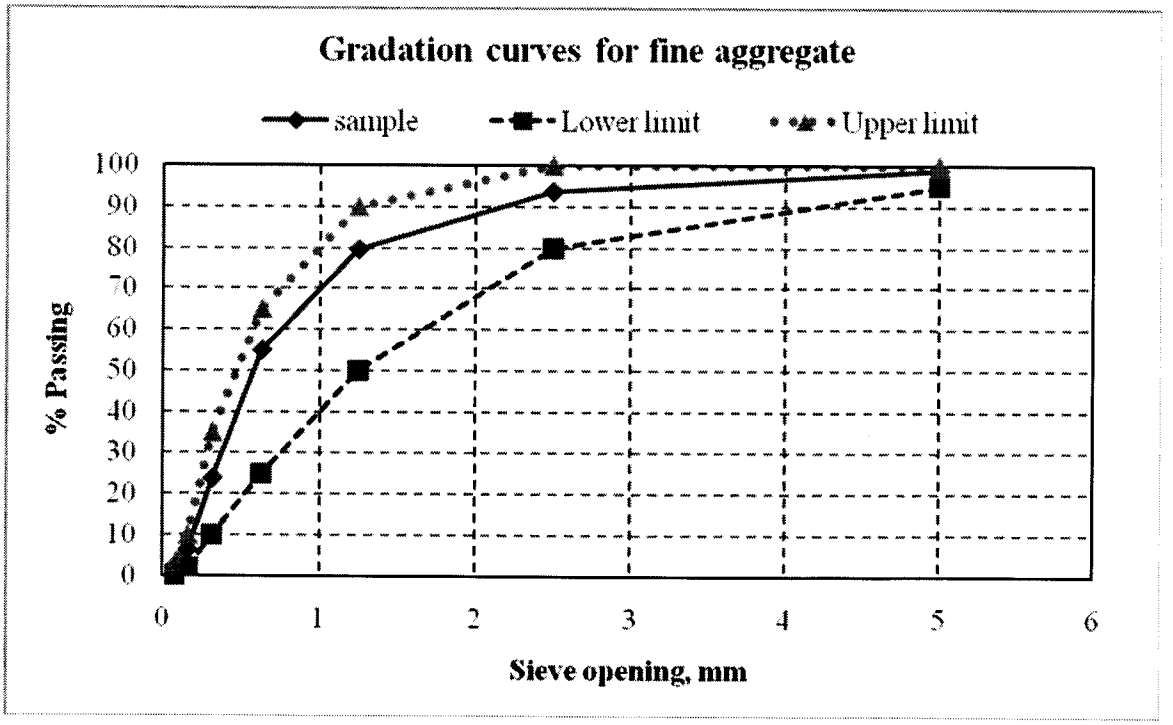

Figure 3.10: Gradation curves for fine aggregate.

3.2.3. Casting and curing

The formwork of the slab and supports was built with plywood. Figures 3.11 and 3.12 show the different stages of construction of the supports and deck, respectively. Figures 3.12(a) and (b) show different stages of construction of the deck formwork. Levelling was carried out using theodolite in order to get a perfectly horizontal surface, as illustrated in Figure 3.12(c). Figure 3.12(d) illustrates the details of the formwork at the section where no load was applied (control section). Figure 3.12(e) shows the completed formwork for the two extreme strips (w/c = 0.35 and 0.50) waiting to be cast.

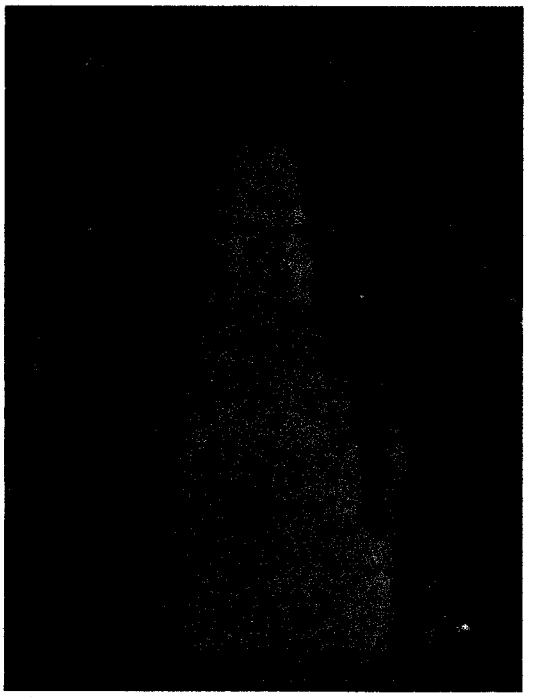

Figure 3.11: Different stages of construction of supports.

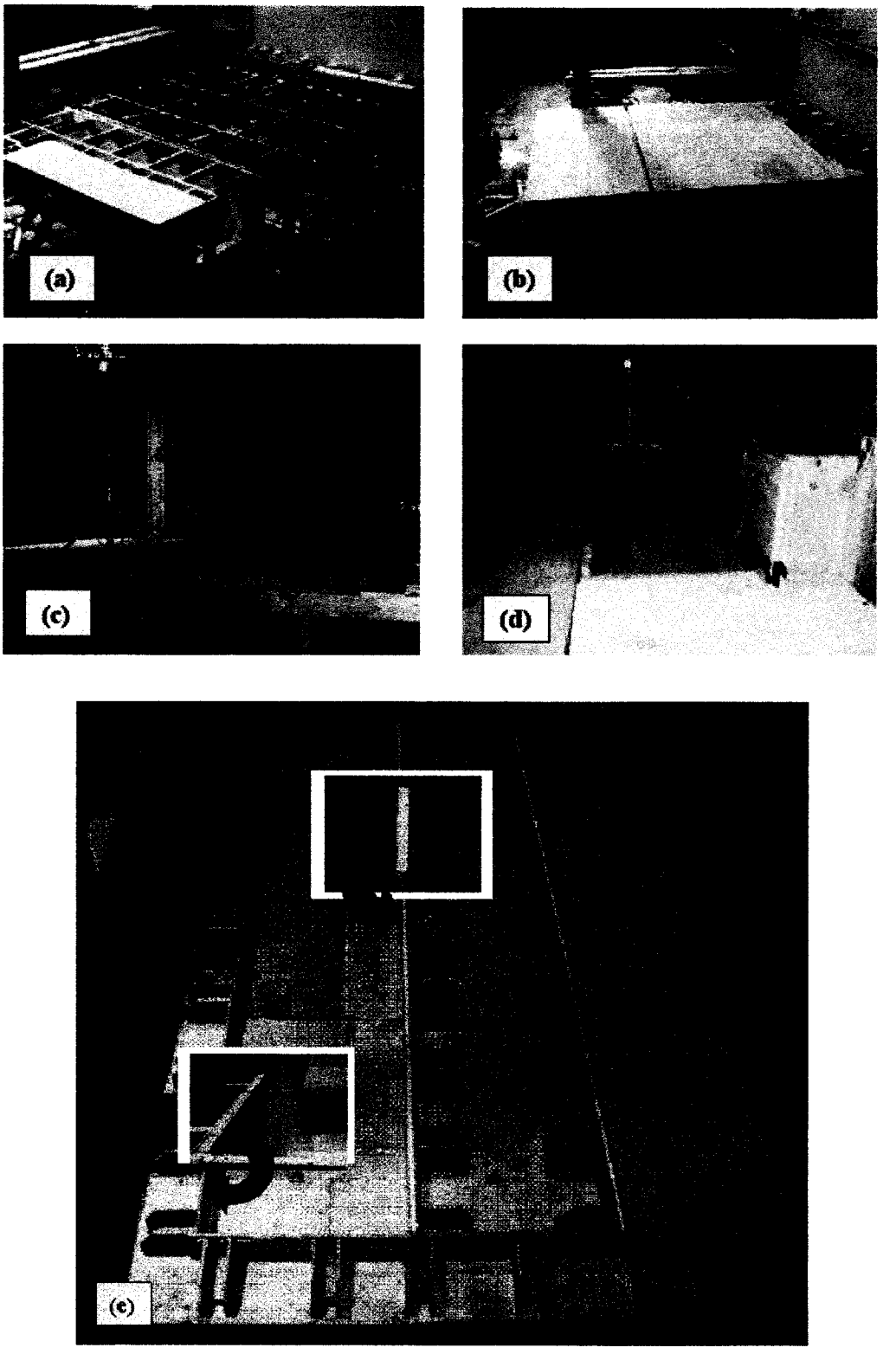

Figure 3.12: Different stages of construction of the deck formwork.

Prior to casting the slab, the plywood formwork was lined with a plastic sheet of 0.152-mm thickness in order to prevent the formwork from absorbing mixing water. Each concrete strip was cast independently of each other, with one week apart in-between castings. The first strip to be cast was that of 0.35 w/c, followed by that of 0.50 w/c (as shown in Figure 3.13). The last strip to be cast was the middle strip of 0.40 w/c (see Figure 3.14). Joints in-between strips were created by placing Styrofoam sheets of 25-mm thickness, so that each RC strip would respond independently of each other when mechanically loaded.

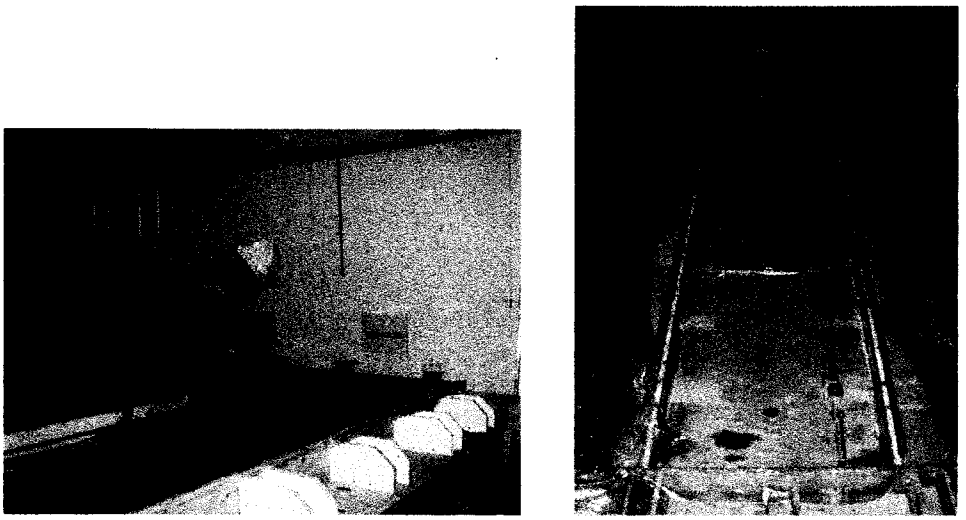

Figure 3.13: Casting process for end strips with w/c = 0.35 and w/c = 0.50.

Figure 3.14: Construction of middle strip with w/c = 0.40.

One day after casting, each concrete strip was covered by wet jute rugs, which were in turn covered by plastic sheets in order to minimize evaporation (see Figure 3.15). This curing regime lasted for 28 days. The average temperature in the Structures Lab was 21°C and the relative humidity was 25%.

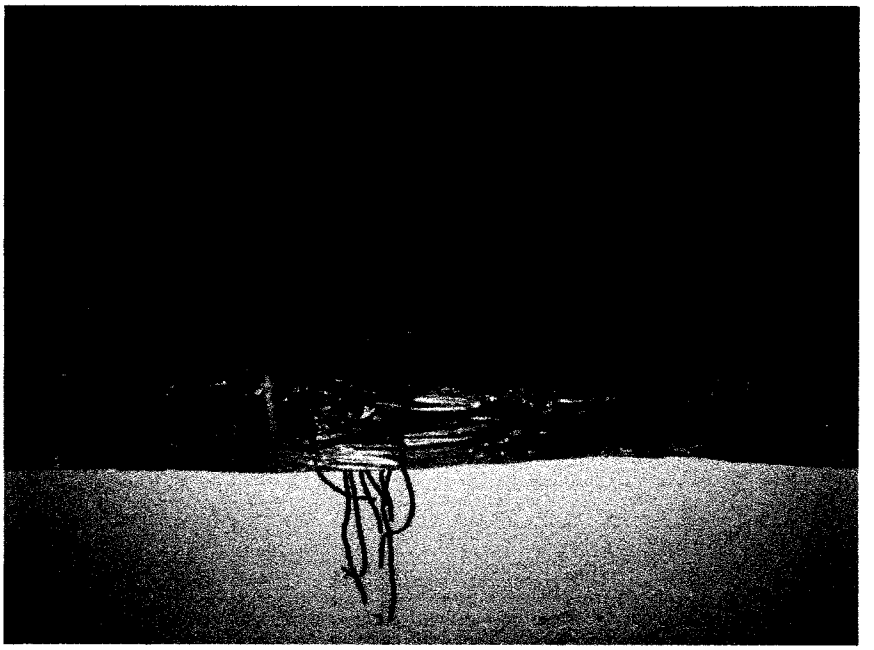

Figure 3.15: The deck undergoing curing.

Eight concrete cylinders (100 mm × 200 mm) were prepared at the time of casting each strip. Four cylinders were tested for compressive strength (f'_c) at 28 days. The average strengths were obtained as 62.1 MPa, 51.5 MPa and 44.7 MPa for the w/c of 0.35, 0.40 and 0.50, respectively. The concrete compressive strengths (f'_c) at the time of loading (200 days after casting) were re-measured, and the average values obtained were 81.0 MPa, 69.4 MPa and 64.5 MPa for the w/c of 0.35, 0.40 and 0.50, respectively. The results of the stress-strain test for four cylinders of each w/c are presented in Appendix A.

3.3. Experimental setup

3.3.1. Loading

Each RC strip was loaded by means of three threaded steel bars, located at the end of the left overhang, 910 mm from the left support, and 910 mm from the right support, respectively (see Figure 3.16). Springs were used at the top of the steel bars to counteract long-term relaxation effects. Shear and bending moment diagrams resulting from the applied loads are shown in Figure 3.17. The applied loads corresponded to 60% of the ultimate moment capacity of the slab (P = 27.5 kN), which is close to the extreme end of the applied service loads. Figure 3.18 shows the details of the threaded bars underneath the deck; this system was used to provide all possible degrees of freedom and to ensure a pure vertical axial load. Note that the bottom end of the threaded bar is below the strong floor of the Structures Lab, held in place by a nut and a washer. The loading set-up is shown in Figure 3.19.

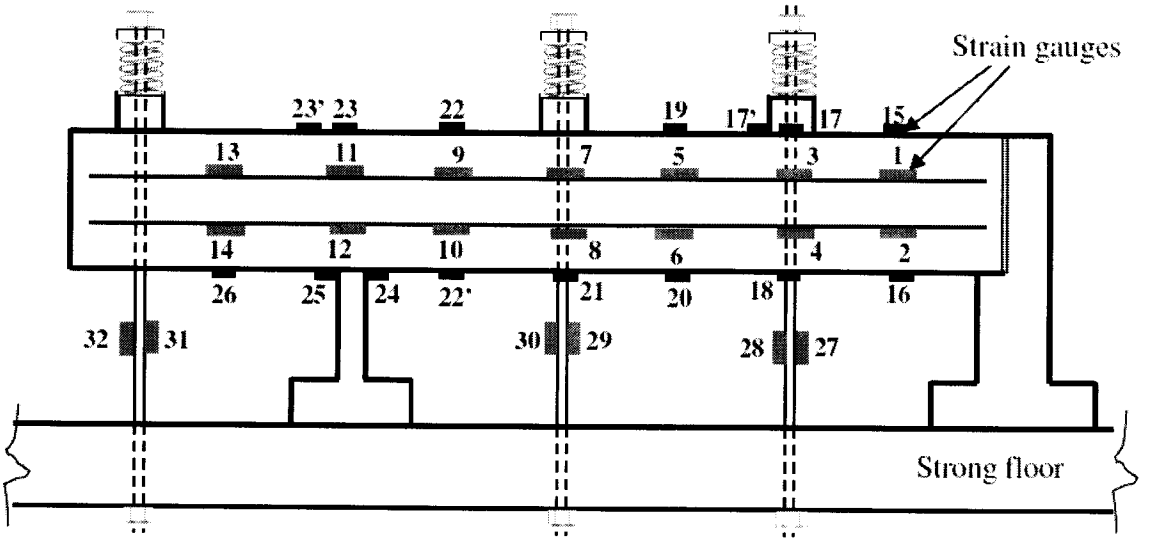

Figure 3.16: Loading system and locations of strain gauges.

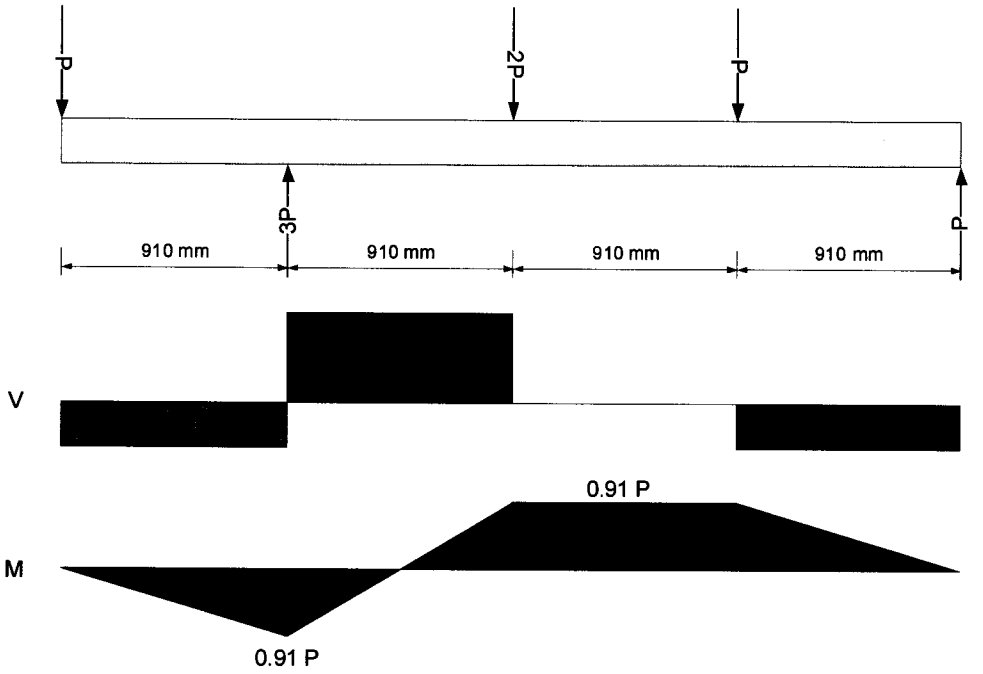

Figure 3.17: Shear force and bending moment diagrams resulting from the applied load on the RC slab (P = 27.5 kN).

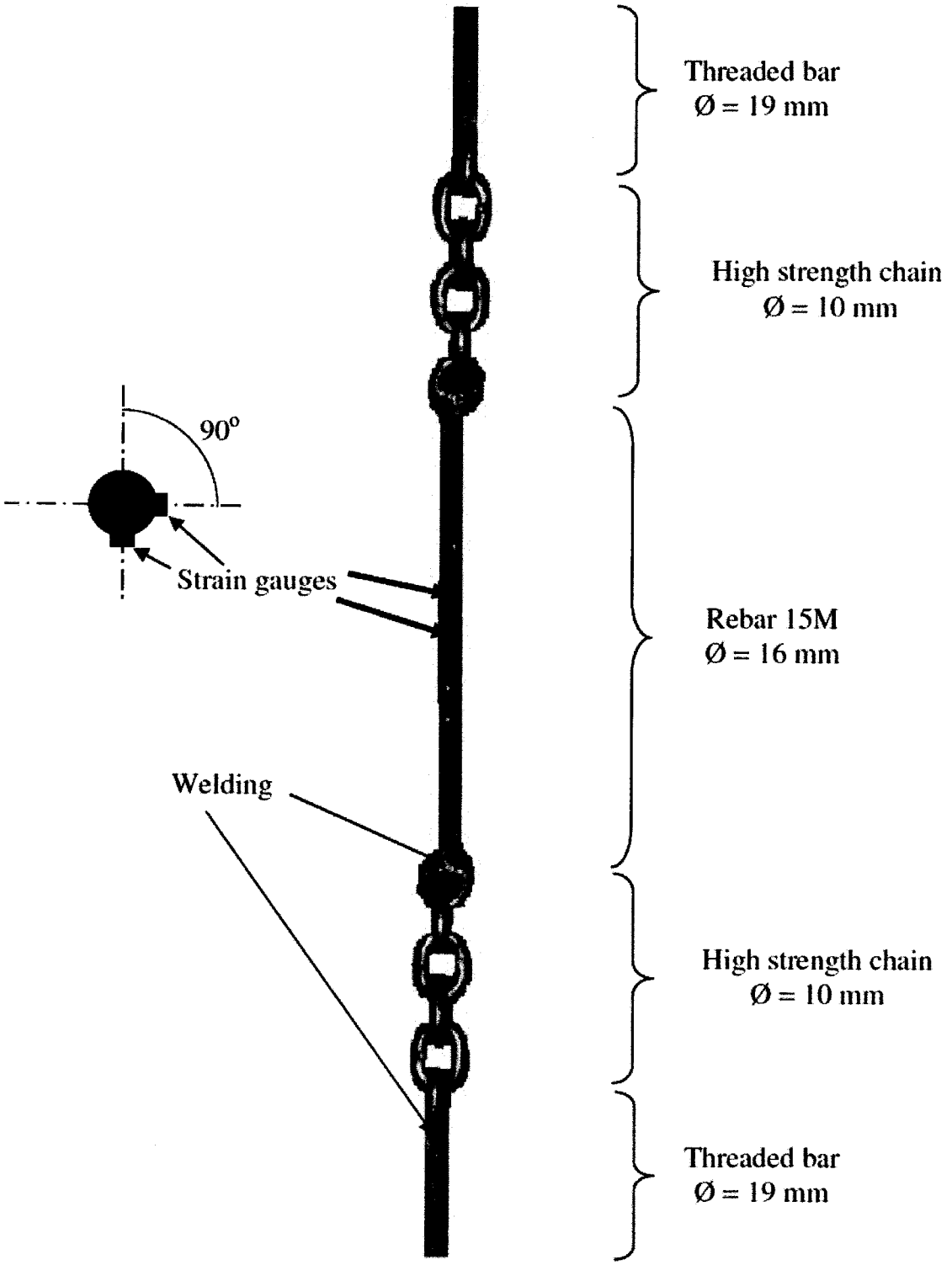

Figure 3.18: Details of threaded bars used for loading.

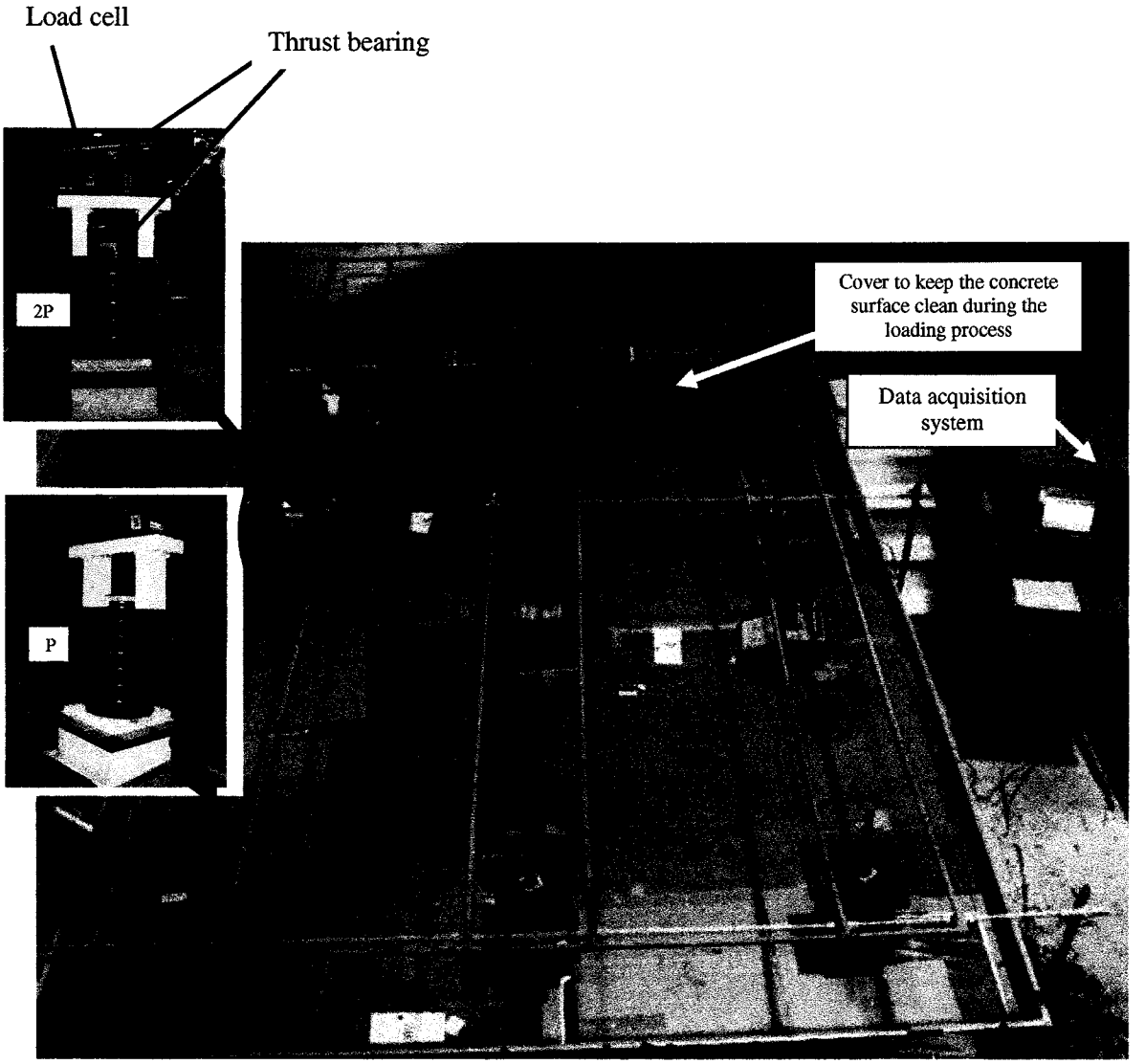

Figure 3.19: Loading set-up.

Figure 3.20 illustrates the setup mechanism used to apply the loads. The loading process was carried out as follows:

1. An initial reading in the load cell was taken before proceeding with the loading.
2. The upper nut was tightened until it touched the upper washer with the upper thrust bearing.

3. Upon the nut touching the upper washer, the load was transferred to the steel plate through the thrust bearing. This steel plate had the function of distributing the applied loads to the load cell uniformly.
4. As soon as the steel plate was loaded, the load cell started to give readings on the data acquisition system or on the strain gauge indicator.
5. The load transferred from the load cell to the steel chair underneath, which started to push the steel plate at the top of the spring. As a result, the spring started to be compressed, and consequently the applied load was transferred to the deck through the concrete block.
6. This process was continued until the targeted load was achieved (P = 27.5 kN).
7. Care was taken by continuous monitoring the lower nut located underneath the steel chair. If the lower nut touched the steel chair, the load would only be transferred to the load cell, which was confined between the upper and lower nuts.
8. The loads were gradually applied at all three loading points along the slab at the same rate. Each RC strip on the deck was loaded at a time.
9. Once the targeted loads were achieved, the lower nut was tightened. By doing so, the load cell was relieved from the loads back to the reference level read before any load was applied.
10. The loading system containing the upper washer, upper thrust bearing, steel plate for the load cell, load cell, and the steel chair could easily be removed by loosening the upper nut.
11. Steps 1 to 10 were repeated for each one of the remaining RC strips.

A view from underneath the deck after the load was applied and the strain gauges board are illustrated in Figures 3.21 and 3.22, respectively.

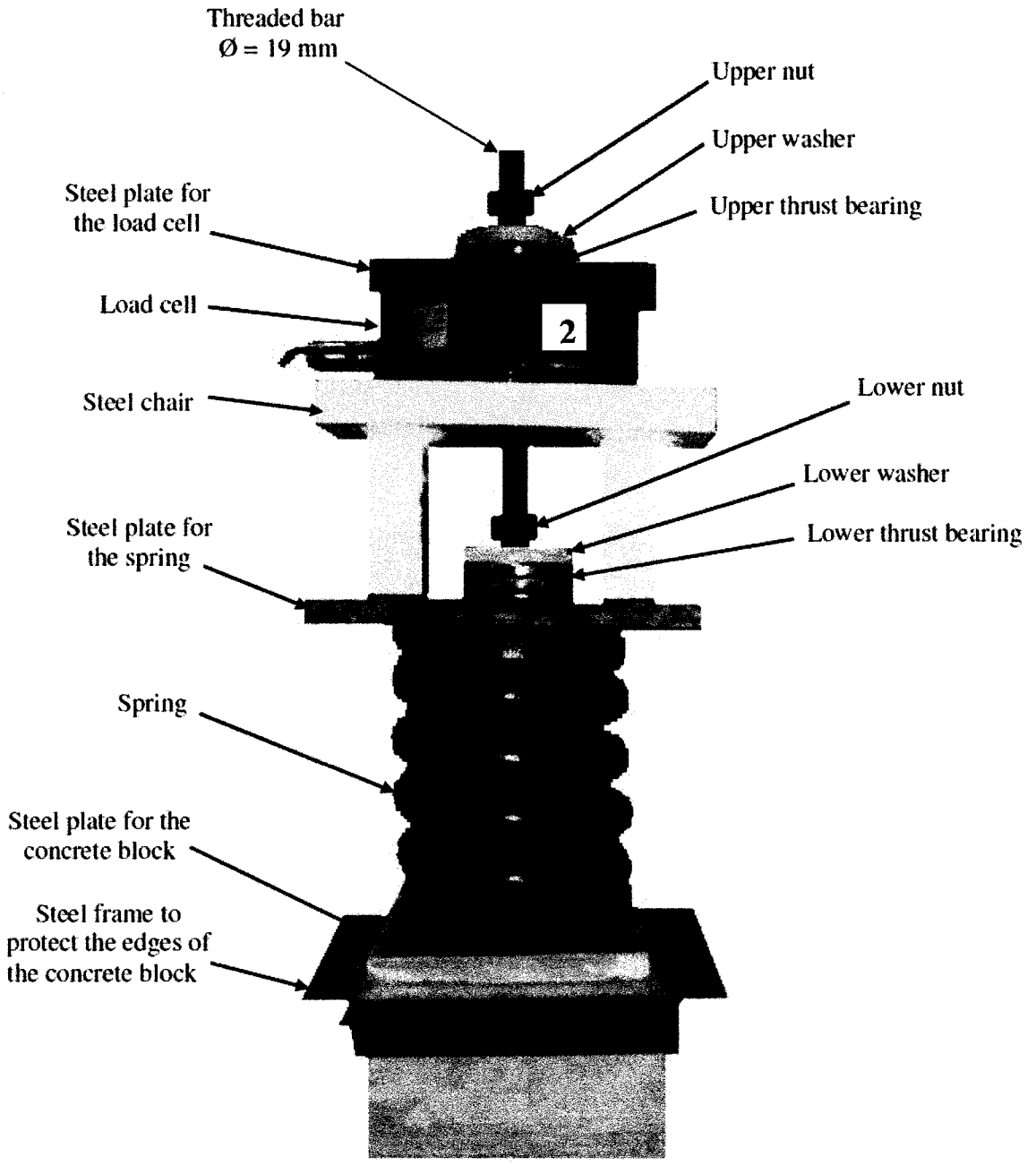

Figure 3.20: The loading mechanism setup.

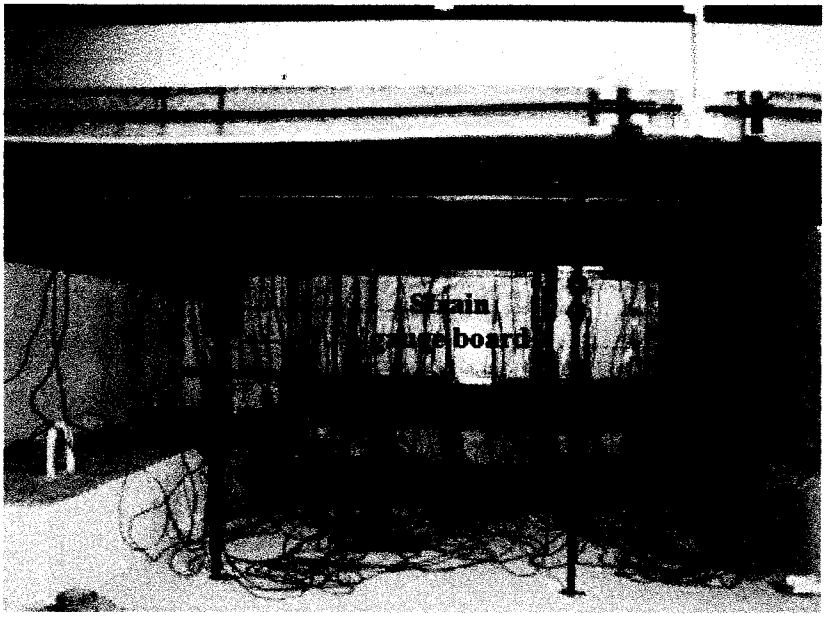

Figure 3.21: View from underneath the deck after the load is applied.

Figure 3.22: Strain gauges board.

3.3.2. Chloride exposure regime

Regular de-icing salt was spread uniformly all over the deck surface. Figure 3.23 (a) to Figure 3.23 (c) show the different stages in applying the salt, which was spread over the deck forming a layer of thickness ranging from 30 to 50 mm (see Figure 3.23 (d)). The density of the salt used was 1222.4 kg/m^3. A spray system was specially designed in order to easily apply water on the slab (see pipes over deck in Figure 3.24). To avoid water spilling over the sides, the deck was surrounded by a 100-mm high frame. During the wetting cycle, the deck was sprayed with water until it reached a depth of approximately 50–60 mm; the time required to reach this water depth was approximately 30 minutes. The slab was then let dry for 90 days to facilitate the removal of the cores. This wetting and drying cycle was repeated two more times. More salt was added right before the third cycle, as it was observed that some salty solution was previously drained. Figure 3.25 illustrates the state of the de-icing salts at the end of the first wetting cycle, whereas the state of the concrete surface right before taking the concrete cores is shown in Figure 3.26. The addition of salt and water on the deck did not significantly change the concrete and steel strains recorded.

The chloride solution that resulted from spraying water over the de-icers was in a saturated condition, as the salt grains were visible. Similar cases of chloride exposure regimes have been found in Ottawa; examples of such conditions were found at the Mackenzie King Bridge and Highway 417 as illustrated in Figures 3.27(a) and 3.27(b), respectively.

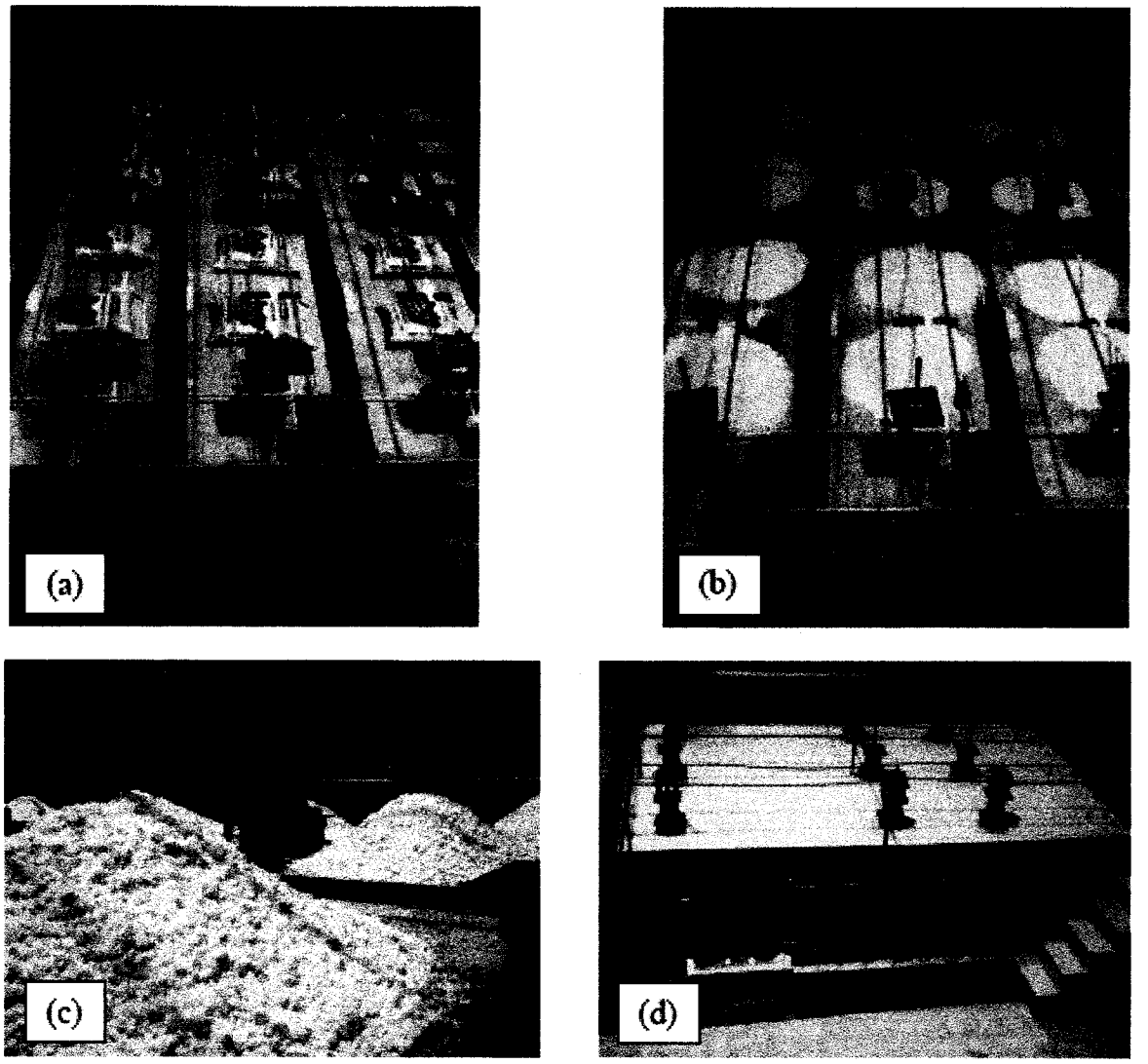

Figure 3.23: De-icing salt application on the deck.

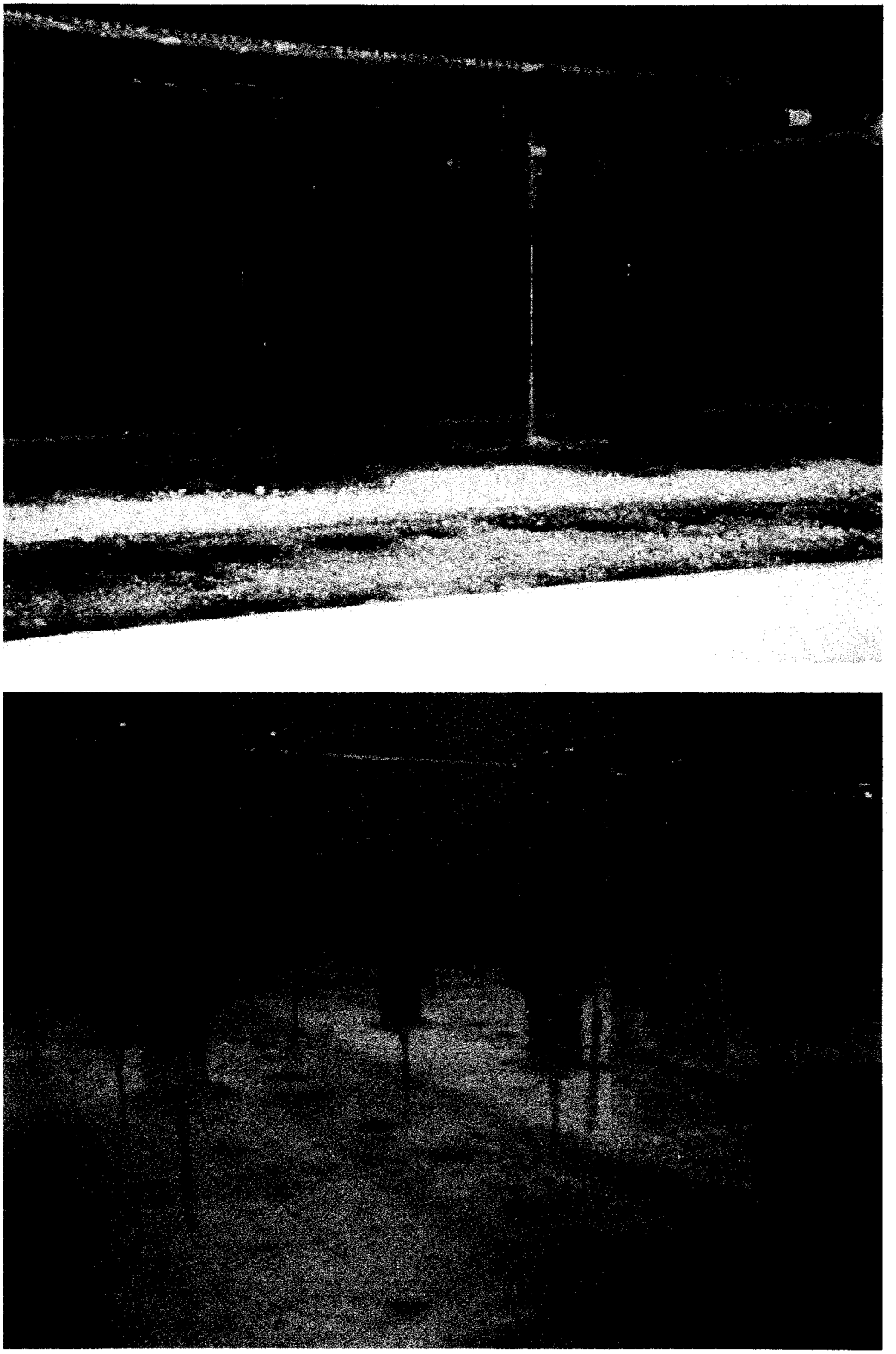

Figure 3.24: Wetting cycle using spray system.

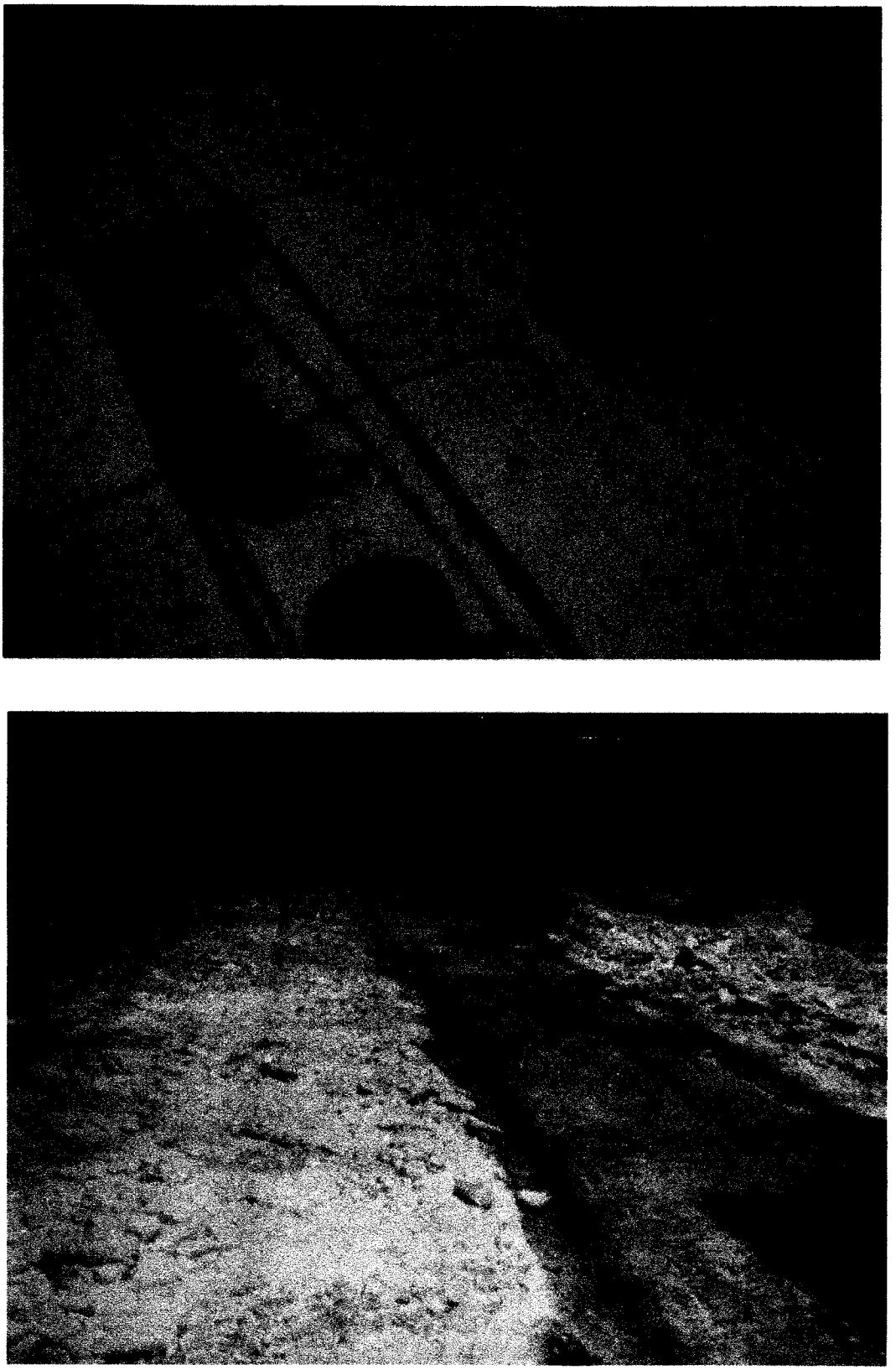

Figure 3.25: State of the salt at the end of the first wetting cycle.

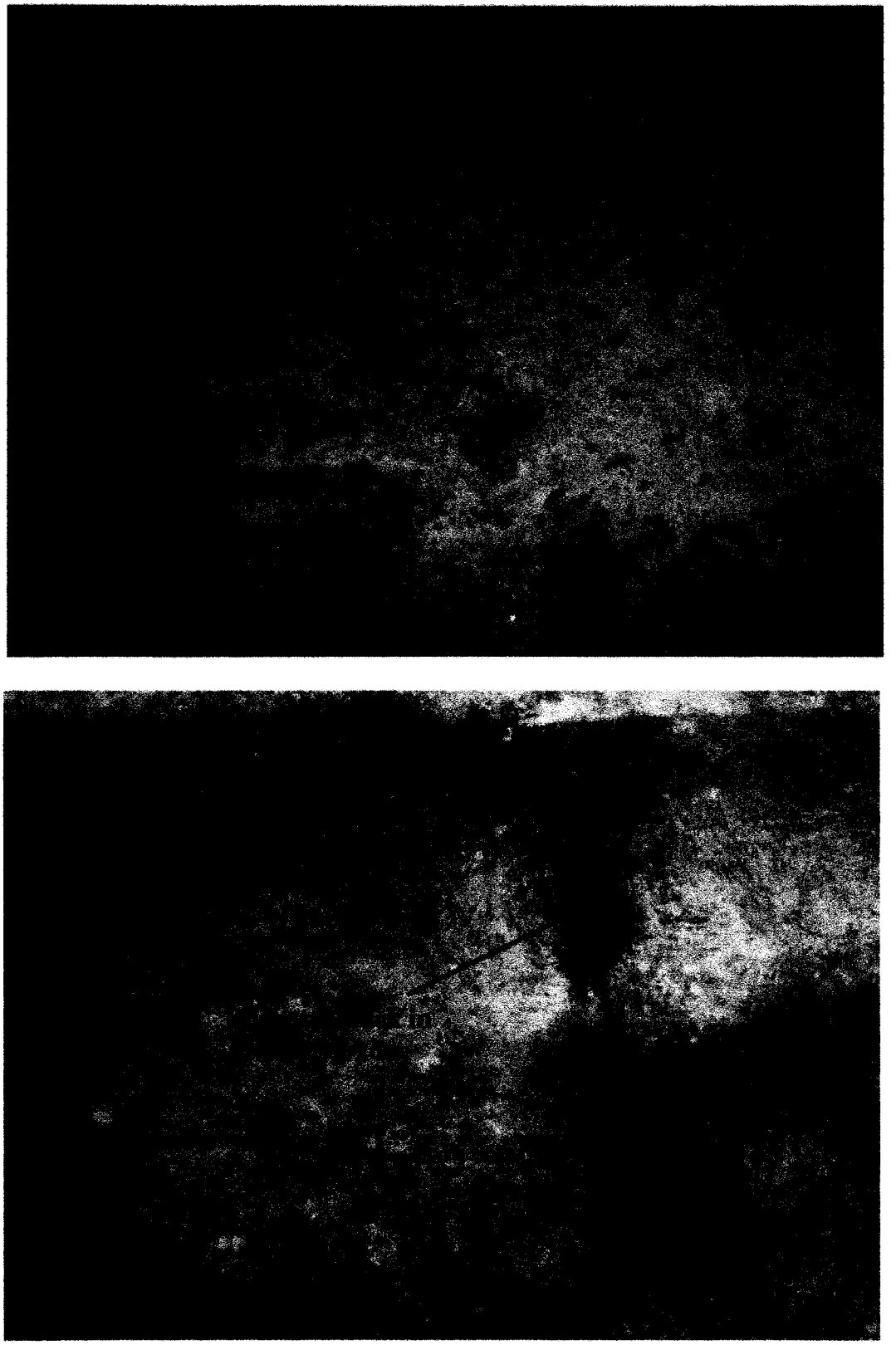

Figure 3.26: State of the top concrete surface before taking cores.

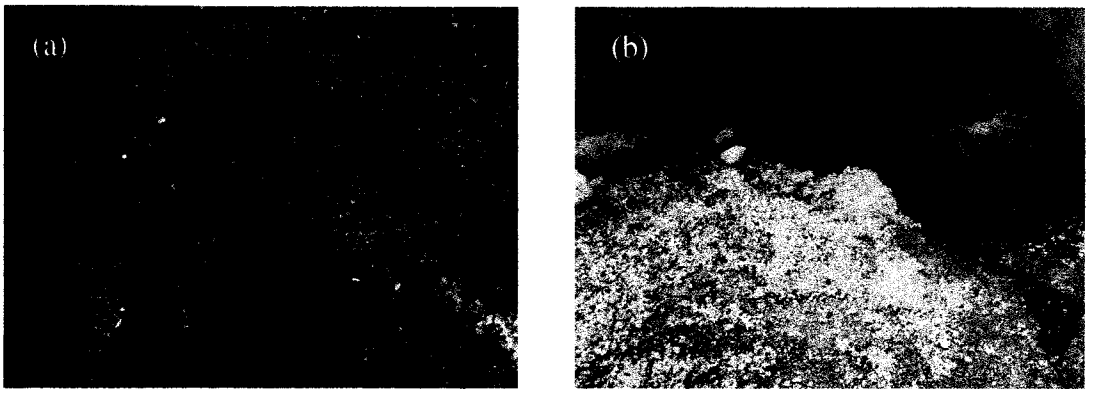

Figure 3.27: Similar chloride exposure regimes found in the field in Ottawa.

3.2. Data collection

3.4.1. Strain measurements

In order to monitor deformation during testing, both concrete and steel electrical strain gauges were used. The location of strain gauges is shown in Figure 3.16. The steel strain gauges, located along the top and bottom reinforcement, are of 10 mm and numbered from 1 to 14. The concrete strain gauges, located at the top and bottoms surfaces of the deck, are of 60 mm and numbered from 15 to 26. In order to ensure that the entire strip width was under the same load, two extra concrete strain gauges were positioned close to the strip edge at 910 mm and 2730 mm from the right end, numbered 17' and 23', respectively, in Figure 3.16. Two strain gauges were also fixed on each threaded bar used to apply the load (numbered from 27 to 32 in Figure 3.16). In order to ensure strain gauges were applied correctly, manufacturer instructions were followed closely. All top concrete strain gauges were sealed in order to protect them during the wetting cycles. Furthermore, the angle of deviation for all strain gauges was never greater than 5° (Tikka et al., 2003; Bonfiglioli et al., 2005). Figure 3.28(a) shows a glued strain gauge on a rebar, and Figure 3.28(b) shows the strain indicator that was used to measure strains during the experimental work.

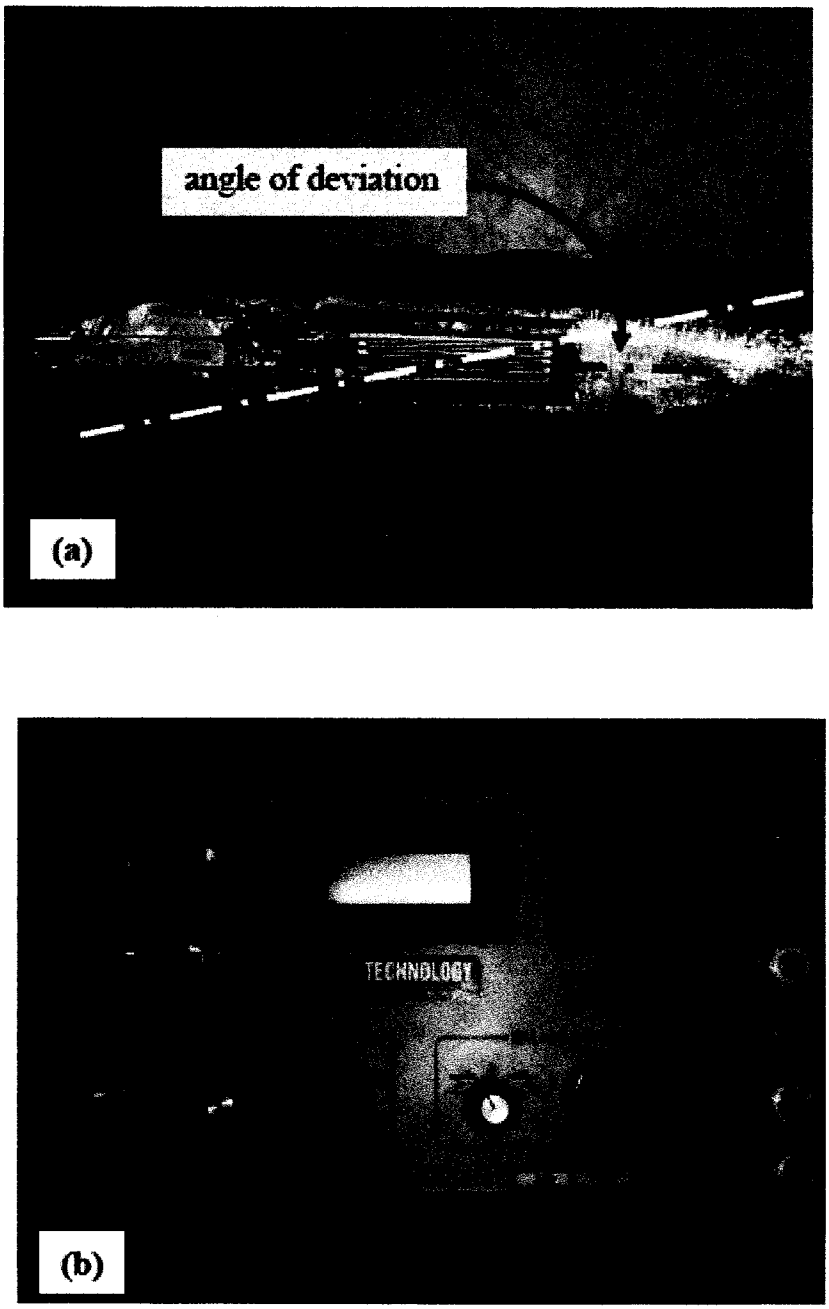

Figure 3.28: (a) Glued steel strain gauge; (b) Strain gauge indicator.

In addition to electrical strain gauges, distributed Brillouin fibre sensors were also used to monitor the concrete strain distribution at the top and bottom surfaces of the RC deck, in order to obtain a continuous strain distribution along the deck. The sensing fibre used in this experiment was a single-mode carbon/polyimide-coated fibre designed for sensing applications in harsh environments. This fibre has a base coating of carbon, which provides the silica core with a hermetic seal to moisture and most chemicals, and

an outer polyimide coating, which allows a wider temperature performance than the conventional acrylate coating. The optical fibres were glued onto the concrete surface using epoxy, as illustrated in Figure 3.29. The data acquisition system for the optical fibre sensor system is shown in Figure 3.30.

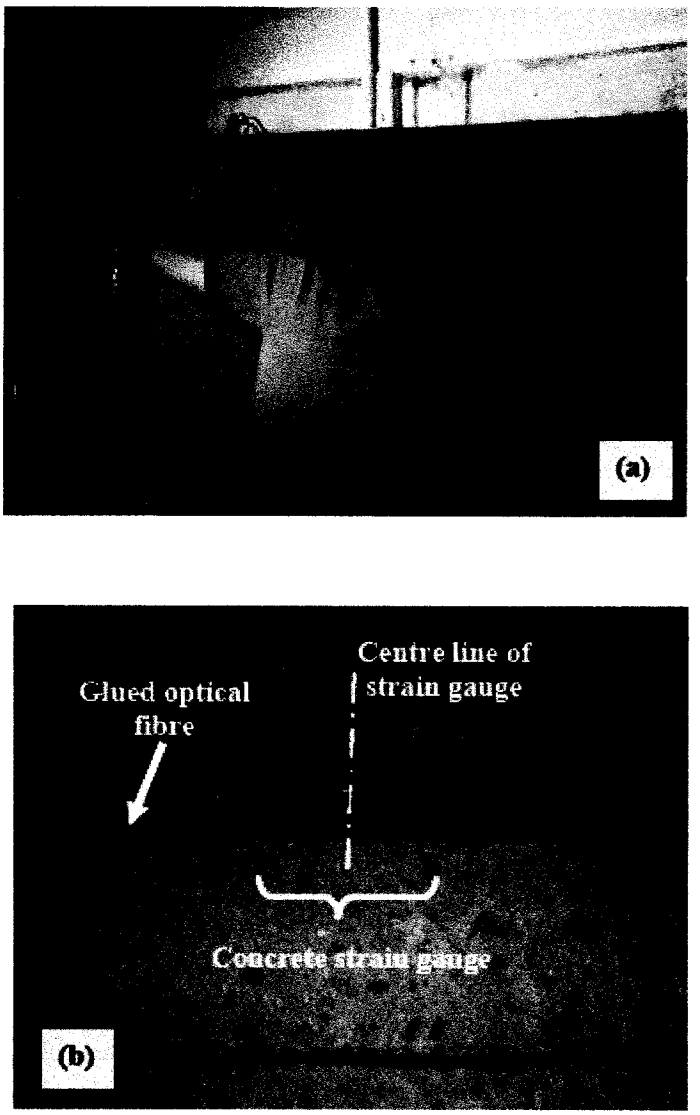

Figure 3.29: (a) Optical fibre installation process; (b) Glued optical fibres and strain gauges.

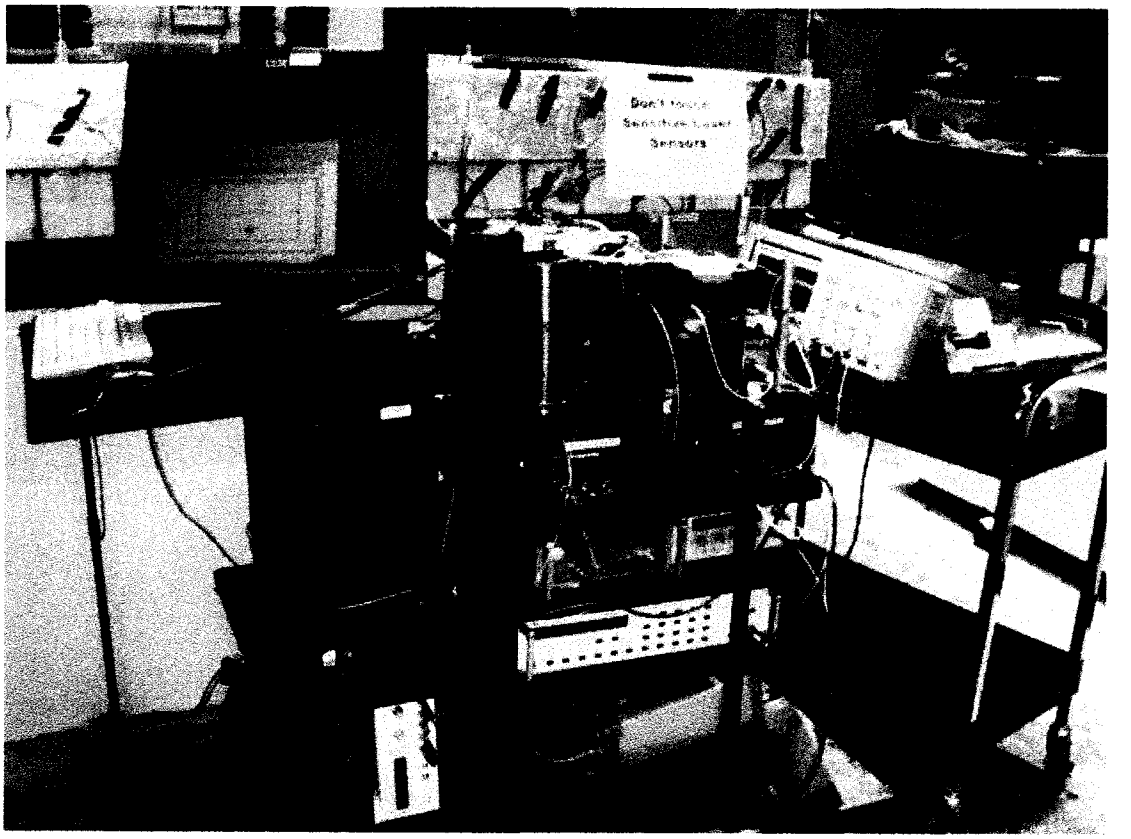

Figure 3.30: Optical fibre data acquisition system.

The distributed Brillouin fibre sensing system used in this work is based on the interaction of a probe pulse laser and a counter-propagating continuous wave laser travelling along the fibre sensor. This system is also known as the Brillouin optical time-domain analyzer or BOTDA. The light sources are two tunable laser beams operating at 1320 nm. The optical pulse is created by use of an electro-optic modulator driven by a pulse generator; a pulse signal with 2 ns pulse width was generated in this experiment, which corresponds to a spatial resolution of the fibre sensor of 20 cm. When the two lasers interact inside the fibre, Brillouin signals are generated in the fibre if the frequency difference between the two lasers is precisely the Brillouin frequency of the fibre at specific strain conditions. When the temperature remains constant, this Brillouin frequency ν_B is proportional to the strain ε experienced by the fibre according to:

$$\nu_B = \nu_{B0} + C_\varepsilon \varepsilon \tag{3.1}$$

where ν_{B0} is the Brillouin frequency of the unstrained fibre and C_ε is the strain coefficient, which needs to be determined for each fibre type used in the measurements. The carbon/polyimide-coated fibre has a strain coefficient of 20 με/MHz. The strain uncertainty of the fibre was calculated by evaluating the standard deviation from the best fit curve to one specific Brillouin spectrum, and it was found to be 20 με. More specific details of the experimental setup used here to measure the stimulated Brillouin scattering can be found in Zhang et al. (2008), Deif et al. (2009), and Deif et al. (2010).

3.4.2. Concrete coring

Because the main objective of this work is to study the effect of load on chloride ingress into concrete, concrete cores were taken after each wet and dry cycle at different sections corresponding to different load levels, as illustrated in Figure 3.31. The diameter of the cores was 63.5 mm. According to Baroghel-Bouny and Maultzsch (2007), the minimum diameter of a core should be 50 mm; if smaller drills are used, then more samples need to be taken (Wall and Nilsson, 2006). From the experience gained during this experimental work, it is recommended to use compressed air to help minimize damage during the coring process.

The deck preparation prior to coring and the coring tools used are shown in Figure 3.32. Figure 3.33 shows the coring in process, while completion of the coring process is shown in Figure 3.34. The holes left from the cores were filled with a fast-hardening non-shrinking mortar (see Figure 3.35), which was allowed to cure for two days. The surface was then covered with epoxy, in order to prevent chloride movement through the vertical core hole. It can be noticed that there are some sections in which concrete cores were taken twice. This is due to some damage observed in the first set of cores taken at these sections before reaching the targeted depth, and consequently a second set of cores was again taken.

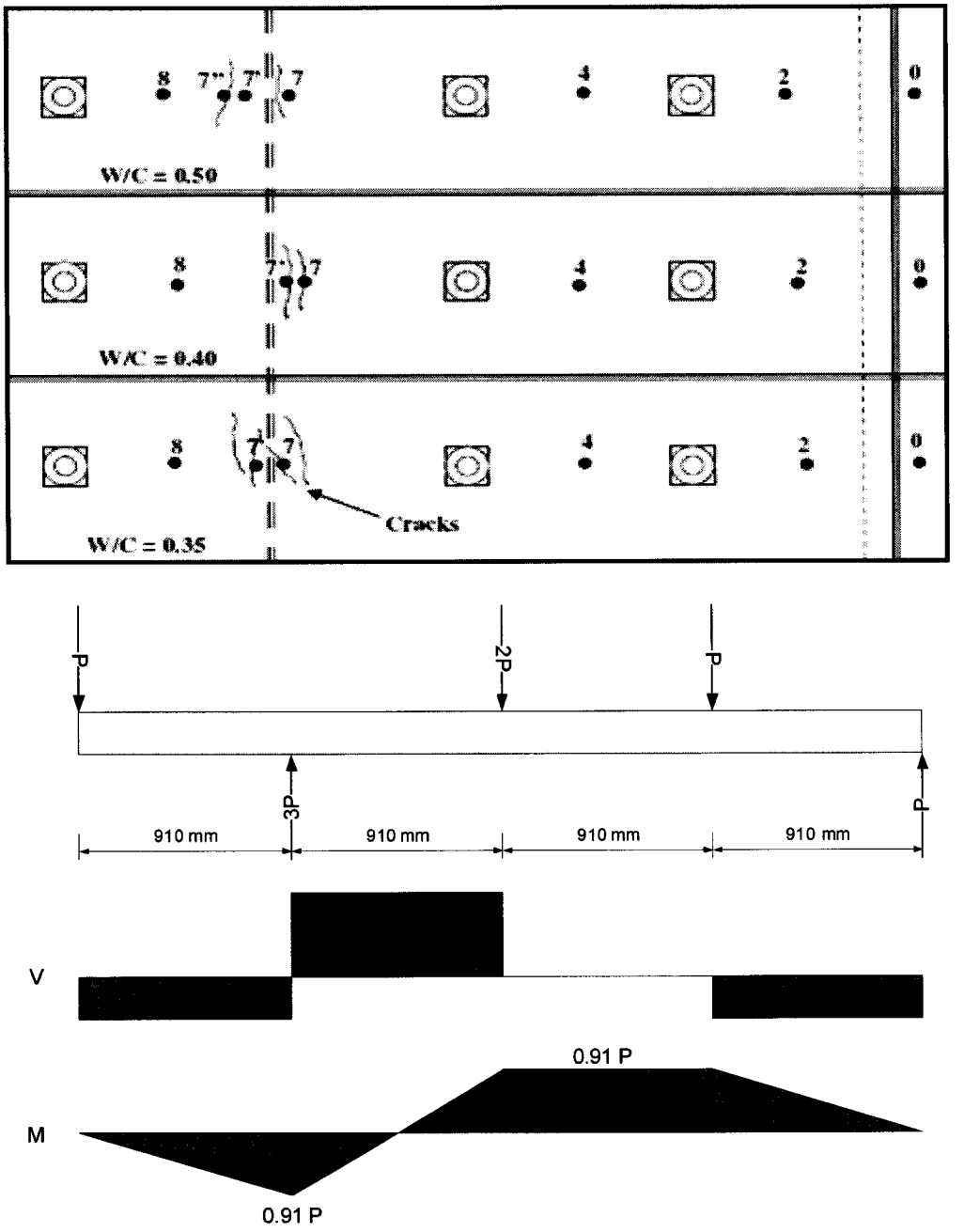

Figure 3.31: Locations where concrete cores were taken.

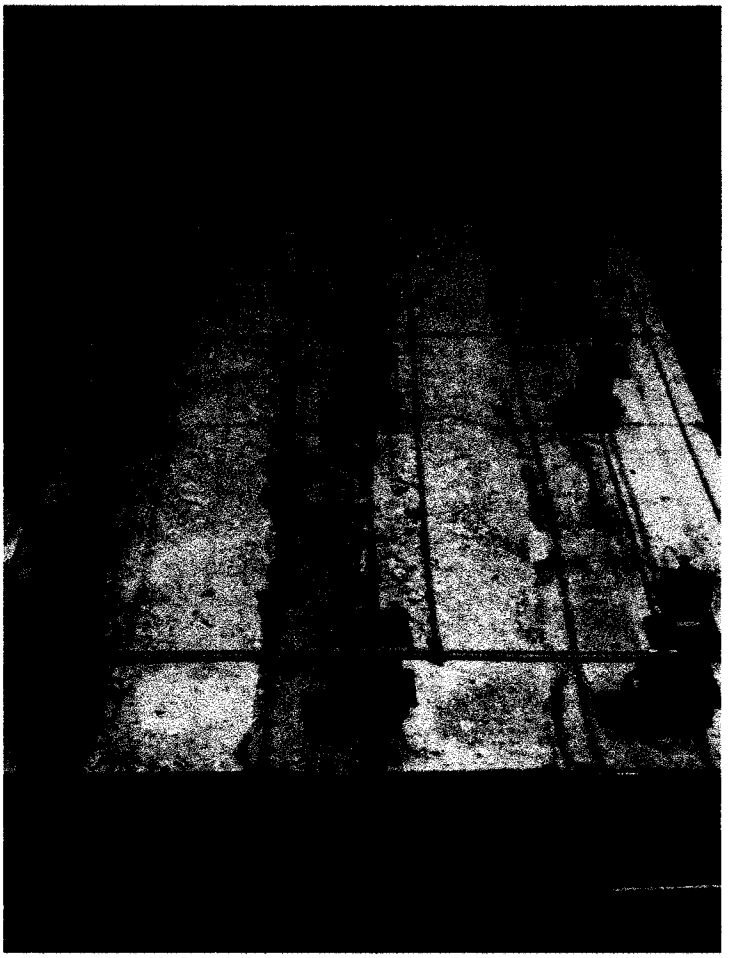

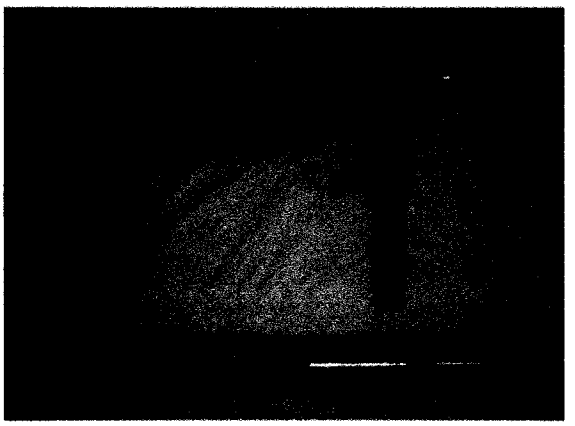

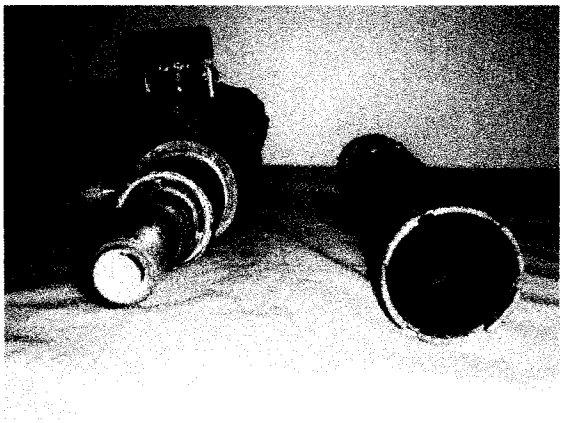

Figure 3.32: Deck preparation for coring process and tools used.

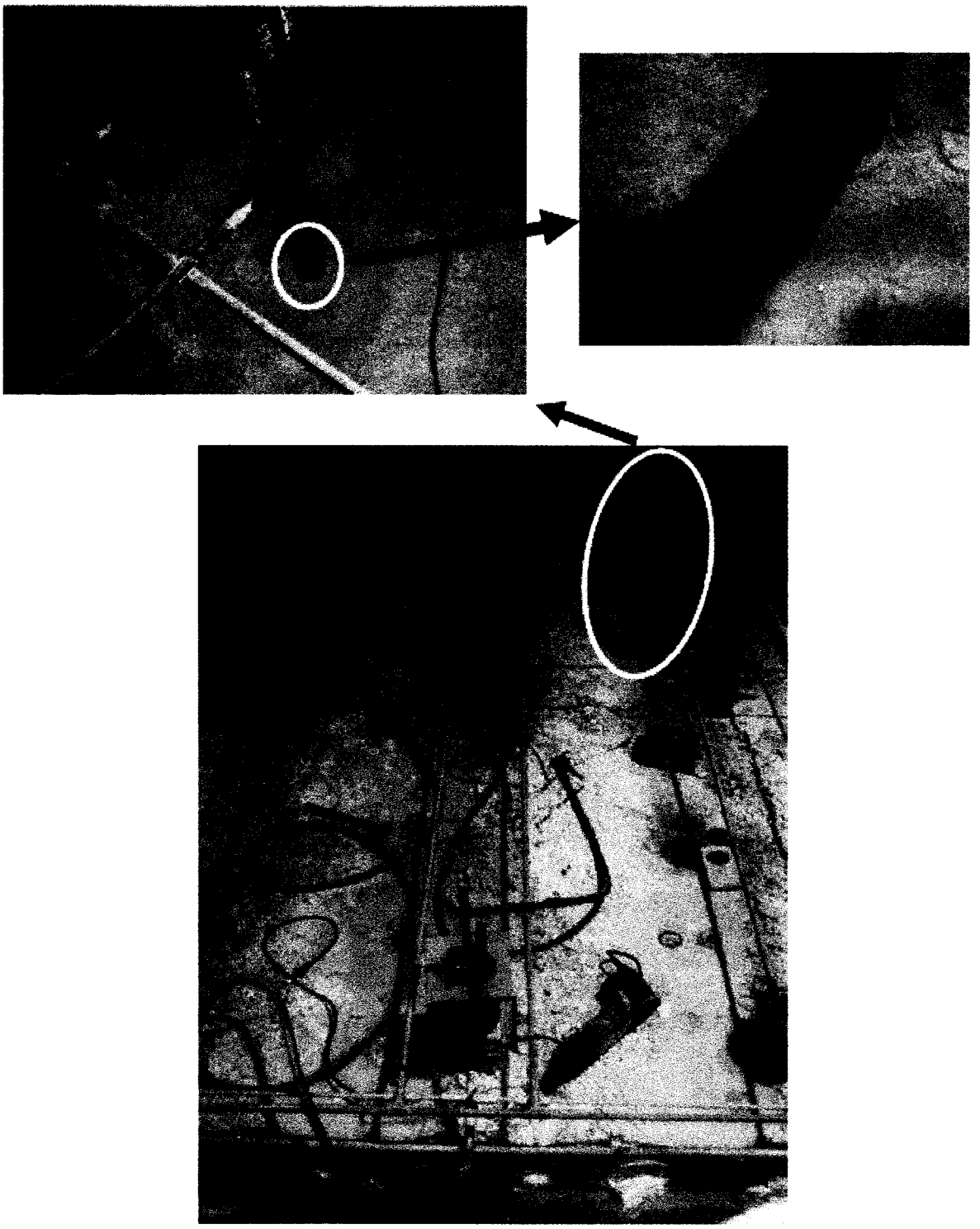

Figure 3.33: Concrete coring in process.

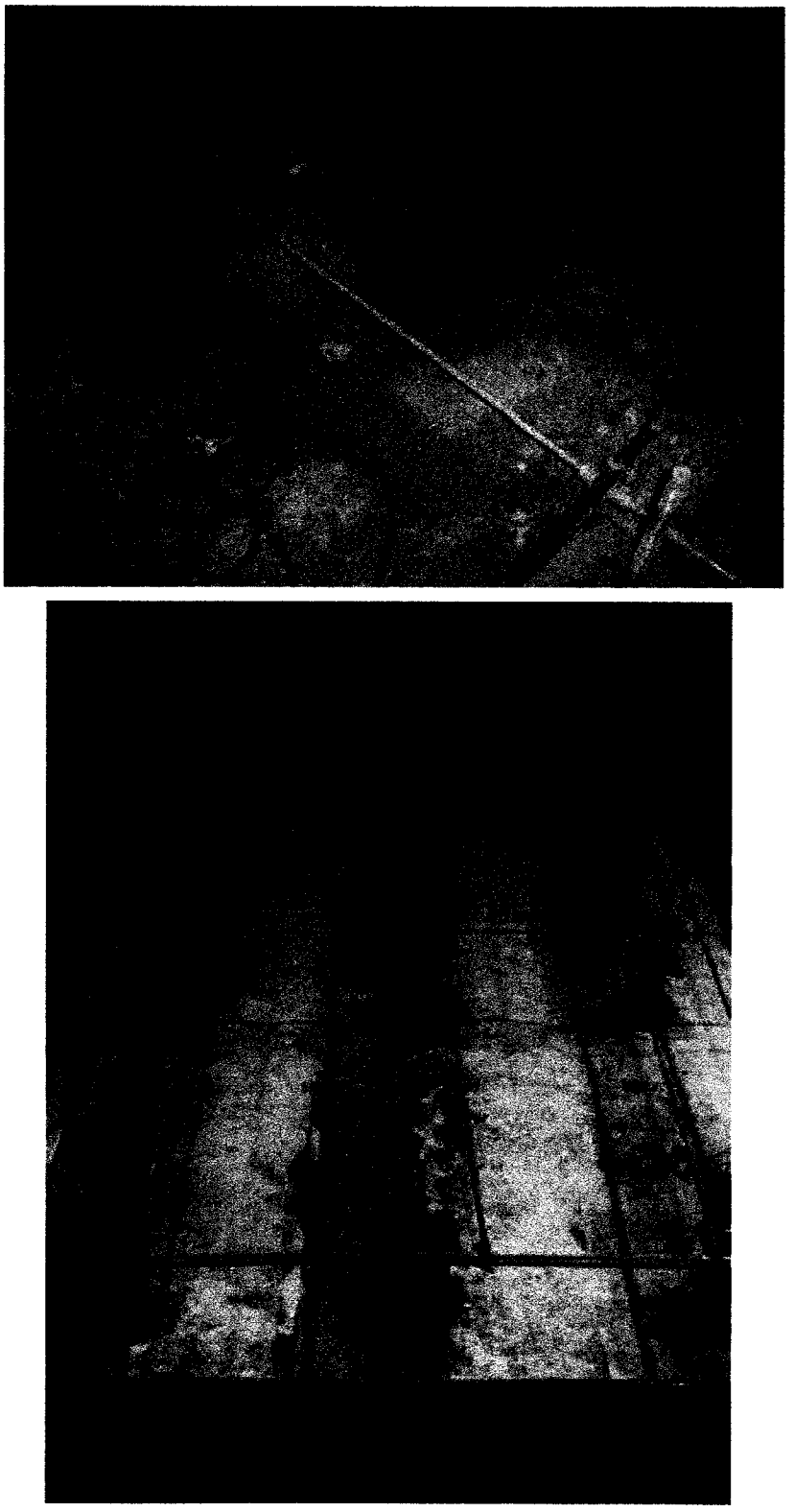

Figure 3.34: Coring process completed.

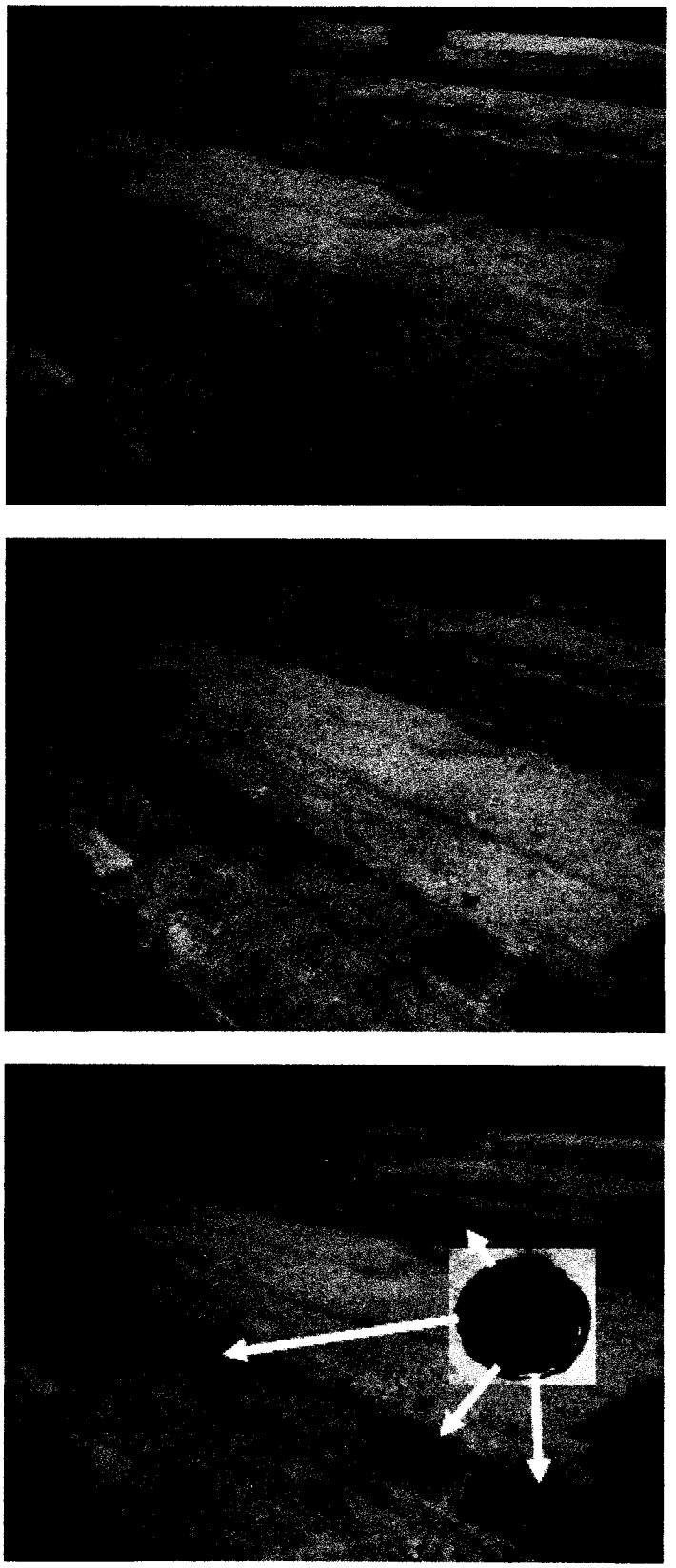

Figure 3.35: Filling up the core holes.

3.4.3. Chloride concentration

The amount of chlorides penetrating the concrete cover as a result of the applied exposure regime was determined through two different methods: a colourimetric technique and a potentiometric titration procedure. The following sections describe the methodologies used to quantify the amount of chlorides in the concrete.

3.4.3.1. Spraying of silver nitrate

The average depth of chloride penetration in each concrete core was determined by spraying a silver nitrate ($AgNO_3$) solution of 0.1 mole/l on freshly split concrete samples. More details on this method have been given in section 2.4.1. Concrete cores were obtained from each RC strip after each wetting and drying cycle, as previously explained. It is important to highlight that the direction of splitting was perpendicular to the applied load and in the same plane of probable cracks; as illustrated in Figure 3.36 (also shown by a black line on the location of concrete cores in the top picture of Figure 3.34).

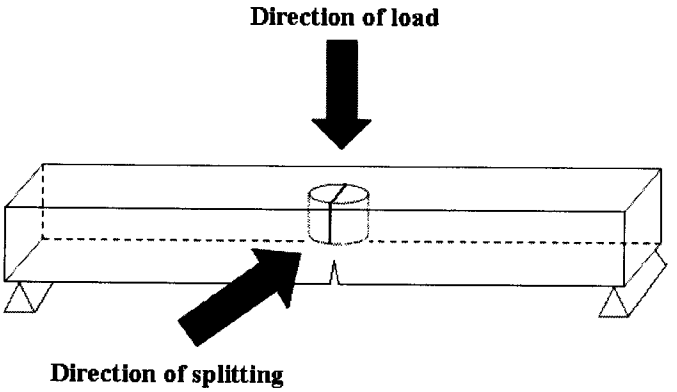

Figure 3.36: Schematic diagram showing the direction of load and the direction of splitting a core sample for $AgNO_3$ spraying.

3.4.3.2. Potentiometric titration method

Since the colourimetric method is a qualitative method, it is important to also quantify the actual chloride concentration at different penetration depths. The procedure described in ASTM C 1152/C 1152M-04 was followed in this work as described in section 2.4.2. The

same split core samples that were sprayed with silver nitrate were also used for the titration chemical analysis.

Titration was carried out on concrete samples that were ground to powder. The procedure outlined in ASTM C114-07 was followed to find the total chloride content (acid-soluble chlorides) in each sample. Each concrete core was sliced every 5 mm from the exposed surface to a depth of 35 mm (as illustrated in Figure 3.37). Each concrete slice was then ground in order to obtain the powder samples required for chemical analysis. After the grinding, powder samples were stored in sealed plastic bags until the titration was carried out. Note that the chemical analysis on powder obtained from a 5-mm slice yields an average chloride concentration value over the 5-mm depth.

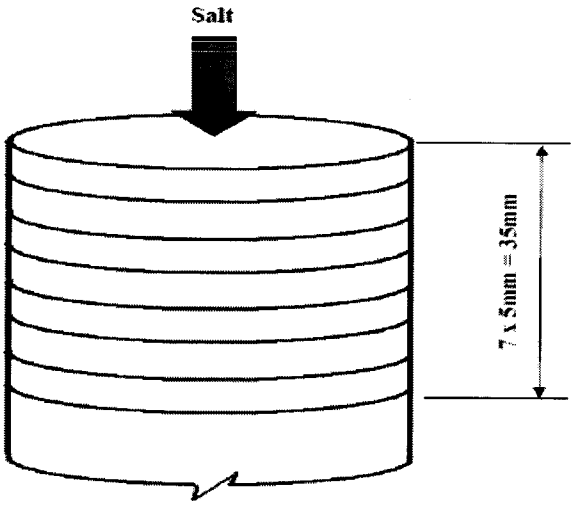

Figure 3.37: Thickness and number of slices in the concrete cores.

Special equipment was designed to grind slices from the split concrete cores. This equipment consists of a steel box containing two steel hemi-cylinders of the same diameter as the concrete core, which are held in place by four screwing bolts: two at the same level facing each other at the top of the box, and two at the same level facing each other at the bottom of the box. These two sets of bolts are perpendicular to each. The purpose of the top two bolts is to hold the concrete core properly, whereas the purpose of the bottom two screwing bolts is to keep the core sample fixed during the grinding process. The steel box is open from the top and bottom sides: the top opening is to

facilitate introducing the core sample, and the bottom opening is to allow the ground powder to fall in a stainless steel drawer that can easily collect it. Figure 3.38(a) shows an isometric view of the box, Figure 3.38(b) illustrates the top view of the box, Figure 3.38(c) shows the two hemi-cylinders, Figure 3.38(d) shows the stainless steel drawer, and Figure 3.38(e) illustrates the equipment with the sample in it.

An additional equipment was necessary to fit and hold the abovementioned system and to make the grinding process for the operator easy and safe. A steel frame as shown in Figure 3.39(a) was built for this purpose. Figure 3.39(b) illustrates the position of the steel box in the steel frame. The steel plate shown in Figure 3.39(c) was used to hold the steel box firmly within the steel frame as illustrated in Figure 3.39(d) and to provide a correct place for the profile grinder (see Figure 3.39(e)). The most important characteristic of this steel plate is that the outer diameter D_1 was designed so that the bit of the grinder does not touch the inner hole of diameter D_2.

It was noticed that when grinding took place some of the powder was coarser than what is allowed in the standard ASTM C114-07, which states that all the powder must pass a 20-mesh sieve. Accordingly, another equipment had to be designed and manufactured to further tamp the sample manually and achieve the grinding requirements. This equipment consists of a steel plate with a frame that has two screw bolts, a steel pipe with openings at the top and bottom with two wings welded on two sides at an angle of 180°, and a solid circular hammer, as shown in Figure 3.40. The wings in the pipe ensure that the pipe is held firmly in the frame by tightening the screw bolts.

The procedure described in Section 19 of the ASTM 114-07 standard was followed to carry out titration on the ground samples. The electrode used for the titration was a silver-chloride electrode. The procedure as outlined in the standard was followed with the exception of the filtration step, which was skipped as it is tedious and very time consuming. As mentioned in section 2.4.2., the results are not affected by this.

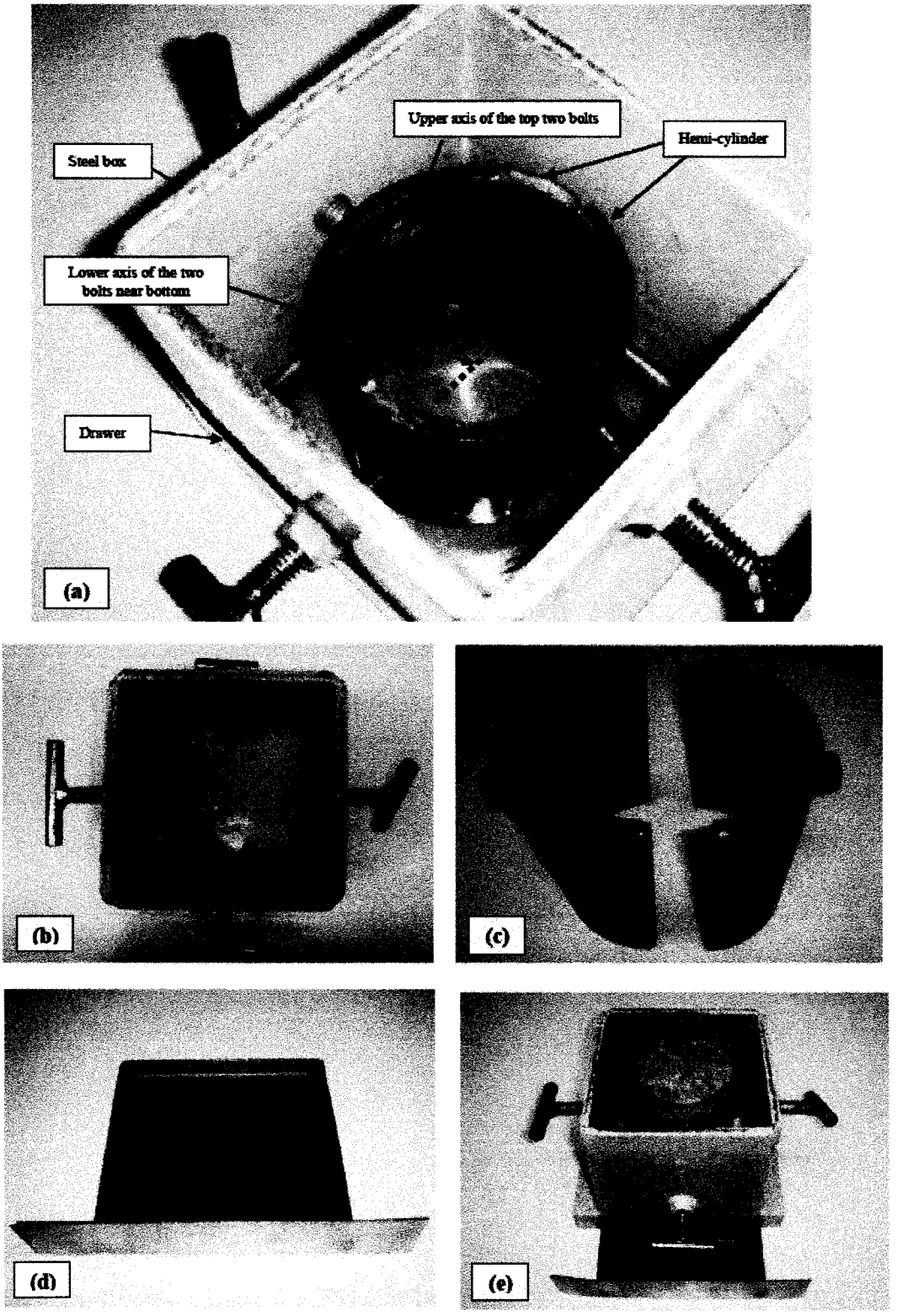

Figure 3.38: Steel box designed for grinding and collection of concrete powder.

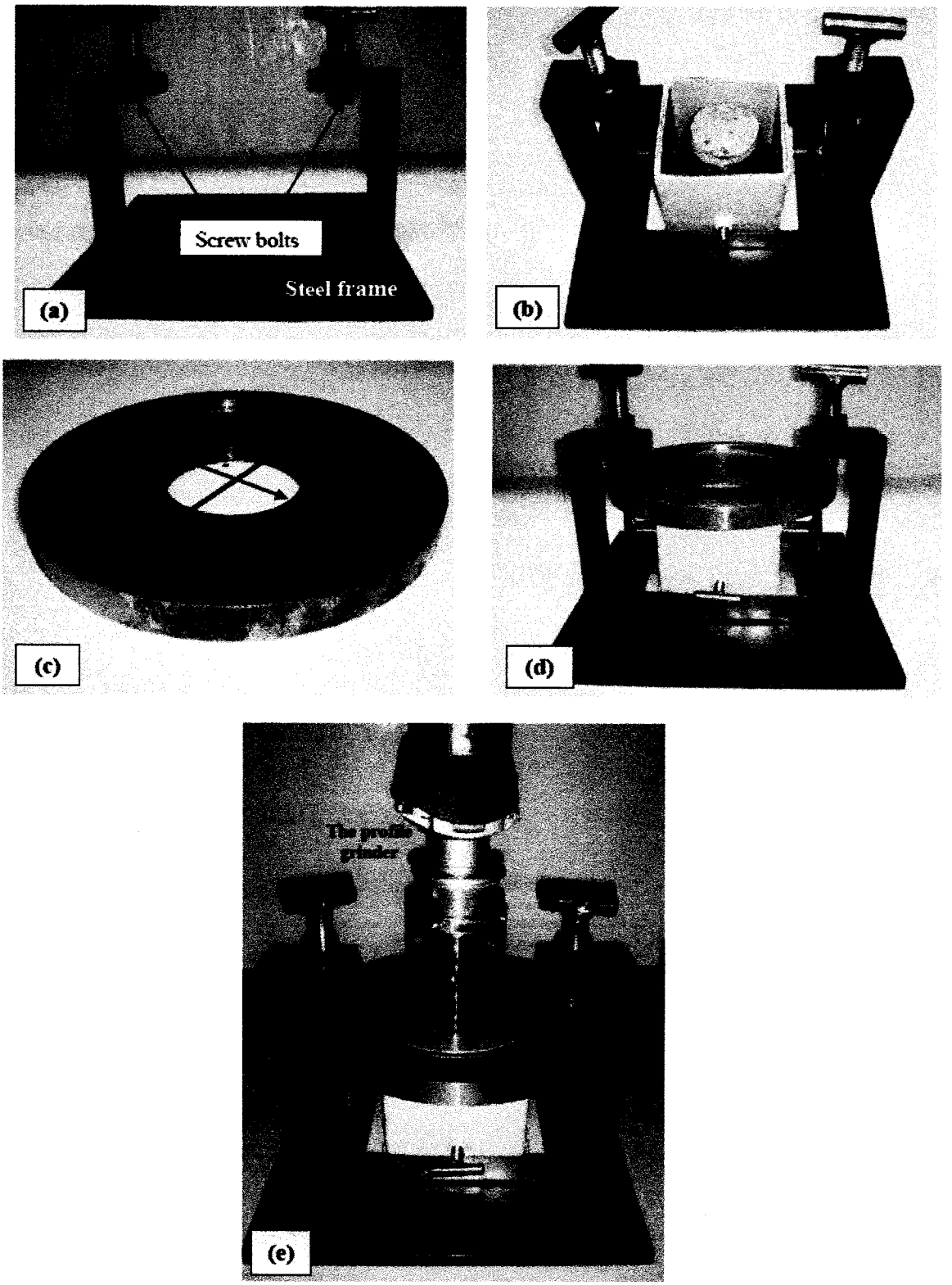

Figure 3.39: Steel frame designed to carry out the grinding process.

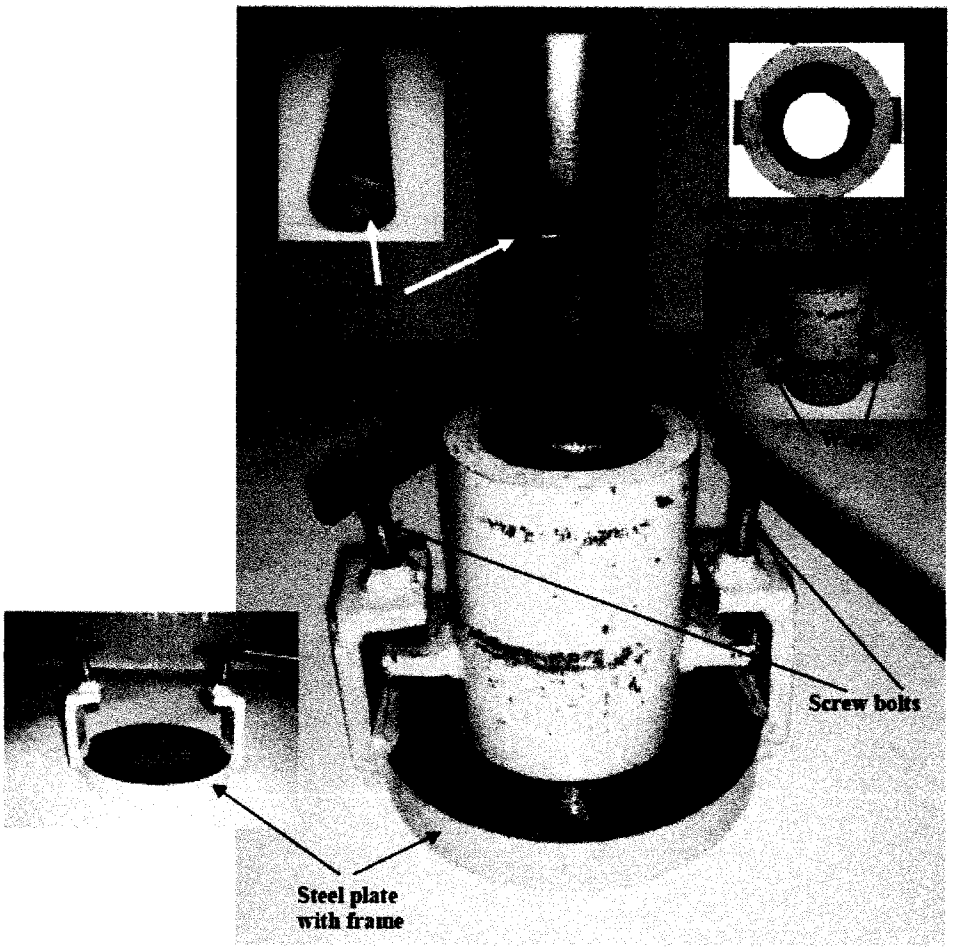

Figure 3.40: Manual grinder.

Instead of using a potentiometer as mentioned in the ASTM standard, a microprocessor-controlled automatic titrator was used, 794 Basic Titrino from Metrohm (see Figure 3.41). This automatic titrator has an automatically varying dosing device for the titration substance and determines automatically the neutral or end point (E.P.) from the steepness of the curve (first derivation), with titration results being directly displayed on the screen. The advantages of using such system are the low risk of misreading on the burette scale and the colour of the end point when using the Volhard method. An automatic titrator has also the capability of detecting low chloride concentrations. In addition, the microprocessor-controlled automatic titrator can detect the titration process even in the flat zone of the titration curve.

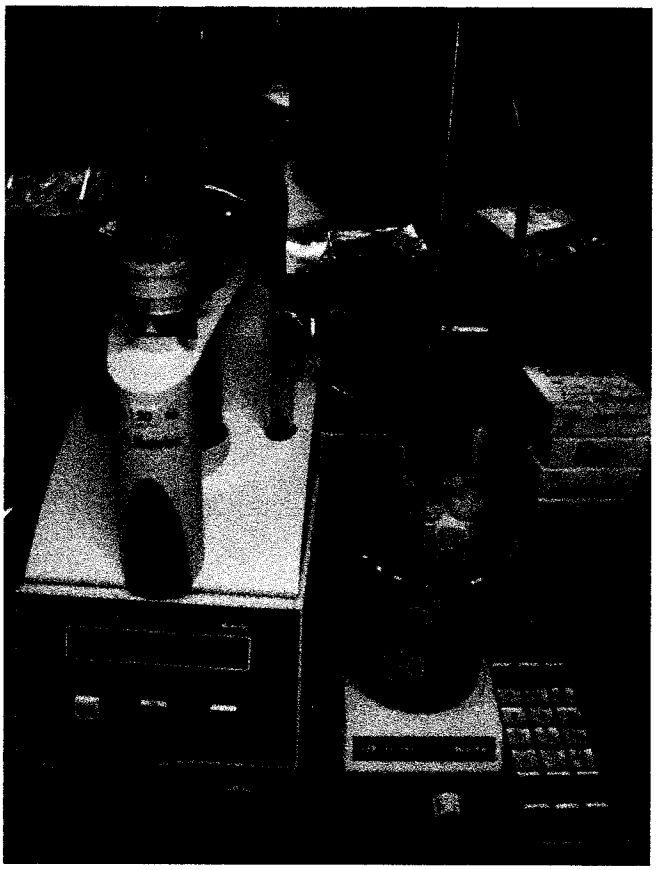

Figure 3.41: Automatic potentiometric titrator.

The mode that the 794 Basic Titrino followed was the Dynamic Equivalence point Titration (DET), in which the reagent feeding is in variable volume increments, depending on the slope of the curve. The DET mode is suitable for most problems, and it is specially recommended if jumps lie very close together or are very flat. Figure 3.42 illustrates the nature of the curve that the titrator follows to perform the titration process; more details can be found in the manual of the equipment.

It is worth mentioning that before using this equipment to quantify the total chloride content of the concrete samples, some preliminary measurements were done using both the Volhard method and the 794 Basic Titrino automatic titrator (by skipping the filtration step). The results are compared in Figure 3.43. The chloride contents obtained from the Volhard method are higher than those obtained from the automatic titration. It is believed that the reason behind this difference is that the automatic titrator starts to add

the reagent at a very slow rate near the E.P., whereas in the Volhard method, the addition of the reagent is manual and susceptible to human errors.

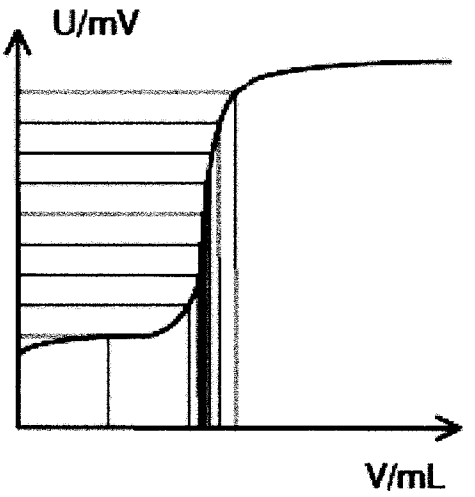

Figure 3.42: Titration mode followed by the titrator – relationship between the electrical potential (mV) and the volume of the reagent (mL) (reproduced from the manual).

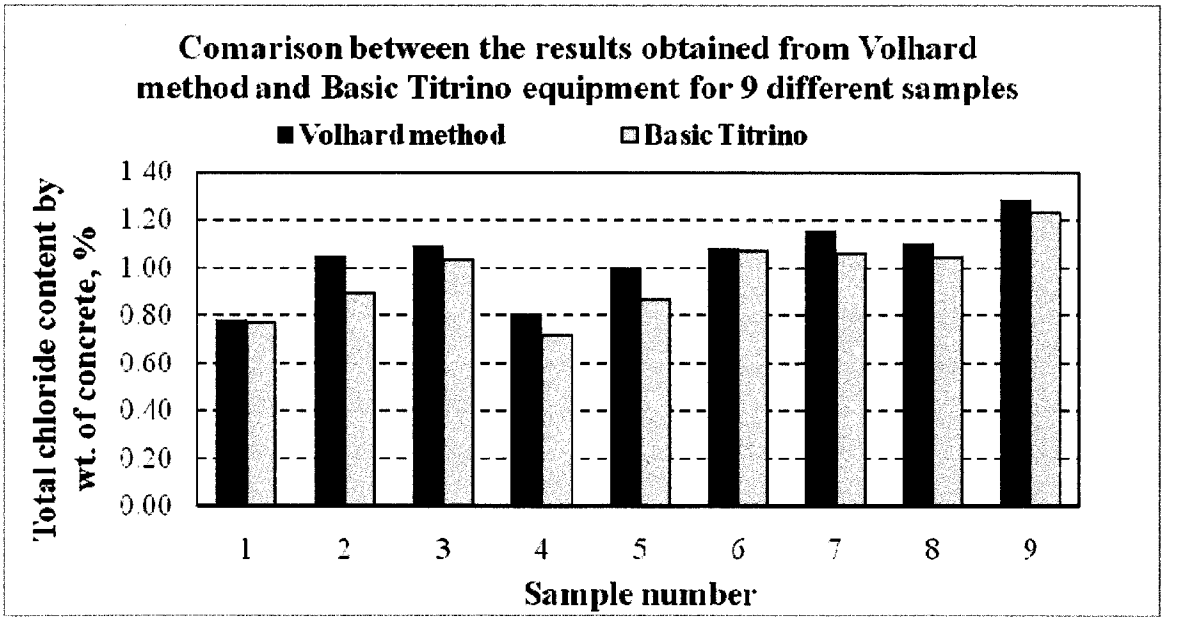

Figure 3.43: Comparison between the results obtained from the Volhard method and the Basic Titrino equipment.

ASTM C114-07 recommends the minimum weight of the sample to be analyzed to be 5 g if the expected chloride content is less than 0.15% Cl^- by weight of concrete. The sample should be dispersed with 75-ml of desalinated water in a 250-ml beaker, and 25-ml of nitric acid should be added immediately and gradually with continuous stirring (Figure 3.44). Dilute nitric acid (1:1) was used from commercial nitric acid of concentration of 70%.

Figure 3.44: Preparing samples for titration (pre-boiling step).

Covering the beaker after adding the nitric acid and during boiling is an important step to avoid losing chlorides due to volatilization. In this work, the beakers were covered firmly by using aluminum foil, as shown in Figure 3.45(a). The purpose for boiling the powder sample in the nitric acid is to decompose it and to dissolve all the chlorides into the solution (Figure 3.45(b)). Maximum care was taken in preparing the chemical analysis in order to avoid the introduction of any possible error (Figure 3.46).

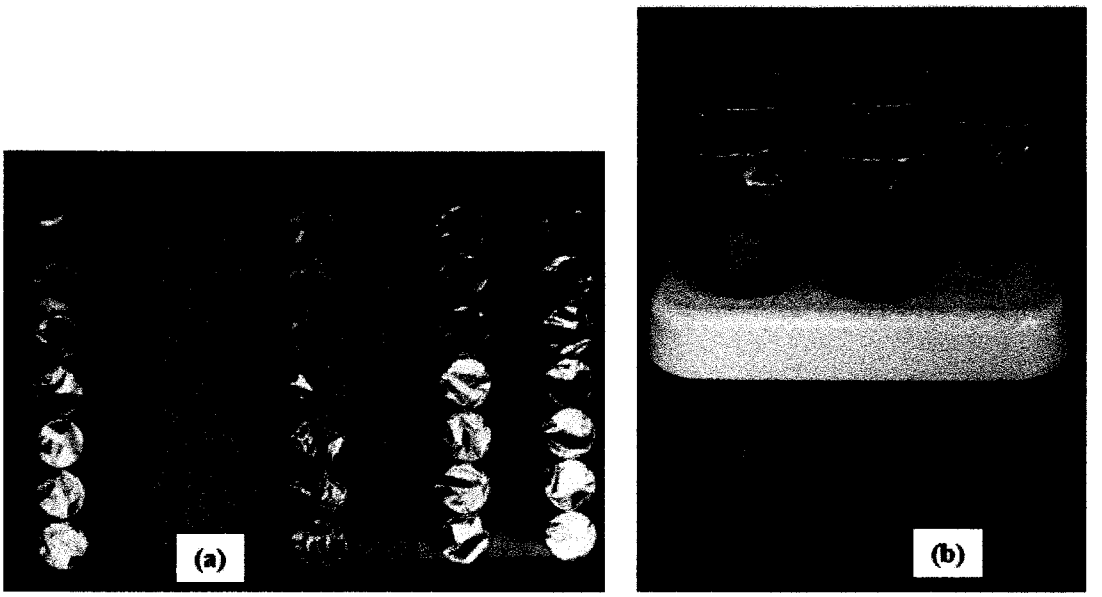

Figure 3.45: Sample preparation for titration: (a) covering of beakers, (b) boiling.

Figure 3.46: Titration in progress.

A 2.00-ml standard 0.05 N NaCl solution was added to the beaker prior to titration, and the silver nitrate was used as a reagent. By using the automatic titrator, the titration was carried out automatically, with indications of the end point being reached when

dropping of the silver nitrate became slow. At this point, it is important to record the volume of silver nitrate consumed. Once the end point is reached, the titrator stops automatically. The percentage of chloride content can be calculated according to ASTM C114-07 from Eq. (3.2):

$$Cl(\%) = \frac{3.545\left[(V_1 - V_2)N\right]}{W} \tag{3.2}$$

where V_1 is the volume of consumed 0.05 N $AgNO_3$ solution at the equivalence point (mL), V_2 is the volume of consumed 0.05 N $AgNO_3$ solution for blank titration at the equivalence point (mL), N is the exact normality of 0.05 N $AgNO_3$ solution, and W is the weight of the concrete sample (g).

3.5 Detection of concrete carbonation in the Structures Lab

In order to check whether concrete carbonation could affect the specimens used for chloride analysis, an examination was carried out by following the steps outlined in the RILEM recommendations CPC-18. Two different samples were used: the first sample was a concrete core of w/c = 0.5 (which is more vulnerable to carbonation), and the second sample was a concrete cylinder over 5-years old found in the lab. The samples were sprayed with a solution of 1% phenolphthalein in 70% ethyl alcohol. The phenolphthalein solution turns pink in non-carbonated concrete and remains colourless in carbonated concrete. The results illustrated in Figures 3.47(a) and 3.47(b) reveal that the environment of the Structures Lab did not promote concrete carbonation.

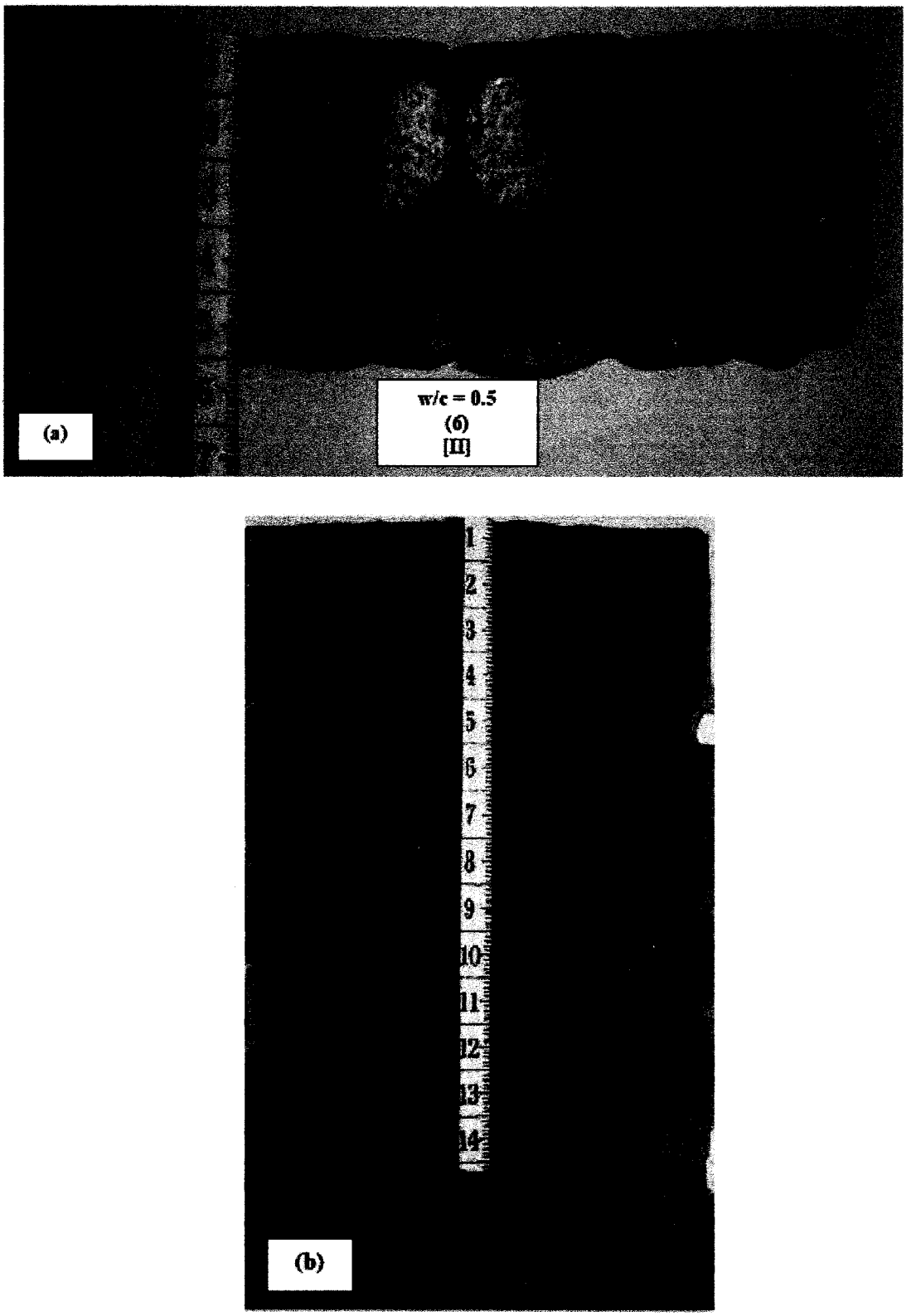

Figure 3.47: Samples used for carbonation detection in the Structures Lab: (a) concrete core of w/c = 0.5, (b) concrete cylinder over 5-years old.

Chapter 4

Experimental Results

4.1. Introduction

This chapter presents the experimental results obtained from carrying out the experimental testing program described in Chapter 3. Section 4.2 gives details of the strain measurements recorded by both electrical strain gauges and distributed Brillouin fibre-optic sensors, and Section 4.3 reports chloride concentration depths and profiles obtained from the colourimetric and potentiometric titration methods, respectively.

4.2. Strain measurements

The deformation experienced by the RC deck as a result of the applied load was monitored by means of electrical strain gauges and distributed Brillouin fibre sensors. The following sections discuss the results obtained through these two techniques.

4.2.1. Strains measured by electrical strain gauges

After the load was applied on the deck, the strains recorded by all the electrical strain gauges were recorded on a weekly basis. The complete set of strain data recorded during the period of this work is presented in Appendix C.

4.2.1.1. Strains on threaded bars

As mentioned in Chapter 3, the load was applied by means of threaded bars. In order to monitor the applied load, electrical strain gauges were also placed on these bars (numbered from 27 to 32 in Figure 3.16). Figures 4.1, 4.2, and 4.3 show the strains on each threaded bar right after loading and before taking core samples after each wet/dry cycle. All the charts indicate that the loading process went as expected; the average strain of those recorded by strain gauges 27 and 28 (which represent one point load of magnitude P) and the average strain of those recorded by strain gauges 31 and 32 (which

also represent one point load of magnitude P) are almost half of those recorded by strain gauges 29 and 30 (which represent a point load of magnitude $2P$). The theoretical strains for point loads P and $2P$ are respectively 780 με and 1560 με; these values are shown by the dashed horizontal lines in Figures 4.1, 4.2, and 4.3. Although extreme care was taken during gluing of the strain gauges, the slight difference between each couple of strain gauges glued on the same tensioned bar could be attributed to the deviation angle mentioned in section 3.4.1 and shown in Figure 3.28(a). Note that the strains on the tension rods barely changed during the duration of the experiment.

4.2.1.2. Strains in the concrete and steel reinforcement

The strain distribution along the top and bottom concrete surfaces as well as on the top and bottom reinforcements right after loading and before concrete coring for the first wet/dry cycle are shown in Figures 4.4, 4.5, and 4.6 for the RC strips of w/c of 0.35, 0.40, and 0.50, respectively. Figures 4.7, 4.8, and 4.9 illustrate the strain distributions along the deck after loading and right before coring for the second wet/dry cycle for the RC strips of w/c of 0.35, 0.40, and 0.50, respectively. Finally, the strain distribution for the third wet/dry cycle for the RC strips of w/c of 0.35, 0.40, and 0.50 are shown in Figures 4.10, 4.11, and 4.12, respectively. From these figures, it is worth to note the following:

- there are no significant differences in the measured strains after the loading takes place and right before taking the core sets; this is a good indication that the spring system used effectively worked in counteracting any relaxation effects;
- the measured strains reflect the expected behaviour for both concrete and reinforcement under the action of the given load; however, concrete strain gauges give incorrect values when located across cracks, and as a result they are not capable of monitoring tensile concrete strains beyond cracking;
- each RC strip worked monolithically for the given load, as the strain gauges readings corresponding to locations 17 and 17' in Figure 4.13 are almost the same for all readings, with the exception of the data corresponding to the strip of 0.35 w/c before taking the third set of cores (see Figure 4.10); and,

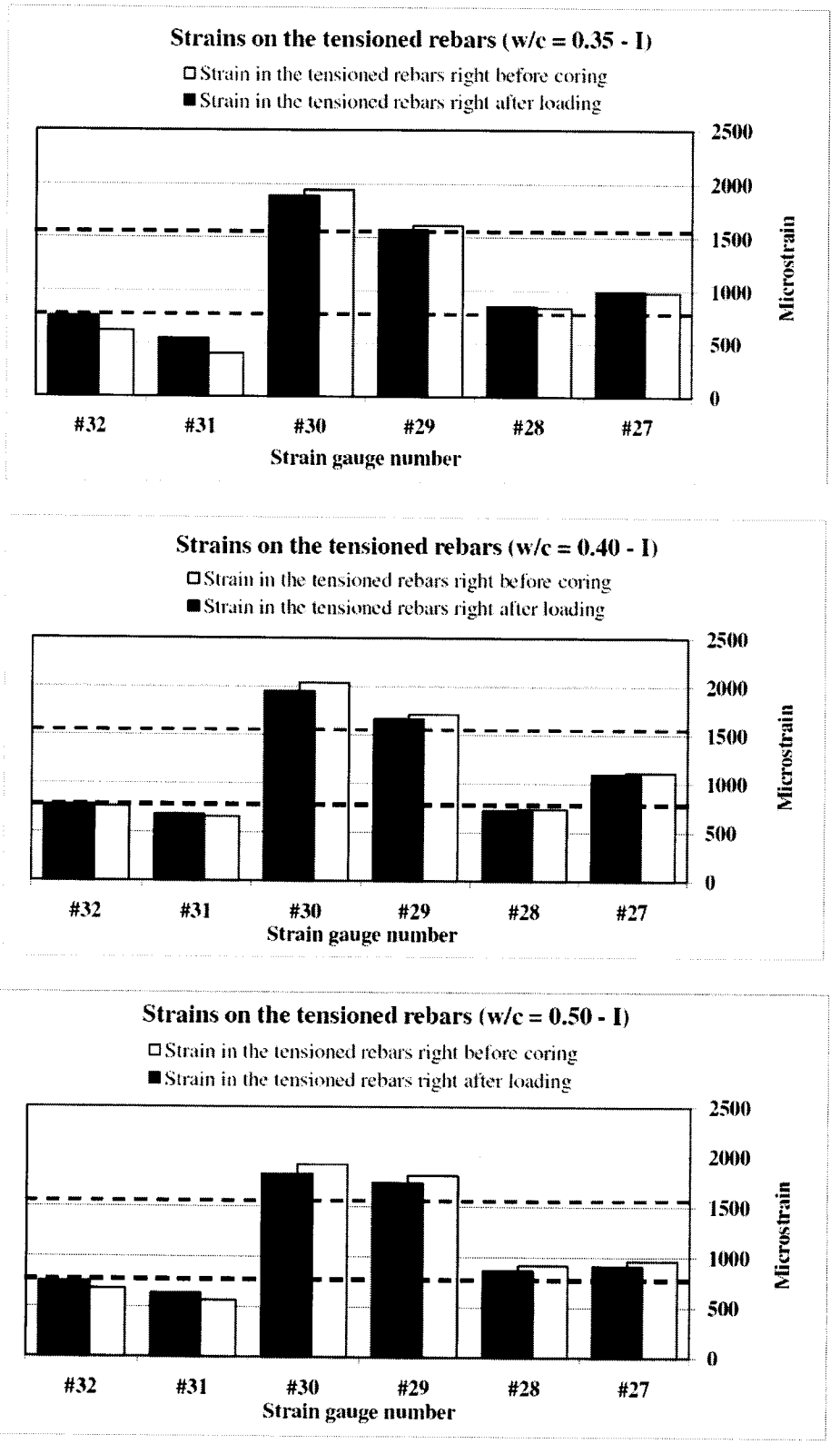

Figure 4.1: Strains on loaded tensioned bars for the three strips after the first wet/dry cycle.

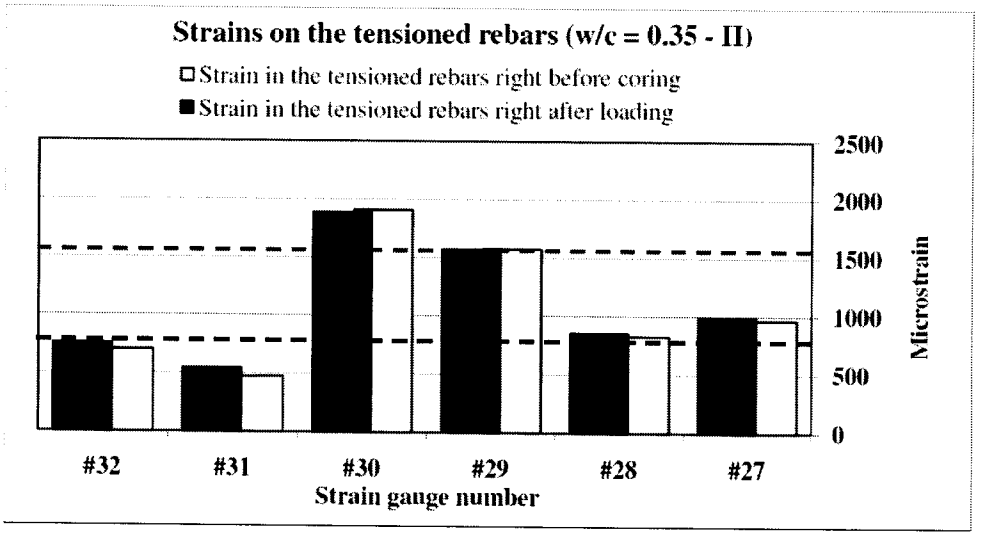

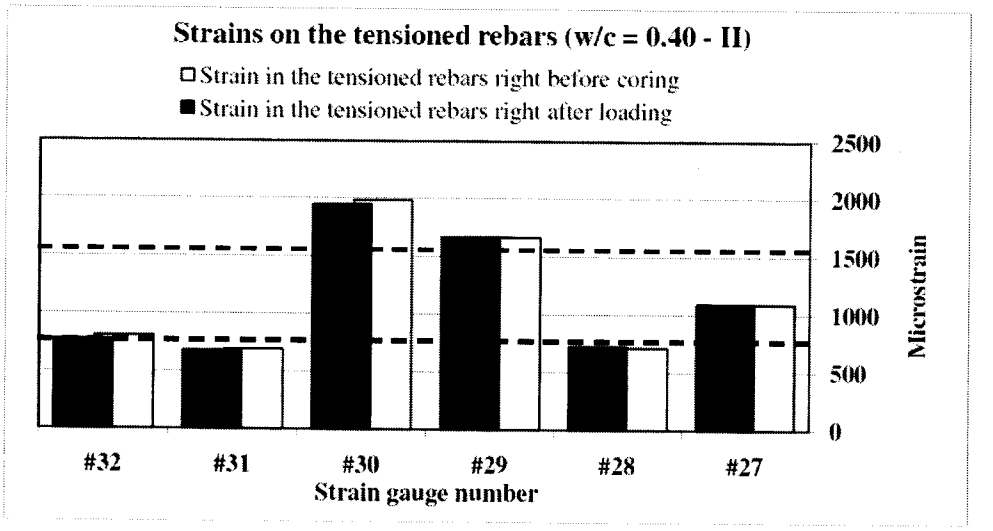

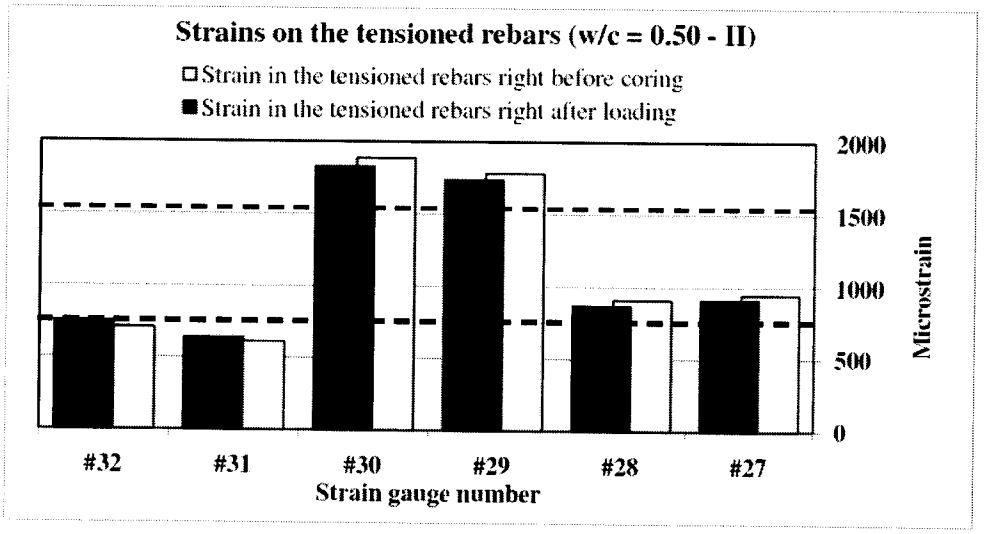

Figure 4.2: Strains on loaded tensioned bars for the three strips after the second wet/dry cycle.

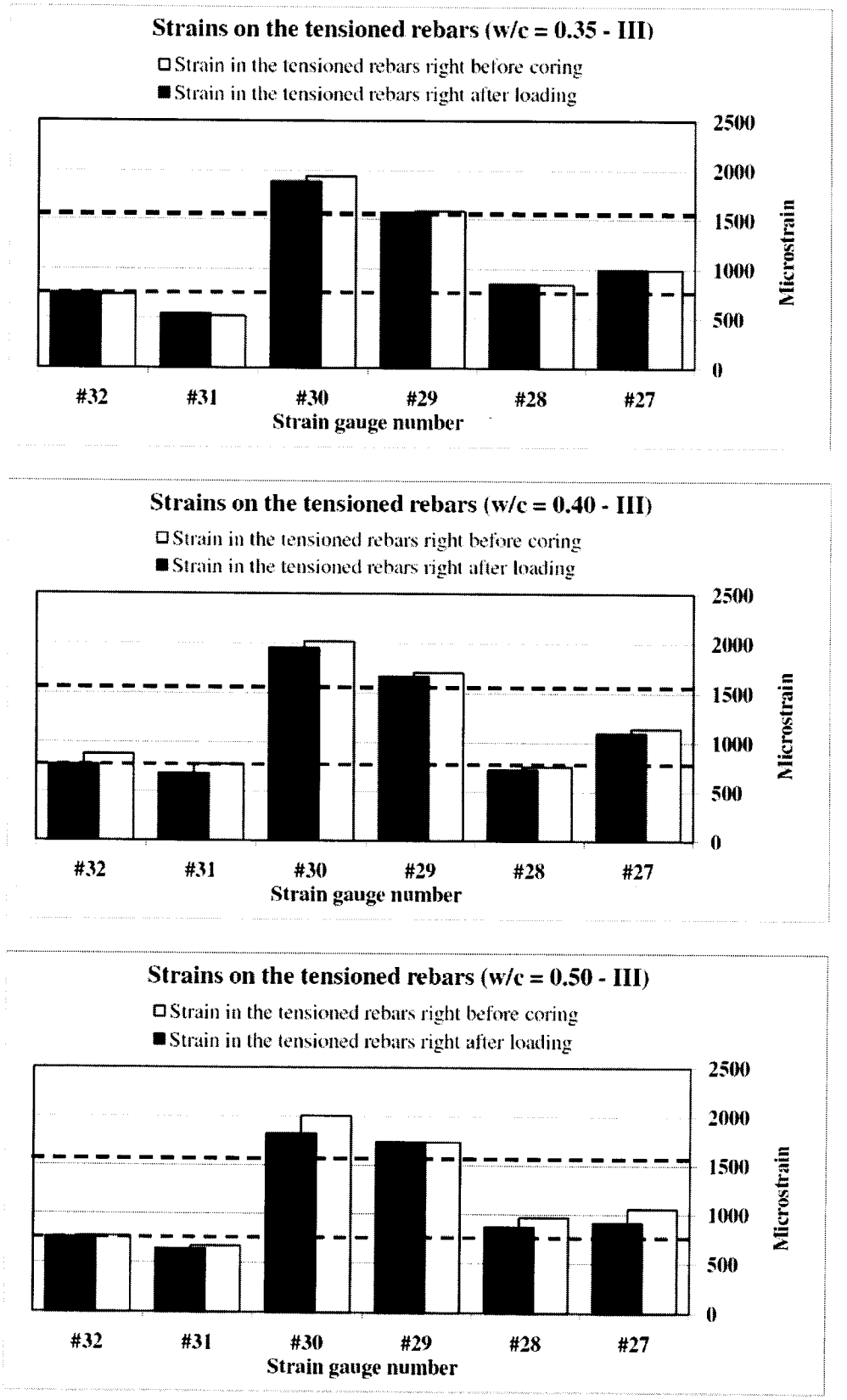

Figure 4.3: Strains on loaded tensioned bars for the three strips after the third wet/dry cycle.

- the strains at a distance of 2.275 m from the right support are almost zero as expected, since the loading was designed for the bending moment to be zero at this section (see bending moment diagram in Figure 3.17).

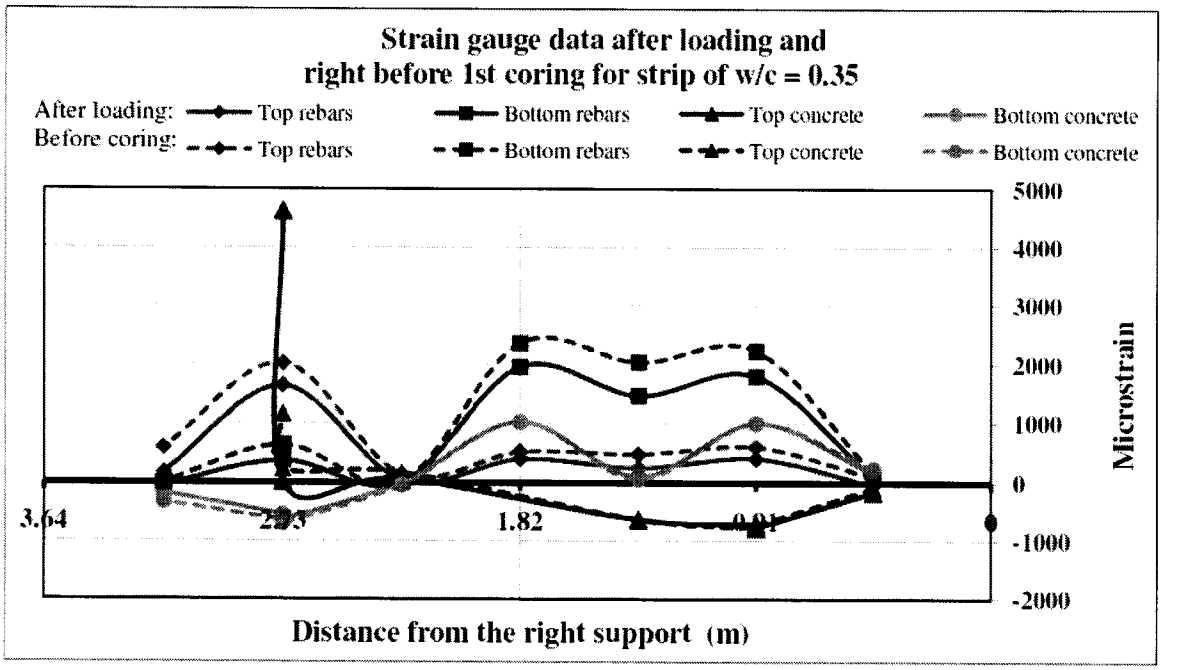

Figure 4.4: Strains for strip of w/c = 0.35 after loading and right before coring for the first set.

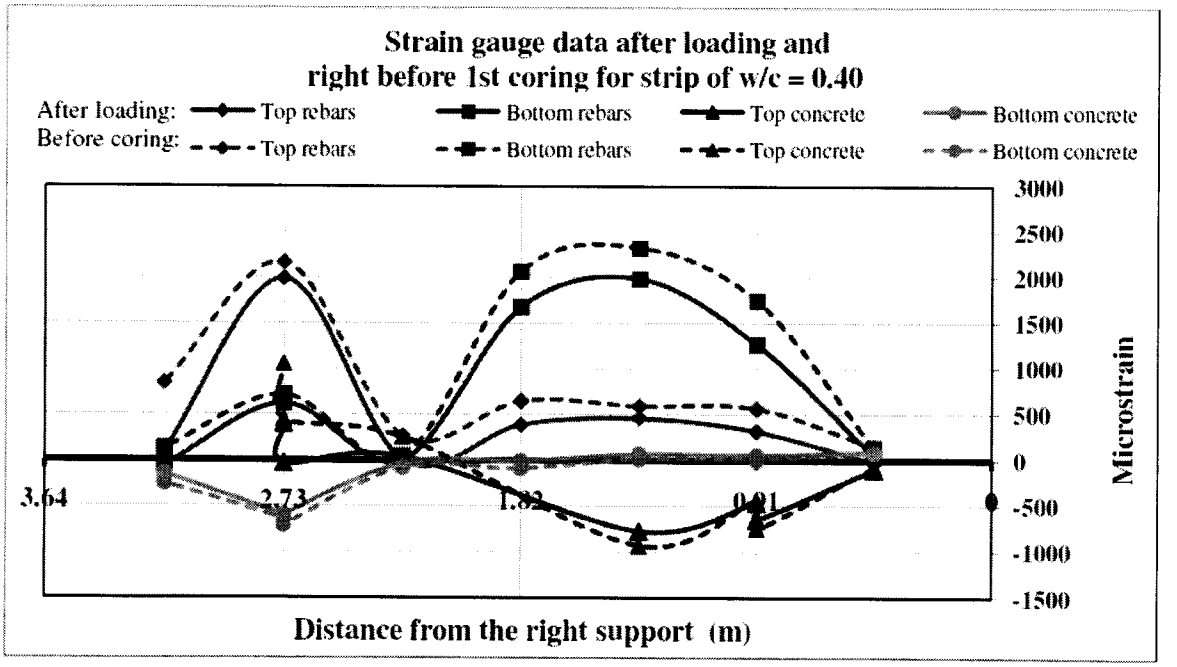

Figure 4.5: Strains for strip of w/c = 0.40 after loading and right before coring for the first set.

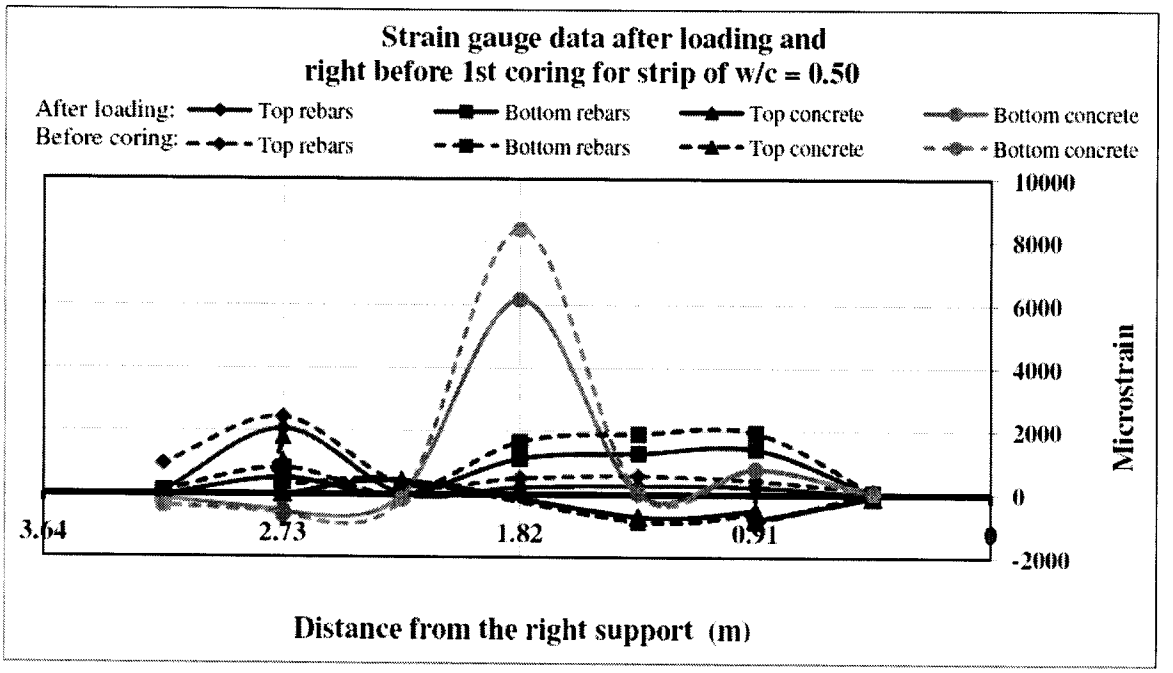

Figure 4.6: Strains for strip of w/c = 0.50 after loading and right before coring for the first set.

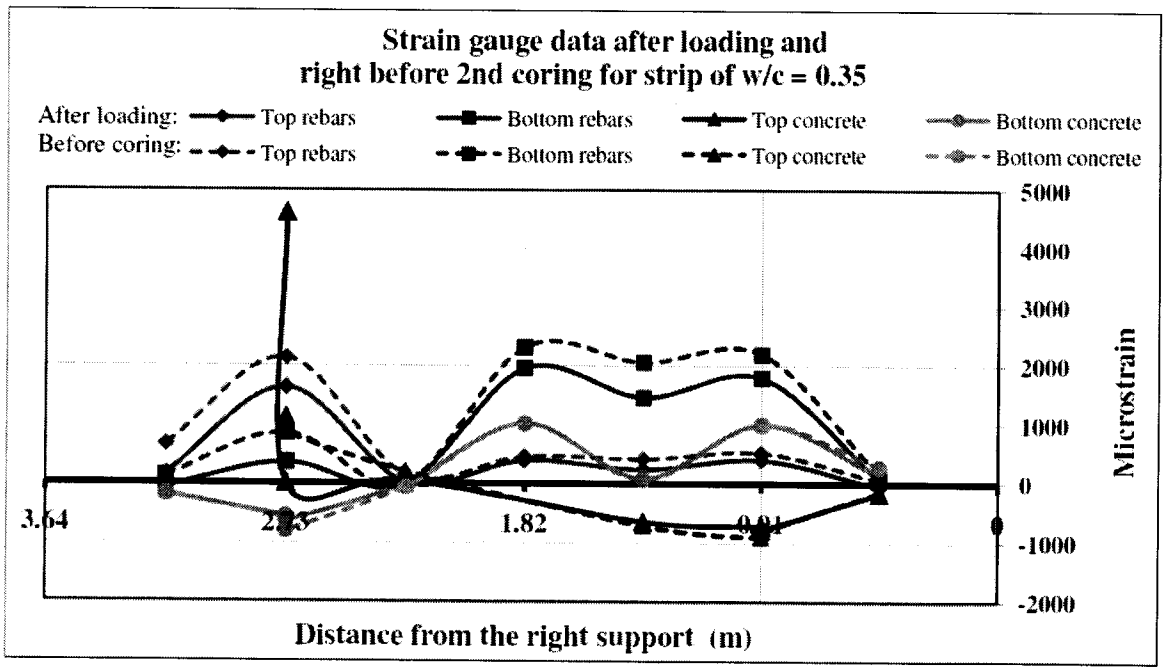

Figure 4.7: Strains for strip of w/c = 0.35 after loading and right before coring for the second set.

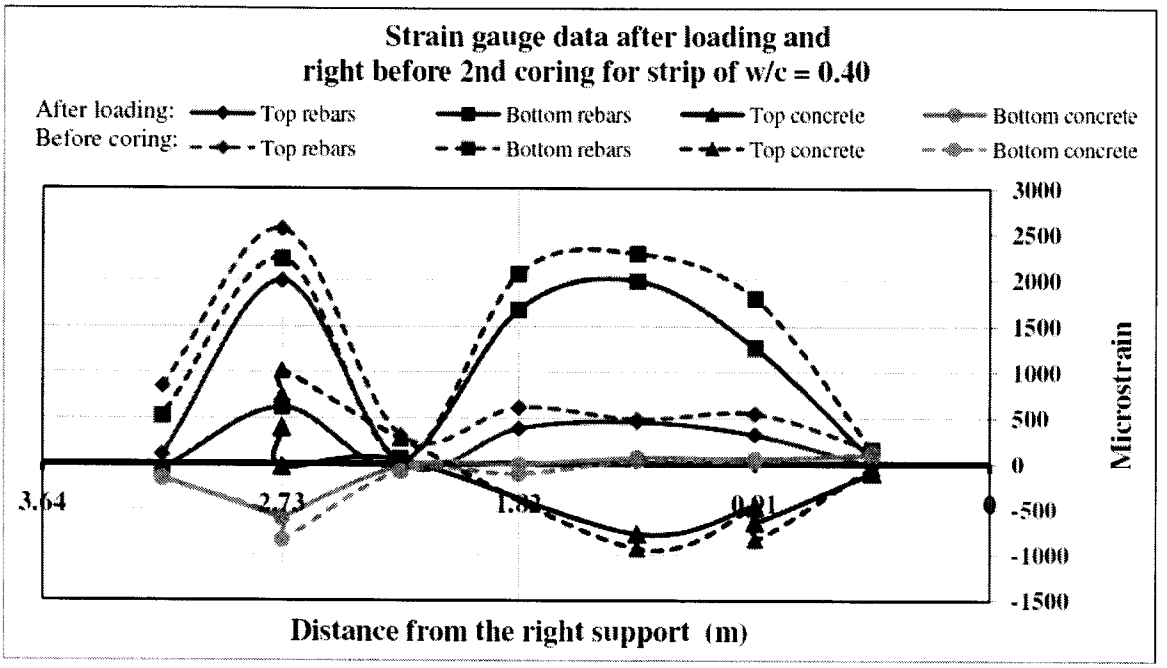

Figure 4.8: Strains for strip of w/c = 0.40 after loading and right before coring for the second set.

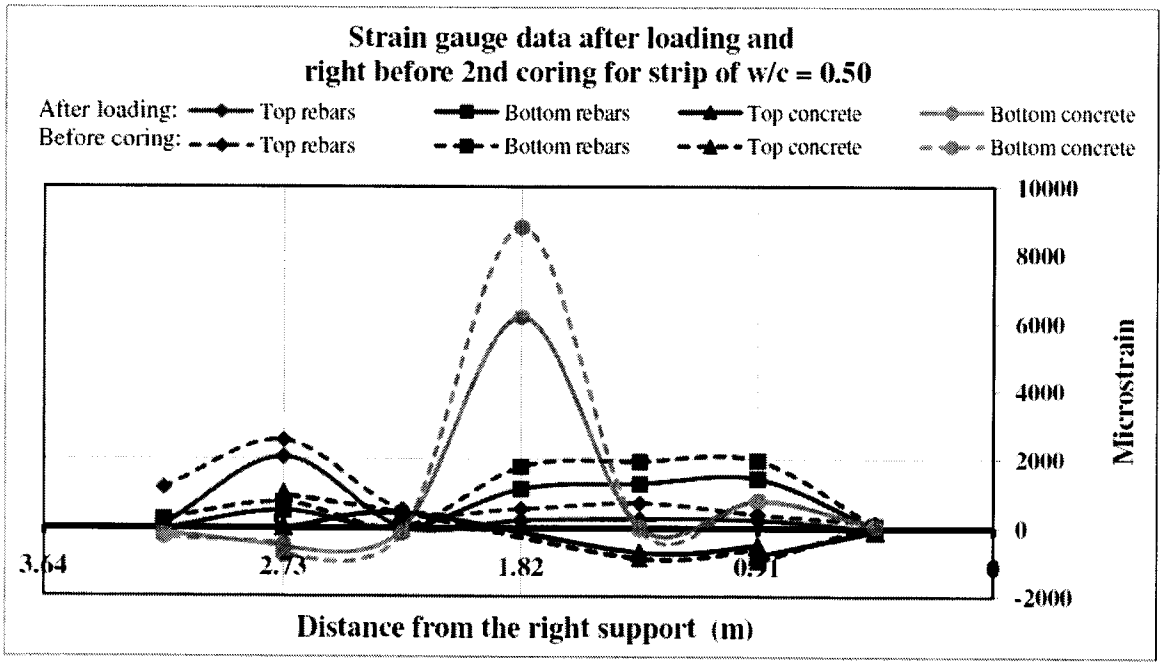

Figure 4.9: Strains for strip of w/c = 0.50 after loading and right before coring for the second set.

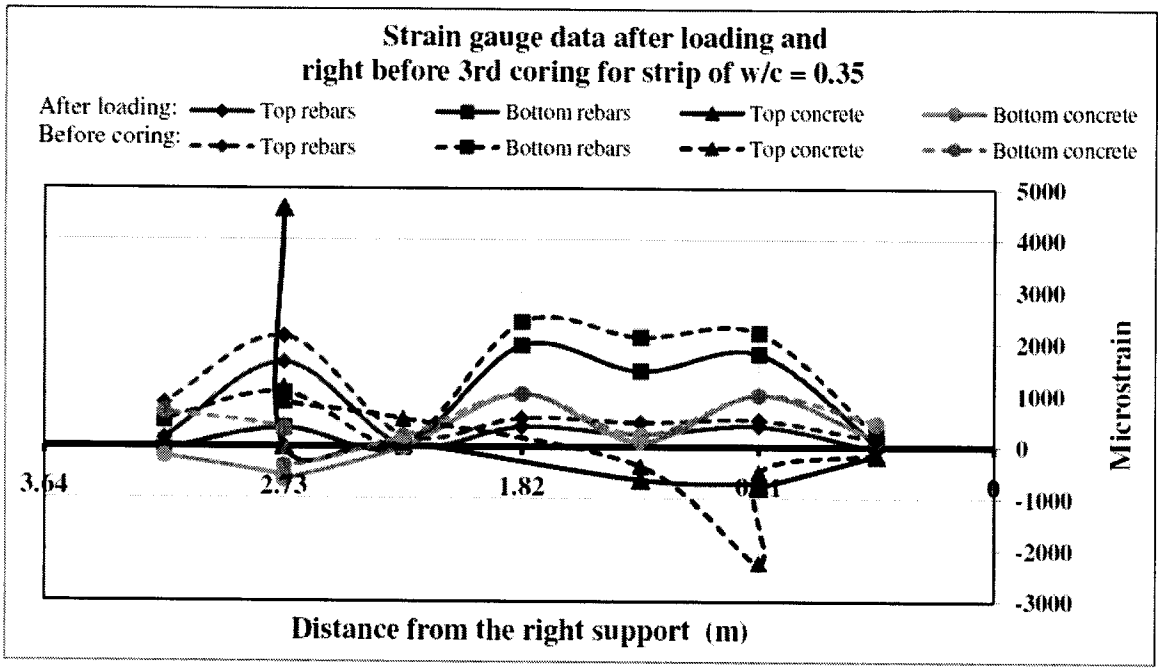

Figure 4.10: Strains for strip of w/c = 0.35 after loading and right before coring for the third set.

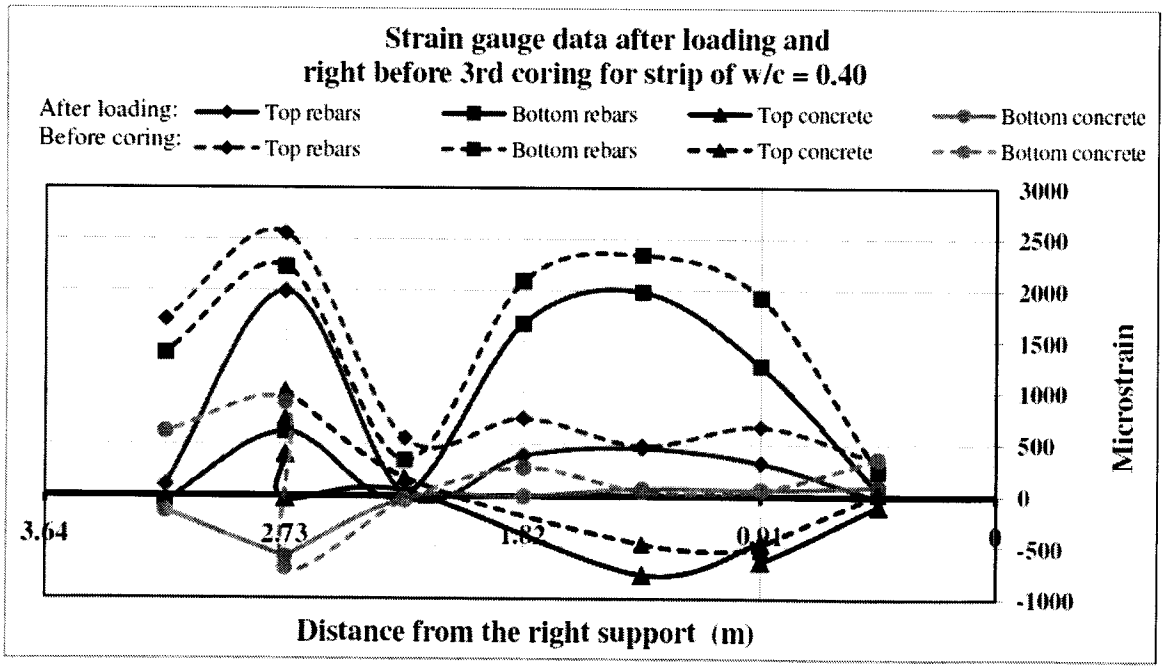

Figure 4.11: Strains for strip of w/c = 0.40 after loading and right before coring for the third set.

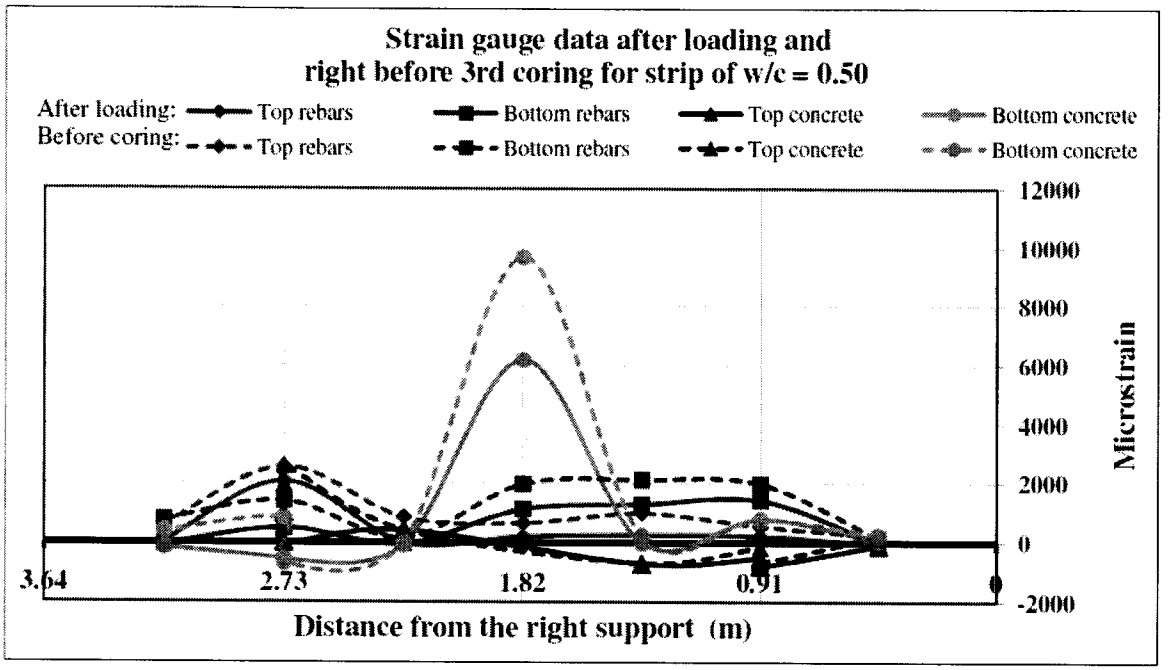

Figure 4.12: Strains for strip of w/c = 0.50 after loading and right before coring for the third first set.

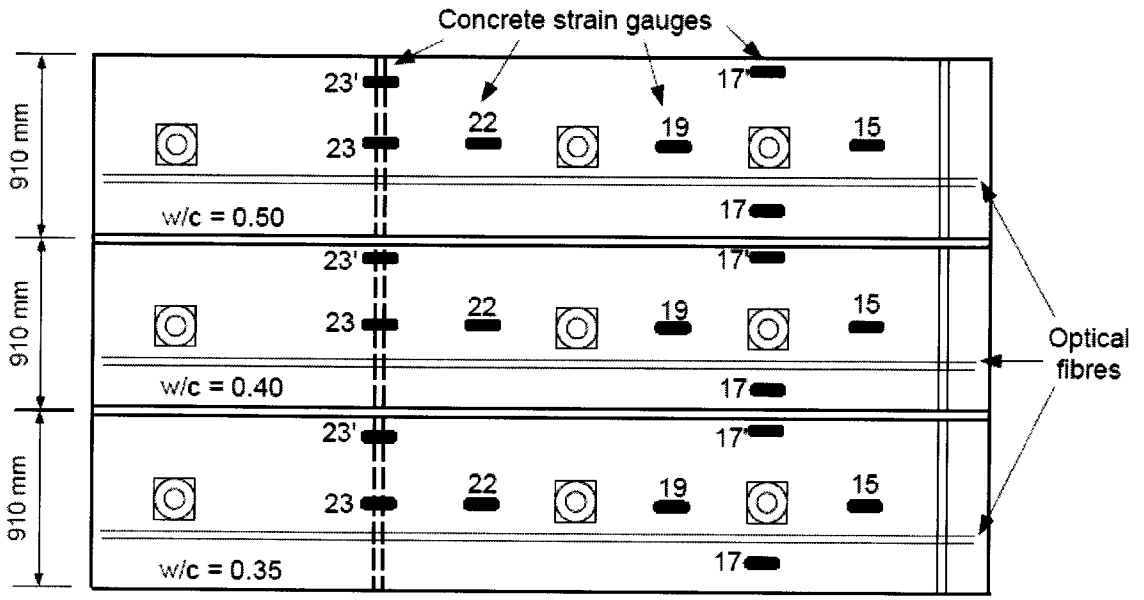

Figure 4.13: Concrete strain gauges at the top surface of the deck.

4.2.2. Strains measured by optical fibres

In addition to electrical strain gauges, concrete deformation at the top and bottom surfaces of the deck was also monitored by means of distributed Brillouin fibre sensors. The strains measured by the distributed Brillouin fibre sensors were those corresponding to right after the load was applied on the deck. The complete strain data as recorded by the optical fibres is presented in Appendix D.

Figures 4.14 and 4.15 show the concrete strain distributions measured by the optical fibres at the top and bottom surfaces of the deck for the three RC strips, respectively. The strains along the sensing fibres were extracted from the recorded Brillouin spectrum for the applied load by using the multiple-peak fitting method (Zhang et al., 2008). The sensing system used had a spatial resolution of 20 cm and a readout resolution of 10 cm, the latter being controlled by the time resolution of the digitizer. Also shown in the figures are the concrete strains measured by the electrical strain gauges. Strain gauges numbered 23, 23', 22, 19, 17, 17', and 15 were used to monitor the strains at the top surfaces of the three strips, whereas strain gauges numbered 26, 25, 24, 22', 21, 20, 18 and 16 were used to monitor the strains at the bottom surfaces of the three strips, as illustrated in Figure 3.16.

Shown in Figures 4.14 and 4.15 as well are the strains calculated according to classical bending theory. The theoretical strains were calculated from the internal bending moments developed from the applied load (see Figure 3.17). In the calculations, the slab was assumed to act elastically at sections where the moment applied is below the cracking moment. In the sections where the moment applied is above the cracking moment, although concrete can no longer resist tensile stresses, concrete compressive stresses resulting from the applied service loads were assumed to be linear elastic. The cracking moment M_{cr} for each RC strip was calculated from the flexure formula as:

$$M_{cr} = \frac{f_r \cdot I_g}{y_t} \tag{4.1}$$

where f_r is the modulus of rupture (given by $f_r = 0.6\lambda\sqrt{f_c'}$ [MPa], where λ = 1 for normal-density concrete), I_g is the moment of inertia of the uncracked transformed section, y_t is the distance from the neutral axis to the extreme tension fibre (77.5 mm),

and f'_c is the compressive strength of concrete (MPa). The calculated cracking moments are respectively 19.46 kN·m, 18.01 kN·m, and 17.37 kN·m for each RC strip of w/c of 0.35, 0.40, and 0.50 (further information is presented in Appendix B).

In regions where the applied moment is less than the cracking moment, the strains in the concrete ε_c are calculated from Hooke's law according to:

$$\varepsilon_c = \frac{M \cdot y}{E_c \cdot I} \tag{4.2}$$

where M is the internal bending moment, y is the distance from the neutral axis to the beam fibre where ε_c is calculated, E_c is the elastic modulus of concrete (calculated from the slope of the concrete stress-strain curve at a load level of 40% f'_c and found to be 40 GPa), and I is the moment of inertia corresponding to the uncracked transformed section. More detailed information on the estimation of E_c is presented in Appendix A. In regions where the applied moment exceeds the cracking moment, the concrete compressive stresses can still be calculated from Eq. (4.2); however, the moment of inertia I in this case corresponds to the cracked transformed section. The position of the neutral axis for the cracked transformed section was found to be 32 mm from the concrete fibre subjected to maximum compressive stress.

By looking at Figure 4.14, both concrete strain gauges and optical fibres readings were consistent with expected results, with the exception of the optical fibre readings at 1.82 m for the strip with w/c of 0.35; here the measured strains should have been in compression while the values displayed are tensile. The strain distribution along the bottom of the three RC strips is also in accordance to the values measured by the electrical strain gauges and those calculated from theory (see Figure 4.15). In fact, the Brillouin fibre sensors capture well the expected regions of tensile and compressive strains, although they tend to underestimate the peak compressive strains at 0.91 m for the 0.40 and 0.50 w/c strips. This might be an indication that the optical fibres became loose once subjected to compression, and that they might need to be prestressed when bonded to the concrete surface in order to be able to measure compressive strains. Of significance is the fact that the Brillouin fibre sensors can provide an estimate of the

strains experienced by the concrete under tension, unlike the electrical strain gauges or theory.

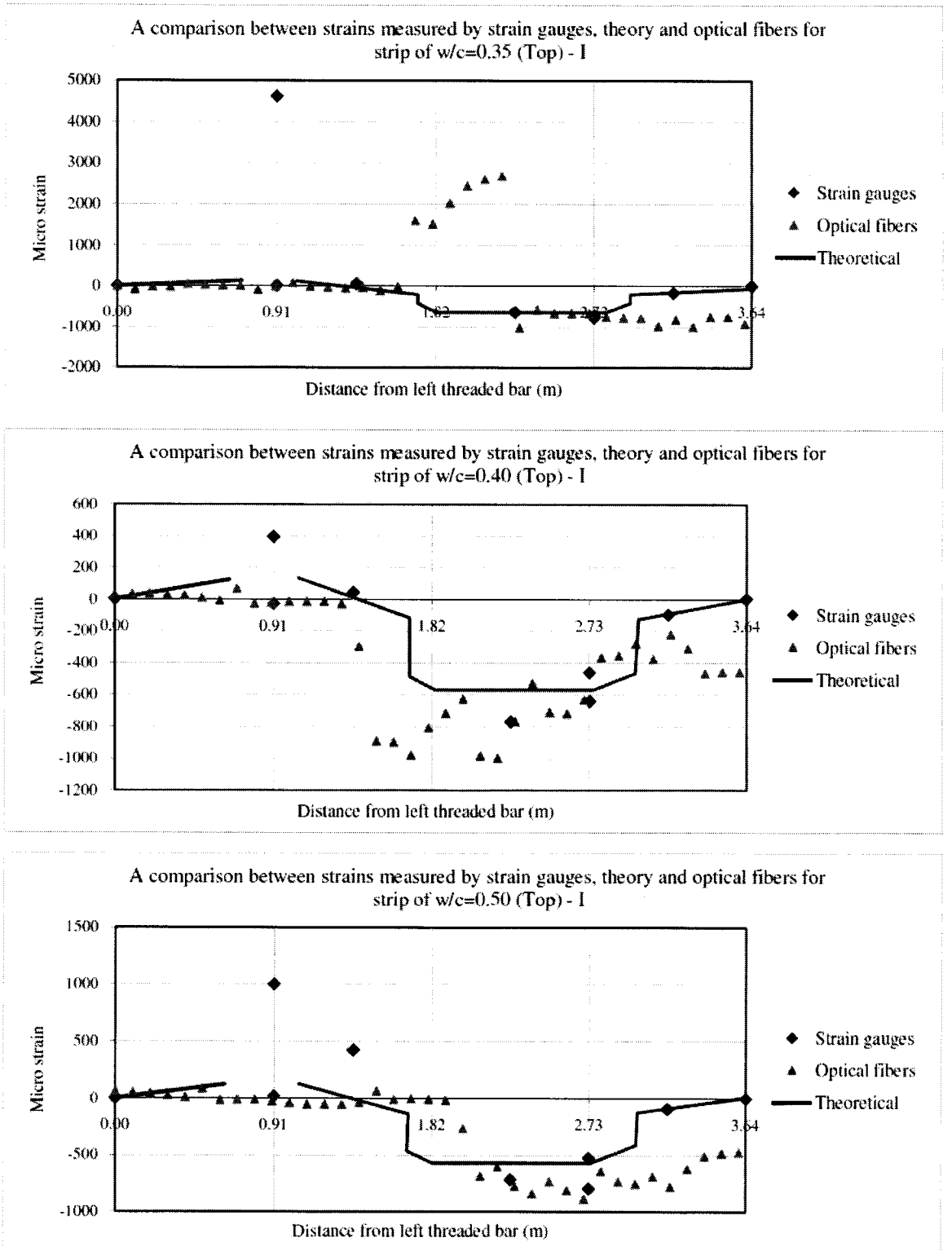

Figure 4.14: Strain distribution along the top surface of the deck according to concrete strain gauges, optical fibres and theoretical strains.

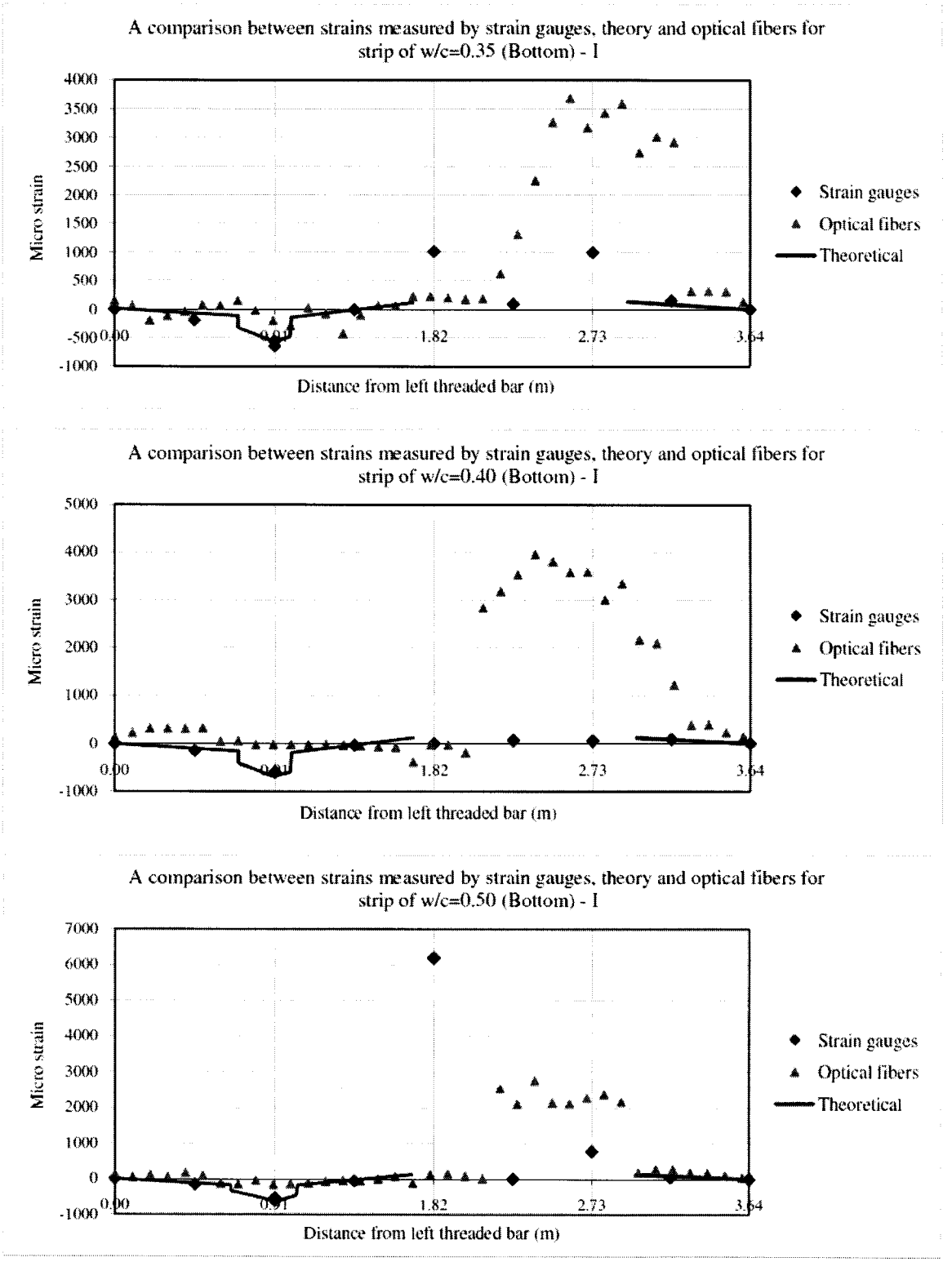

Figure 4.15: Strain distribution along the bottom surface of the deck according to concrete strain gauges, optical fibres and theoretical strains.

4.3. Chloride content measurements

4.3.1. Colourimetric method

After each wetting and drying cycle, concrete cores were taken at the locations specified in Figure 3.31; one set of cores for each strip and at sections 0, 2, 4, 7 and 8, as illustrated in Figure 4.16. Each concrete core was split in half along the same plane of expected crack(s), and the split surface was sprayed with a 0.1N solution of $AgNO_3$ to identify an average depth of chloride penetration.

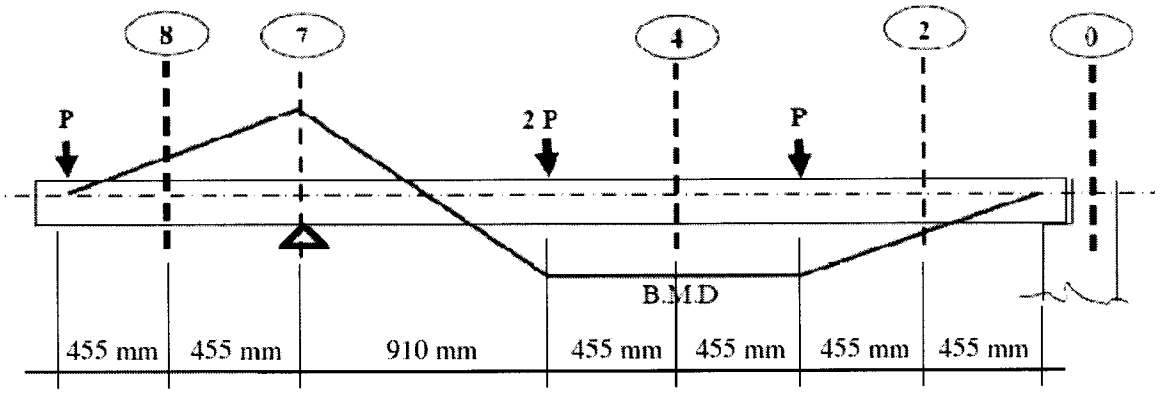

Figure 4.16: Sections along the deck where concrete cores were taken from.

Figures 4.17 through 4.19 show respectively the chloride penetration depths as revealed by the whitish silver chloride precipitate at sections 0 (control section), 2, 4, and 8 for the strips of w/c of 0.35, 0.40, and 0.50 after three months of exposure (i.e., at the end of the first wet/dry cycle). Note that the scale shown in the figures is in centimetres. Two parallel lines to the external horizontal surface have been traced on each split core to indicate the minimum and maximum observed peaks of the colour-change boundary resulting from spraying the $AgNO_3$. The traced curved line is the actual boundary line that separates chloride-contaminated concrete (whitish color due to the silver chloride precipitate) from free-chloride concrete (dark grey). Likewise, Figures 4.20-4.22 and Figures 4.23-4.25 show the chloride penetration depths for the same sections and water-

to-cement ratios using the colourimetric method after six and nine months of exposure, respectively.

The concrete cores corresponding to section 7 were taken at the location of flexural cracks, where maximum tensile stresses develop at the top of the deck. Figure 4.26 shows the chloride penetration depths resulting from the colourimetric method at section 7 for all the strips after 3 months of exposure. According to the pictures displayed in Figure 4.26, the chloride penetration front reached the whole depth of the concrete core for the strips of 0.40 and 0.5 w/c after only 3 months of exposure. The reason behind this was that these cores were taken at crack locations, as previously mentioned. Since it was therefore difficult to determine an average penetration depth for these two concrete cores, the bottom surface of these cores was also sprayed with silver nitrate to have an indication of the chloride ingress front perpendicular to the crack surface (see Figure 4.27). From this figure, it is appreciable that chloride ingress took place along the plane perpendicular to the crack.

Figure 4.28 shows the chloride penetration depths at section 7 for all RC strips after 6 months of exposure (i.e., after the second wetting/drying cycle). As in the data obtained for section 7 after the first wet/dry cycle, it was difficult to determine an average chloride penetration depth for the strips with w/c of 0.35 and 0.50 as the whitish precipitate have covered the entire concrete cores depth. An indication of how far chloride had ingressed perpendicular to the crack plane was obtained by further splitting one half of these cores and spraying them with the silver nitrate solution, as illustrated in Figure 4.29. The penetration depths were estimated by assuming a linear decrease with increasing core depth, as illustrated in Figure 4.29. For both strips, it was found that the chloride penetration depths exceeded the slab thickness (155 mm). For the concrete core with w/c of 0.50, the chloride penetration front normal to the crack surface reached beyond the radius of the concrete core. It is interesting to note that different chloride ingress behaviour was observed in the concrete core of w/c of 0.40 taken at section 7' after 6 months of exposure, as seen in Figure 4.28, in which the maximum chloride penetration depth was measured as approximately 40 mm.

Figure 4.30 illustrates the results of the colourimetric test on concrete cores taken at section 7 for all RC strips after 9 months of chloride exposure. As previously noted for

the first two sets of data, the chloride penetration fronts as revealed by the silver chloride precipitate reached the depth of the cores for all w/c. Figure 4.31 shows the chloride penetration front normal to the crack surface for all strips after 9 months of exposure. These fronts were obtained by further splitting one half of the cores in Figure 4.30 and spraying them with the $AgNO_3$ solution.

A summary of the maximum, minimum, and average chloride penetration depths as observed in the previous figures is tabulated in Table 4.1. To illustrate the effect of the concrete water-to-cement ratio on the measured chloride penetration depths, the data displayed in Table 4.1 is plotted against the location of each section along the deck span in Figures 4.32, 4.33, and 4.34 after the 1^{st}, 2^{nd}, and 3^{rd} wetting/drying cycles, respectively. From Figure 4.32, it can be observed that the higher the w/c, the higher the chloride penetration depth. With the exception of section 7, these differences are not significant in the other two data sets, i.e., 2^{nd} and 3^{rd} sets (see Figures 4.33 and 4.34).

The effect of exposure time on the measured penetration depths tabulated in Table 4.1 is illustrated in Figures 4.35, 4.36 and 4.37, which plot the average and maximum chloride penetration depths along the deck span after the three wetting and drying cycles for the RC strips with w/c of 0.35, 0.40, and 0.50, respectively. Excluding the data from section 7, there is a slight increase in the chloride penetration fronts as times goes by. Inconsistencies with data associated to section 7 are due to the fact that some of the concrete cores were taken at crack locations whereas others were not (see Figure 3.29). Note that the values in Figures 4.32 through 4.37 are discrete relative to each other, and the graph lines joining them do not necessarily imply trend values in between.

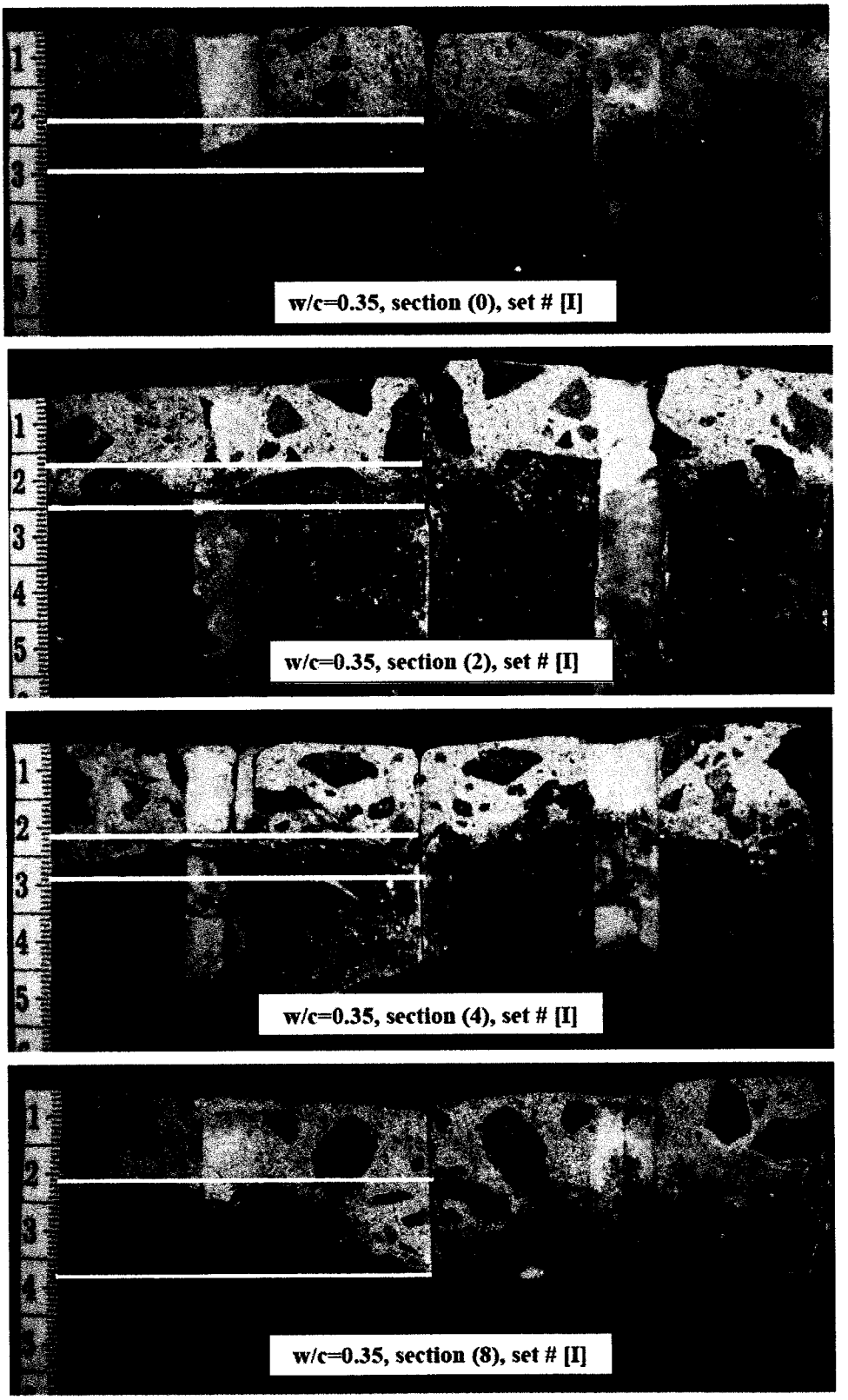

Figure 4.17: Chloride penetration depths for strip of w/c=0.35 after 3 months.

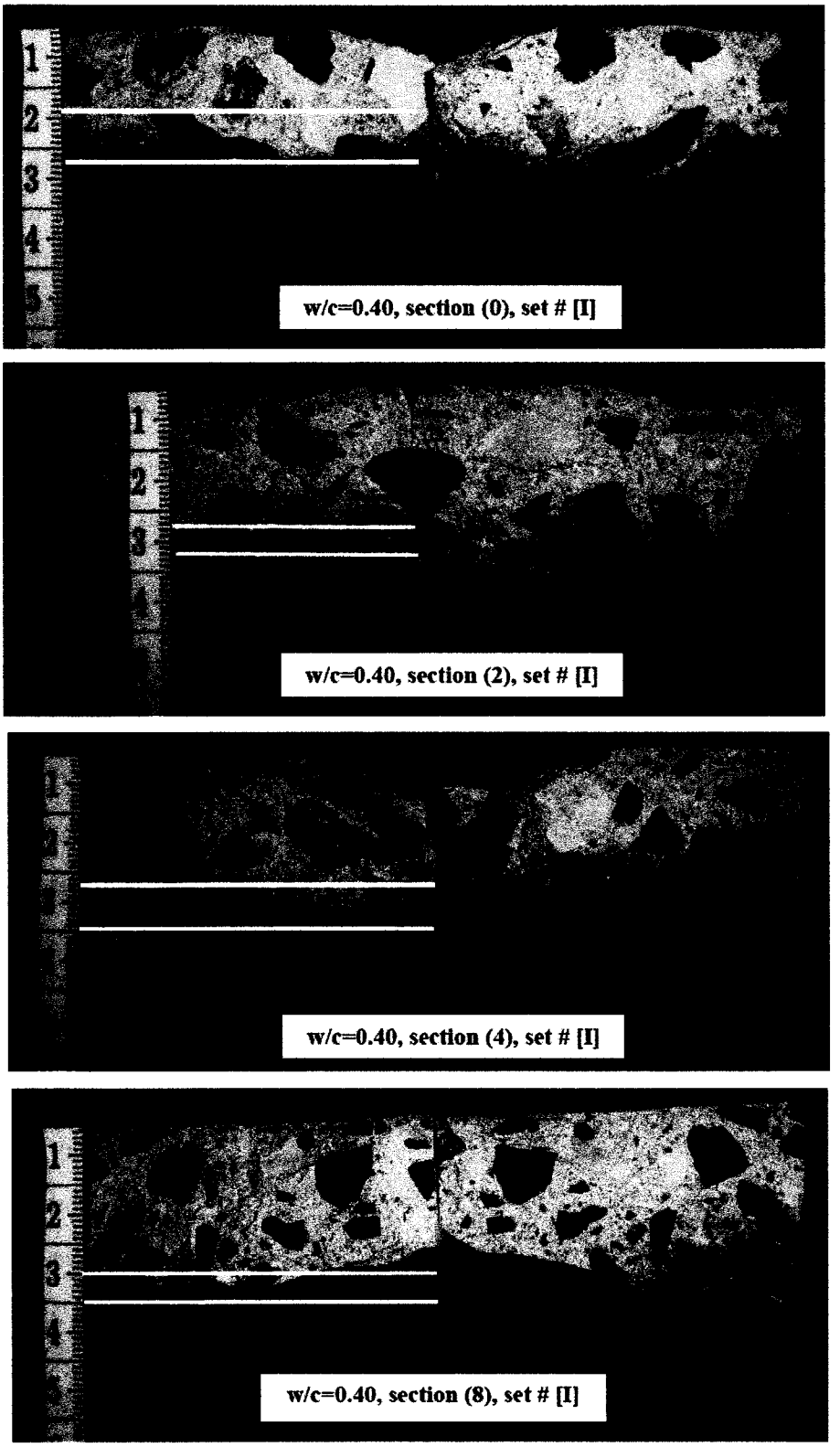

Figure 4.18: Chloride penetration depths for strip of w/c=0.40 after 3 months.

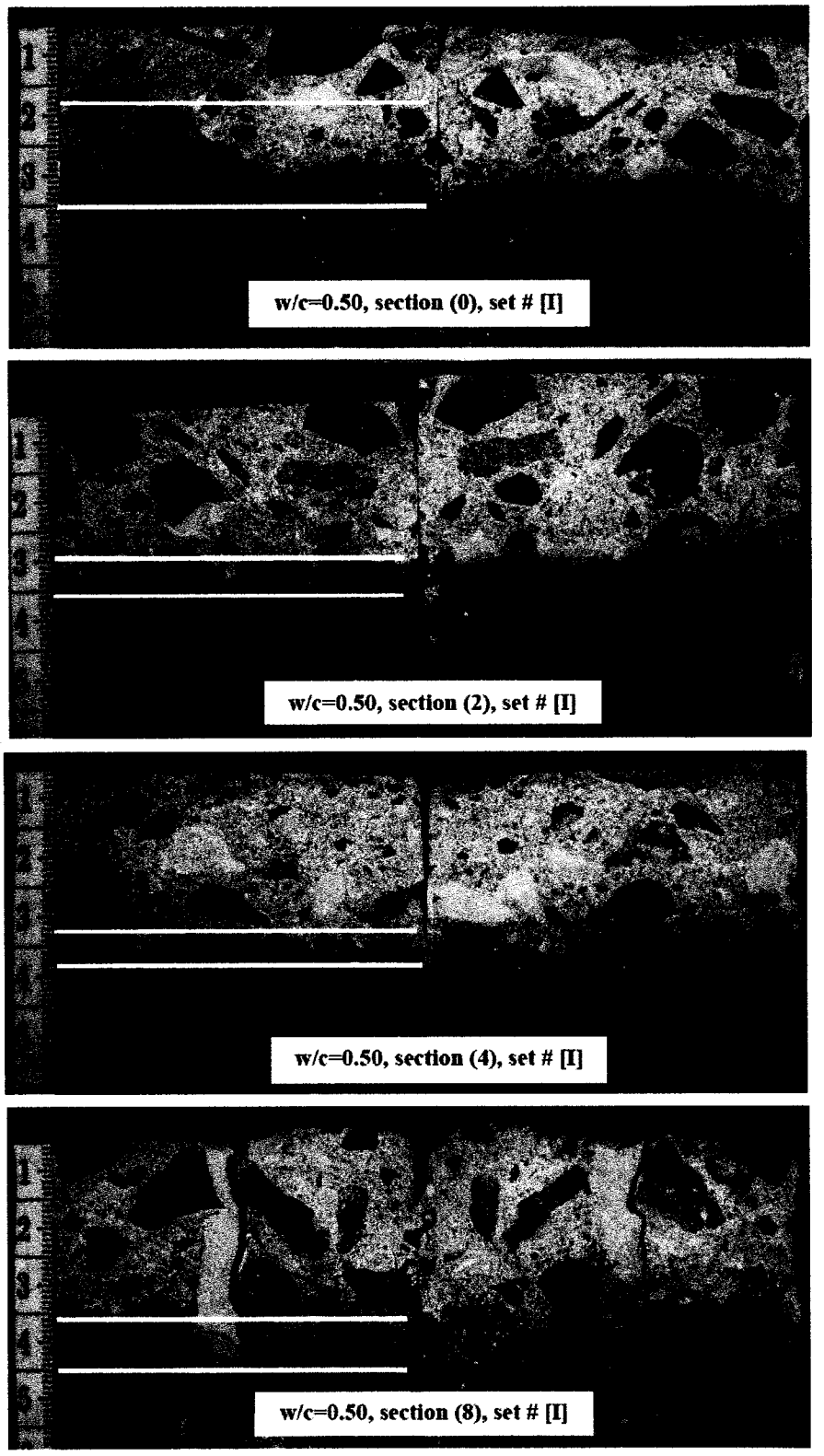

Figure 4.19: Chloride penetration depths for strip of w/c=0.50 after 3 months.

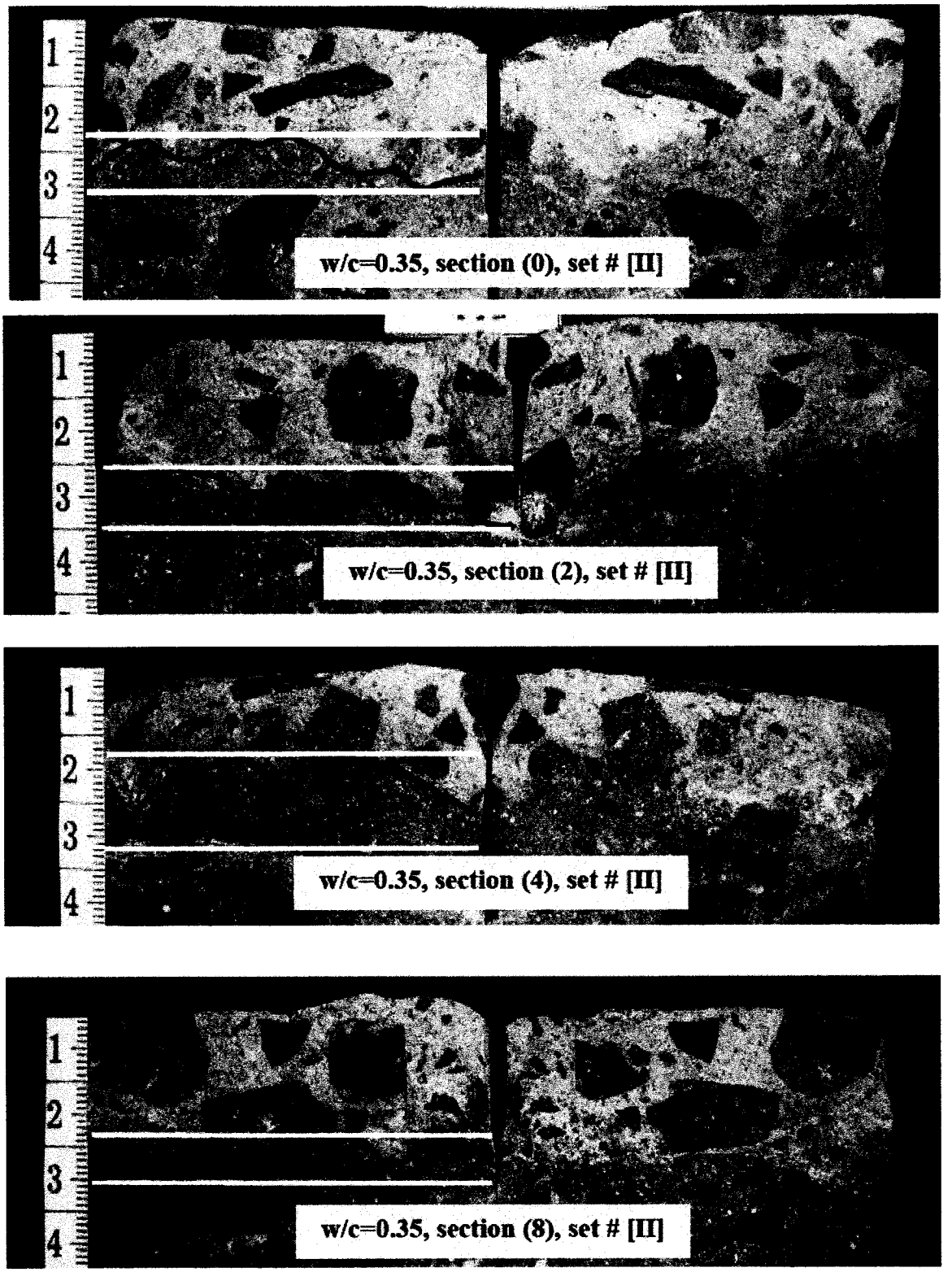

Figure 4.20: Chloride penetration depths for strip of w/c=0.35 after 6 months.

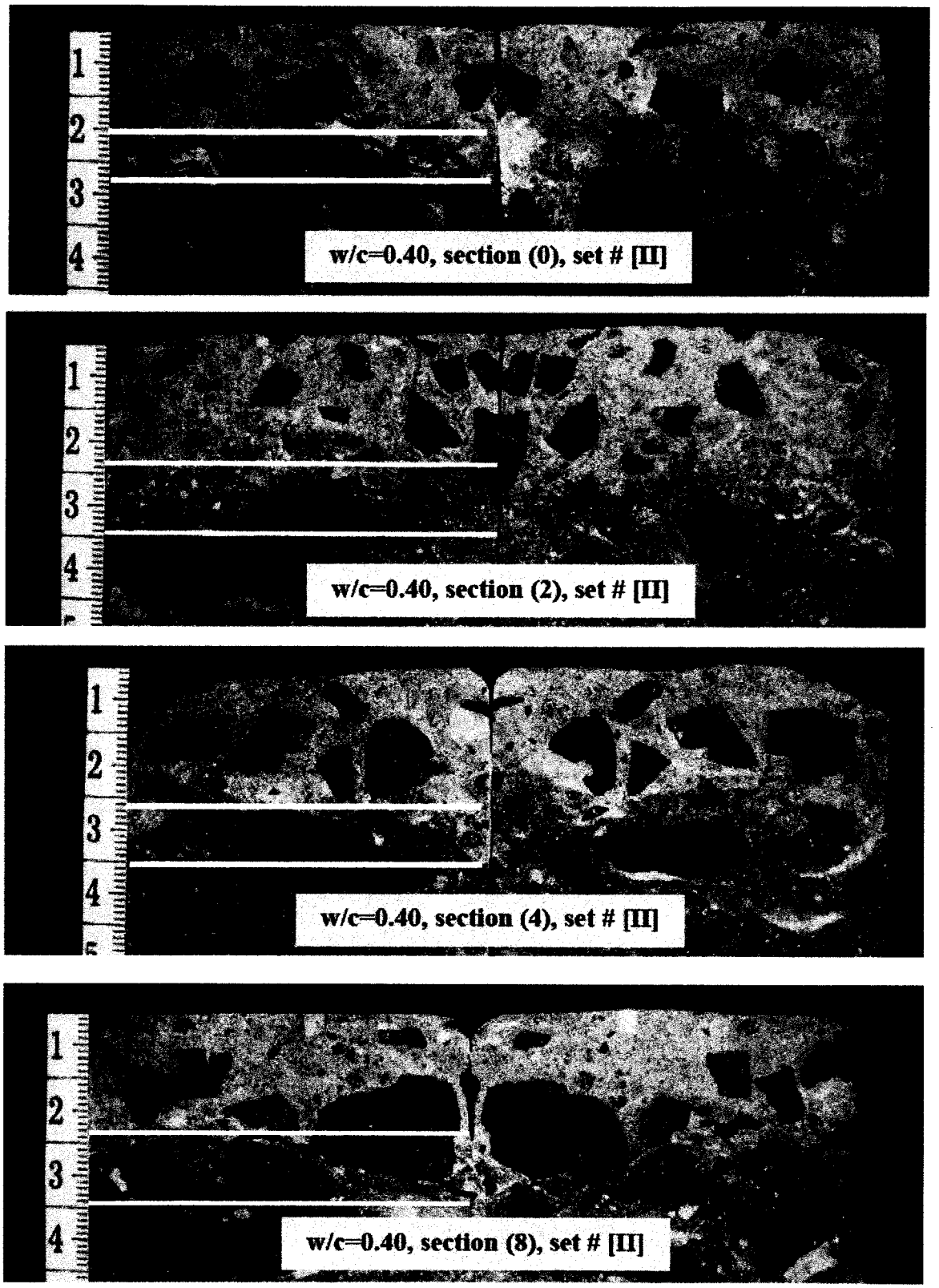

Figure 4.21: Chloride penetration depths for strip of w/c=0.40 after 6 months.

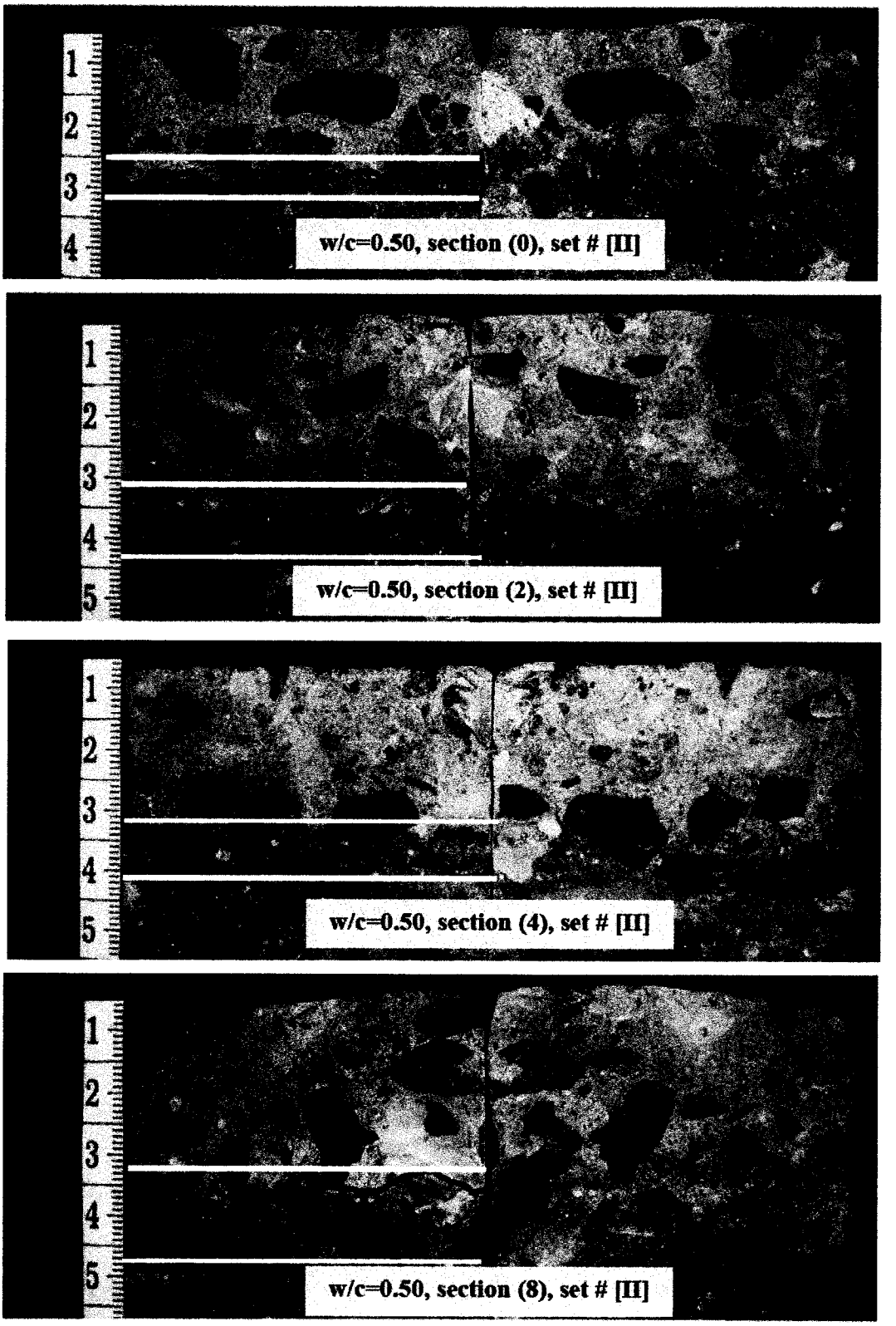

Figure 4.22: Chloride penetration depths for strip of w/c=0.40 after 6 months.

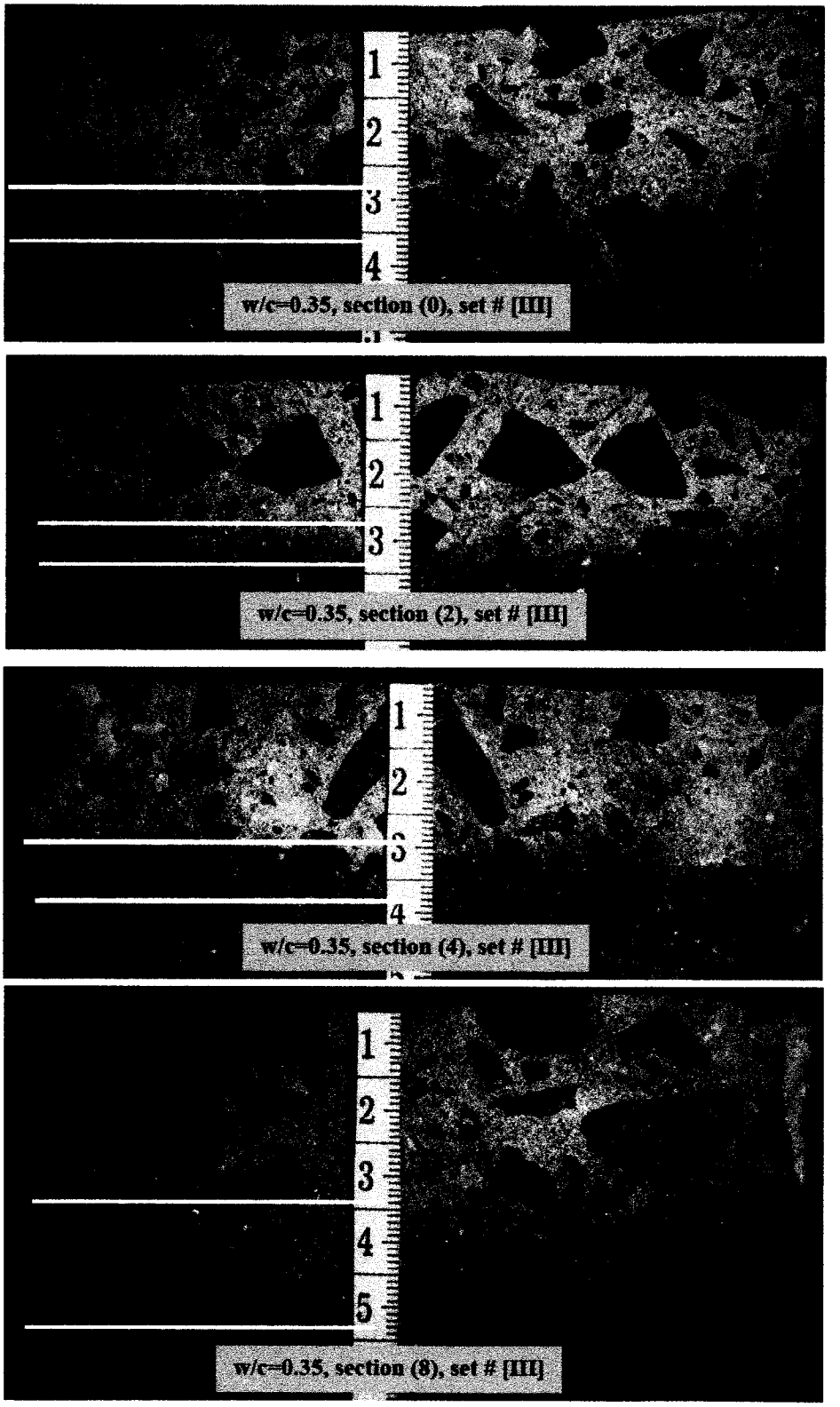

Figure 4.23: Chloride penetration depths for strip of w/c=0.35 after 9 months.

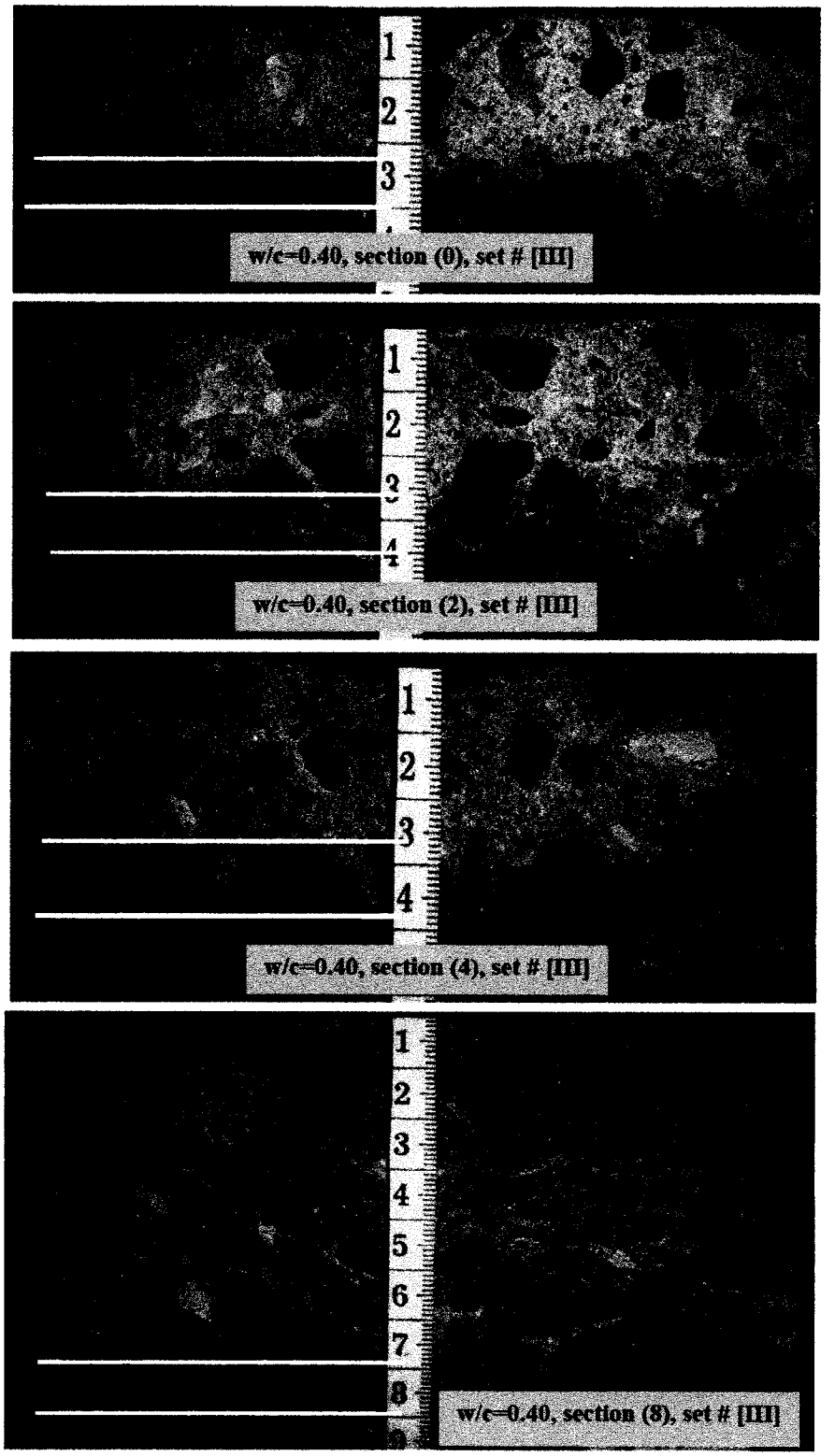

Figure 4.24: Chloride penetration depths for strip of w/c=0.40 after 9 months.

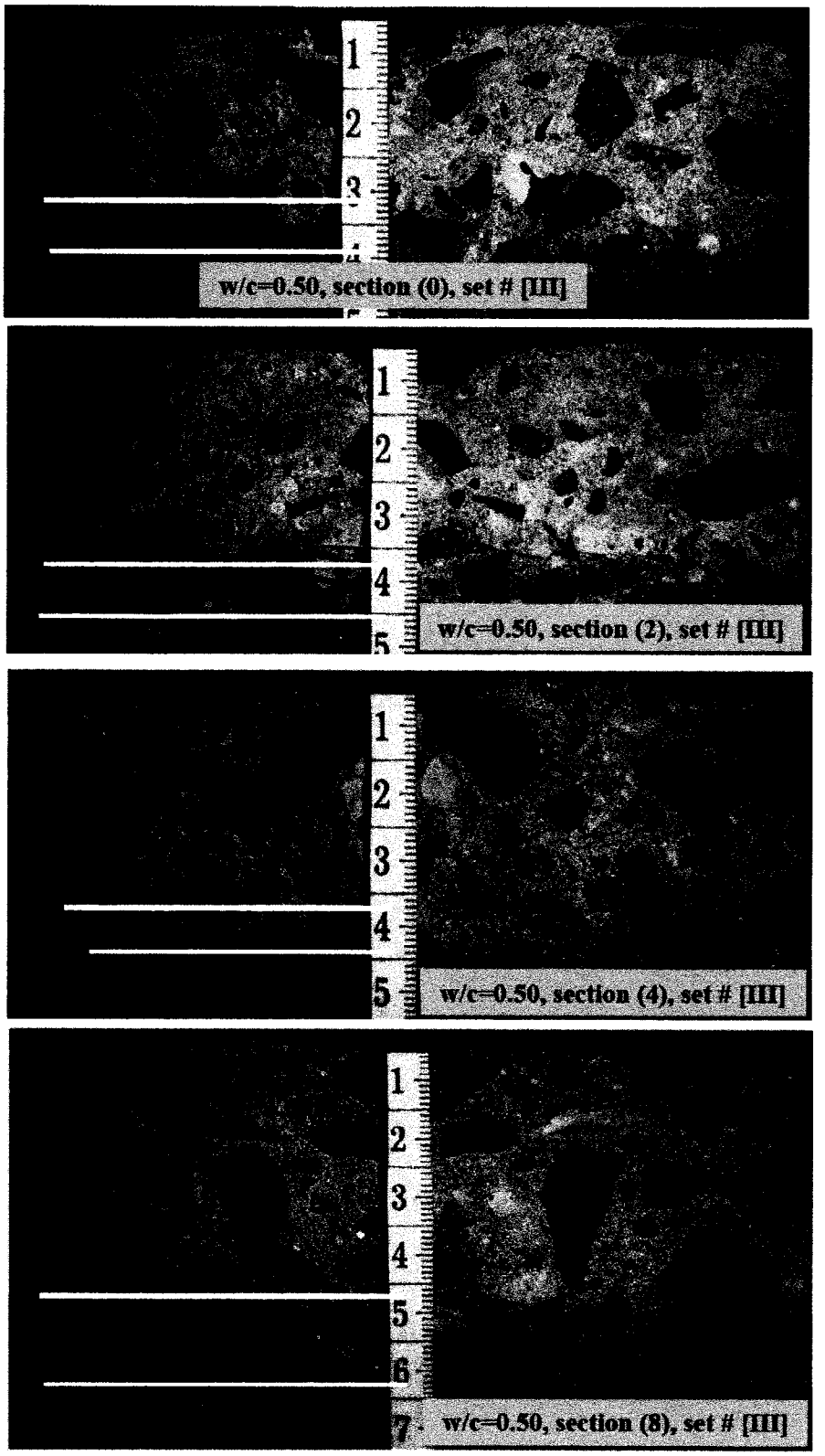

Figure 4.25: Chloride penetration depths for strip of w/c=0.50 after 9 months.

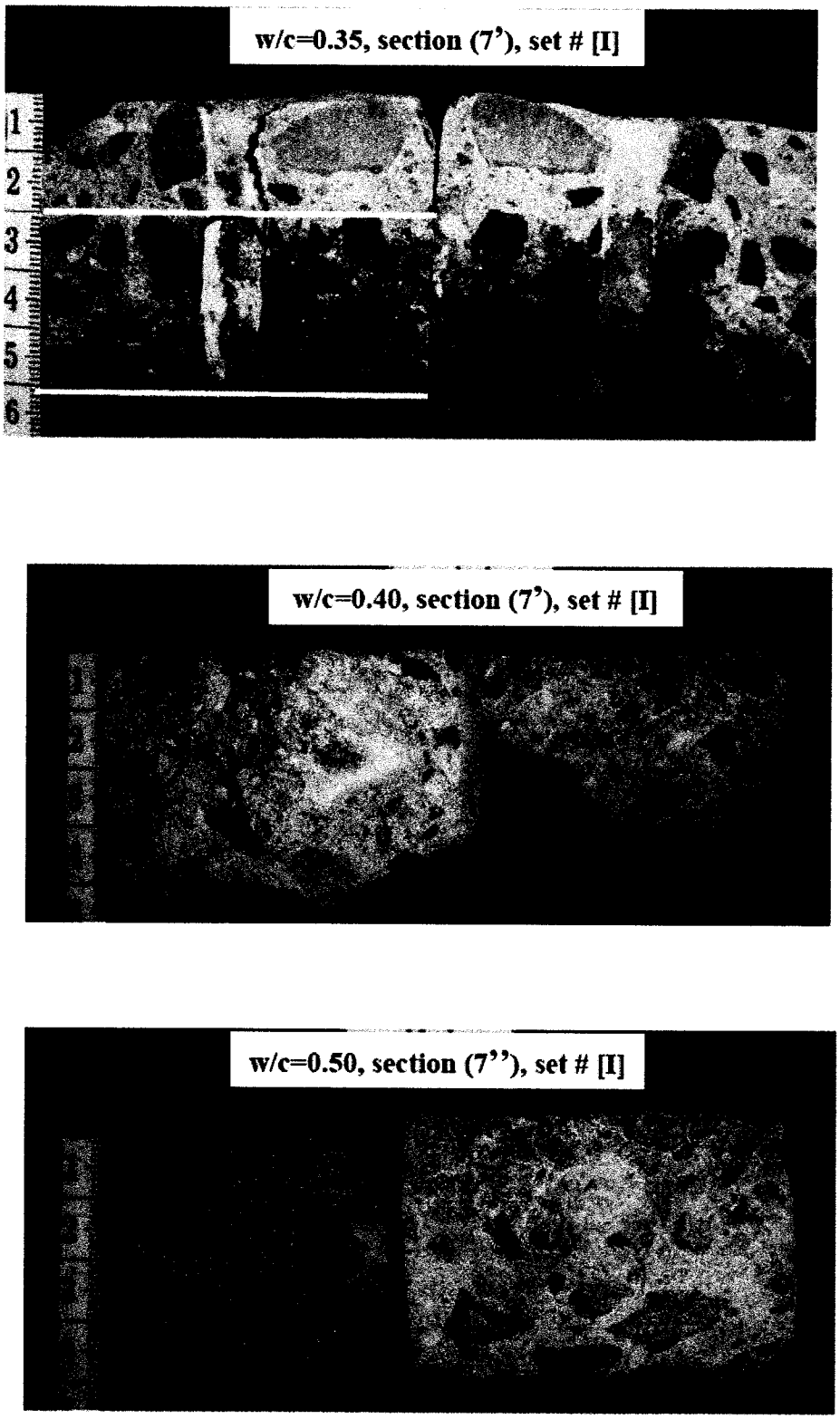

Figure 4.26: Chloride penetration depths at section (7) for all strips after 3 months.

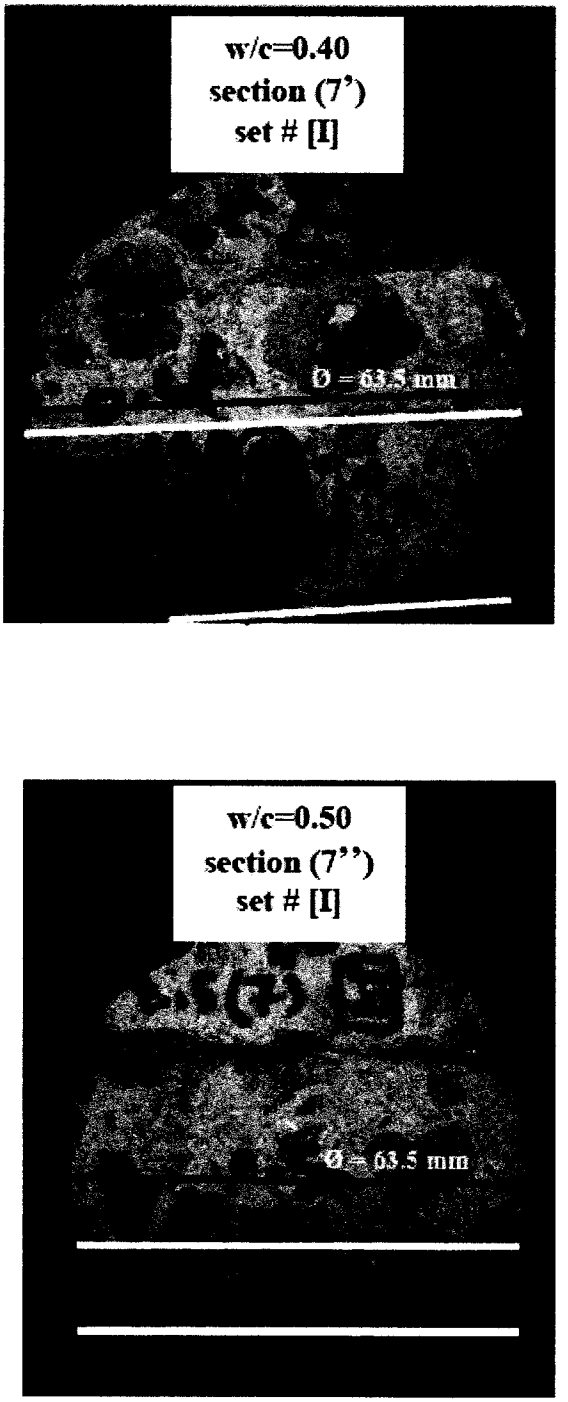

Figure 4.27: Chloride penetration front perpendicular to crack surface at sections 7' and 7'' for w/c = 0.40 and 0.50, respectively, after 3 months of exposure.

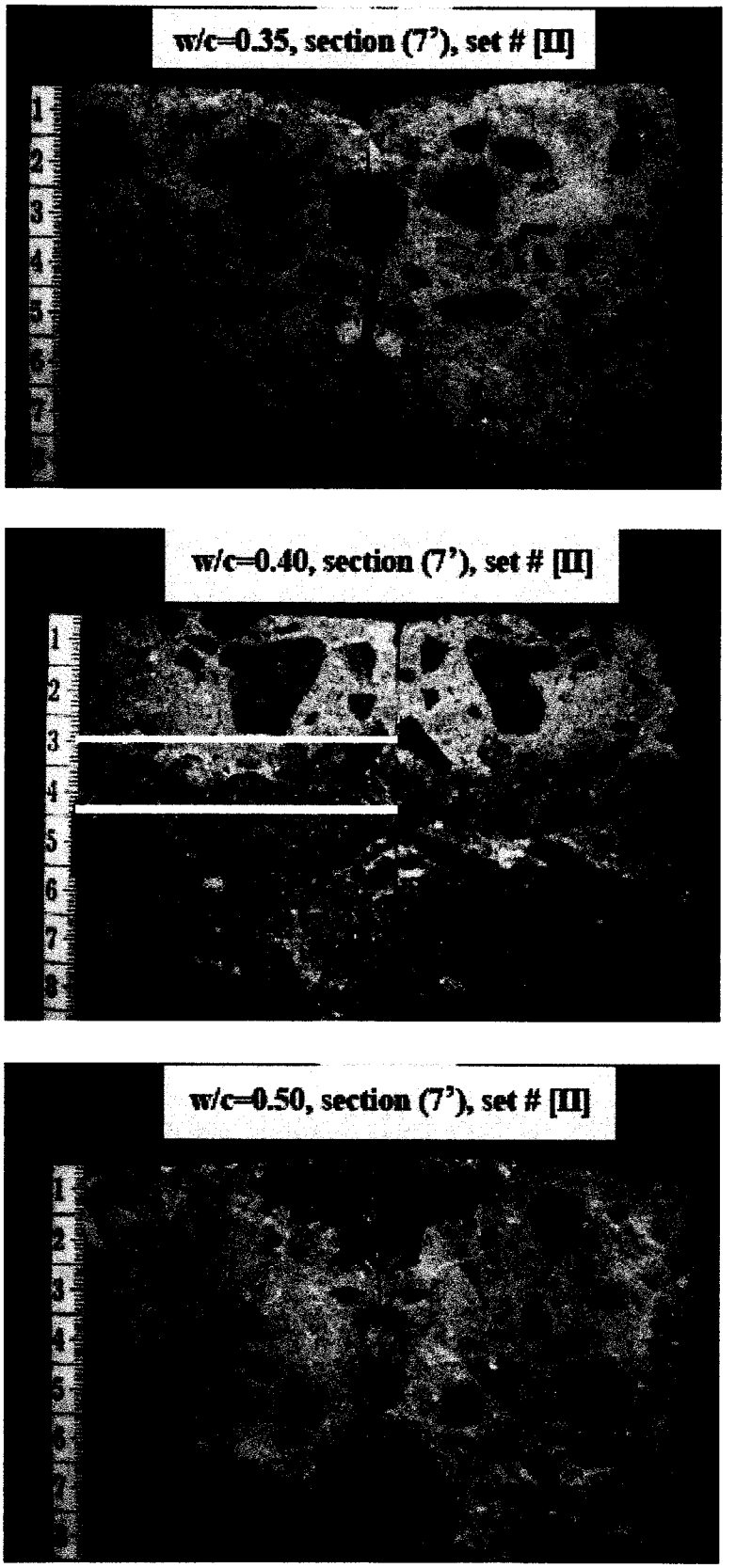

Figure 4.28: Chloride penetration depths at section 7 for all strips after 6 months.

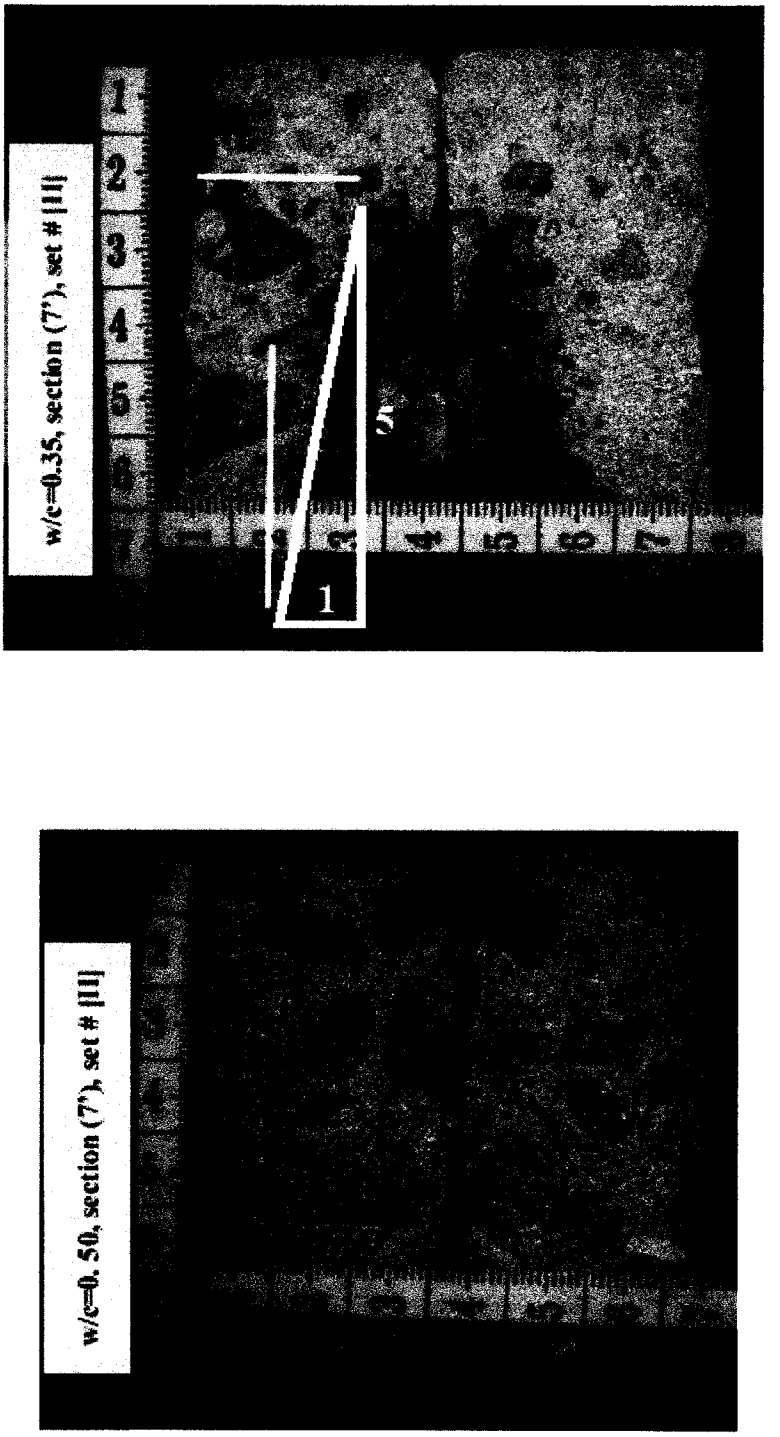

Figure 4.29: Chloride penetration depths normal to the crack plane at section7' for w/c = 0.35 and 0.50, respectively, after 6 months of exposure.

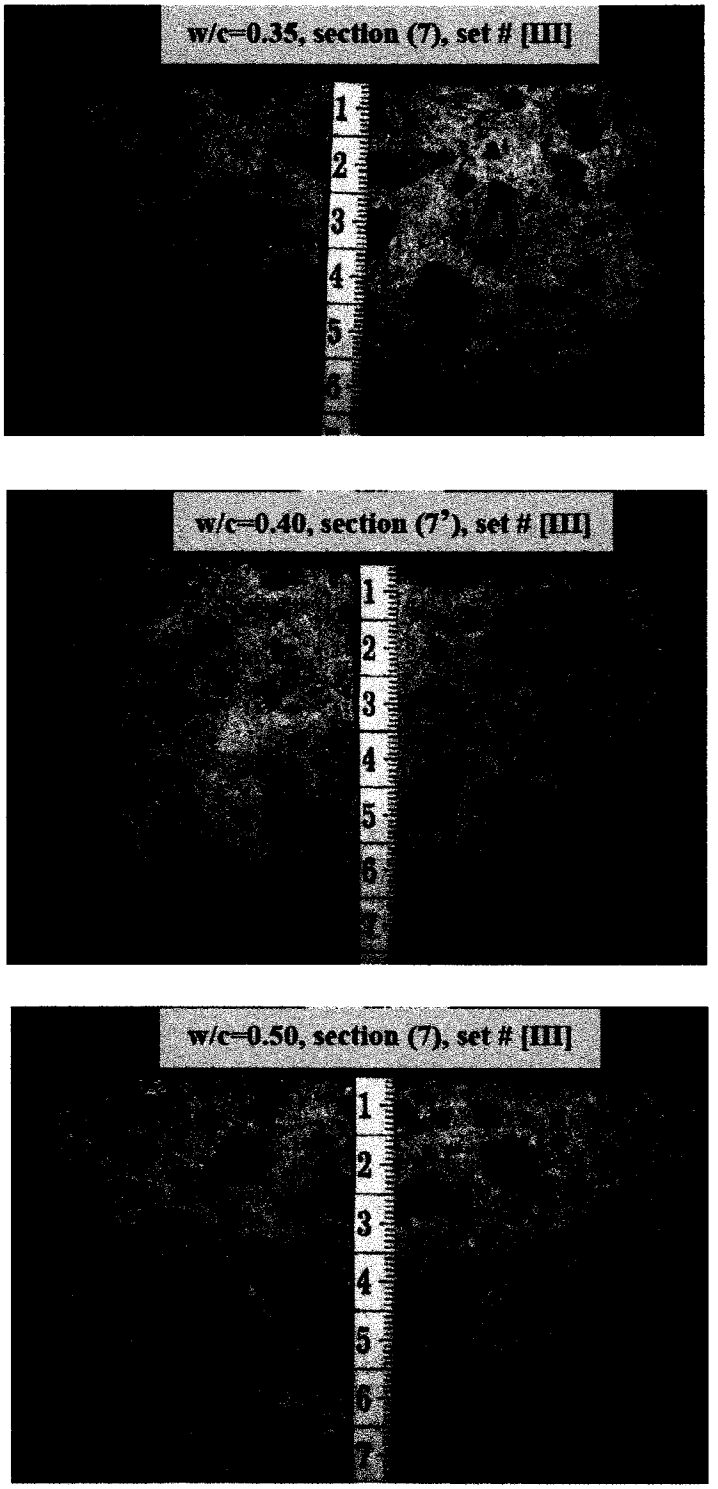

Figure 4.30: Chloride penetration depths at section 7 for all strips after 9 months.

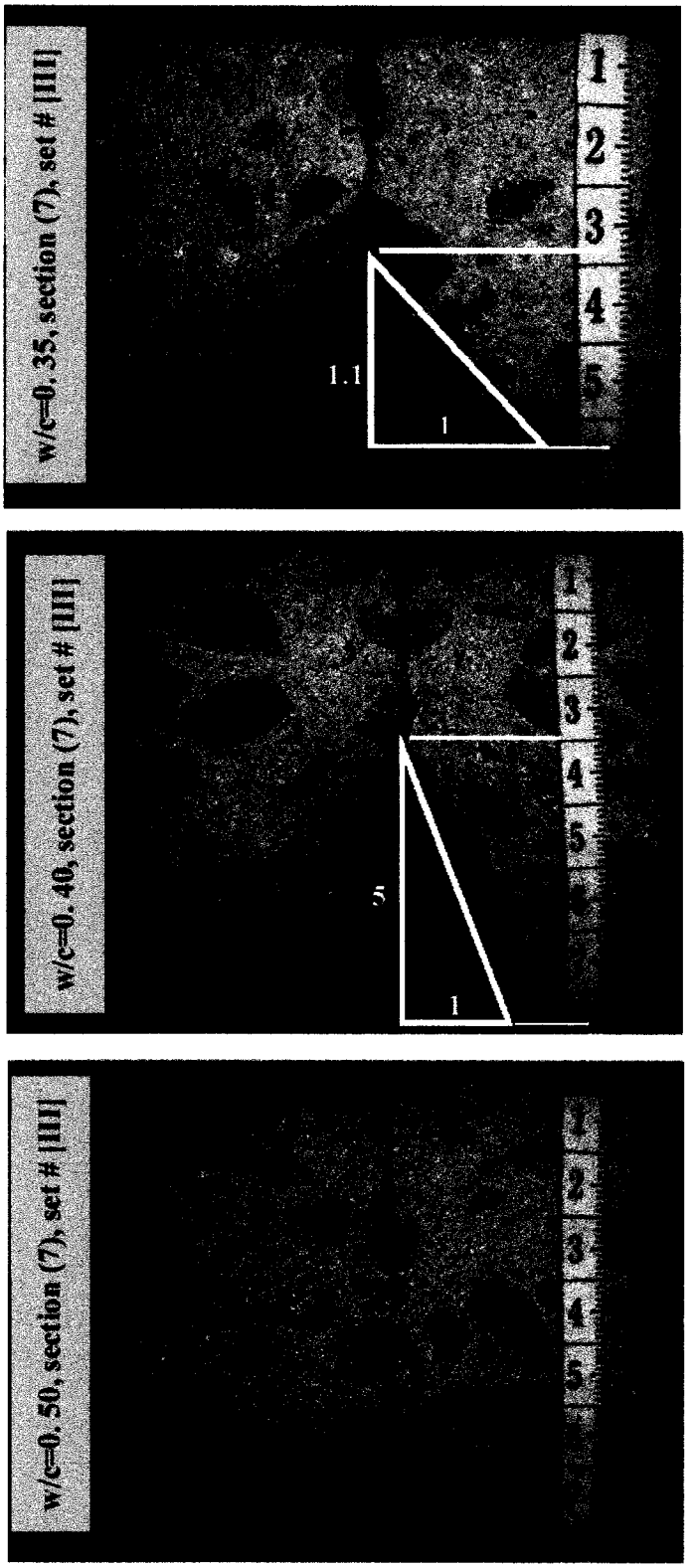

Figure 4.31: Chloride penetration fronts normal to the crack plane for all strips after 9 months.

Table 4.1: Summary of chloride penetration depths obtained by the colourimetric method.

Strip	Section	1st cycle			2nd cycle			3rd cycle			Location (mm)
		max	min	average	max	min	average	max	min	average	
0.35	0	25	16	20.5	26	17.5	21.75	31.5	23.5	27.5	0
	2	20	12	16	30	20.5	25.25	29	22.5	25.75	455
	4	24	17	20.5	27	13	20	33.5	24.5	29	1365
	7	**51**	**20**	**35.5**	**155**	**155**	**155**	**80**	**80**	**80**	2730
	8	33	16	24.5	25.5	18	21.75	48	29	38.5	3185
0.4	0	22.5	14	18.25	23	16	19.5	30	22.5	26.25	0
	2	27	22.5	24.75	30	19	24.5	35	26	30.5	455
	4	29.5	22	25.75	30.5	21.5	26	38	26.5	32.25	1365
	7	**103**	**87**	**95**	**155**	**155**	**155**	**155**	**155**	**155**	2730
	8	30	25	27.5	29.5	18.5	24	79.5	69	74.25	3185
0.5	0	30.5	13	21.75	27	20	23.5	34	26.5	30.25	0
	2	30.5	24.5	27.5	38.5	26.5	32.5	40.5	33	36.75	455
	4	33	27.5	30.25	36	26.5	31.25	39	32	35.5	1365
	7	**92**	**58**	**75**	**155**	**155**	**155**	**155**	**155**	**155**	2730
	8	40	31	35.5	42.5	27	34.75	58	42.5	50.25	3185

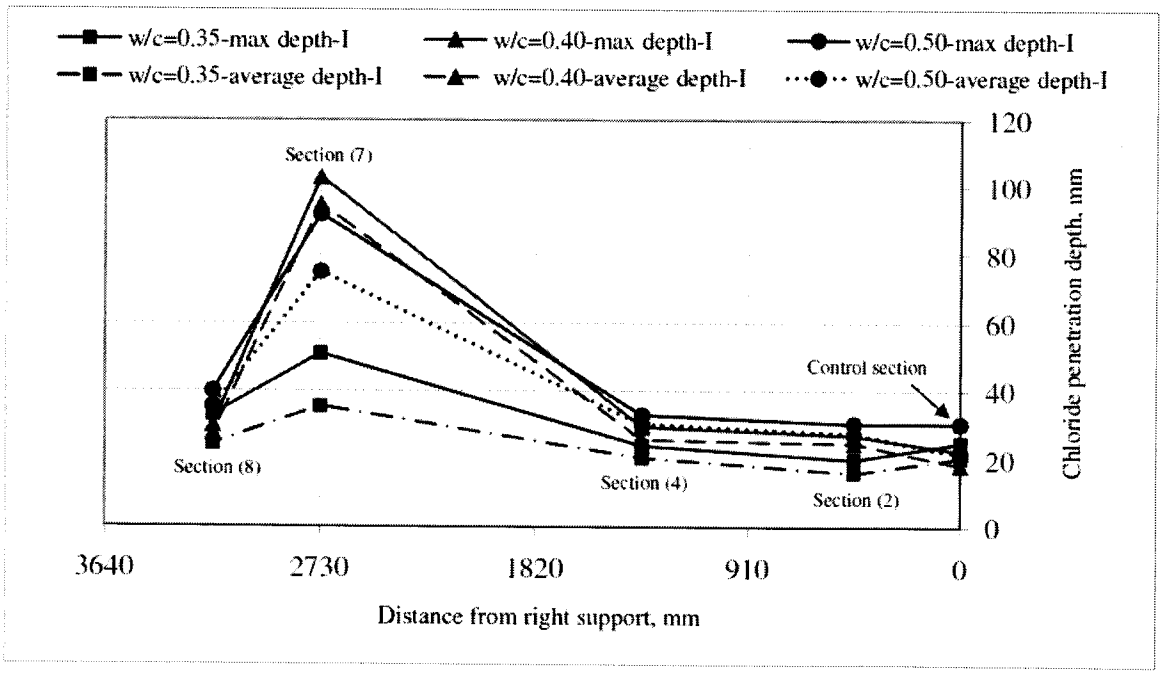

Figure 4.32: Average and maximum chloride penetration depths along the deck span for each w/c after the 1st wet/dry cycle.

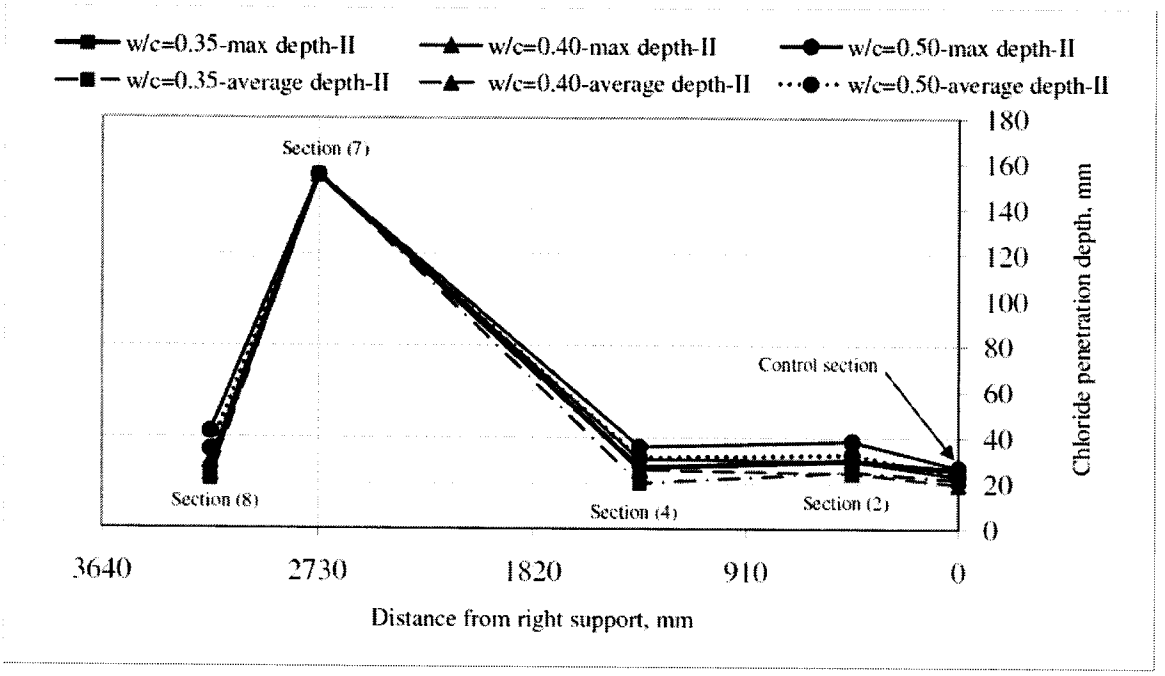

Figure 4.33: Average and maximum chloride penetration depths along the deck span for each w/c after the 2nd wet/dry cycle.

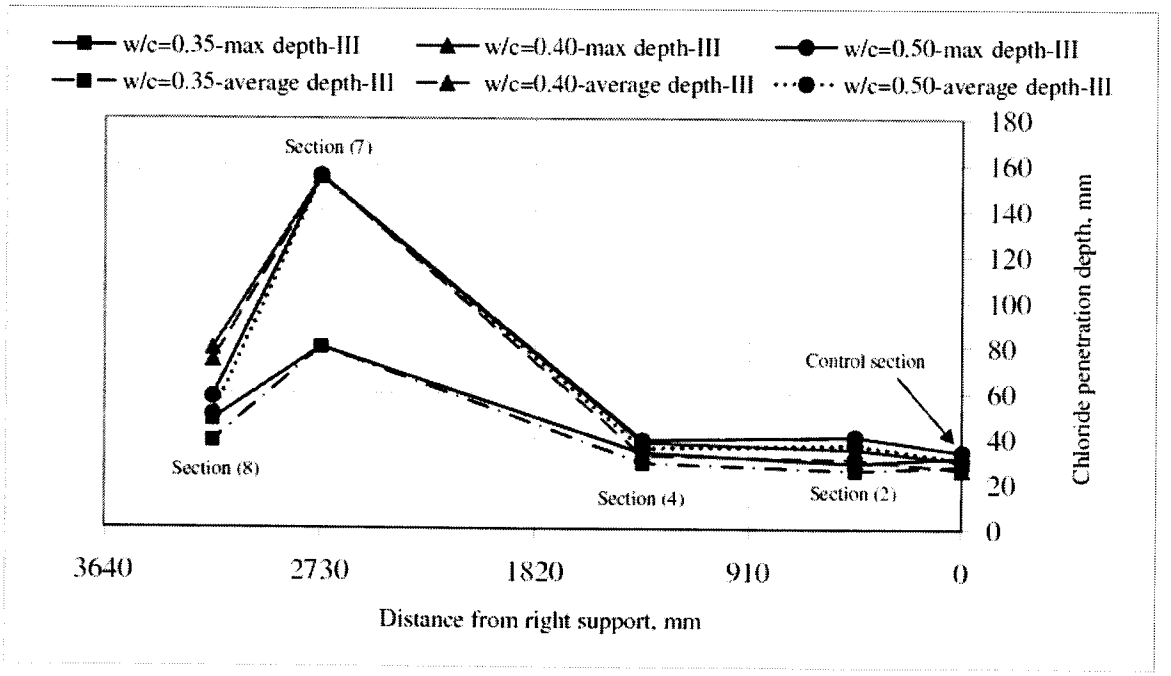

Figure 4.34: Average and maximum chloride penetration depths along the deck span for each w/c after the 3rd wet/dry cycle.

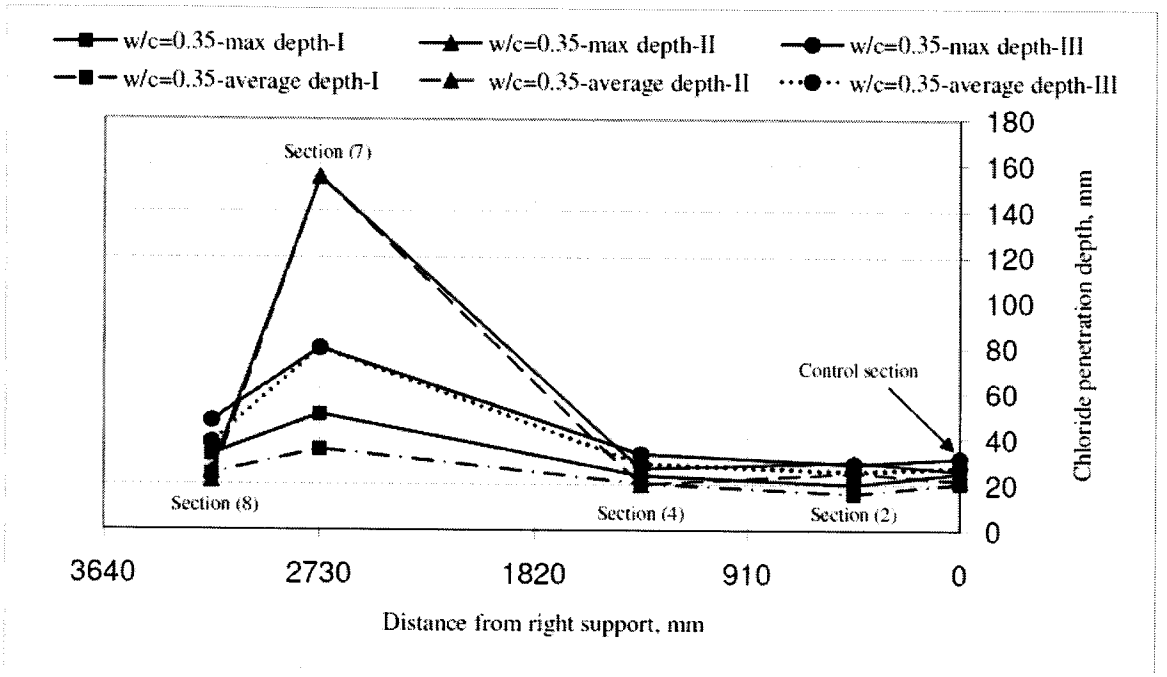

Figure 4.35: Average and maximum chloride penetration depths along the deck span for w/c = 0.35 after all wet/dry cycles.

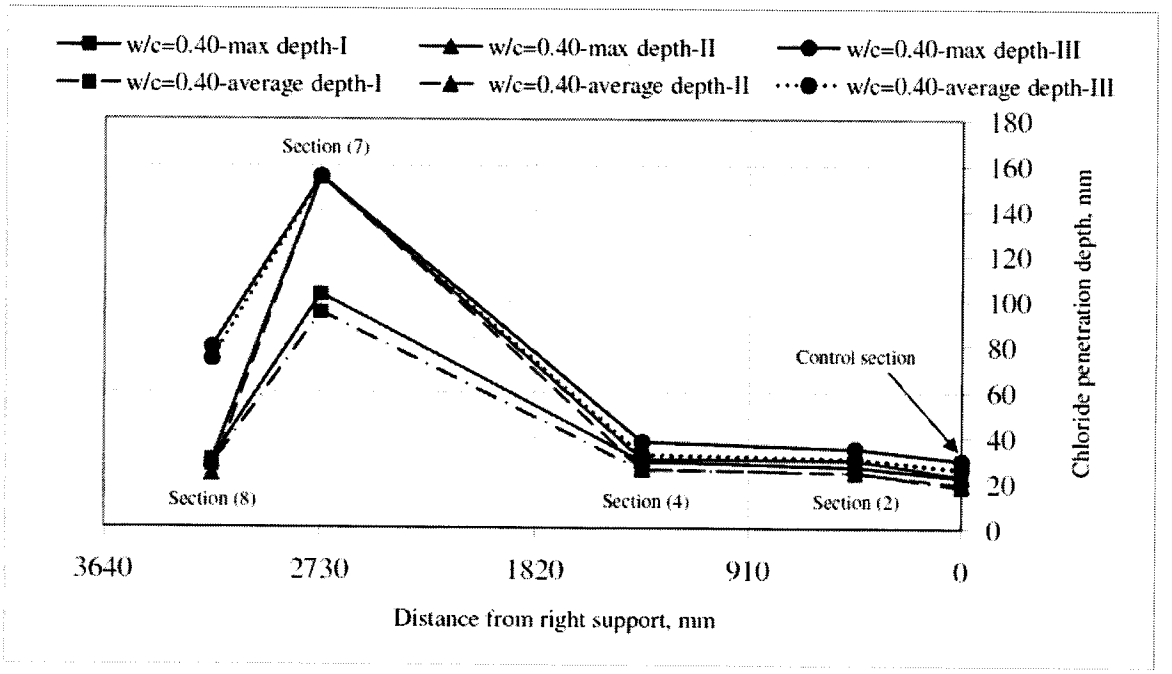

Figure 4.36: Average and maximum chloride penetration depths along the deck span for w/c = 0.40 after all wet/dry cycles.

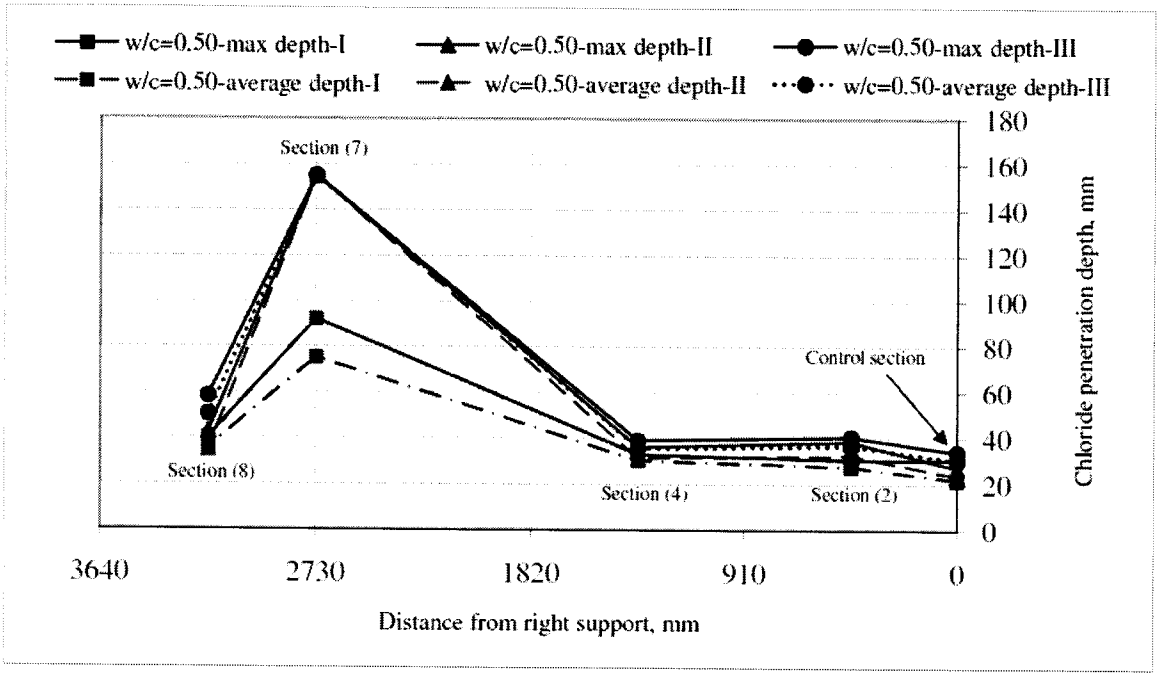

Figure 4.37: Average and maximum chloride penetration depths along the deck span for w/c = 0.50 after all wet/dry cycles.

4.3.2. Potentiometric titration method

This section presents the results from carrying out the potentiometric titration on the concrete cores taken at the locations specified in Figure 3.31 after each wetting and drying cycle. The total chloride content, which was measured according to ASTM C 1152/C 1152M-04 and ASTM C114-07, is given in % by weight of the concrete sample and was calculated according to Eq. (3.2). Note that the total chloride content from the powder sample obtained from a concrete core slice of 5 mm represents the average value for that slice, and therefore that value is plotted at a depth corresponding to the mid-way depth of the concrete slice.

The total chloride concentration profiles obtained at different sections after the first wet/dry cycle are respectively illustrated in Figures 4.38, 4.39, and 4.40 for the RC strips of w/c of 0.35, 0.40, and 0.50. The strip with a w/c of 0.40 displayed chloride profiles as expected (see Figure 4.39). For this strip, it can be observed that the highest values of chloride concentration correspond to the chloride profile obtained from section 8, which was located in a tensile uncracked zone. The lowest chloride concentrations correspond

to the "control" section, which did not sustain any stress. The chloride profiles corresponding to sections 2 and 4, located in a compressed zone, fall in between the others. Similar trends can be found on the chloride profiles obtained from the RC strip with 0.35 w/c (Figure 4.38), although the differences between sections are not significant. However, expected results were not confirmed by the chloride profiles obtained from the RC strip with 0.50 w/c, as illustrated in Figure 4.40. It is possible that for this strip, which was made of a more porous concrete, chloride ingress might have been highly dependent on chloride convective movement rather than pure diffusion, and this change in the governing transport mechanism is reflected in the obtained chloride profiles (see profile for section 2 in Figure 4.40). Note that section 2 was subjected not only to compressive stresses due to bending but also to diagonal tension due to shear (see Figure 3.31). It is also important to highlight that observed anomalies might be due to handling errors during core grinding, storing and potentiometric titration.

The effect of the concrete cores w/c on the total chloride concentration profiles can be observed in Figures 4.41, 4.42, 4.43 and 4.44, which illustrate respectively chloride concentration profiles at sections 0, 2, 4, and 8 for all the RC strips after the first dry/wet cycle. In general, it can be observed that as the w/c of the concrete decreases, so do the total chloride concentrations. It is interesting to note though that for the unstressed section 0, the difference between the chloride profiles from concrete cores with w/c of 0.35 and 0.40 is almost negligible (see Figure 4.41). However, this general trend is not observed in section 8 (see Figure 4.44), in which the chloride concentrations corresponding to the RC strip with w/c of 0.40 tend to be much higher than that of w/c of 0.35. More flexural cracking was observed at section 7 for the strip with w/c = 0.40 than for the strip with w/c = 0.50 (see Figures 4.45 and 4.46).

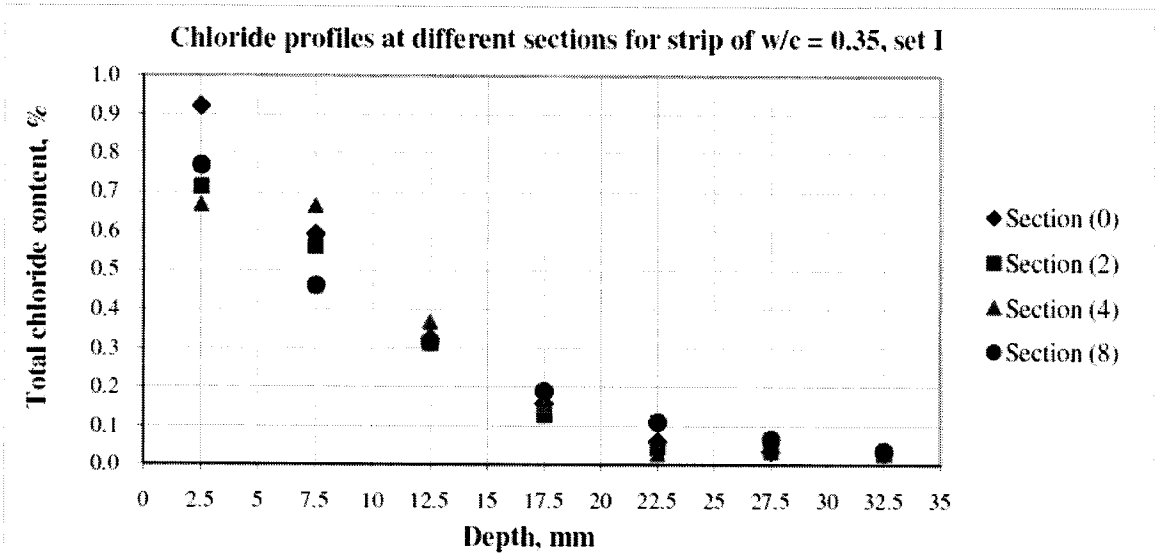

Figure 4.38: Chloride concentration profiles for the strip of w/c = 0.35 at different sections (set # I).

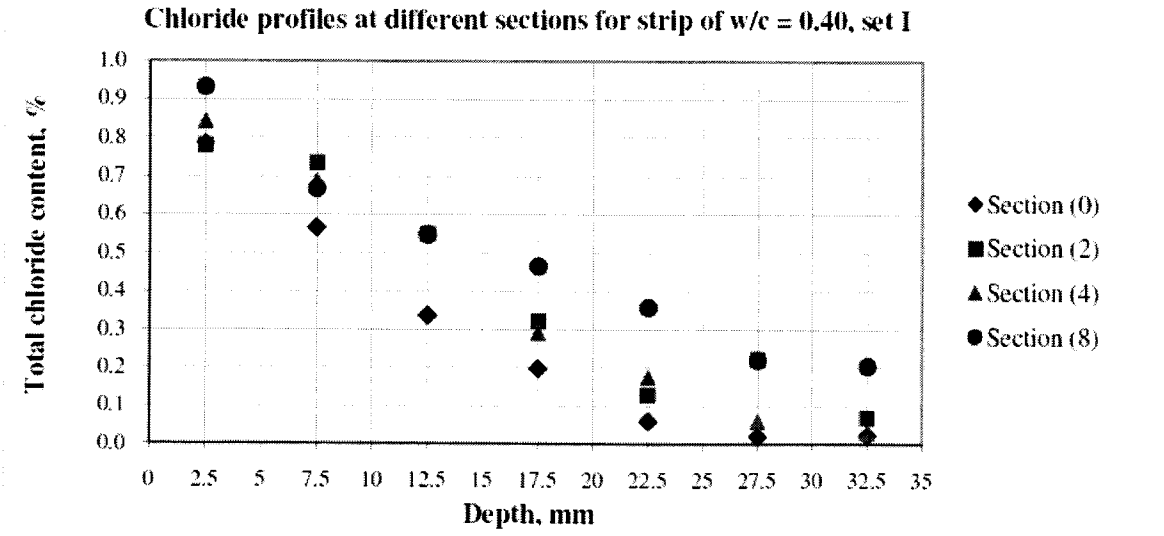

Figure 4.39: Chloride concentration profiles for the strip of w/c = 0.40 at different sections (set # I).

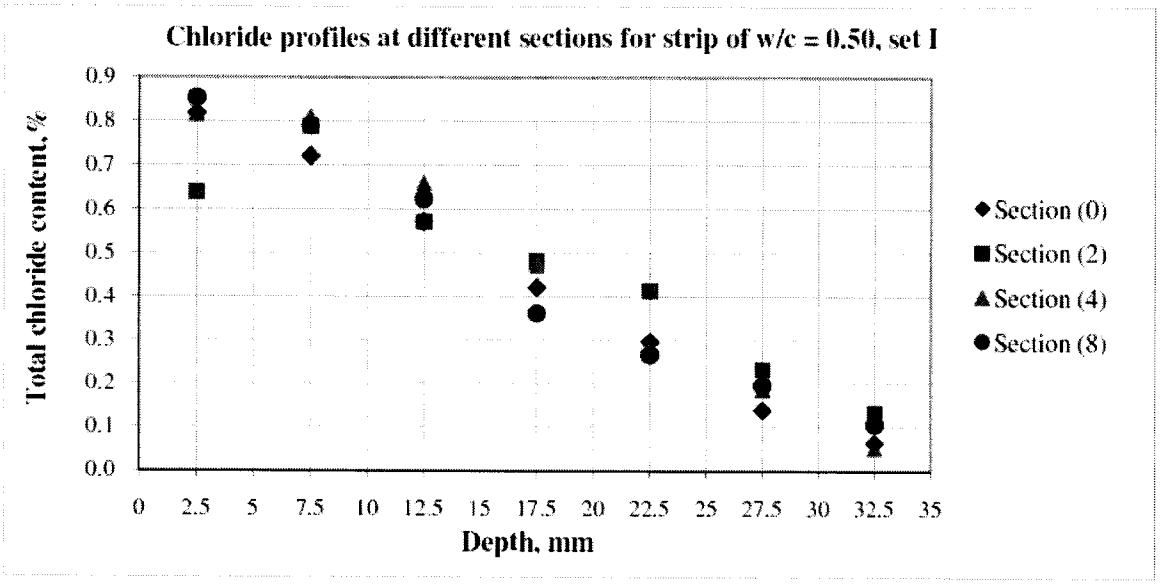

Figure 4.40: Chloride concentration profiles for the strip of w/c = 0.50 at different sections (set # I).

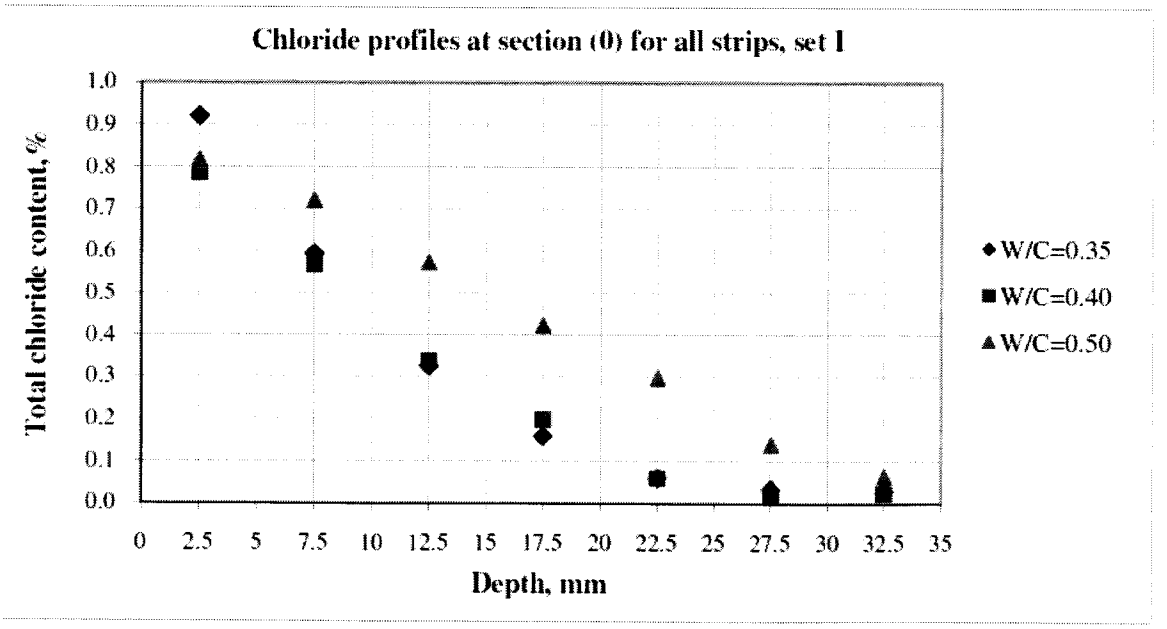

Figure 4.41: Chloride concentration profiles at section (0) for all strips (set # I).

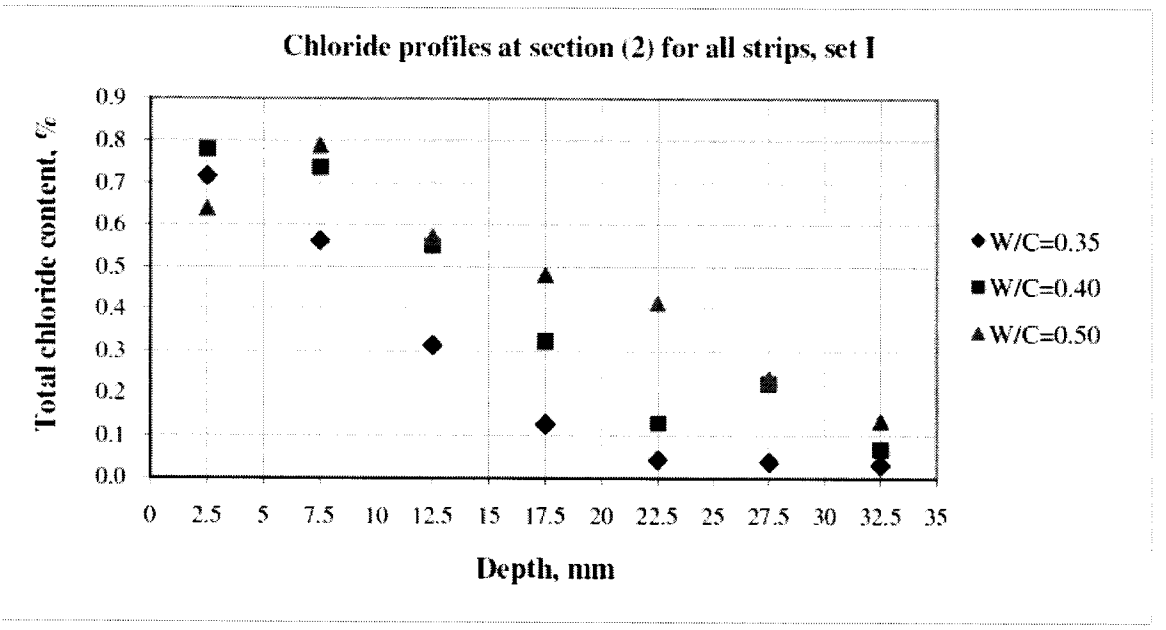

Figure 4.42: Chloride concentration profiles at section (2) for all strips (set # I).

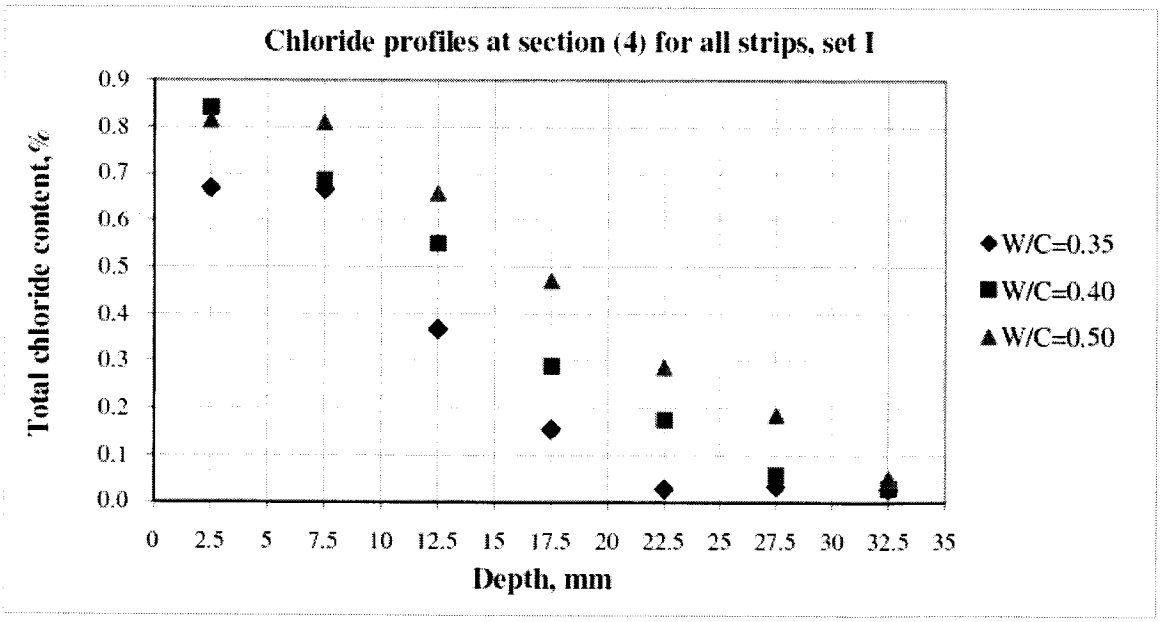

Figure 4.43: Chloride concentration profiles at section (4) for all strips (set # I).

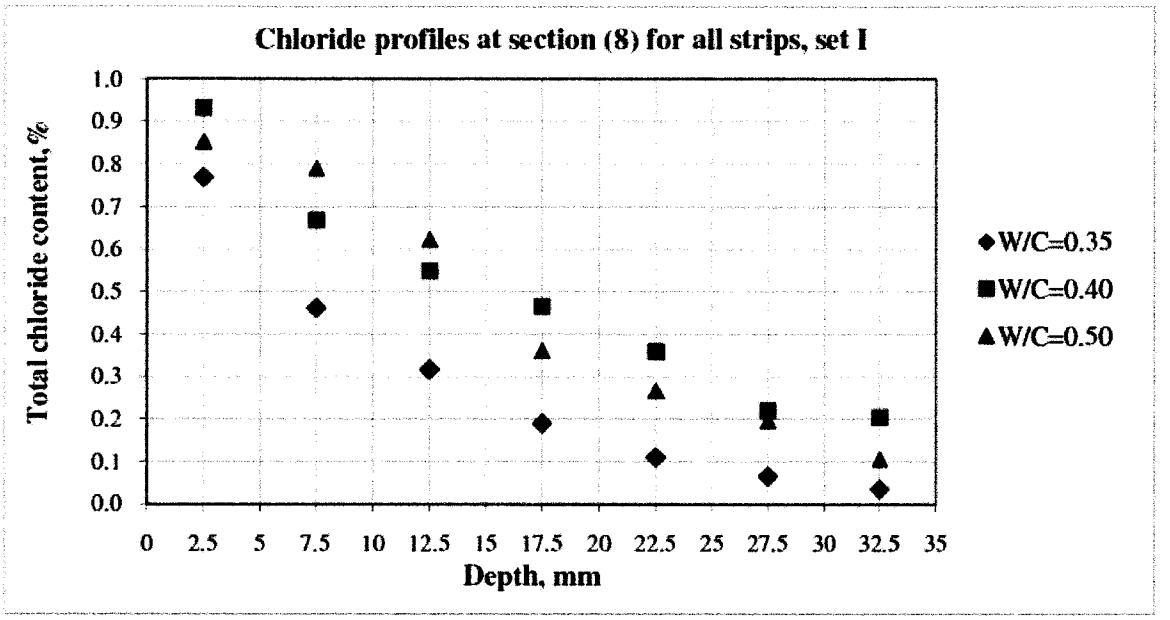

Figure 4.44: Chloride concentration profiles at section (8) for all strips (set # I).

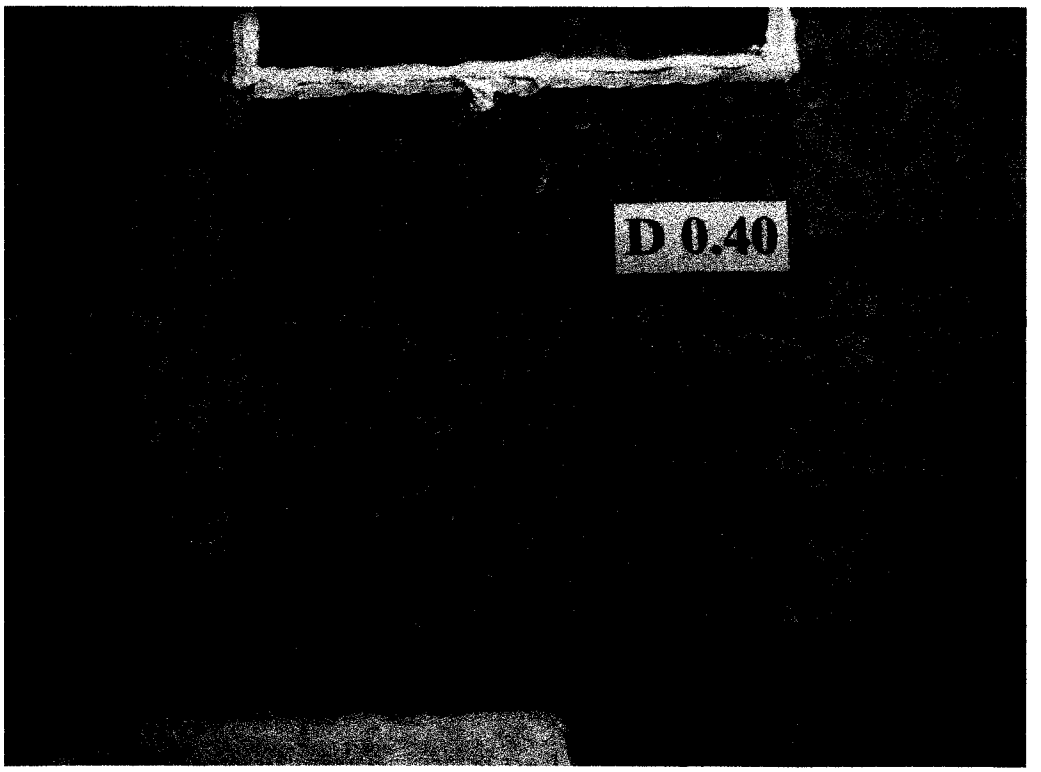

Figure 4.45: Flexural crack pattern at section (7) for strip of w/c = 0.40.

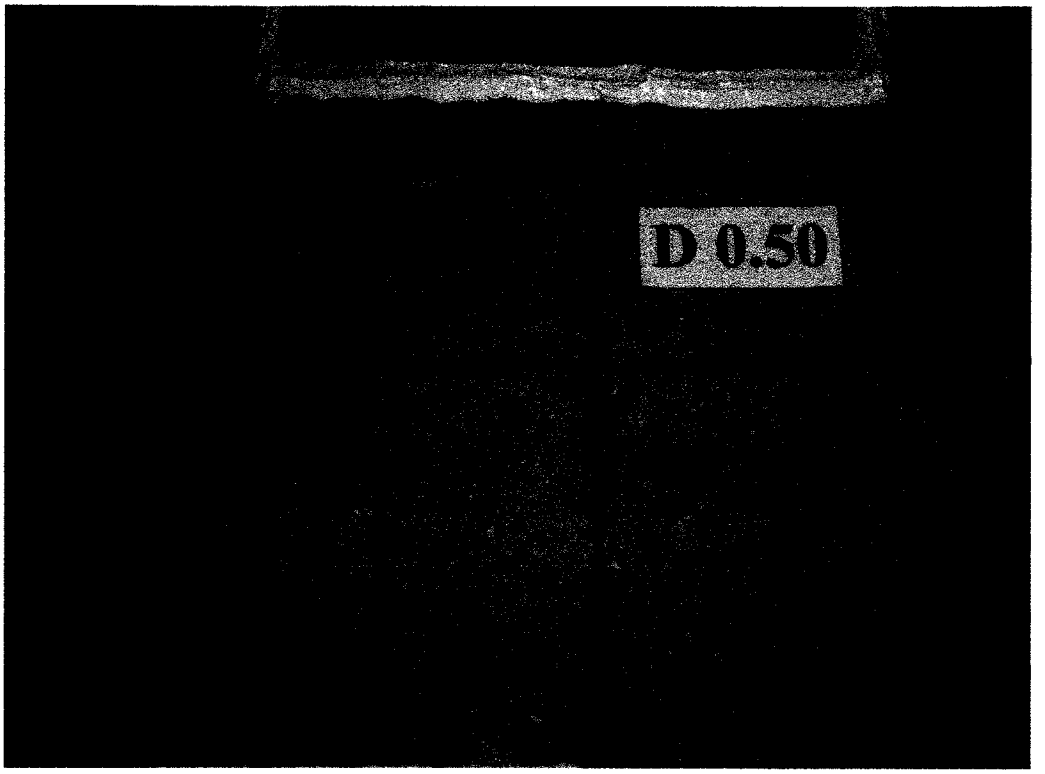

Figure 4.46: Flexural crack pattern at section (7) for strip of w/c = 0.50.

The total chloride concentration profiles at different sections after the second wet/dry cycle (i.e., after 6 months of exposure) are respectively plotted in Figures 4.47, 4.48, and 4.49 for the RC strips of w/c of 0.35, 0.40, and 0.50. Similar observations as previously noted can be drawn from these figures. Chloride concentration values are lower for sections 0 and 4, which correspond to an unstressed section and a section subjected to maximum compression at the top of the deck, respectively. Gowripalan et al. (2000) have also observed lower chloride concentration values at sections subjected to compression, suggesting that compressive stresses at service loads reduce the porosity and the rate of chloride ingress. The chloride profiles corresponding to section 8 display an anomalous behaviour at the skin of the concrete surface (see Figures 4.47 and 4.49). Here, the concentration values are the lowest for section 8, hinting to a chloride transport mechanism more indicative of convection than diffusion. This might be the case as the tensile stresses in this section might lead to a higher variation of the concrete moisture content in the first few millimetres of the concrete cover. Also worth noting in these figures is the higher concentration values for section 2 as depth increases. Although this

section is under compression due to flexural stresses, it is also subjected to shear, and thus to tension resulting from associated shear stresses.

The effect of the concrete cores w/c on the total chloride concentration profiles after 6 months of exposure can be observed in Figures 4.50, 4.51, 4.52, and 4.53, which illustrate respectively chloride concentration profiles at sections 0, 2, 4, and 8 for all the RC strips. Similar observations to those made for the first wet/dry cycle can be drawn, with the exception that the difference between profiles from the RC strips of 0.35 and 0.40 becomes small for all deck sections, regardless of the mechanical state under which the section is subjected.

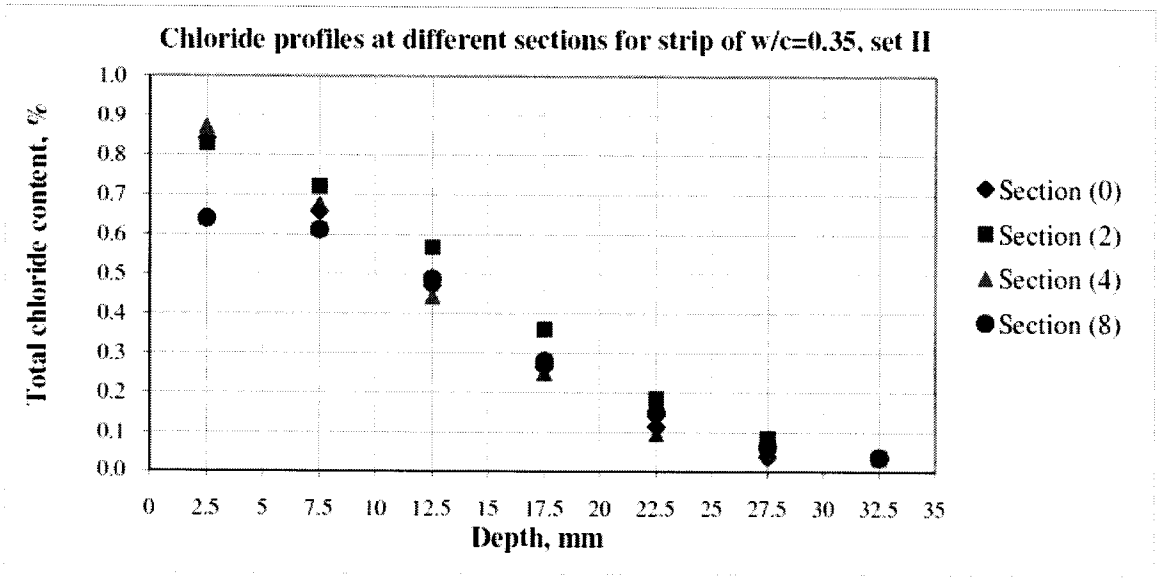

Figure 4.47: Chloride concentration profiles for the strip of w/c = 0.35 at different sections (set # II).

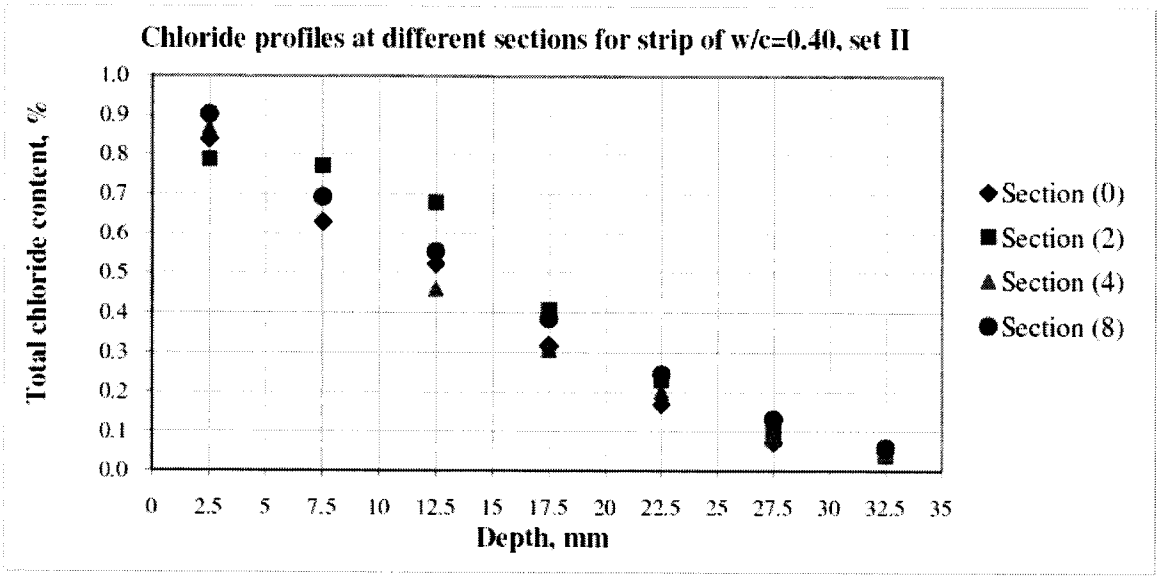

Figure 4.48: Chloride concentration profiles for the strip of w/c = 0.40 at different sections (set # II).

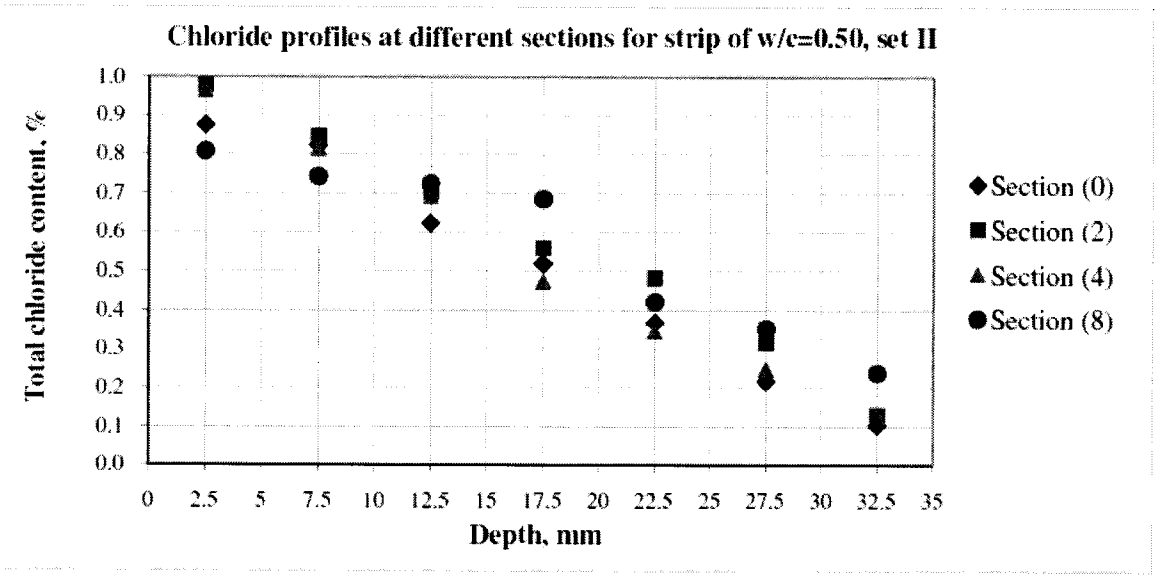

Figure 4.49: Chloride concentration profiles for the strip of w/c = 0.50 at different sections (set # II).

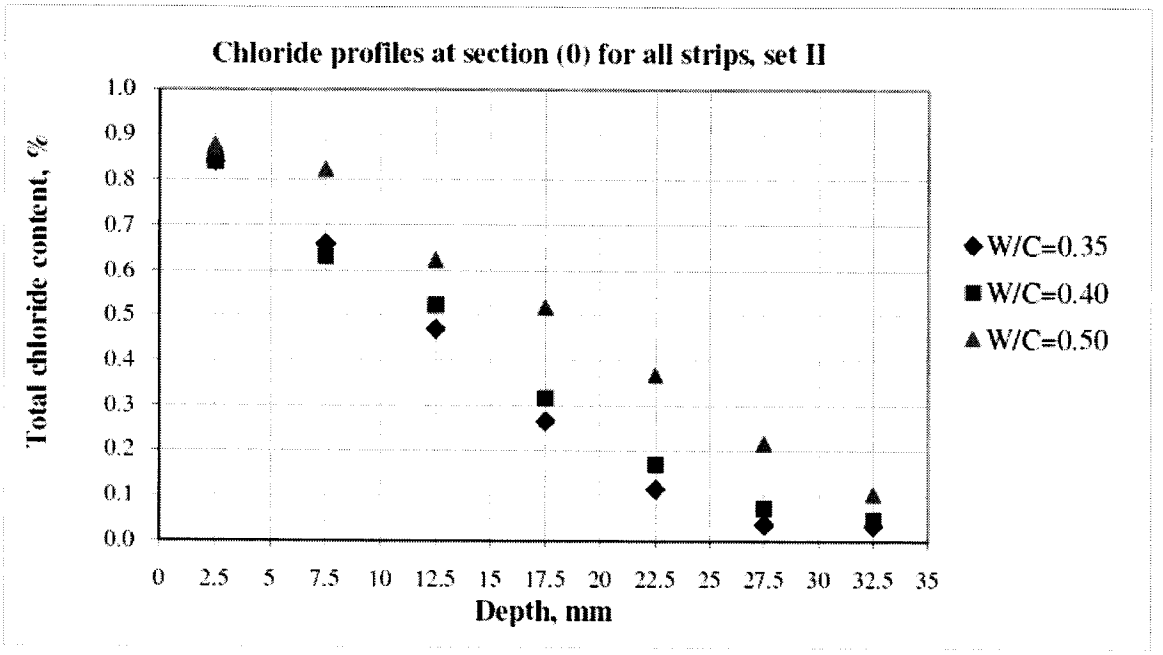

Figure 4.50: Chloride concentration profiles at section (0) for all strips (set # II).

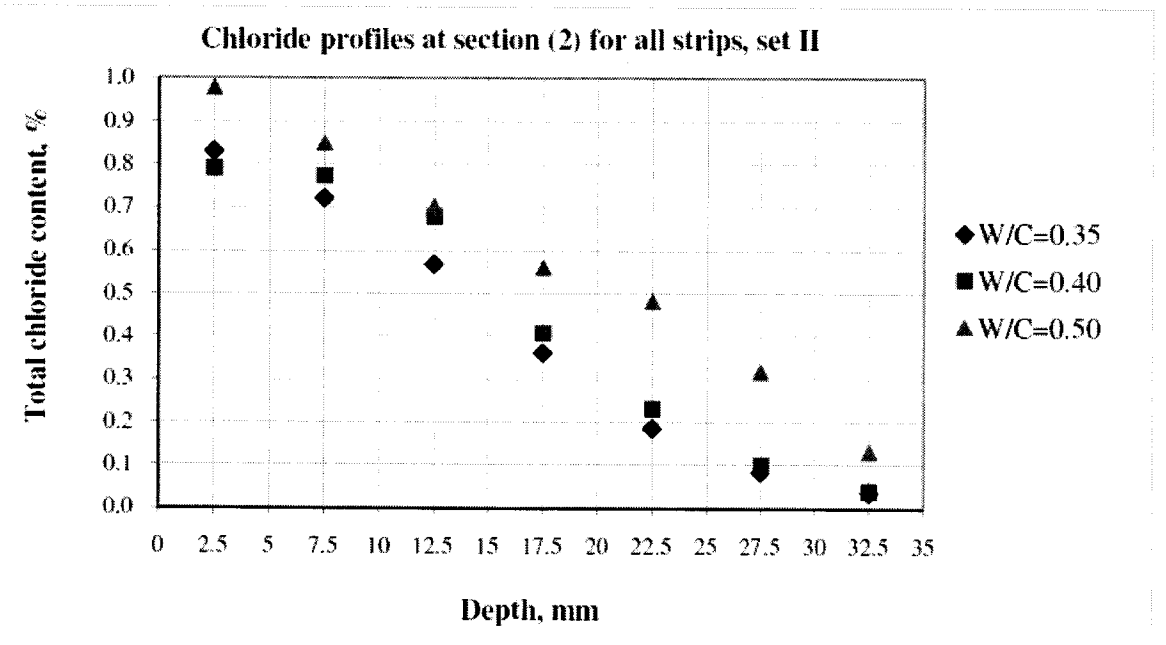

Figure 4.51: Chloride concentration profiles at section (2) for all strips (set # II).

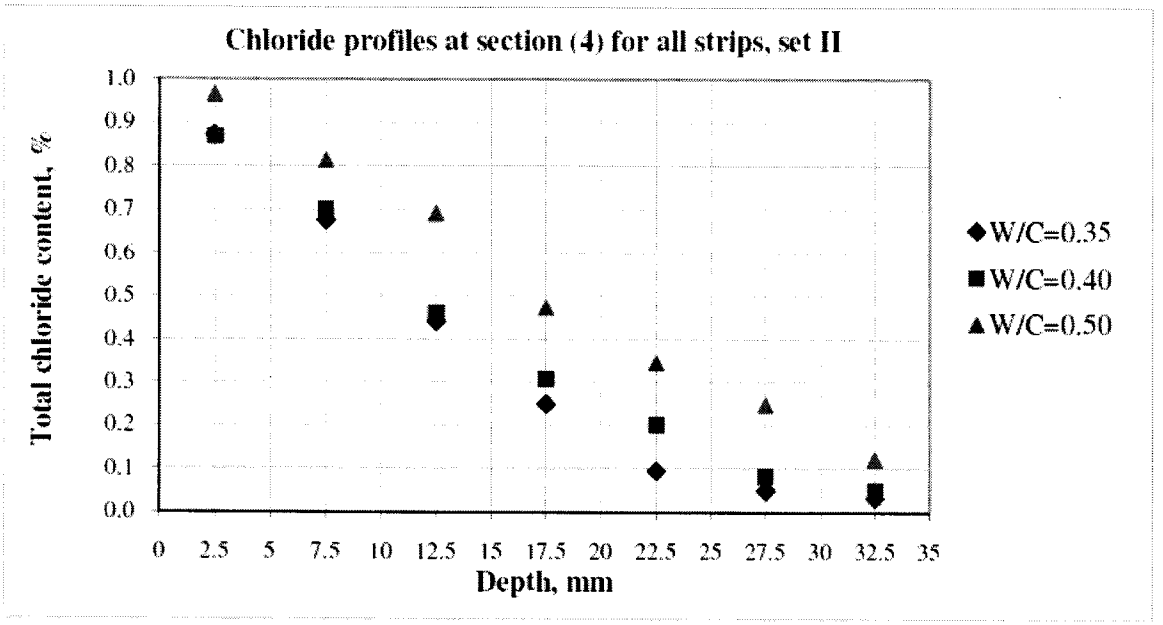

Figure 4.52: Chloride concentration profiles at section (4) for all strips (set # II).

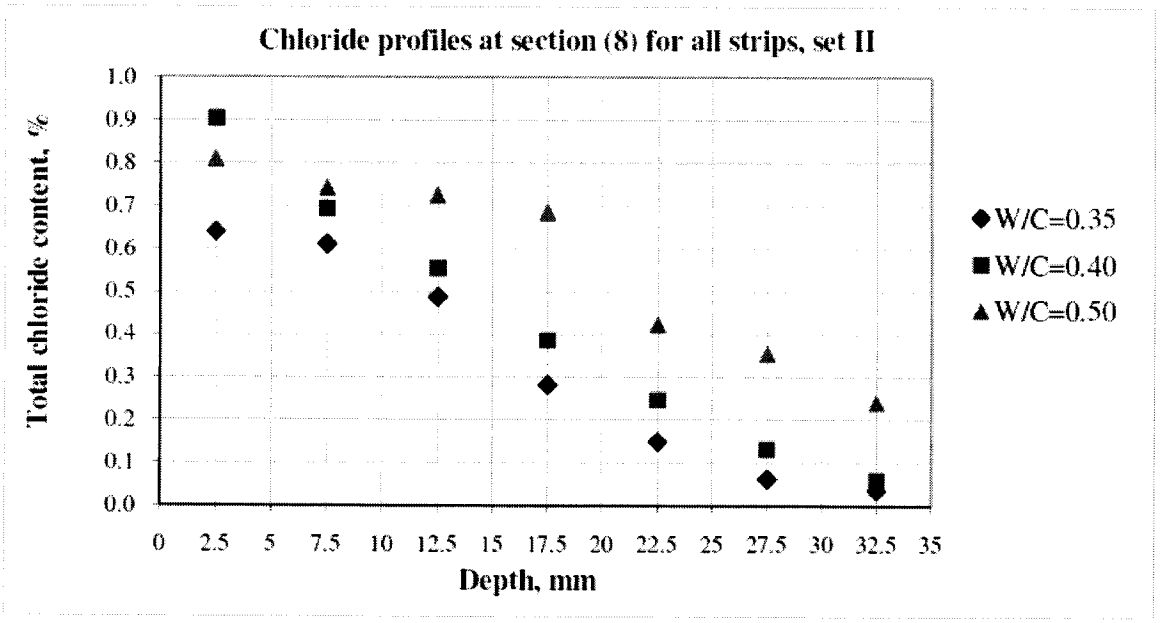

Figure 4.53: Chloride concentration profiles at section (8) for all strips (set # II).

Finally, the total chloride concentration profiles at different sections after the third wet/dry cycle (i.e., after 9 months of exposure) are respectively plotted in Figures 4.54, 4.55, and 4.56 for the RC strips of w/c of 0.35, 0.40, and 0.50. The chloride profiles at section 8 are the highest for all w/c. The difference in profiles between sections is less pronounced for the RC strip with w/c of 0.5, as this corresponds to a more porous concrete. This suggests that the influence of w/c on chloride ingress might be stronger than the effect of mechanical load for concretes made with higher w/c. Also, the chloride contents in section 4 are in general lower than those in section 2. Note that section 2, unlike section 4, is also subjected to shear stresses.

The effect of the concrete cores w/c on the total chloride concentration profiles after 9 months of exposure can be observed in Figures 4.57, 4.58, 4.59, and 4.60, which illustrate respectively chloride concentration profiles at sections 0, 2, 4, and 8 for all the RC strips. In general, the chloride content is lower for lower w/c except in case of section 8, where the RC strip of w/c of 0.40 shows higher chloride contents than that of w/c of 0.50 for depths greater than 22.5 mm.

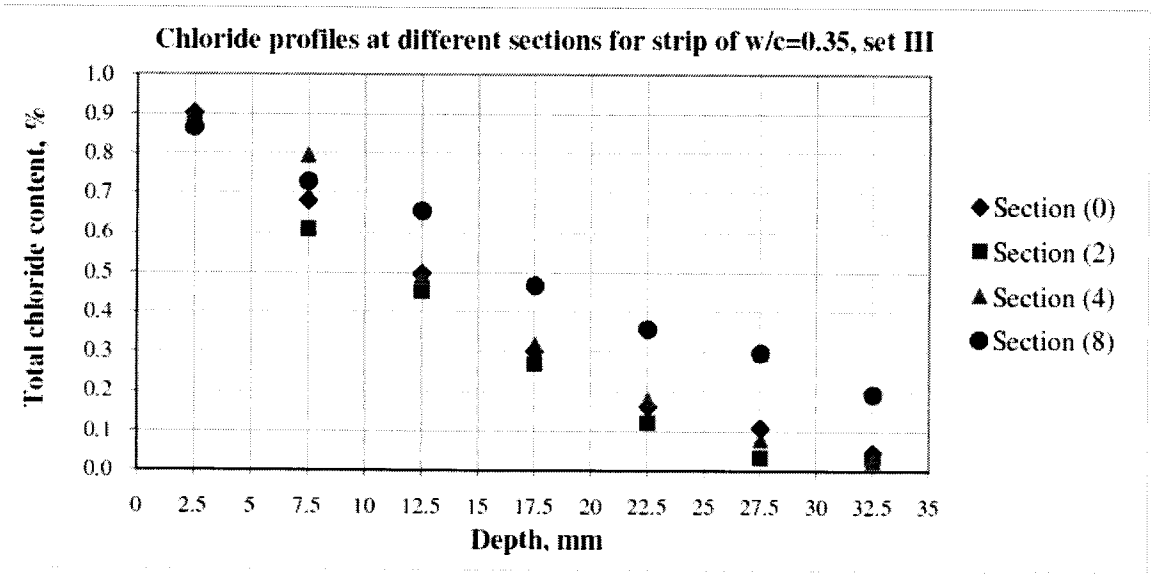

Figure 4.54: Chloride concentration profiles for the strip of w/c = 0.35 at different sections (set # III).

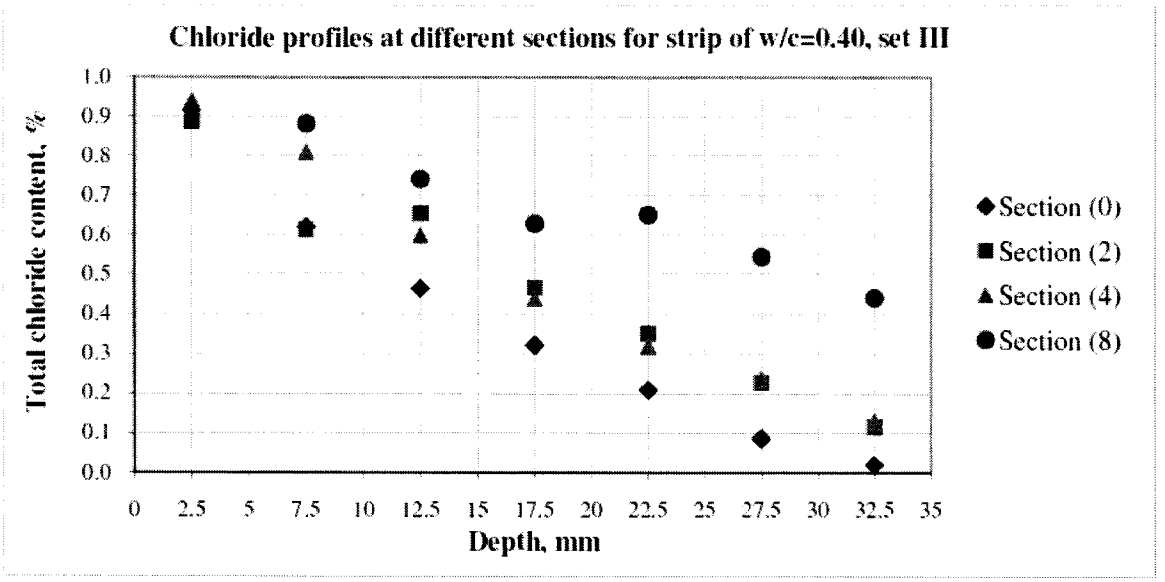

Figure 4.55: Chloride concentration profiles for the strip of w/c = 0.40 at different sections (set # III).

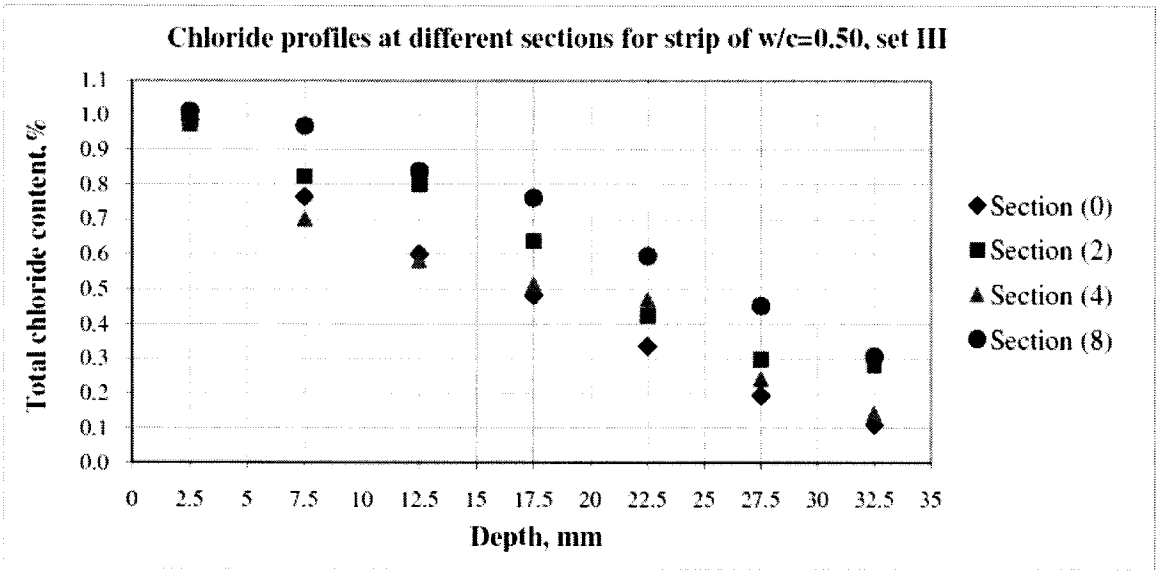

Figure 4.56: Chloride concentration profiles for the strip of w/c = 0.50 at different sections (set # III).

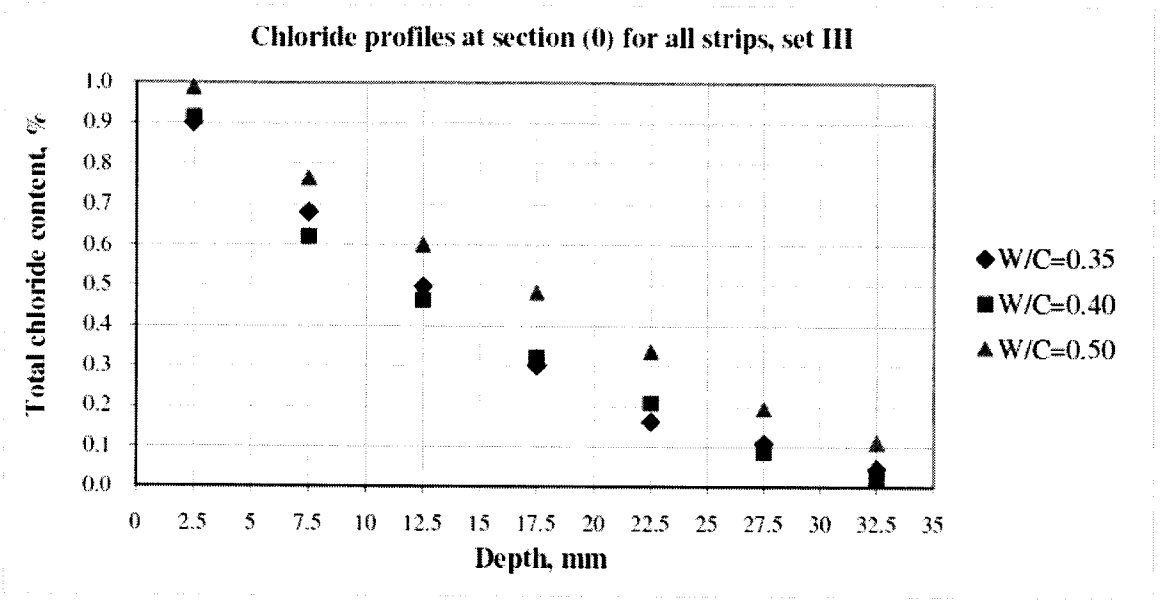

Figure 4.57: Chloride concentration profiles at section (0) for all strips (set # III).

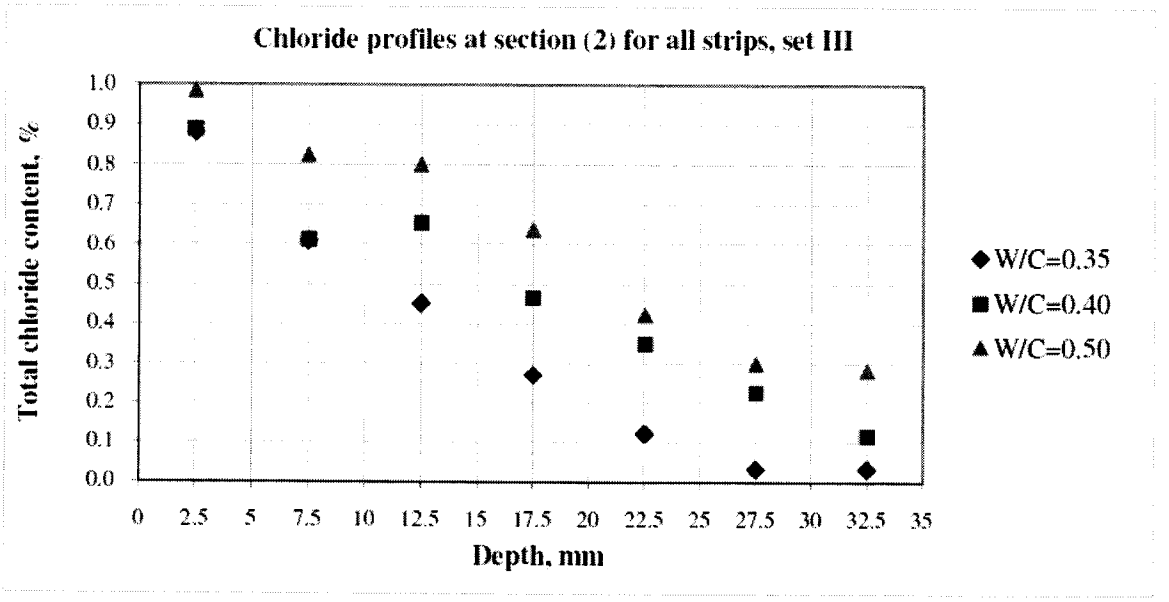

Figure 4.58: Chloride concentration profiles at section (2) for all strips (set # III).

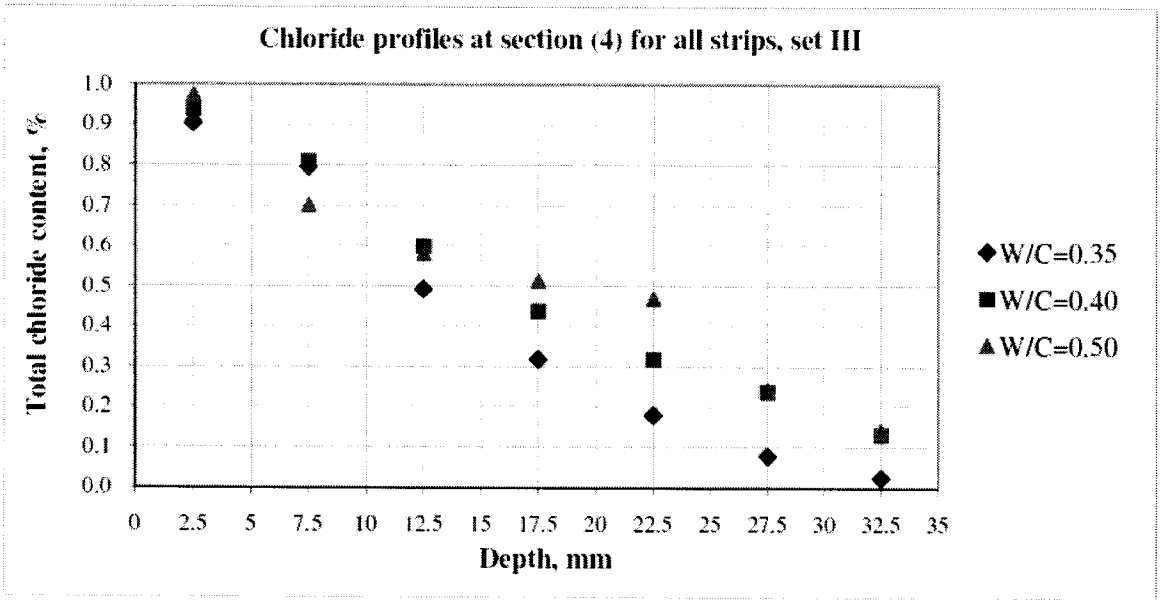

Figure 4.59: Chloride concentration profiles at section (4) for all strips (set # III).

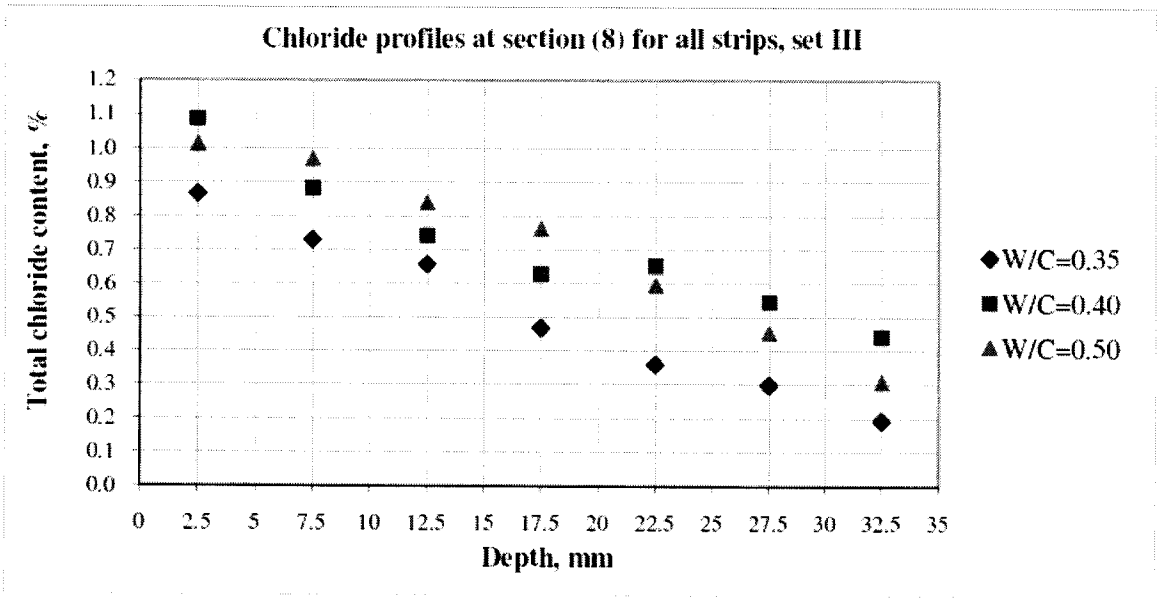

Figure 4.60: Chloride concentration profiles at section (8) for all strips (set # III).

Chapter 5

Assessment of Chloride Ingress Properties

5.1. Introduction

This chapter presents the analysis of chloride concentration data introduced in Chapter 4. First, chloride diffusion coefficients are determined from the chloride data obtained from both potentiometric titration and $AgNO_3$ spraying. The results of both methods are compared to establish the reliability of the colourimetric spray indicator. Second, the effect of stress, time of exposure and w/c on the chloride diffusivity of concrete sustaining load is discussed in light of the obtained results.

5.2. Chloride diffusivity

The ingress of chloride ions into concrete is due to various transport mechanisms:

(i) liquid phase filtration mainly driven by capillary effects;

(ii) diffusion and ionic interactions;

(iii) electro-migration due to an electrical field; and,

(iv) physical and chemical binding to the cement hydrates.

Models intending to account for the whole complexity of all transfer processes are difficult to apply from an engineering point of view. This is the reason why chloride content profiles have been traditionally assumed to result from a pure diffusion process, which mathematically is expressed by Fick's second law of diffusion (see Eq. (2.4)). For the same reasons, the diffusion analogy will be also applied here to the analysis of the chloride data obtained in Chapter 4.

5.2.1. Determination of diffusivity from chloride profiles

Although there are several methods to quantify the chloride diffusivity in concrete, the current practice in the field is to fit acid-soluble chloride profiles with Crank's solution to

Fick's 2nd law (Bentur et al., 1997). By applying non-linear regression analysis of the actual chloride data according to Eq. (2.5), two apparent values are determined for the diffusion coefficient and chloride surface concentration for a given time of exposure. These values are termed "apparent" because Crank's solution is actually only valid when both the chloride diffusion coefficient and surface concentration are constant in space and time. Since this is not the case in concrete, due to its heterogeneous nature and the time evolution of its material properties, the values of D_a and C_o thus obtained do not reflect an intrinsic property of the material, but rather the cumulative effect of all the factors involved in the chloride transport process.

Tables 5.1, 5.2 and 5.3 tabulate the apparent values of C_o (by weight of concrete) and D_a obtained from fitting the chloride profile data to Eq. (2.5) after 90, 180, and 270 days of exposure, respectively. The coefficients of determination of the regression analyses are given as well. In general, Crank's solution to Fick's 2nd law provides a good description of the chloride content variation with depth for all core specimens at the three time intervals. An exception is the values obtained for section 7, in which the R^2 values indicate a poor correlation of the data to Eq. (2.5). Section 7 corresponds to the negative moment region of the slab, where flexural cracks due to the service loading were visible. From these results, it can be observed that chloride diffusion in concrete that contains cracks cannot be idealized by Eq. (2.5).

Table 5.1: Surface chloride content, apparent diffusion coefficient, and correlation factor obtained by fitting chloride profiles for the first set of samples.

	w/c	Section	C_o (%)	D_a ($\times 10^{-12}$ m^2/s)	R^2
First set (90 days)	0.35	0 (control)	1.104	9.27	0.999
		2 (compression)	0.882	11.17	0.983
		4 (compression)	0.875	13.45	0.931
		7 (tension, cracked)	3.207	32.49	0.957
		8 (tension, uncracked)	0.860	12.72	0.989
	0.4	0 (control)	0.938	11.83	0.996
		2 (compression)	0.940	24.60	0.938
		4 (compression)	1.004	18.87	0.978
		7 (tension, cracked)	3.369	114.09	0.602
		8 (tension, uncracked)	0.960	37.50	0.977
	0.5	0 (control)	0.957	28.90	0.976
		2 (compression)	0.826	53.61	0.847
		4 (compression)	1.006	31.32	0.940
		7 (tension, cracked)	4.535	62.45	0.797
		8 (tension, uncracked)	1.009	28.45	0.972

Table 5.2: Surface chloride content, apparent diffusion coefficient, and correlation factor obtained by fitting chloride profiles for the second set of samples.

	w/c	Section	C_o (%)	D_a ($\times 10^{-12}$ m^2/s)	R^2
Second set (180 days)	0.35	0 (control)	1.001	7.86	0.988
		2 (compression)	0.997	10.84	0.972
		4 (compression)	1.040	7.14	0.993
		7 (tension, cracked)	2.770	53.98	0.969
		8 (tension, uncracked)	0.800	11.30	0.946
	0.4	0 (control)	0.966	9.84	0.987
		2 (compression)	0.996	13.29	0.921
		4 (compression)	1.007	9.40	0.995
		7 (tension, cracked)	3.129	32.03	0.959
		8 (tension, uncracked)	1.019	11.76	0.995
	0.5	0 (control)	1.026	17.81	0.970
		2 (compression)	1.093	21.39	0.972
		4 (compression)	1.091	16.44	0.989
		7 (tension, cracked)	3.364	38.23	0.936
		8 (tension, uncracked)	0.927	35.38	0.893

Table 5.3: Surface chloride content, apparent diffusion coefficient, and correlation factor obtained by fitting chloride profiles for the third set of samples.

	w/c	Section	C_o (%)	D_a ($\times 10^{-12}$ m^2/s)	R^2
Second set (270 days)	0.35	0 (control)	1.035	5.98	0.998
		2 (compression)	1.014	4.95	0.994
		4 (compression)	1.092	5.89	0.983
		7 (tension, cracked)	3.496	38.89	0.809
		8 (tension, uncracked)	0.950	15.00	0.990
	0.4	0 (control)	1.015	5.98	0.992
		2 (compression)	0.944	12.47	0.950
		4 (compression)	1.055	10.33	0.996
		7 (tension, cracked)	3.688	91.24	0.861
		8 (tension, uncracked)	1.072	32.20	0.938
	0.5	0 (control)	1.083	9.76	0.994
		2 (compression)	1.088	17.07	0.962
		4 (compression)	1.010	13.14	0.951
		7 (tension, cracked)	4.596	49.98	0.714
		8 (tension, uncracked)	1.147	23.91	0.959

The data presented in the previous tables is illustrated in Figures 5.1, 5.2 and 5.3, in which the variation of the diffusion coefficient at different sections along the deck is plotted after 90, 180, and 270 days of exposure, respectively. With the exception of the values corresponding to sections under tensile stresses, sections 7 and 8, the diffusion coefficient increases with the water-to-cement ratio and decreases with time. In general, the diffusion coefficient at section 2 is higher than that at section 4, even though both sections are under compressive stresses and section 4 is subjected to a higher bending moment. There are two possible reasons for this behaviour: (i) the higher compressive stresses might contribute to the reduction of capillary porosity, thus decreasing the penetration of chloride solution, as reported by Heideman and Sundstrom (1995) and Gowripalan et al. (2000); (ii) whereas section 4 is subjected to pure bending, section 2 is also subjected to diagonal tension as a result of shear stresses.

As opposed to the other sections, sections 7 and 8 are subjected to tensile stresses resulting from the applied bending moments. Section 8 is under a bending moment lower than that required to crack the reinforced concrete slab section. By comparing the diffusion coefficients of this section with those corresponding to sections under

compressive stresses, it is clear that these tensile stresses have an effect on increasing D_a, in particular as the time of exposure increases (see Figure 5.3). Section 7, on the other hand, although also subjected to tensile stresses, sustains a bending moment higher than that required to crack the section. Visible flexural cracks were observed at this section in all three RC strips of the slab. In fact, the higher D_a values at this section seen in Figures 5.1 to 5.3 were obtained from concrete cores which were already split by the flexural cracks. Indeed, the main mode of chloride penetration at this section is through chloride-laden water filtration along the pathway created by the cracks. The D_a value thus obtained for this cracked section is not representative of the actual rate of chloride ingress. However, the effect of the presence of flexural cracks can be clearly observed by comparing the diffusion coefficients of both sections 7 and 8.

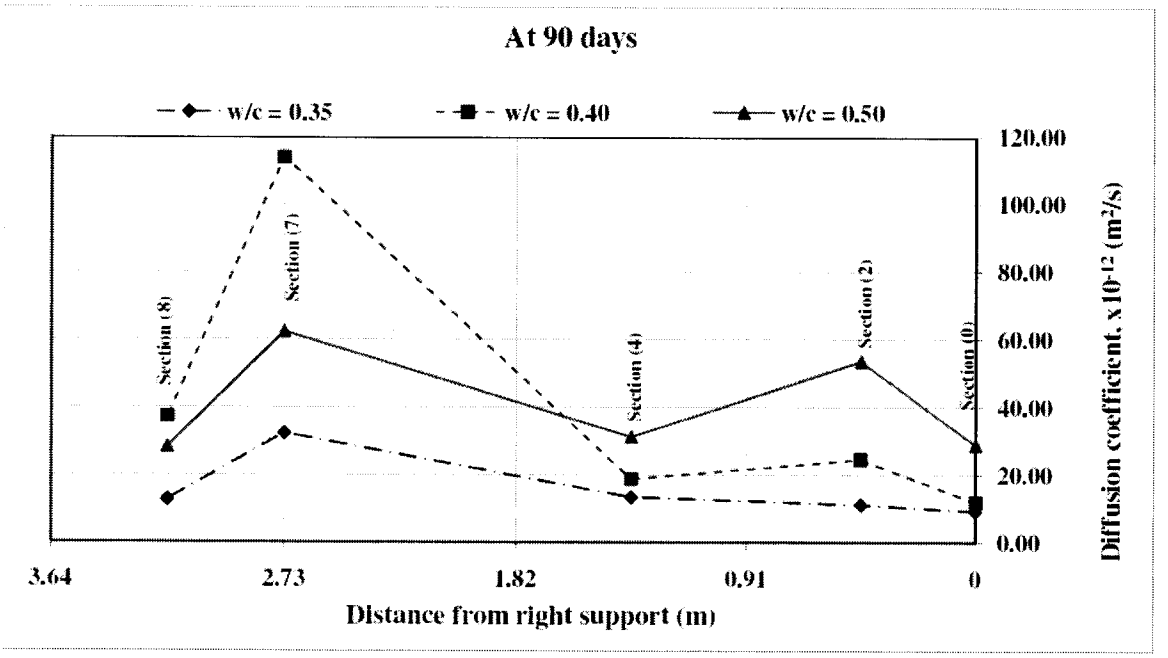

Figure 5.1: Variation of apparent diffusion coefficient at different sections for the first set.

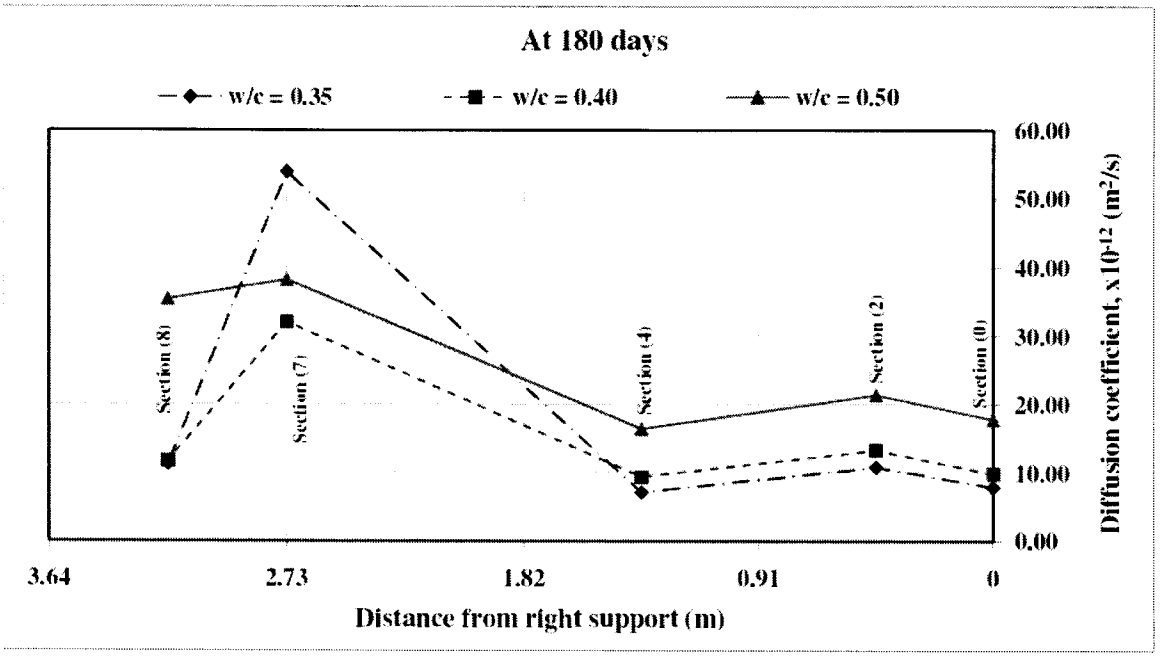

Figure 5.2: Variation of apparent diffusion coefficient at different sections for the second set.

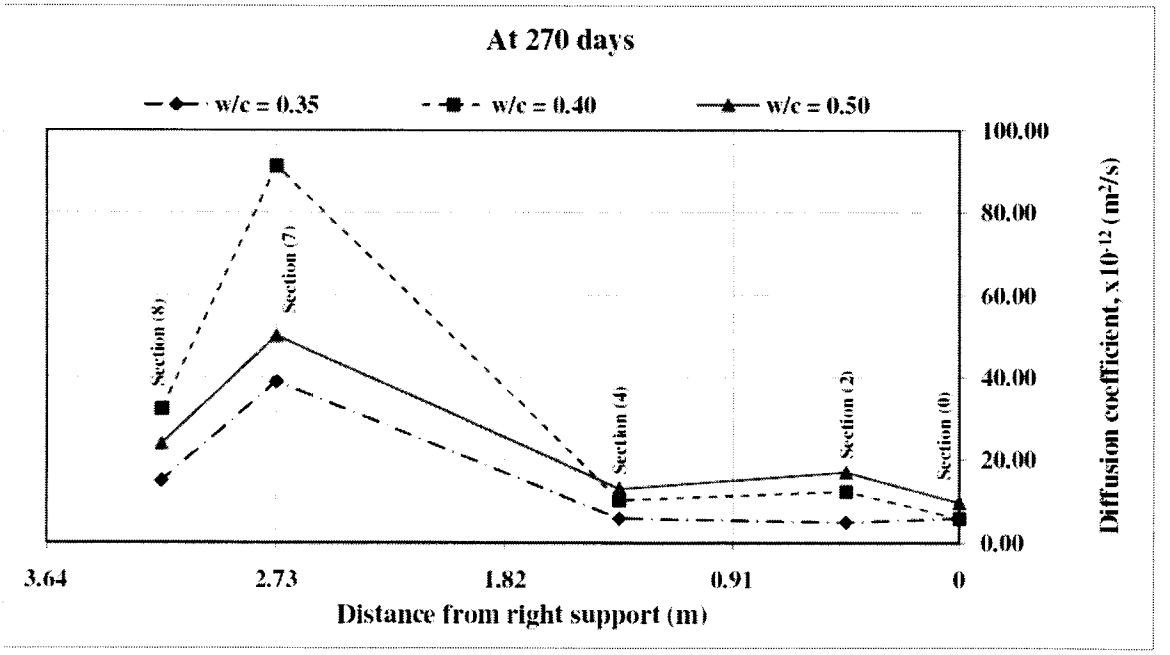

Figure 5.3: Variation of apparent diffusion coefficient at different sections for the third set.

In order to further study the behaviour of chloride ingress through the flexural cracks, the chloride profiles of sections 8 and 7 are respectively plotted in Figures 5.4 and 5.5 after 90 days of exposure. Also plotted in the figures are the theoretical profiles obtained by using Eq. (2.5) with the values of D_a and C_o reported in Table 5.1. Likewise, Figures 5.6 and 5.7 illustrate the chloride profiles for sections 8 and 7 after 180 days of exposure, respectively, and Figures 5.8 and 5.9 display the chloride profiles for sections 8 and 7 after 270 days of exposure, respectively. By comparing the profiles between both sections, the total chloride content along the concrete cover depth is much higher for section 7 than for section 8 for all times of exposure. Furthermore, the effect of the quality of the concrete as given by the w/c is not significant for the cracked section 7. Here the crack characteristics and not the concrete quality govern the rate of chloride ingress. Crank's solution to Fick's 2nd law correlates well to the experimentally obtained chloride profiles for section 8, as expressed by the R^2 values in Tables 5.1, 5.2 and 5.3. However, according to Figures 5.5, 5.7 and 5.9, the total chloride profiles for section 7 decrease linearly with increasing depth, suggesting a constant flux of chloride solution through the crack. The slope of the line describing the decrease of chloride content with depth is not affected by the w/c of the RC strip, thus confirming the significance of the nature of the cracks in the penetration of the chloride solution.

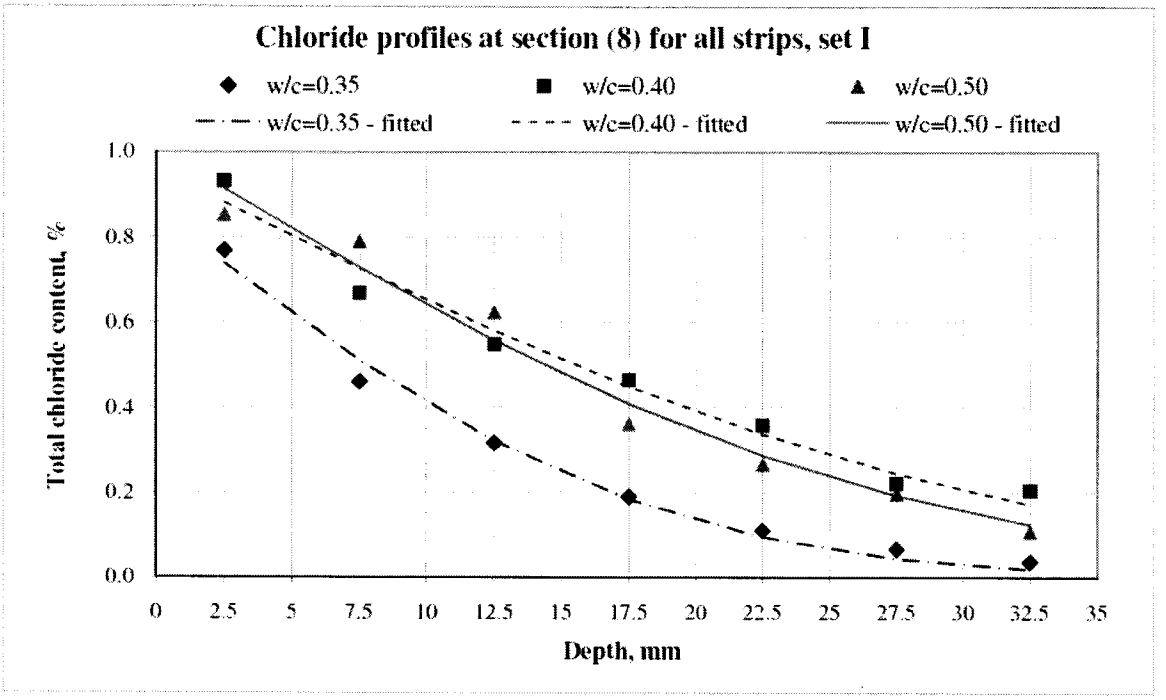

Figure 5.4: Chloride profile for section (8)-uncracked for all RC strips after 1st wet/dry cycle.

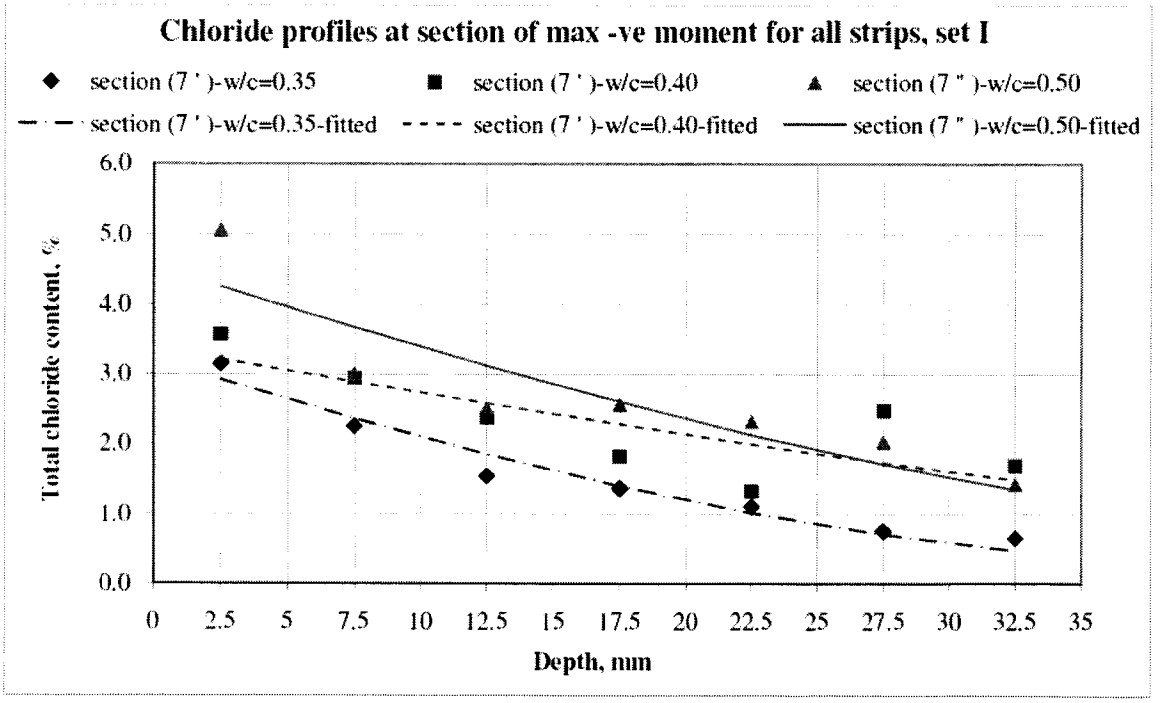

Figure 5.5: Chloride profile for section (7)-cracked, for all RC strips after 1st wet/dry cycle.

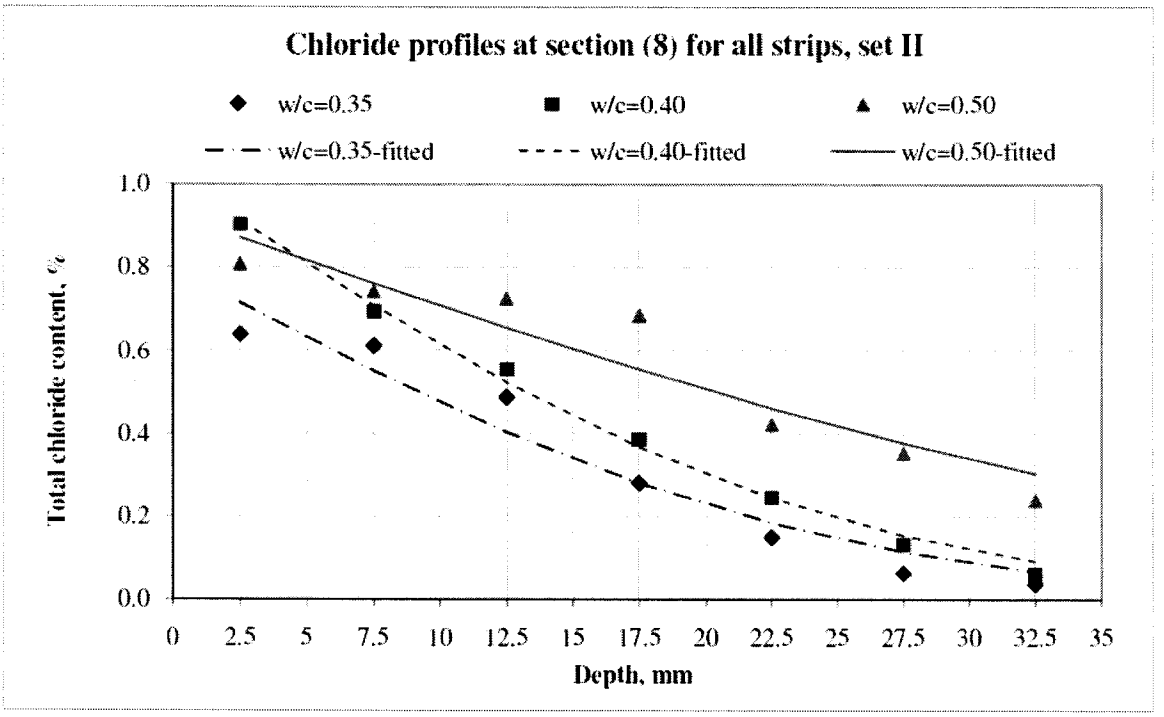

Figure 5.6: Chloride profile for section (8)-uncracked for all RC strips after 2nd wet/dry cycle.

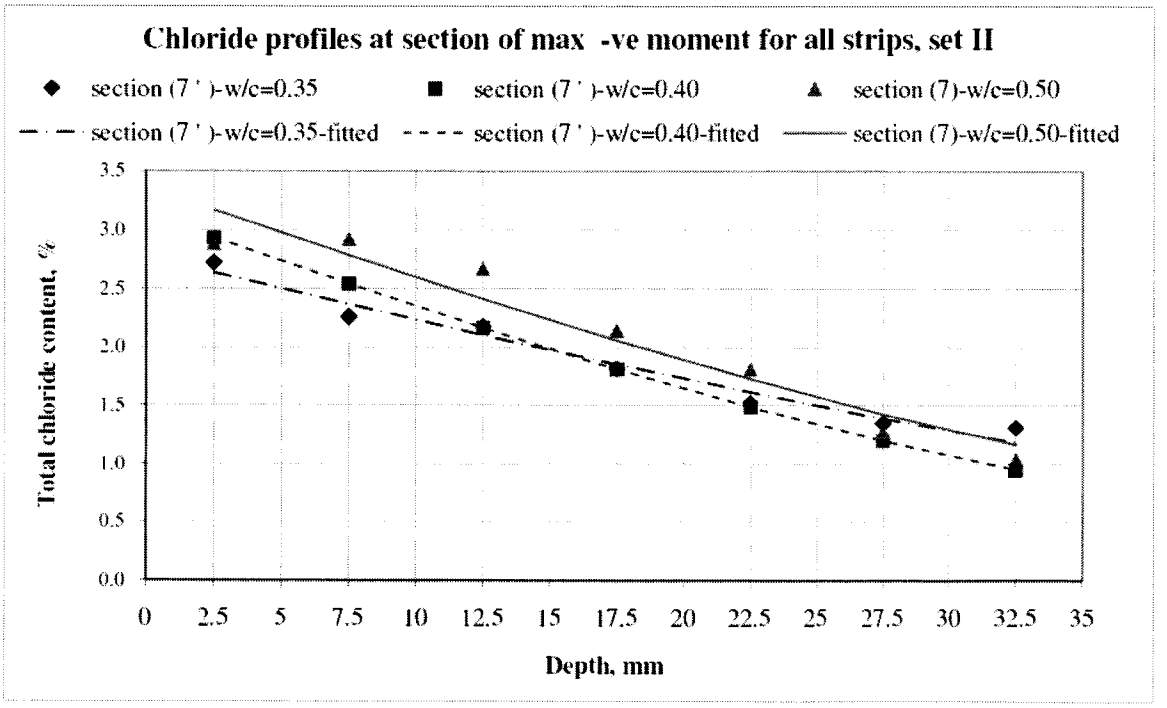

Figure 5.7: Chloride profile for section (7)-cracked for all RC strips after 2nd wet/dry cycle.

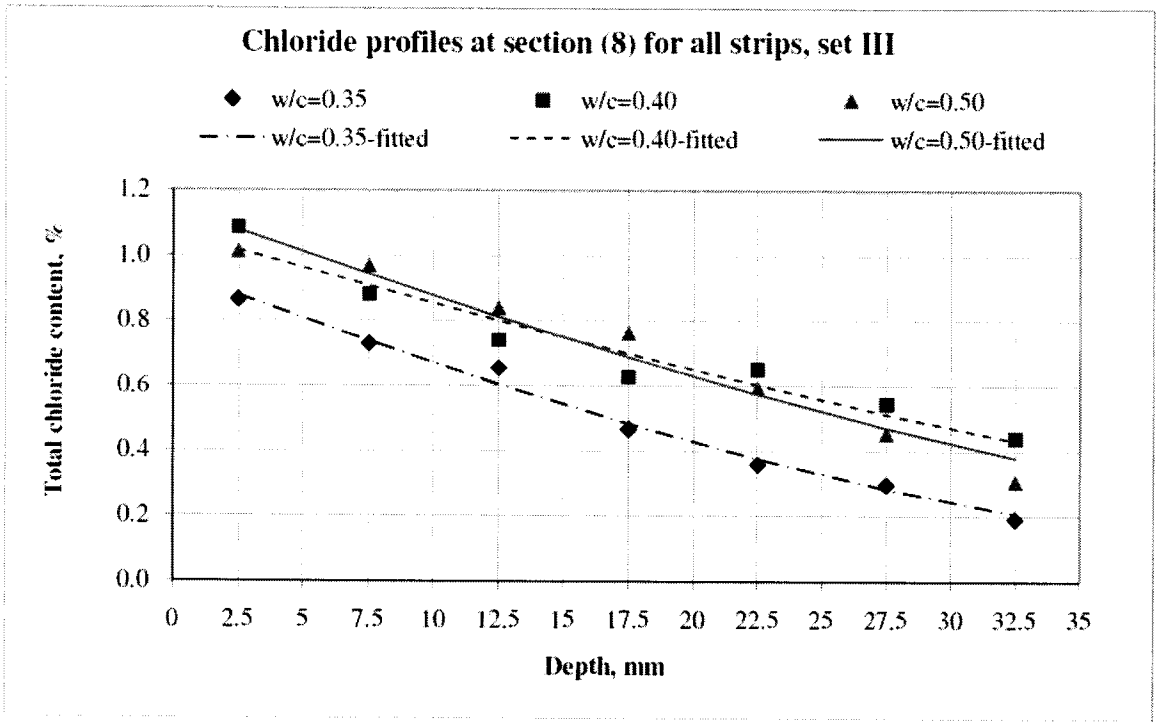

Figure 5.8: Chloride profile for section (8)-uncracked for all RC strips after 3rd wet/dry cycle.

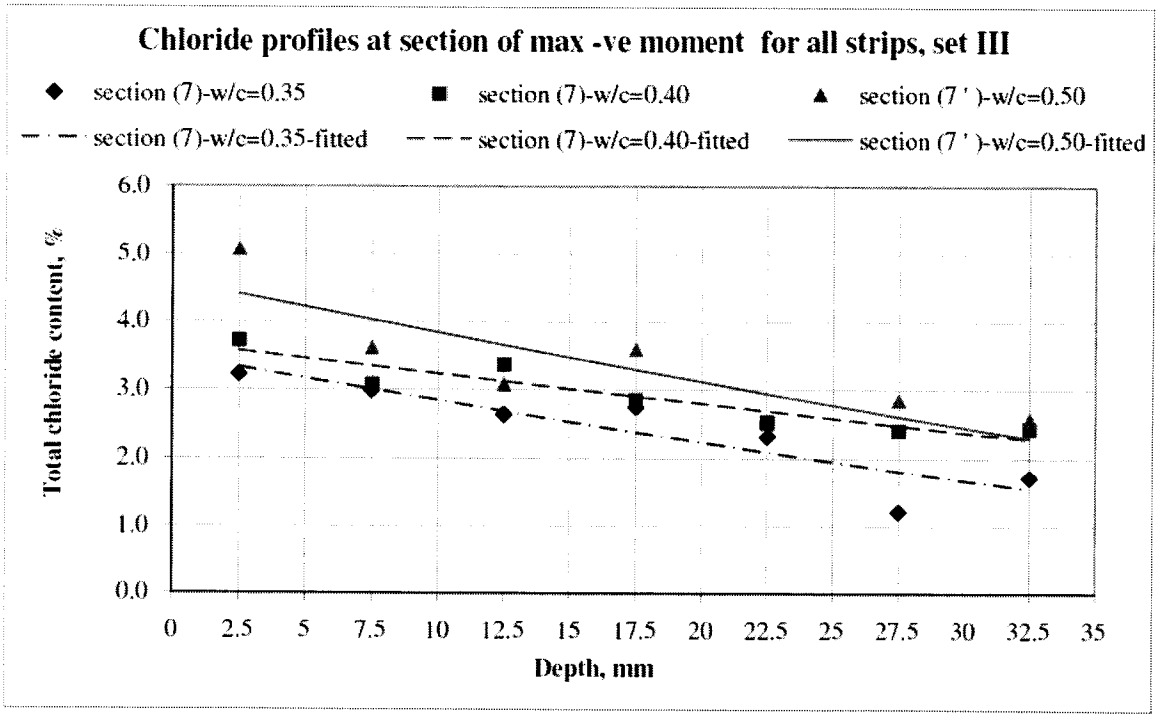

Figure 5.9: Chloride profile for section (7)-cracked for all RC strips after 3rd wet/dry cycle.

Excluding the data from section 7, the surface chloride concentration C_o in Tables 5.1, 5.2 and 5.3 ranges from 0.800 to 1.104% by weight of concrete (mean value μ = 0.995%, standard deviation σ = ±0.072%), reflecting the fact that all three RC strips and sections were subjected to the same boundary conditions. Differences are due to the fact that the slab was subjected to three wet/dry cycles, promoting moisture variation at the surface of the slab. Section 7 displays a much higher surface concentration, with a mean value μ of 3.573% and a standard deviation σ of ±0.618%. The surface chloride concentration data is plotted in Figures 5.10, 5.11 and 5.12 for all sets for each strip of w/c of 0.35, 0.4 and 0.5, respectively. The variability in C_o at section 7 is very clear in the figures. It is interesting to note that at this section the determined value for C_o is always lower at the second time interval than at the first time interval for all RC strips. It is believed that the reason for this is the leaking of chloride solution through the flexural cracks in section 7. At the beginning of the third wet and dry cycle, more chloride salt was added to the deck, resulting in a higher C_o as observed in the figures.

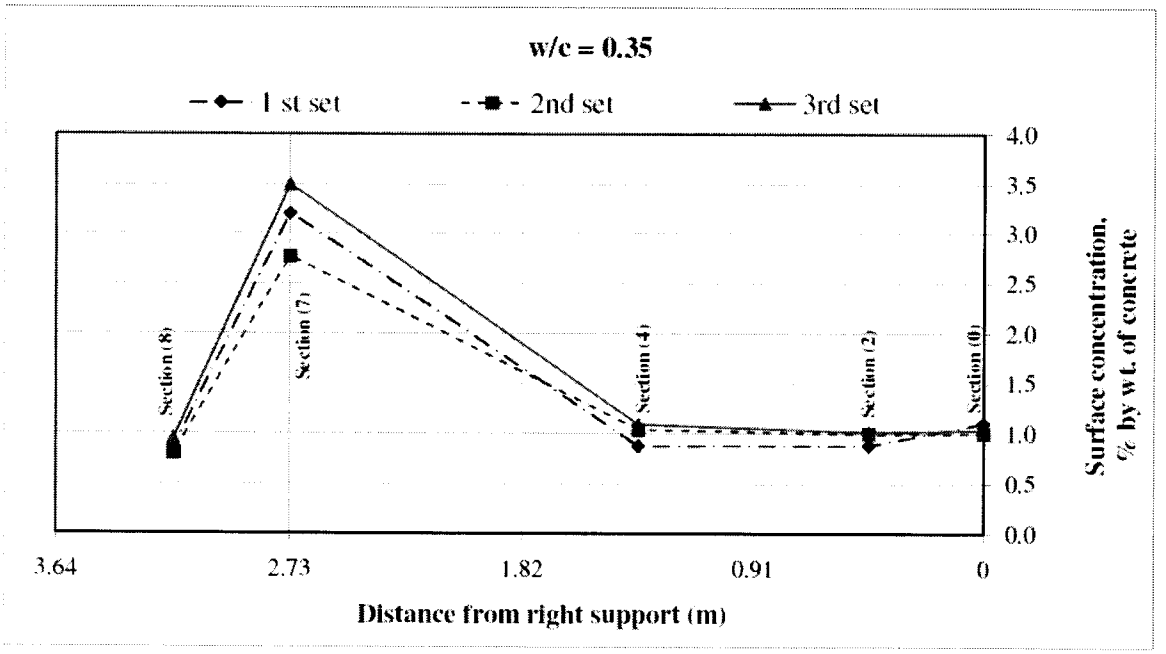

Figure 5.10: Surface concentration at different sections for the RC strip of w/c = 0.35 after the three wet/dry cycles.

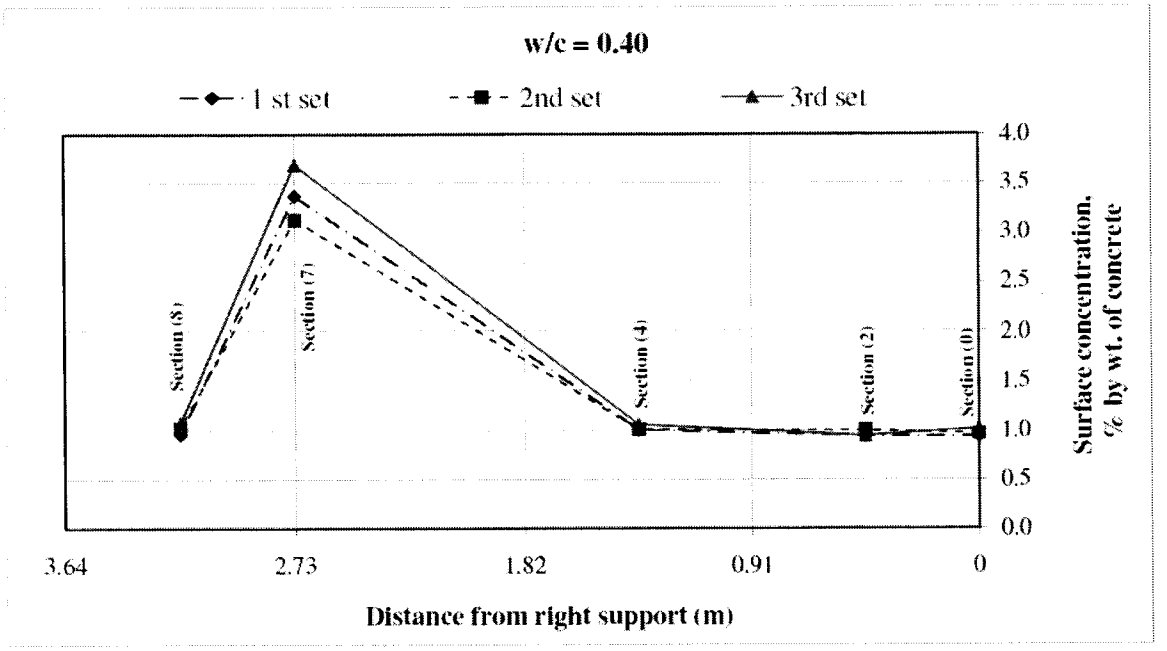

Figure 5.11: Surface concentration at different sections for the RC strip of w/c = 0.40 after the three wet/dry cycles.

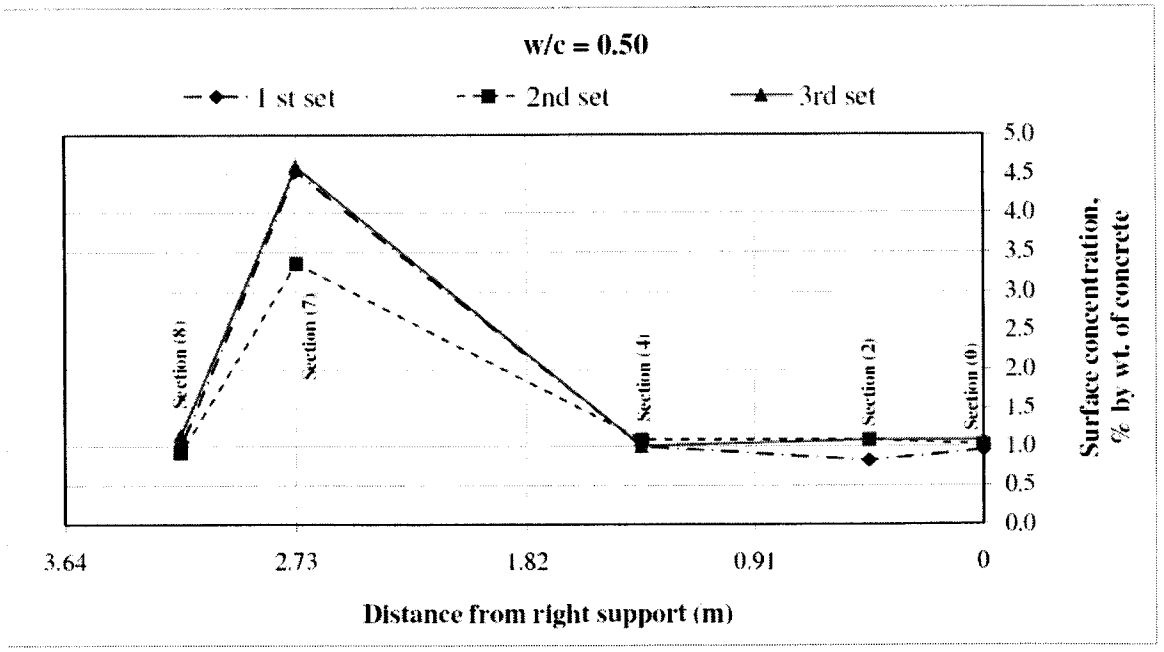

Figure 5.12: Surface concentration at different sections for the RC strip of w/c = 0.5 after the three wet/dry cycles.

5.2.2. Determination of diffusivity from $AgNO_3$ spraying

The colourimetric method based on spraying silver nitrate on the concrete surface only gives an indication of the average chloride penetration depth, and it does not provide any information on the rate of that penetration. However, by assuming that the chloride concentration at the colour front given by the silver nitrate is the same for each sample, an estimate of the ratio between diffusion coefficients of each sample can be obtained. Thus, assuming that $C(x_i,t) = C(x_o,t)$, where x_i is the measured average chloride depth for section i and x_o is the measured average chloride depth for the control section, and assuming that C_o is the same for section i and o, the following expression results from applying Crank's solution:

$$erf\left(\frac{x_i}{2\sqrt{D_i t}}\right) = erf\left(\frac{x_o}{2\sqrt{D_o t}}\right) \tag{5.1}$$

where D_i is the apparent diffusion coefficient for section i, and D_o is the apparent diffusion coefficient for the control section. The assumption of C_o being the same for all sections is applicable according to the values reported in Tables 5.1, 5.2 and 5.3, with the exception of those corresponding to section 7. Since the error function is a one-to-one function, rearranging Eq. (5.1) results in:

$$\frac{D_i}{D_o} = \left(\frac{x_i}{x_o}\right)^2 \tag{5.2}$$

Thus the average penetration data obtained from the colourimetric method can be used to obtain a relative value of the diffusivity among different sections along the RC deck according to Eq. (5.2).

In order to test the implied assumption in Eq. (5.2) of equal chloride concentration at the colour front for all samples, Crank's equation along with the diffusion coefficients and surface chloride concentrations listed in Tables 5.1 through 5.3 were used to determine the chloride concentration at the measured average penetration depths given by the colourimetric method. The measured average penetration depths and the corresponding calculated total chloride concentrations are tabulated in Tables 5.4, 5.5 and

5.6 for the three sets, respectively. Note that only the control section and the two sections under compressive stresses, sections 2 and 4, were used in this analysis.

Table 5.4: Average chloride penetration depth and corresponding total chloride concentration for the first set of samples.

	w/c	Section	Average depth (mm)	Corresponding concentration $C(x,t)$, %
First set (90 days)	0.35	0 (control)	20.50	0.097
		2 (compression)	16.00	0.198
		4 (compression)	20.50	0.137
	0.40	0 (control)	18.25	0.167
		2 (compression)	24.75	0.193
		4 (compression)	25.75	0.133
	0.50	0 (control)	21.75	0.292
		2 (compression)	27.50	0.282
		4 (compression)	30.25	0.172

Table 5.5: Average chloride penetration depth and corresponding total chloride concentration for the second set of samples.

	w/c	Section	Average depth (mm)	Corresponding concentration $C(x,t)$, %
Second set (180 days)	0.35	0 (control)	21.75	0.097
		2 (compression)	25.25	0.198
		4 (compression)	20.00	0.137
	0.40	0 (control)	19.50	0.167
		2 (compression)	24.50	0.193
		4 (compression)	26.00	0.133
	0.50	0 (control)	23.50	0.292
		2 (compression)	32.50	0.282
		4 (compression)	31.25	0.172

Table 5.6: Average chloride penetration depth and corresponding total chloride concentration for the third set of samples.

	w/c	Section	Average depth (mm)	Corresponding concentration $C(x,t)$, %
Third set (270 days)	**0.35**	0 (control)	27.50	0.103
		2 (compression)	25.75	0.091
		4 (compression)	29.00	0.088
	0.40	0 (control)	26.25	0.118
		2 (compression)	30.50	0.195
		4 (compression)	32.25	0.150
	0.50	0 (control)	30.25	0.169
		2 (compression)	36.75	0.210
		4 (compression)	35.50	0.153

The data tabulated in Tables 5.4, 5.5. and 5.6 is plotted in Figures 5.13, 5.14 and 5.15 for the RC strips of w/c of 0.35, 0.40 and 0.50, respectively. Note that the data presented in each graph corresponds to the three sections, sections 0, 2 and 4, and three time frames, 90, 180 and 270 days of exposure. In the figures, the variability of the calculated total chloride concentration corresponding to the measured average penetration depths is denoted by bands A, B and C for sections 0, 2 and 4, respectively. The average and standard deviation of the values within each band are reported in Figures 5.16 and 5.17, respectively. It is interesting to notice that there is less variability at sections 2 and 4 compared to section 0. This suggests that the w/c has less impact on chloride ingress when concrete is subjected to compressive load.

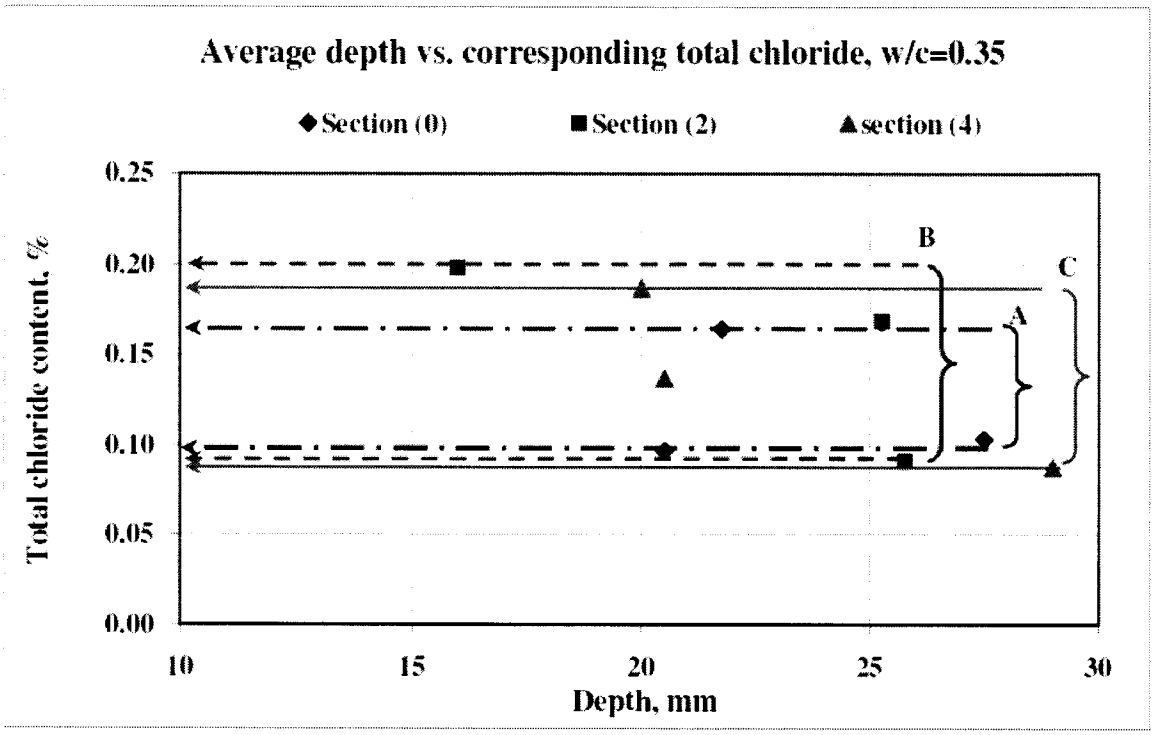

Figure 5.13: Average chloride penetration depth versus total chloride content for the RC strip with w/c = 0.35.

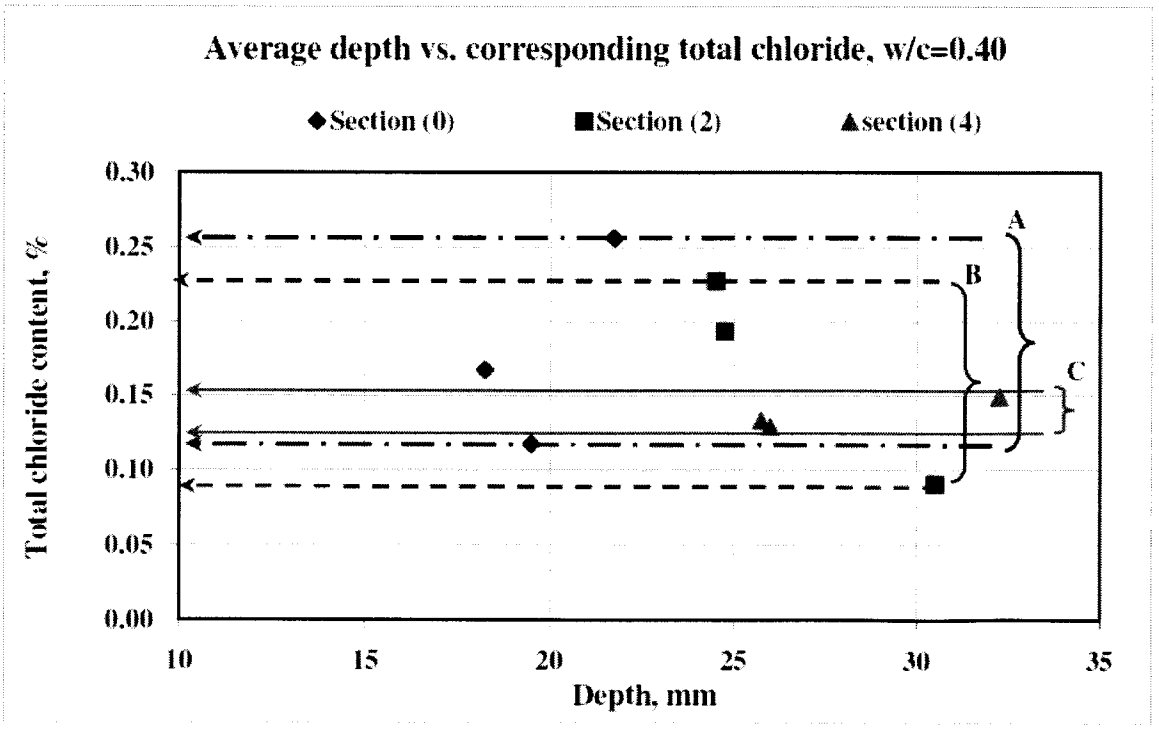

Figure 5.14: Average chloride penetration depth versus total chloride content for the RC strip with w/c = 0.40.

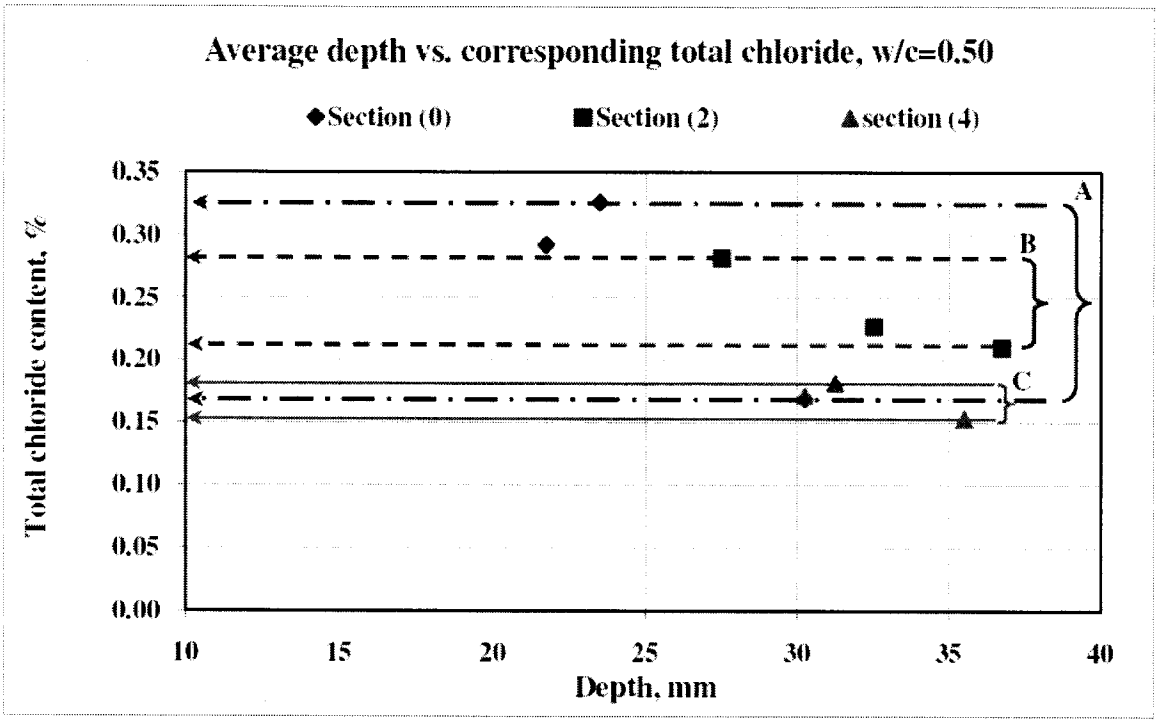

Figure 5.15: Average chloride penetration depth versus total chloride content for the RC strip with w/c = 0.50.

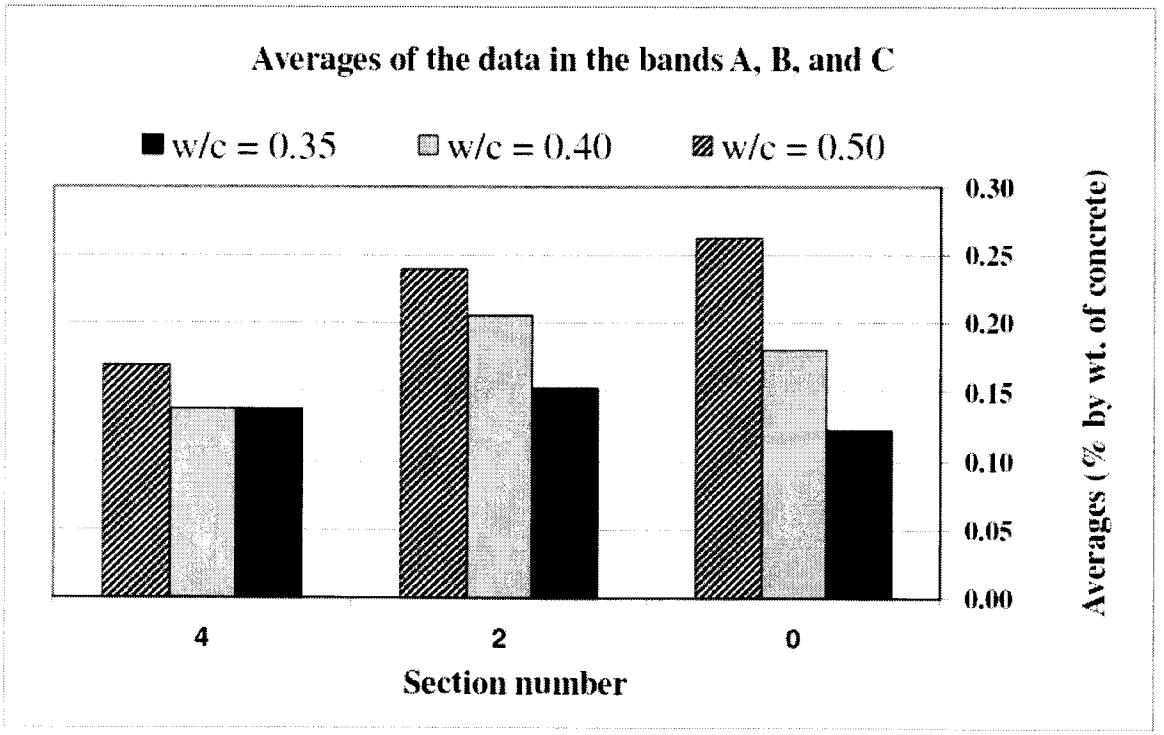

Figure 5.16: Averages of the data in the bands A, B, and C.

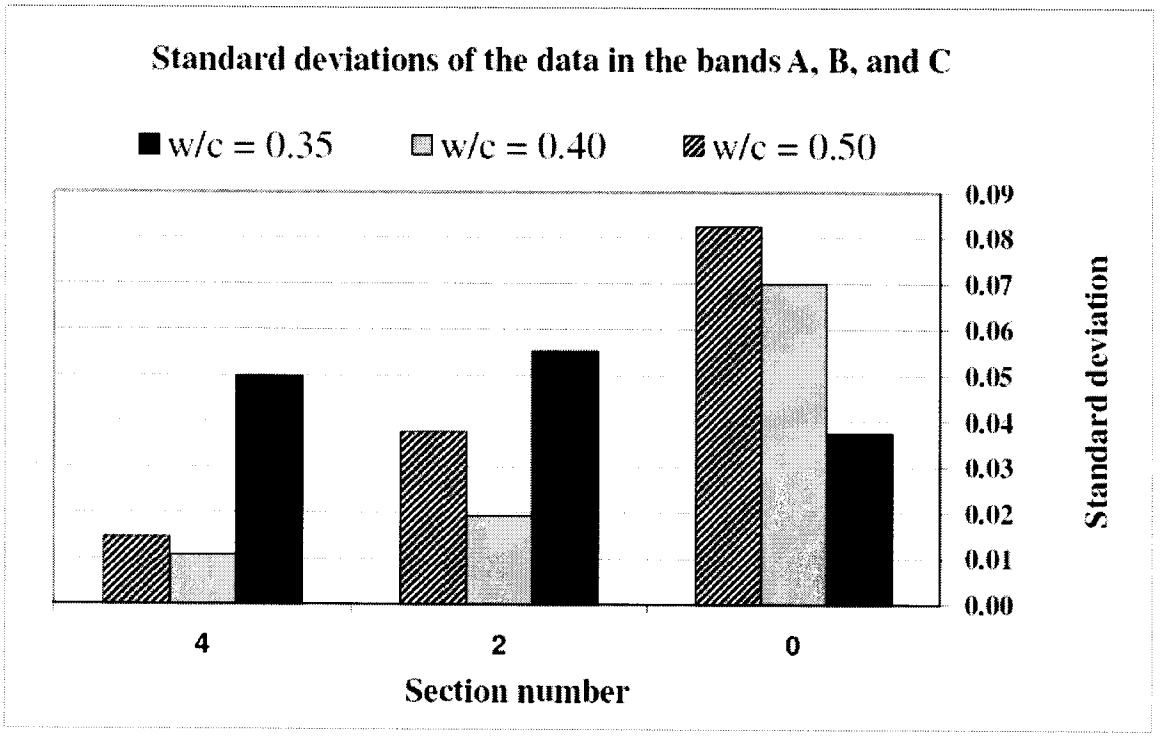

Figure 5.17: Standard deviations of the data in the bands A, B, and C.

5.2.3. Comparison between both methods

In order to compare the chloride diffusivities obtained from the colourimetric method and the potentiometric titration analysis, it was necessary to calculate the ratios of the chloride diffusivity of each sample to the chloride diffusivity of the control section (unstressed section), since the data obtained from the colourimetric method can only give an indication of the relative value of theses diffusivities according to Eq. (5.2). The ratios thus obtained from both methods are plotted in Figures 5.18, 5.19 and 5.20 after 90, 180, and 270 days of exposure, respectively. The data obtained from core samples subjected to tensile stresses was excluded in the figures.

In general, the ratios obtained from potentiometric titration measurements are larger than those obtained from the colourimetric measurements. As the time of exposure increases, the difference between both sets of ratios becomes smaller. This means that the colourimetric method could be used as a quick tool to detect average chloride penetration fronts after at least one year of exposure. Moreover, the colourimetric method can provide a better estimate of the diffusion ratio D_i/D_o than average penetration depths as

illustrated in Figures 5.13, 5.14, and 5.15. This is further confirmed in Figures 5.21, 5.22, and 5.23, which plot the average of the normal distances of each D_i/D_o ratio to the 45° line against time of exposure for the RC strips of w/c = 0.35, 0.4, and 0.5, respectively.

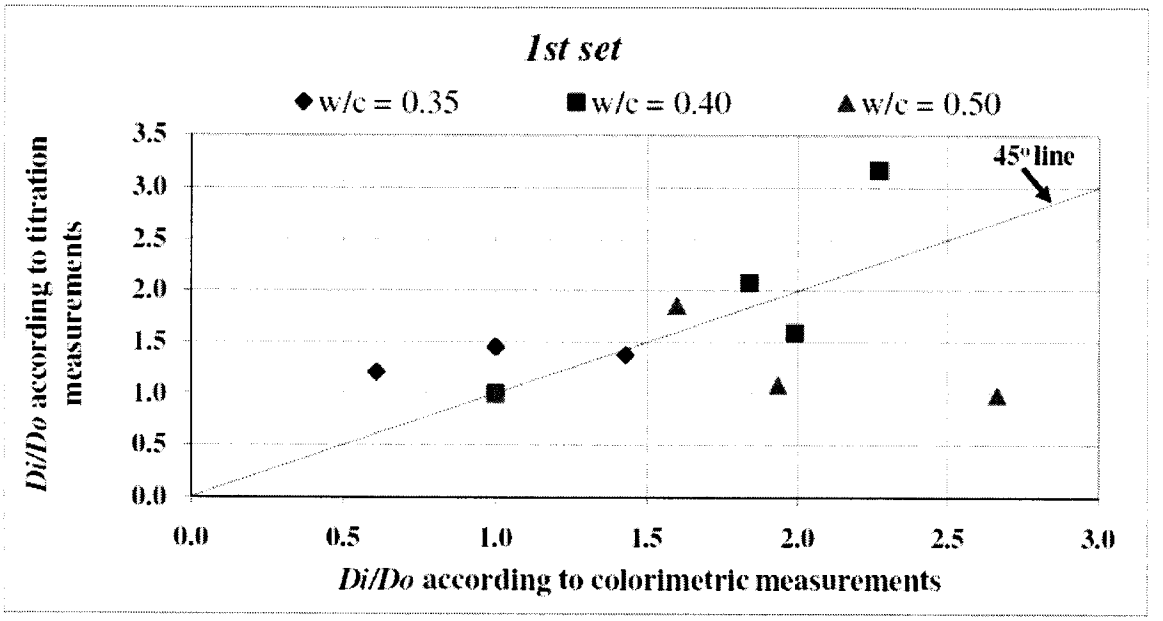

Figure 5.18: D_i/D_o from colourimetric method versus D_i/D_o from titration method for the first cycle.

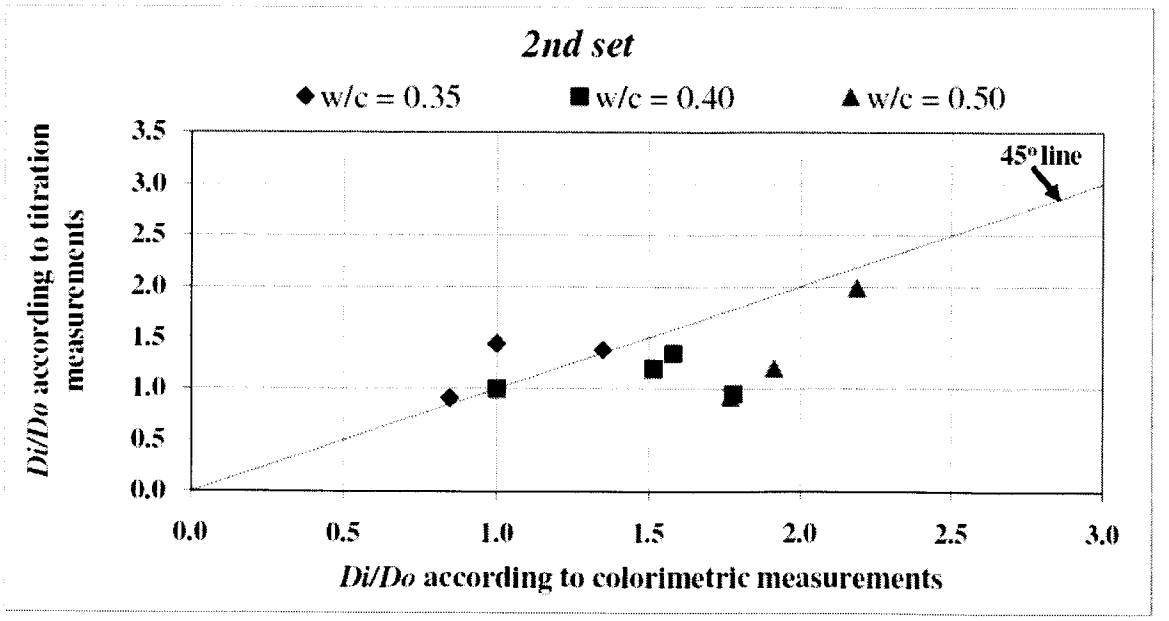

Figure 5.19: D_i/D_o from colourimetric method versus D_i/D_o from titration method for the second cycle.

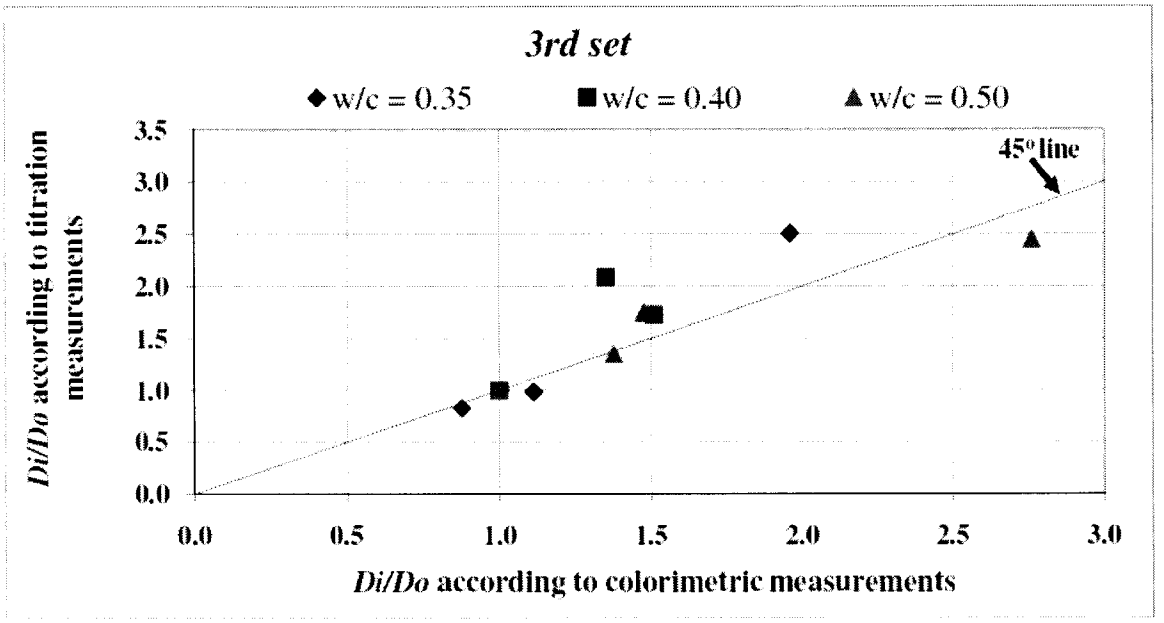

Figure 5.20: D_i/D_o from colourimetric method versus D_i/D_o from titration method for the third cycle.

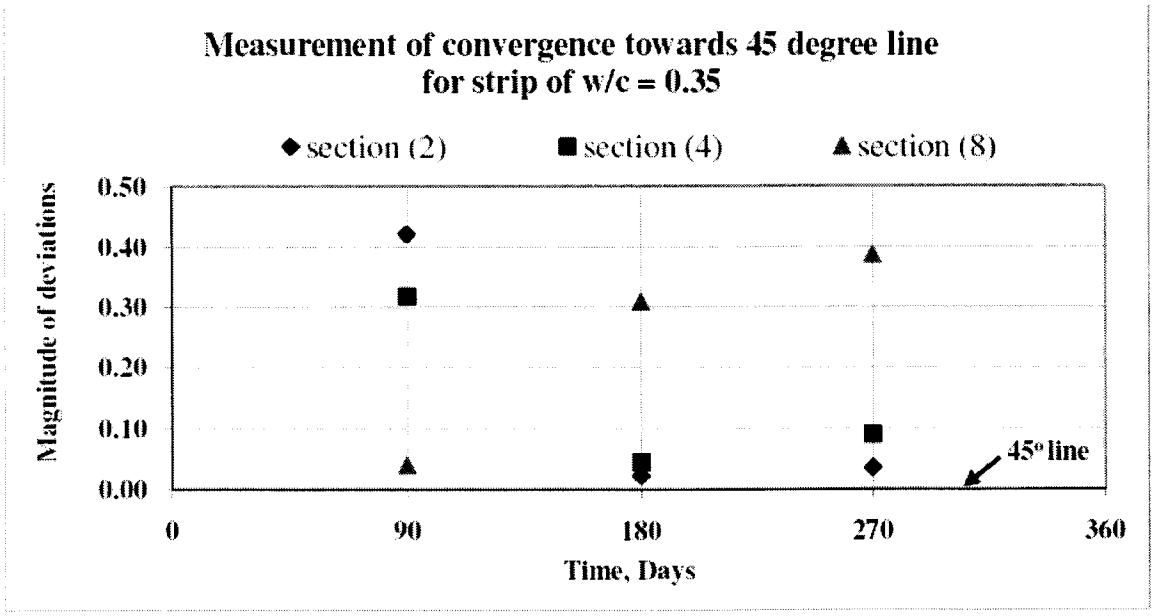

Figure 5.21: Deviations from 45° line with time for strip of w/c = 0.35.

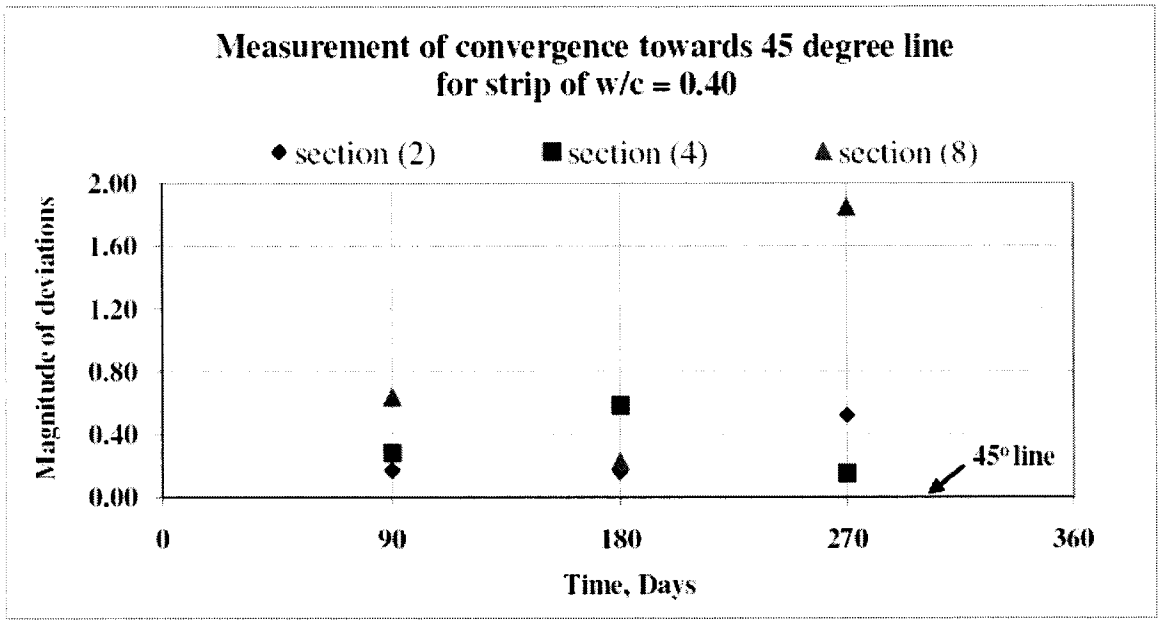

Figure 5.22: Deviations from 45° line with time for strip of w/c = 0.40.

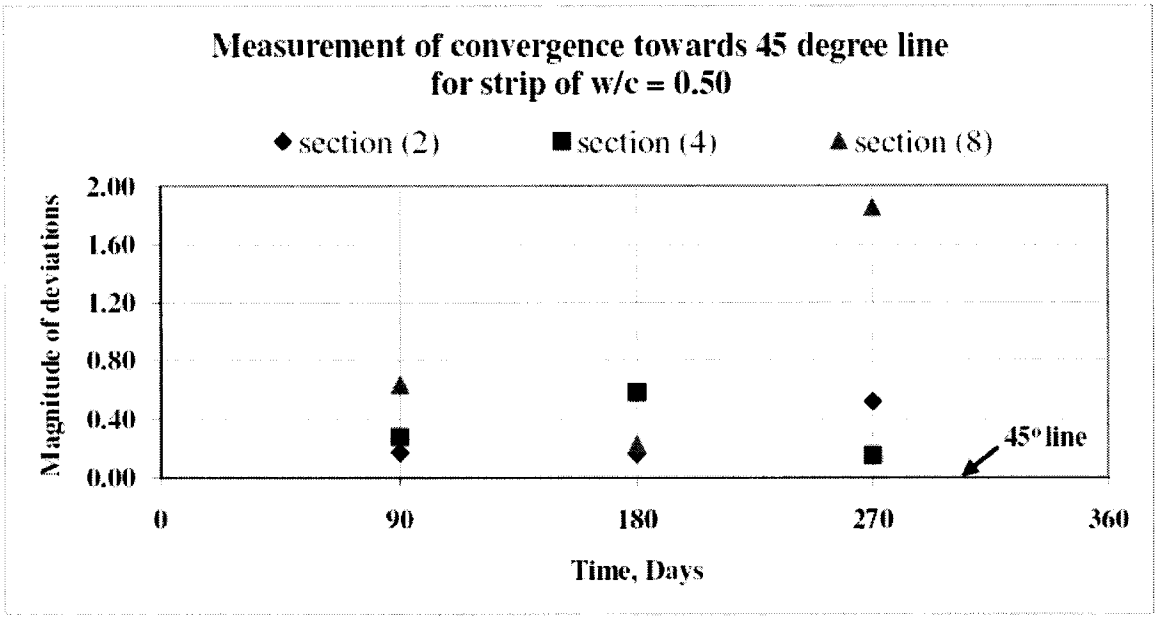

Figure 5.23: Deviations from 45° line with time for strip of w/c = 0.50.

Further analysis was done in order to examine the total chloride content (% by weight of concrete) at the border line where the colour due to $AgNO_3$ spraying changes. The result obtained from this study is compared to three values: (i) 0.2% by weight of cement

as reported in ACI 222, which is equivalent to 0.033%, 0.033, and 0.034% by weight of concrete for strips of w/c = 0.35, 0.4, and 0.5, respectively; (ii) 0.15% by weight of cement as reported by Otsuki et al. (1992), which is equivalent to 0.025% by weight of concrete for all strips; and, (iii) 0.5 % by weight of cement as reported by Otsuki et al. (1992), which is equivalent to 0.082%, 0.083%, 0.084 % for strips of w/c = 0.35, 0.4, and 0.5, respectively. These values of total chloride were substituted into Eq. (2.5), and the corresponding depths were plotted along with those that were measured by the colourimetric method. Figures 5.24, 5.25 and 5.26 show the comparison between the depths measured by the colourimetric method and Eq. (2.5) at the abovementioned chloride concentrations for strips of w/c = 0.35, 0.4, and 0.5, respectively, for the first set of samples. Figures 5.27, 5.28, and 5.29 illustrate this comparison for the second set of samples, whereas Figures 5.30, 5.31, and 5.32 plot the comparison for the third set of samples.

In general, the depths calculated using Eq. (2.5) are higher than those measured by the $AgNO_3$ spray method. Although there are differences between the sections due to differences in w/c and stress levels, as the time of exposure increases, this difference becomes smaller. An exception is section 7, in which flexural cracks permitted the passage of chloride solution through the whole thickness of the slab after the second wet/dry cycle. Among the values used in this comparison, the chloride concentration found by Otsuki et al. (1992) of 0.5 % by weight of cement (0.082, 0.083, and 0.084 % by weight of concrete for w/c = 0.35, 0.4, and 0.5, respectively) represents best the chloride concentration at the boundary of colour change. However, neither Otsuki et al. (1992) nor ACI 222 are able to predict the chloride concentration through actual cracks, as it can be clearly seen in section 7 in Figures 5.27, 5.28, 5.29 and 5.32, where visible cracks were crossing the core samples (see Figure 3.31).

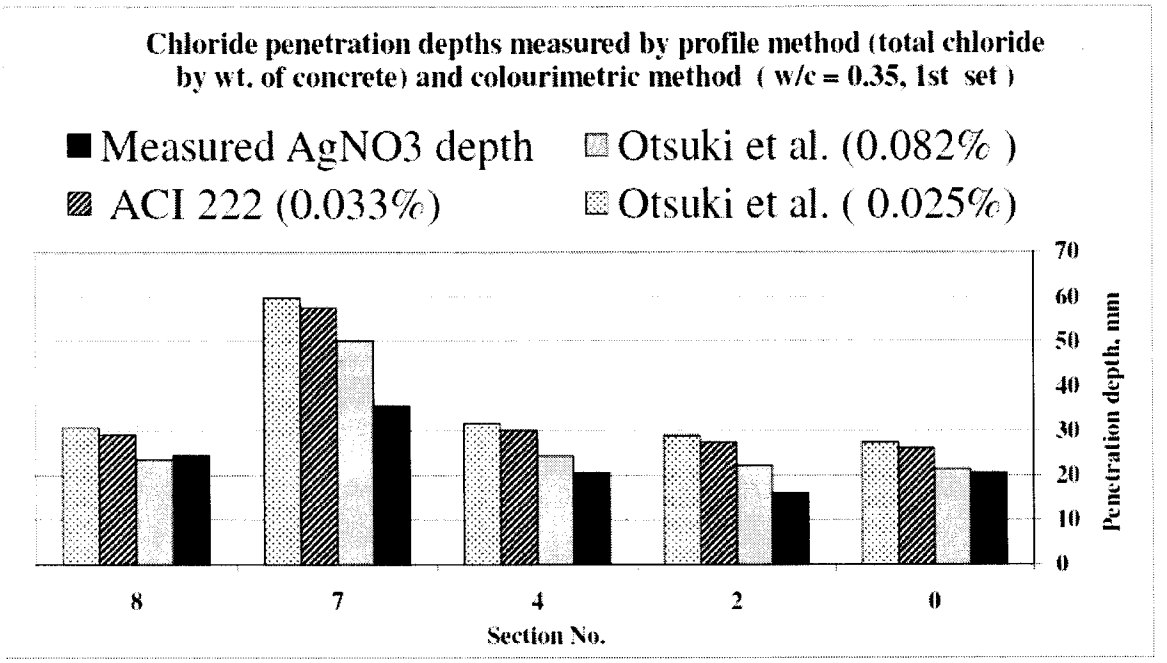

Figure 5.24: Comparison between colourimetric method and Eq. (2.5) at different chloride concentrations for the strip of w/c = 0.35 (1st set).

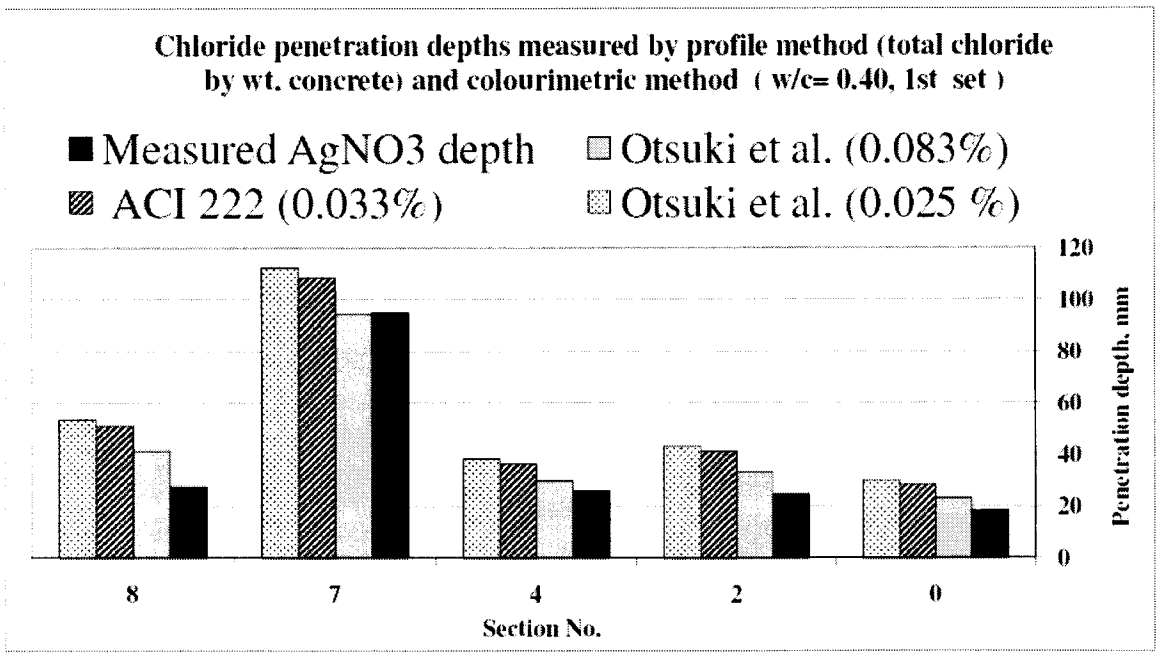

Figure 5.25: Comparison between colourimetric method and Eq. (2.5) at different chloride concentrations for the strip of w/c = 0.40 (1st set).

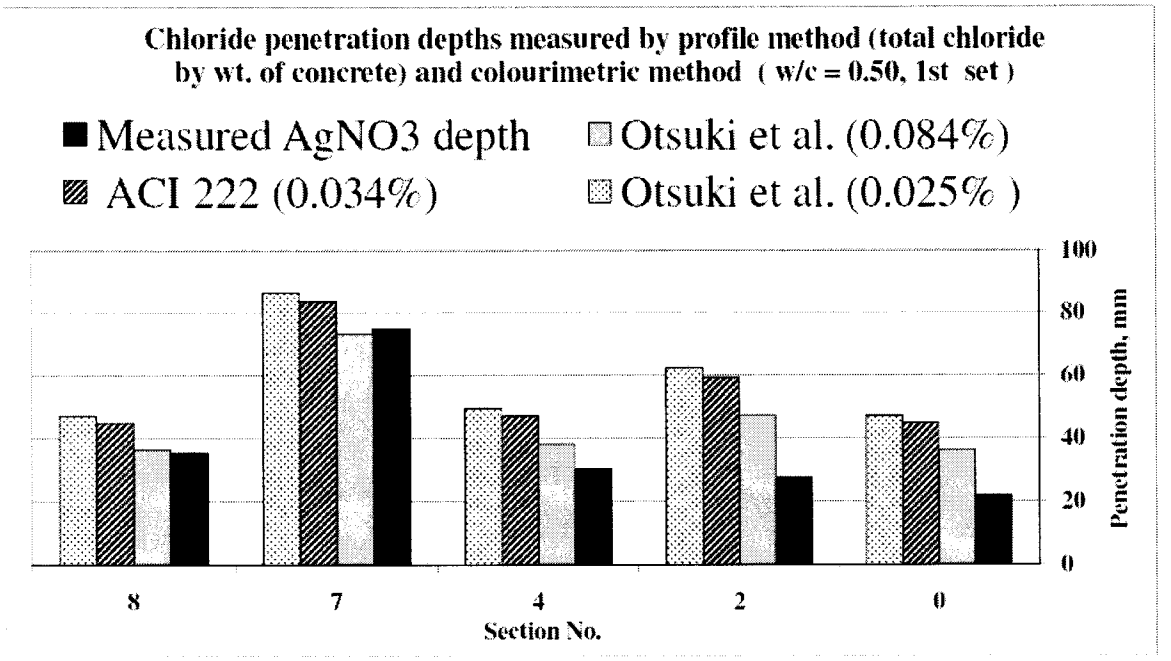

Figure 5.26: Comparison between colourimetric method and Eq. (2.5) at different chloride concentrations for the strip of w/c = 0.50 (1st set).

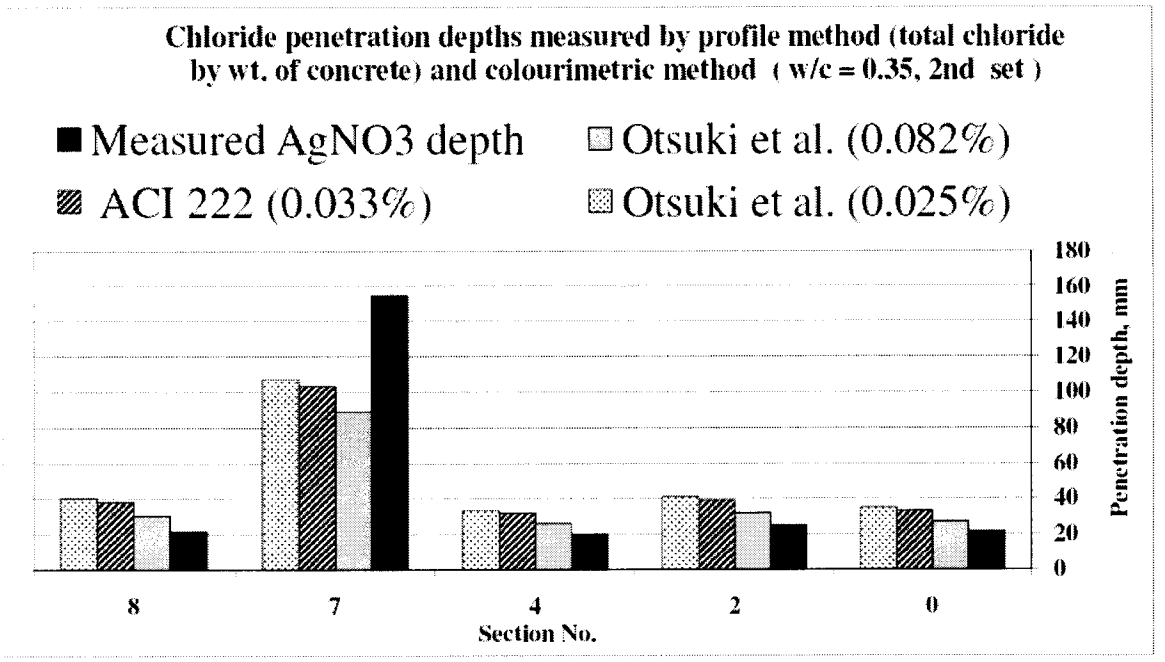

Figure 5.27: Comparison between colourimetric method and Eq. (2.5) at different chloride concentrations for the strip of w/c = 0.35 (2nd set).

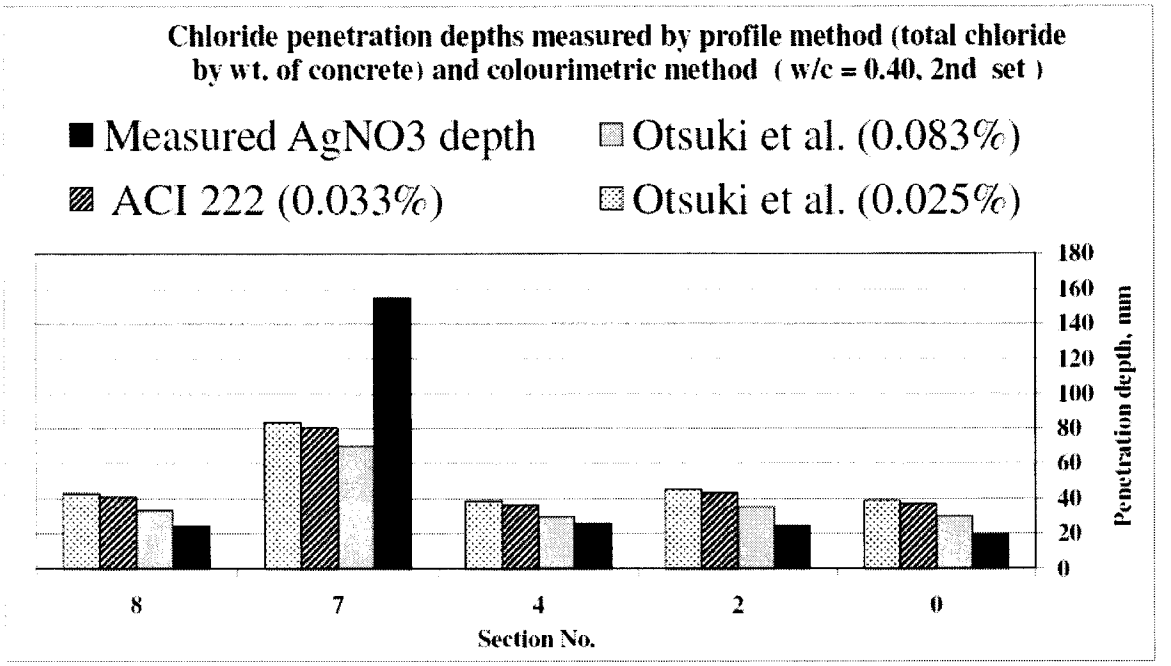

Figure 5.28: Comparison between colourimetric method and Eq. (2.5) at different chloride concentrations for the strip of w/c = 0.40 (2^{nd} set).

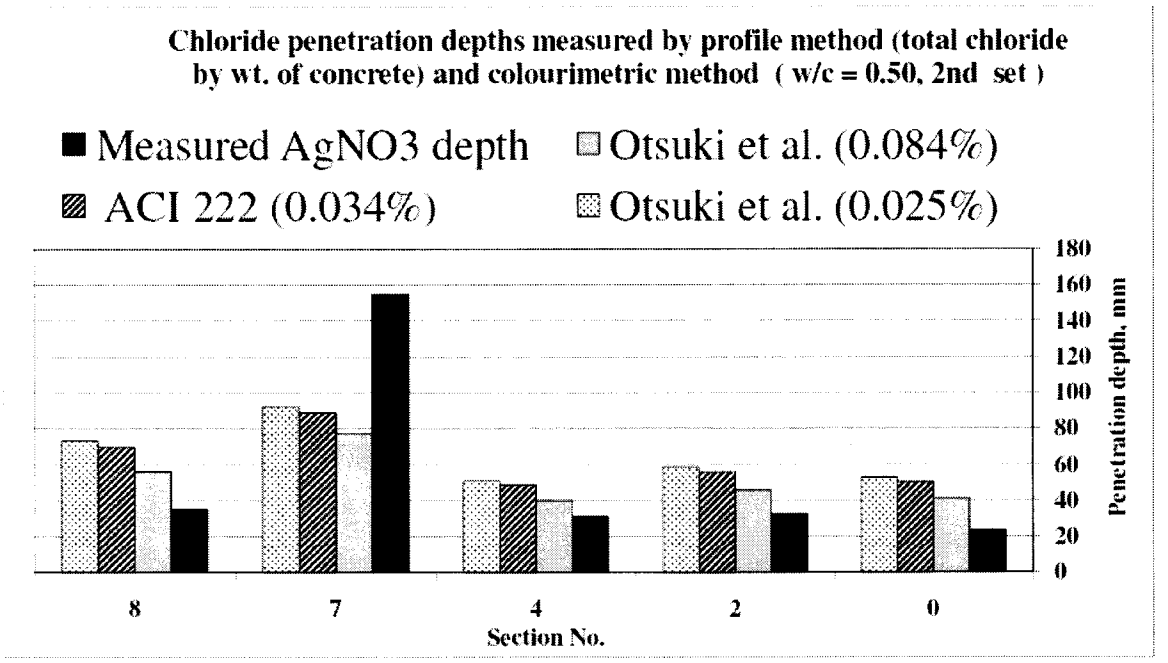

Figure 5.29: Comparison between colourimetric method and Eq. (2.5) at different chloride concentrations for the strip of w/c = 0.50 (2^{nd} set).

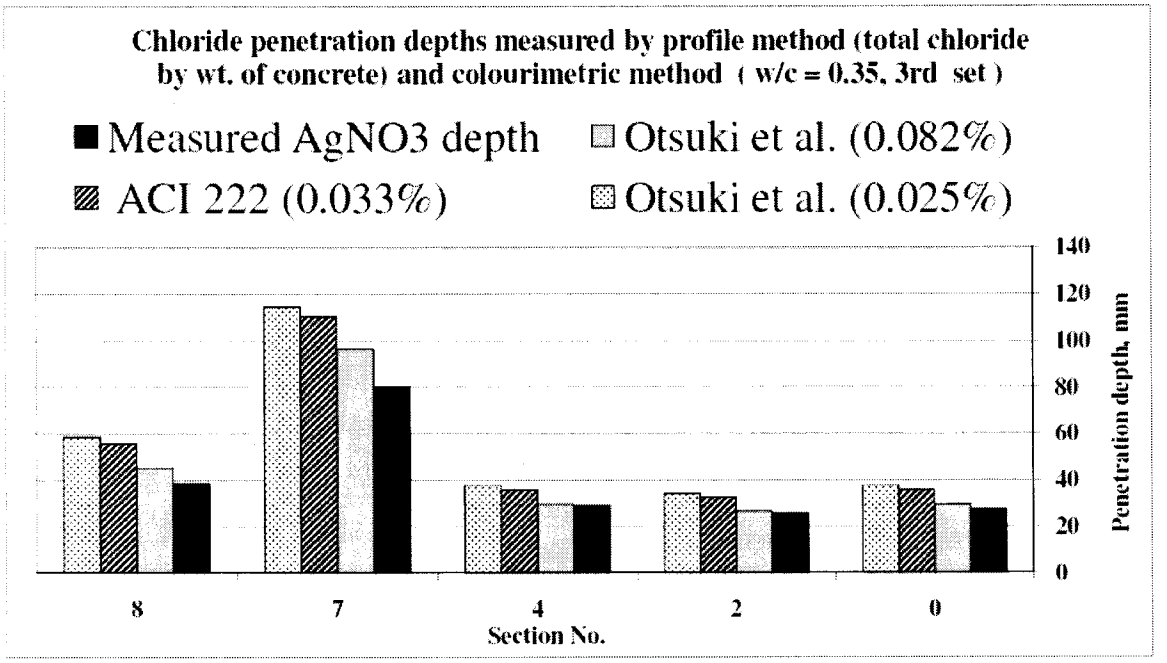

Figure 5.30: Comparison between colourimetric method and Eq. (2.5) at different chloride concentrations for strip of w/c = 0.35 (3rd set).

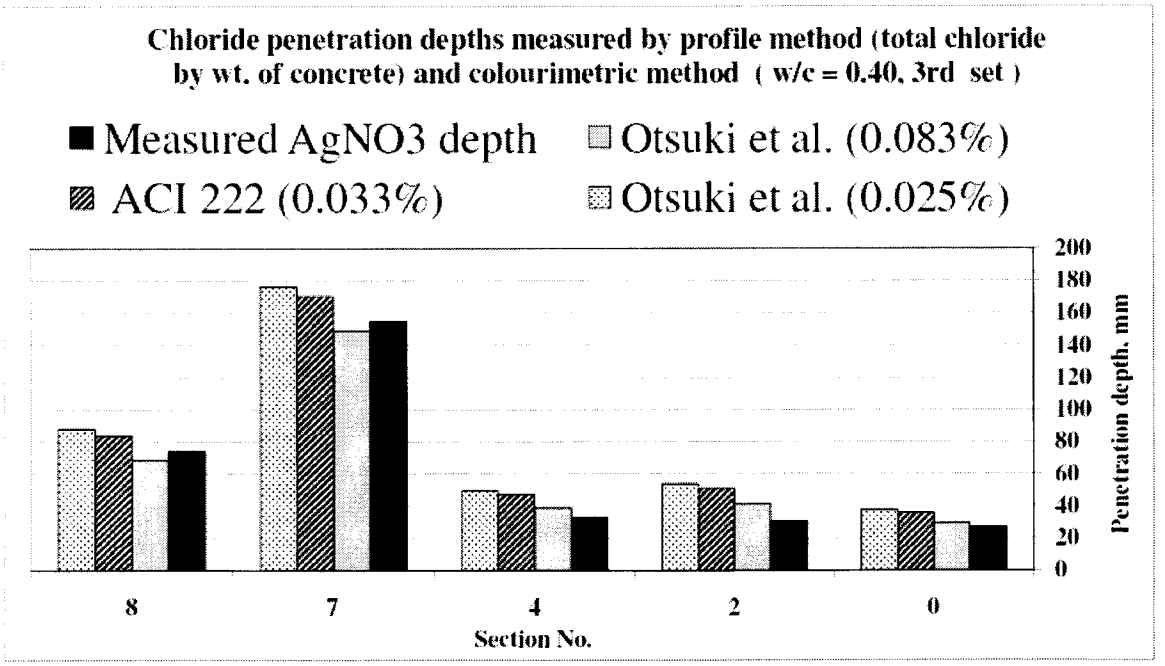

Figure 5.31: Comparison between colourimetric method and Eq. (2.5) at different chloride concentrations for the strip of w/c = 0.40 (3rd set).

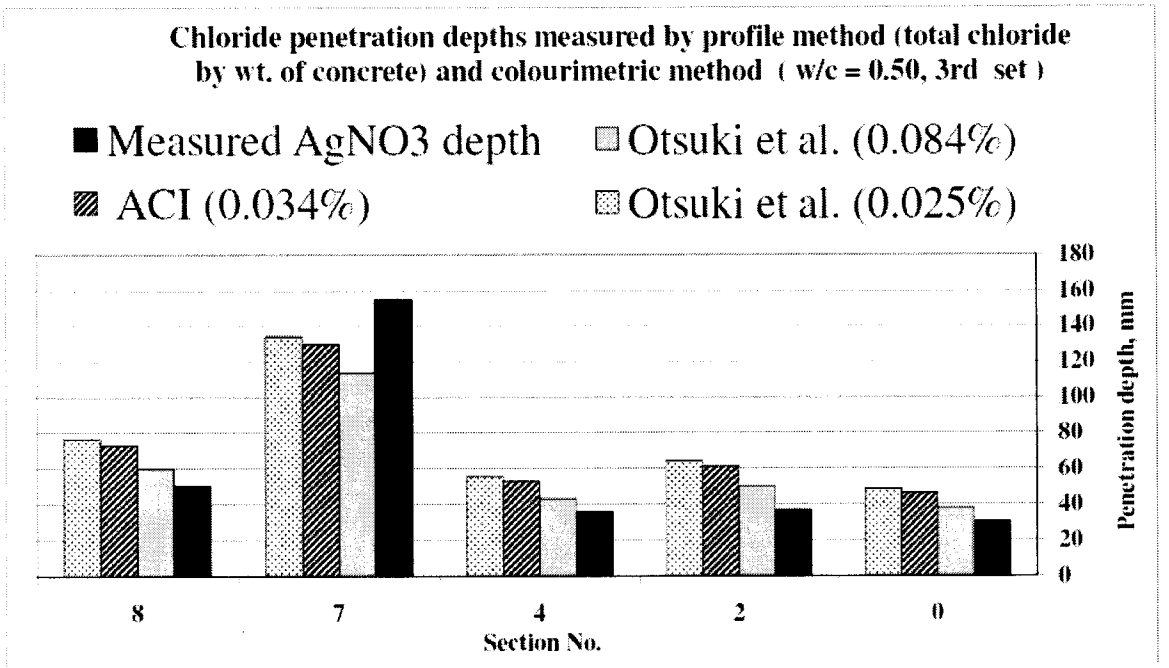

Figure 5.32: Comparison between colourimetric method and Eq. (2.5) at different chloride concentrations for strip of w/c = 0.50 (3rd set).

5.3. Chloride diffusivity as a function of stress state

At first the strain in the concrete induced by the applied loads seems to be the parameter of choice to represent the mechanical state in the concrete and thus relate it to the rate of chloride penetration. However, this approach is limited from a practical point of view, since tensile stresses/strains in the concrete cannot be calculated by elastic bending theory in sections where the applied moment is above that causing cracking. A structural parameter that is easy to calculate instead is the applied bending moment. If this parameter is chosen as the structural indicator influencing the rate of chloride ingress in concrete, there has to be an acceptable correspondence between the strain values experimentally recorded by the electrical strain gauges and those theoretically computed from the applied bending moments. From Figures 4.14 and 4.15, it can be observed that in general there is a good agreement between measured and calculated strain values.

In order to relate the chloride diffusivity to the applied bending moment for each section, the ratio of applied bending moment M to the theoretical cracking moment M_{cr} was plotted against the D_i/D_o ratio, where D_i and D_o denote the apparent chloride

diffusivities of sections *i* and the control section, respectively. The theoretical cracking moments were calculated as 19.8 kN.m, 18.3 kN.m, and 17.7 kN.m for the RC strips of w/c of 0.35, 0.40, and 0.50, respectively. The values of f'_c and modulus of elasticity for all strips are given in Appendix A, and the procedure used to calculate the cracking moment is included in Appendix B. The ratio M/M_{cr} versus D_i/D_o for data obtained from both the colourimetric and potentiometric titration methods after the first wet/dry cycle is plotted in Figures 5.33 and 5.34, respectively. Likewise, the relation of M/M_{cr} against D_i/D_o for data obtained from both the colourimetric and potentiometric titration methods after the second wet/dry cycle is plotted in Figures 5.35 and 5.36, respectively. Finally, Figures 5.37 and 5.38 respectively plot the ratio M/M_{cr} versus D_i/D_o for data obtained from both the colourimetric and potentiometric titration methods after the third wet/dry cycle. Note that the right quadrant of the figures represents values in sections where the top concrete fibre is in compression, whereas the left quadrant of the figures represents values in sections where the top concrete fibre is in tension. The values obtained from section 7 were excluded as the apparent chloride diffusivities obtained correlated poorly to the experimental data (see Tables 5.1-5.3).

By observing the figures, one can notice the following:

1. In general, the chloride diffusivity decreases with time for sections subjected to both tension and compression, and for both sets of data;
2. The ratio of diffusivities decreases by increasing the M/M_{cr} ratio for sections subjected to compressive stresses;
3. On the other hand, this ratio increases by increasing the M/M_{cr} ratio for sections subjected to tensile stresses;
4. With the exception of section 8, the effect of load on the diffusivity ratio decreases as the time of exposure increases.

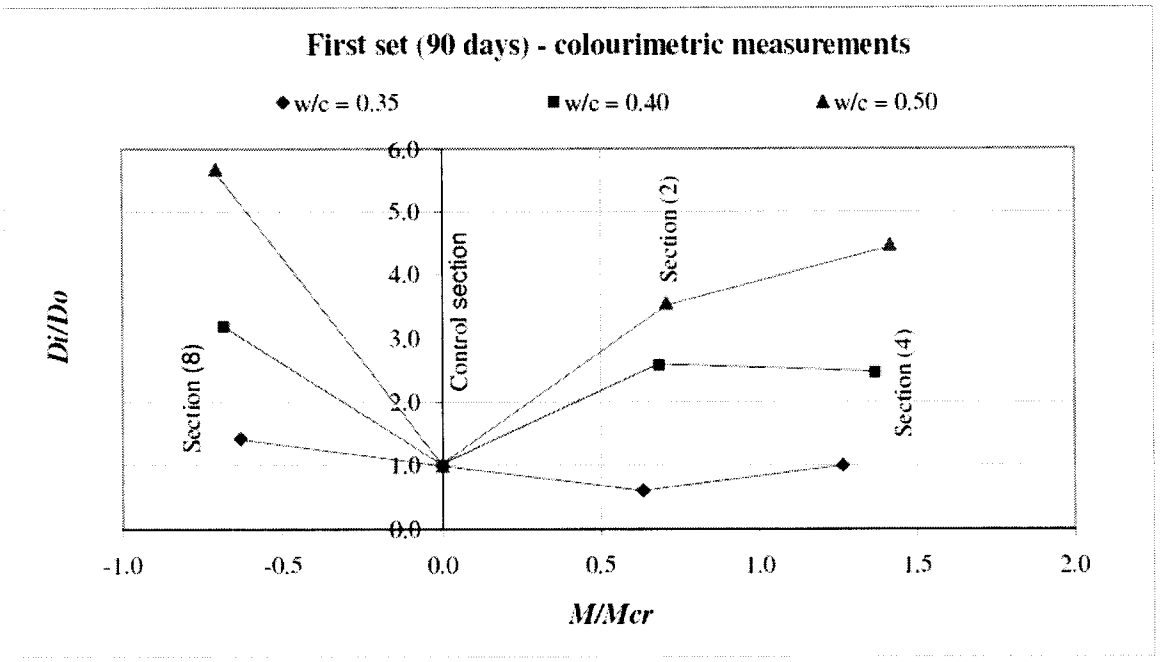

Figure 5.33: D_i/D_o versus corresponding M/M_{cr} for colourimetric method (first cycle).

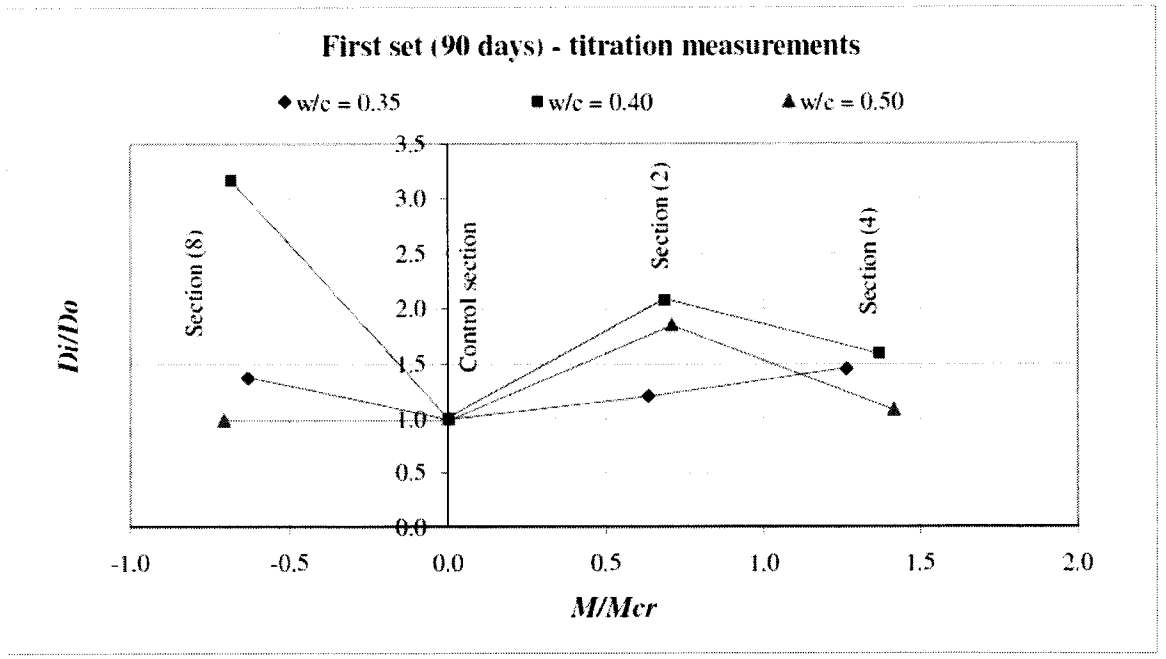

Figure 5.34: D_i/D_o versus corresponding M/M_{cr} for titration method (first cycle).

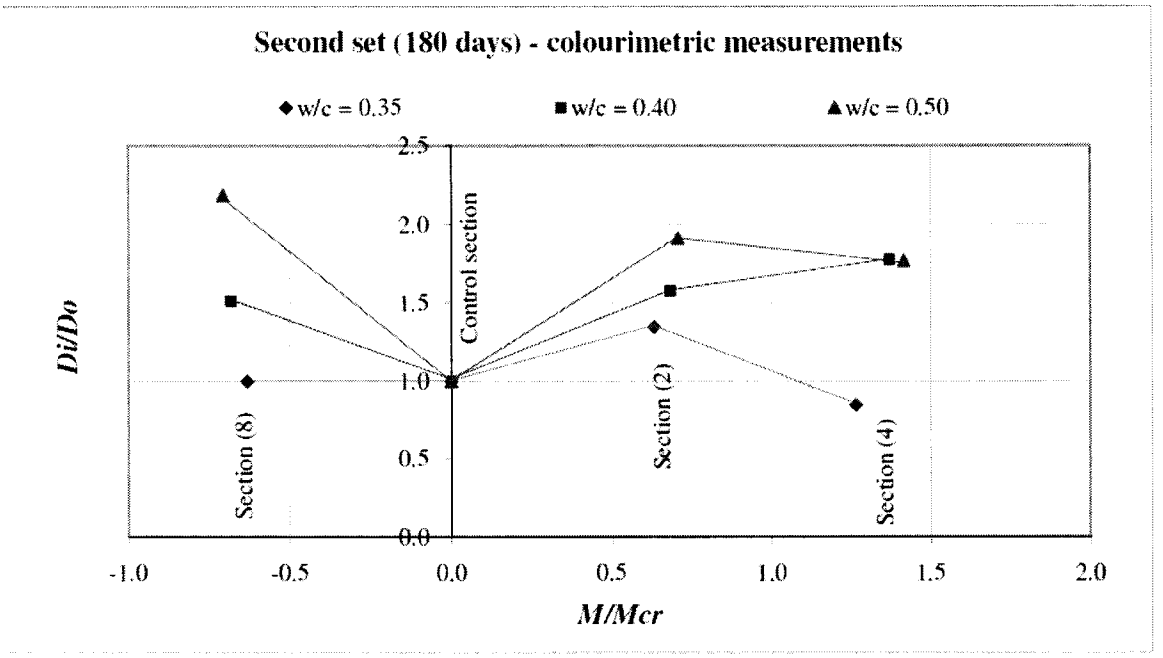

Figure 5.35: D_i/D_o versus corresponding M/M_{cr} for colourimetric method (second cycle).

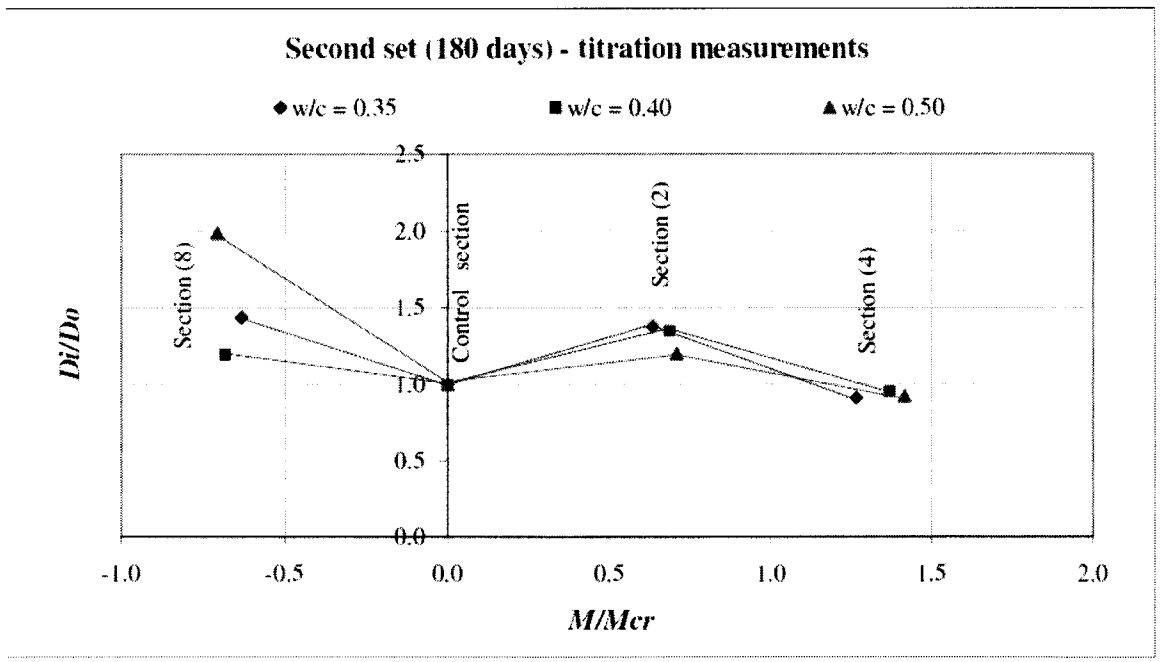

Figure 5.36: D_i/D_o versus corresponding M/M_{cr} for titration method (second cycle).

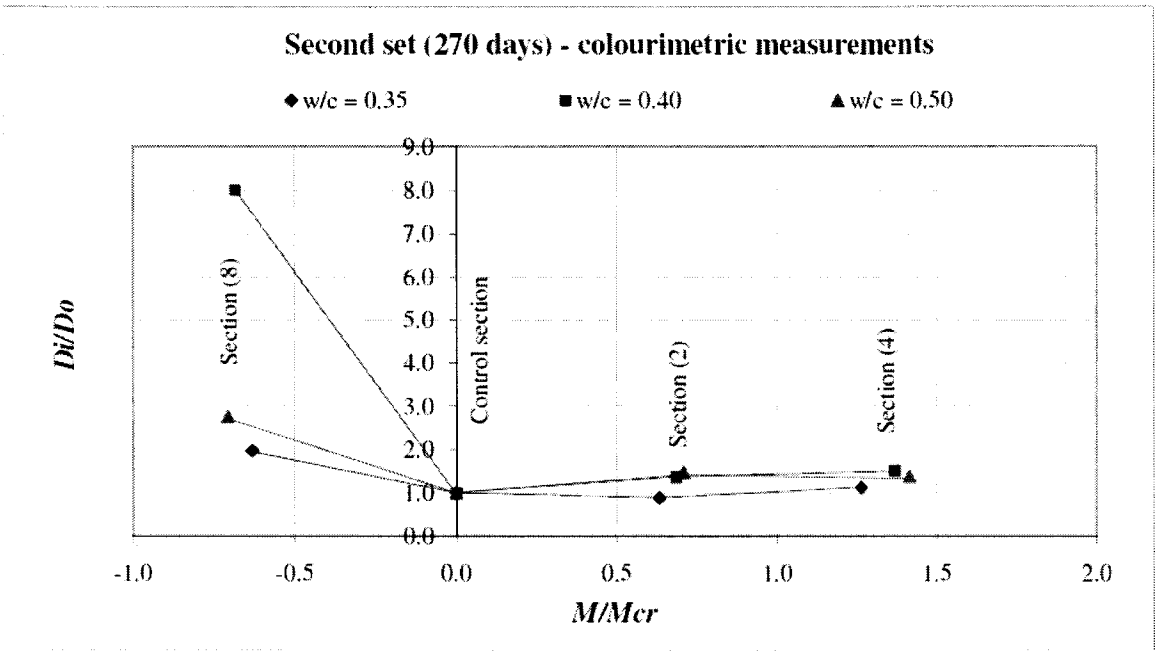

Figure 5.37: D_i/D_o versus corresponding M/M_{cr} for colourimetric method (third cycle).

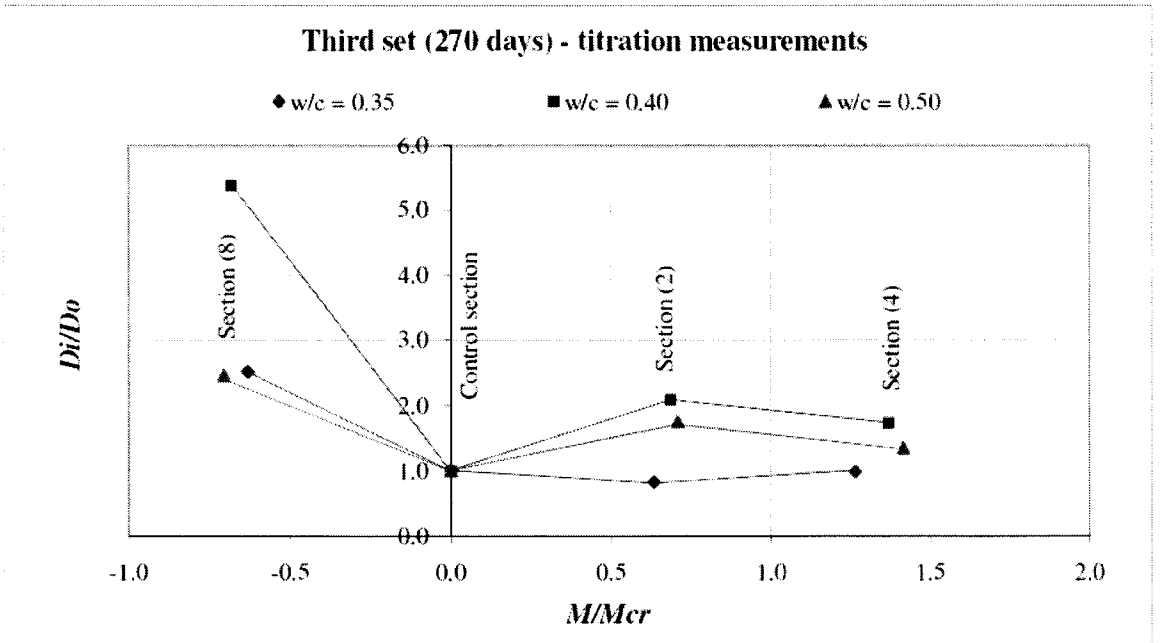

Figure 5.38: D_i/D_o versus corresponding M/M_{cr} for titration method (third cycle).

In order to compare the data in this research with the literature, the model suggested by Konin et al. (1998) and given by Eq. (2.13) was investigated to examine its applicability in the present study. Values used in Eq. (2.13) were the strains measured at the tension zones from strain gauges numbered 11 and 13 (shown in Figure 3.16 and tabulated in Appendix C) and the diffusion coefficients for the unstressed concrete (section 0 for the strip of w/c = 0.35 in this case). The results are presented in Table 5.7. The model proposed by Konin et al. (1998) does not correlate well with the data in this work. Examination of Konin's data reveals that the maximum stress for which their model is applicable was much smaller than the maximum stresses developed in the reinforcing steel of the RC deck. Therefore, this simple calculation reveals that this model needs to be improved for higher ranges of stresses.

Table 5.7: Diffusion coefficients found by Konin et al. and found by titration for strip of w/c = 0.35.

Set #	D_0 (x10^{-12}), (m^2/s) Section (0)	Section (7)			Section (8)		
		Micro-strains	D (x10^{-12}), (m^2/s) (from titration)	D, (m^2/s) by Konin *et al.*	Micro-strains	D (x10^{-12}), (m^2/s) (from titration)	D, (m^2/s) by Konin *et al.*
I	9.27	2011	32.49	-4.82498E+20	576	12.72	-1.13378E+19
II	7.86	2130	53.98	-4.86118E+20	654	11.3	-1.40713E+19
III	5.98	2130	38.89	-3.69845E+20	837	15	-2.24418E+19

5.4. Chloride diffusivity as a function of exposure time

Reported experimental research has shown that the chloride diffusion coefficient decreases with time due to the increase in maturity of the exposed concrete. This time dependency of chloride diffusivity in concrete is considered to be caused by the decrease in capillary porosity due to continuous hydration and by chloride binding to the cement

hydrates (Nilsson et al., 1996). A common expression encountered in the literature to mathematically describe the decay of D with time is given by (Mangat and Molloy, 1994; Bamforth, 1998):

$$D = D_{ref}\left(\frac{t_{ref}}{t}\right)^{m} \tag{5.3}$$

where D_{ref} is the apparent diffusion coefficient determined at time t_{ref}, t is the time of exposure, and m is a constant. The age reduction factor m is dependent on variables such as the type of cementitious materials used and the mixture proportions (Mangat and Molloy, 1994; Bamforth, 1998).

Changes in diffusion coefficients with time were also investigated. Each section was studied individually in order to avoid the effect of loading. The evolution of D_a with time for sections 0, 2, 4, 7, and 8 are presented in Figures 5.39 through 5.43, respectively.

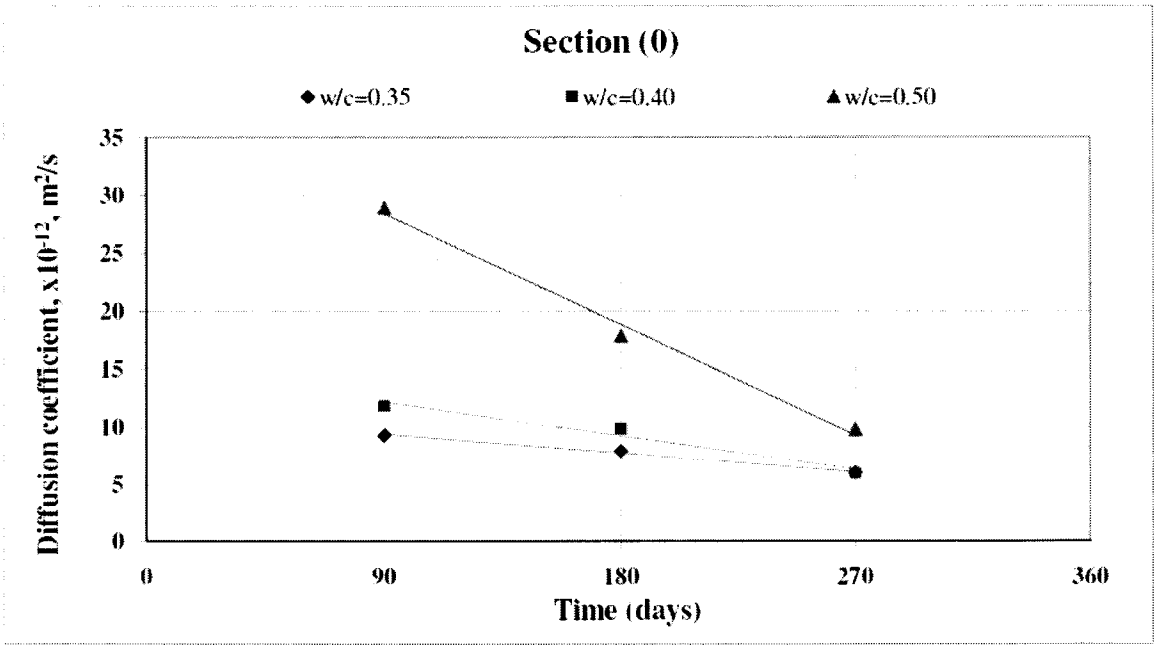

Figure 5.39: Diffusion coefficient versus time for control section for all strips.

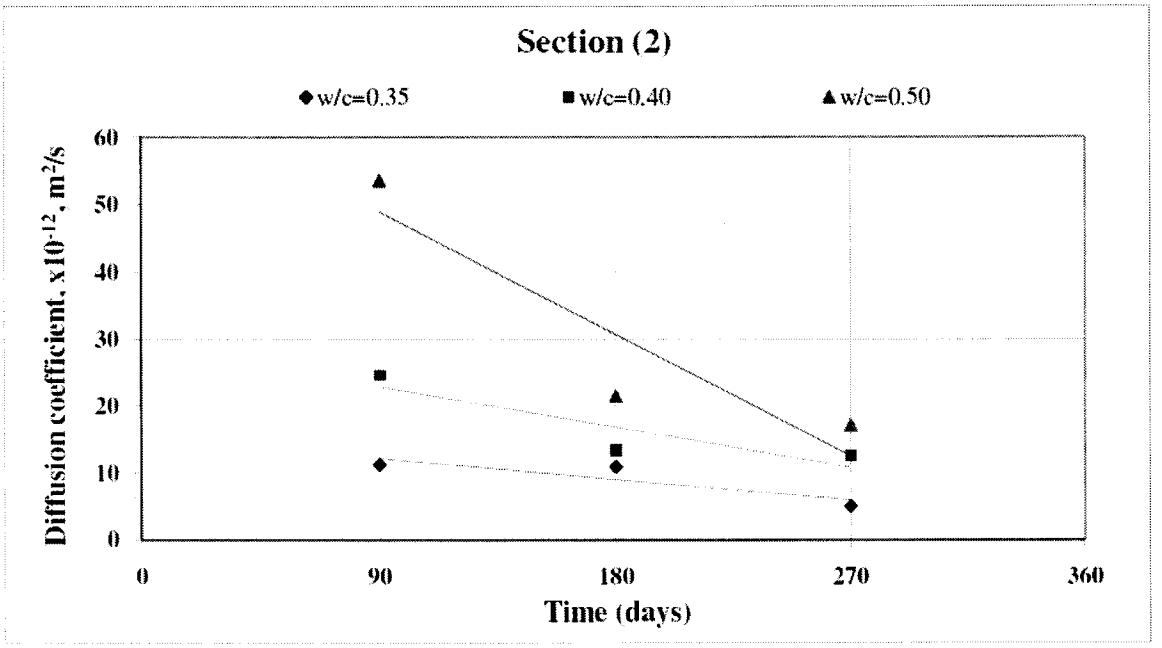

Figure 5.40: Diffusion coefficient versus time for section (2) for all strips.

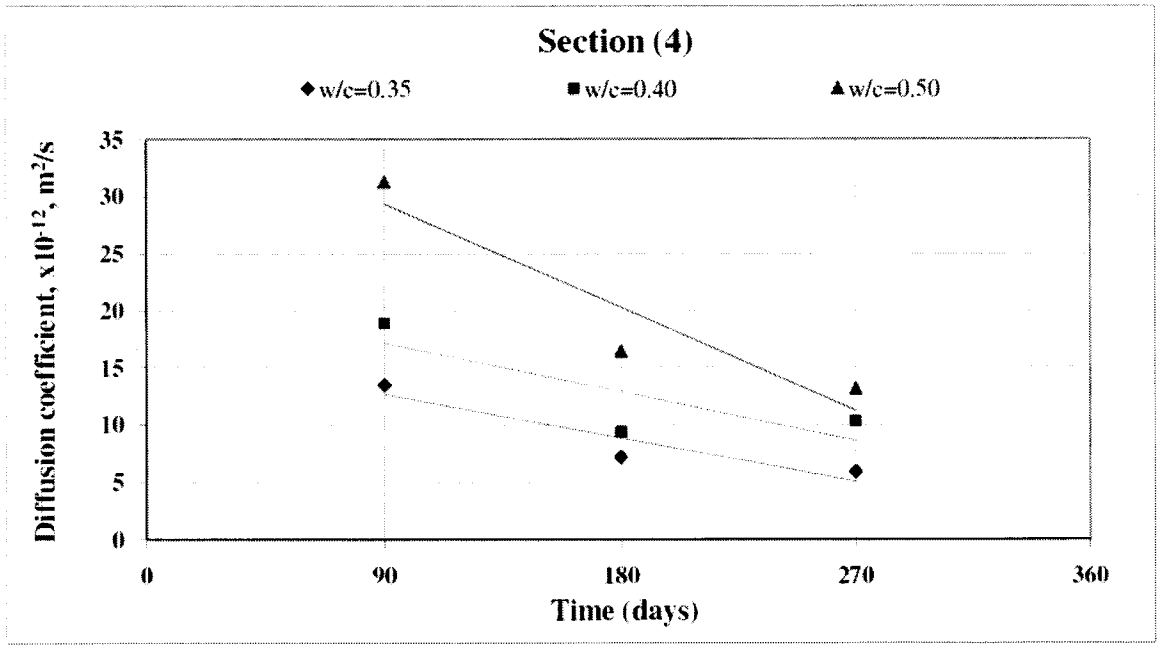

Figure 5.41: Diffusion coefficient versus time for section (4) for all strips.

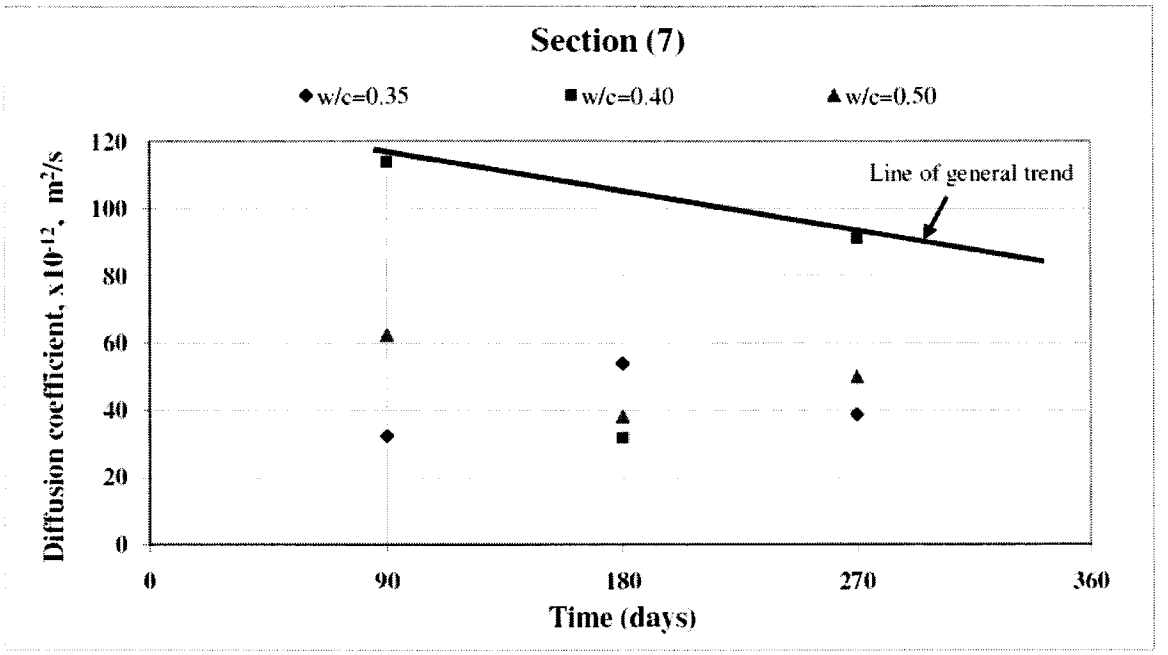

Figure 5.42: Diffusion coefficient versus time for section (7) for all strips.

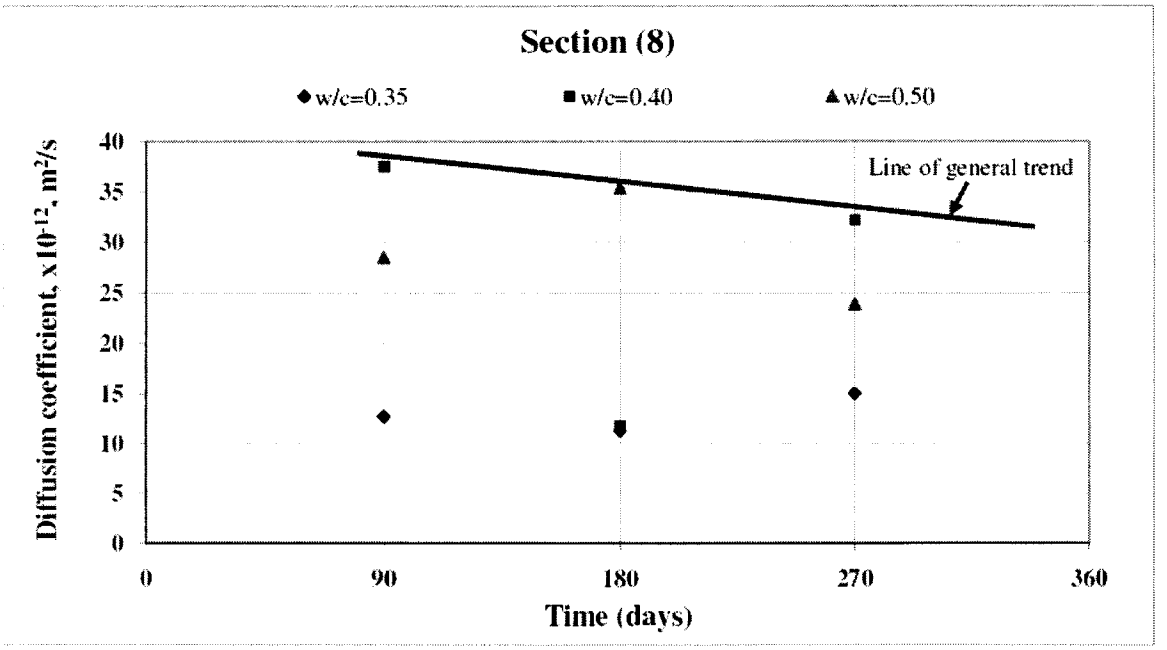

Figure 5.43: Diffusion coefficient versus time for section (8) for all strips.

The data in sections 0, 2, and 4 clearly show the decrease of the diffusion coefficients with time as reported in the literature (Takewaka et al., 1988; Andrade et. al, 2000; Lindvall et al., 2000). The time-dependent decrease of D_a is the lowest for the strip with a w/c of 0.35 and highest for the strip with a w/c of 0.5. The results do not follow the same trend for the sections subjected to tensile stresses; see Figure 5.42 for cracked section 7 and Figure 5.43 for un-cracked section 8.

The data in Figures 5.39, 5.40 and 5.41 suggests that the relation between D_a and time is linear; however, note that this data was obtained within the first year of exposure. It has been shown that this relationship becomes nonlinear as the time of exposure increases, as expressed by Eq. (5.3) (Mangat and Molloy, 1994; Bamforth, 1998; Nokken et al., 2000). However, because the data obtained represents early exposure, it did not correlate well with the expression given by Eq. (5.3).

The effect of time on the average penetration depth data obtained by spraying $AgNO_3$ was also investigated by relating the measured penetration depth X_d of each individual core sample to the square root of the exposure time according to (Baroghel-Bouny, 2007):

$$X_d = A\sqrt{t} + B \tag{5.4}$$

where X_d is the average chloride penetration depth as indicated by the $AgNO_3$ spray (mm), t is the exposure time (days), and A and B are constants. The values of A and B have been determined by fitting the experimental data to Eq. (5.4) and are given in Table 5.8. Figures 5.44, 5.45 and 5.46 plot the average penetration depth X_d with the square root of time for the RC strips of w/c of 0.35, 0.4 and 0.5, respectively.

Table 5.8: Constants and correlation factors from Eq. (5.4).

Section	w/c	A	B	R^2
0	0.35	0.97	10.48	0.83
	0.4	1.11	6.77	0.81
	0.5	1.19	9.62	0.85
2	0.35	1.45	3.30	0.85
	0.4	0.79	16.3	0.65
	0.5	1.33	14.83	1.00
4	0.35	1.16	7.99	0.63
	0.4	0.89	16.29	0.71
	0.5	0.73	22.75	0.83
8	0.35	1.88	3.58	0.53
	0.4	6.36	41.40	0.62
	0.5	2.01	13.82	0.64

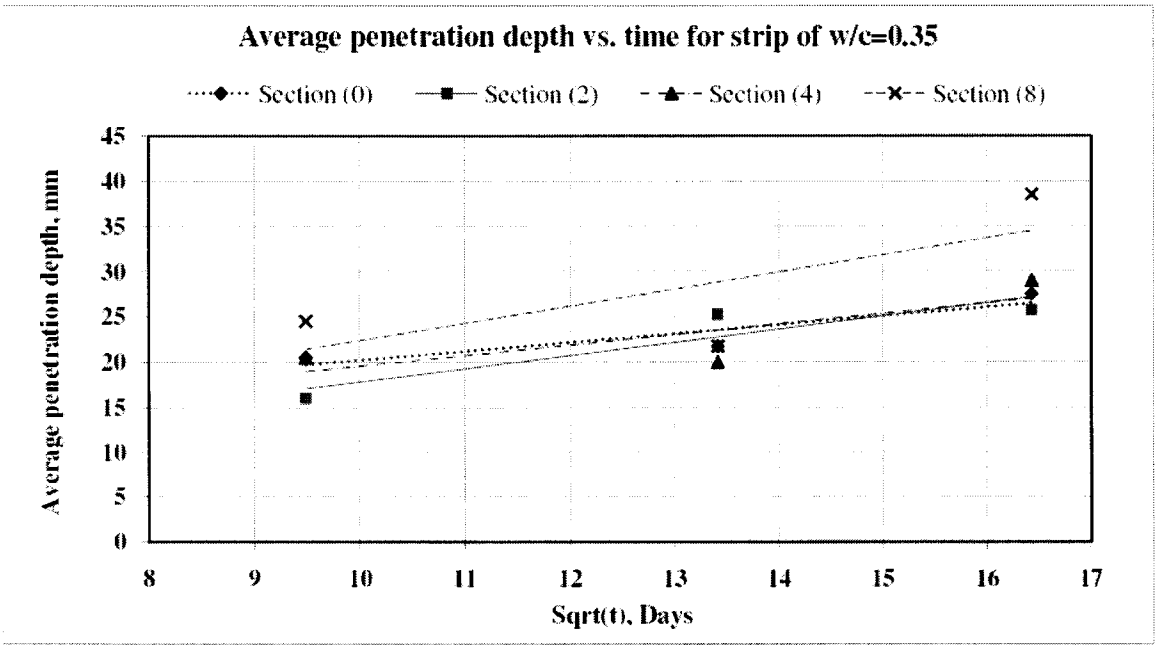

Figure (5.44): Average penetration depth X_d versus time for the RC strip of w/c = 0.35.

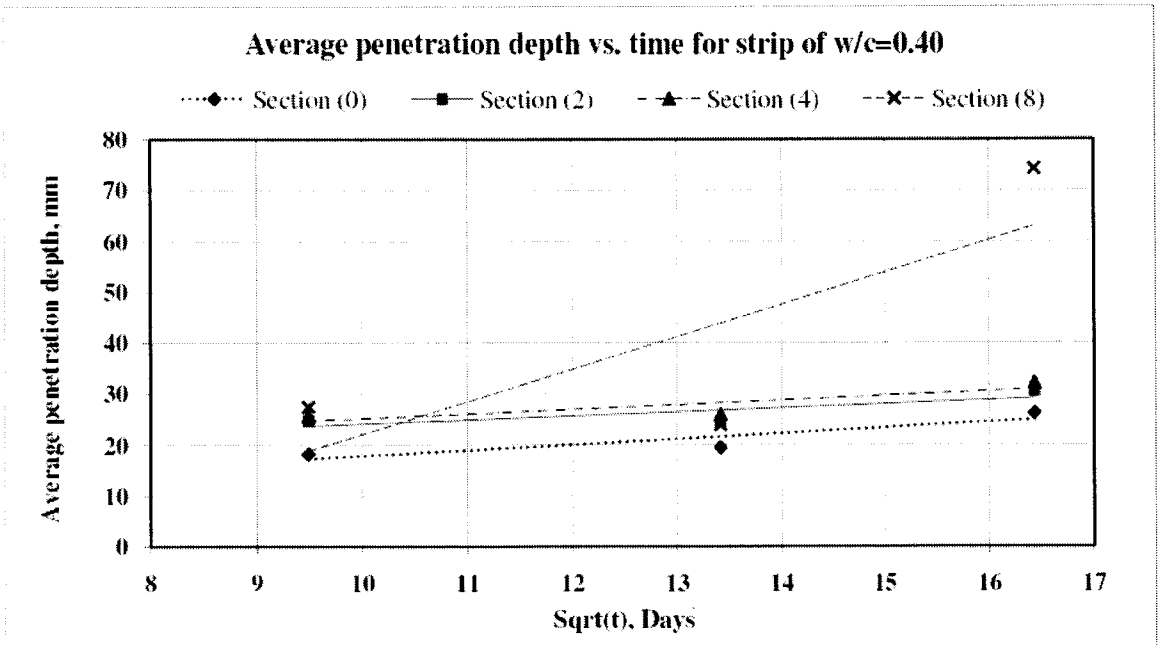

Figure 5.45: Average penetration depth X_d versus time for the RC strip of w/c = 0.40.

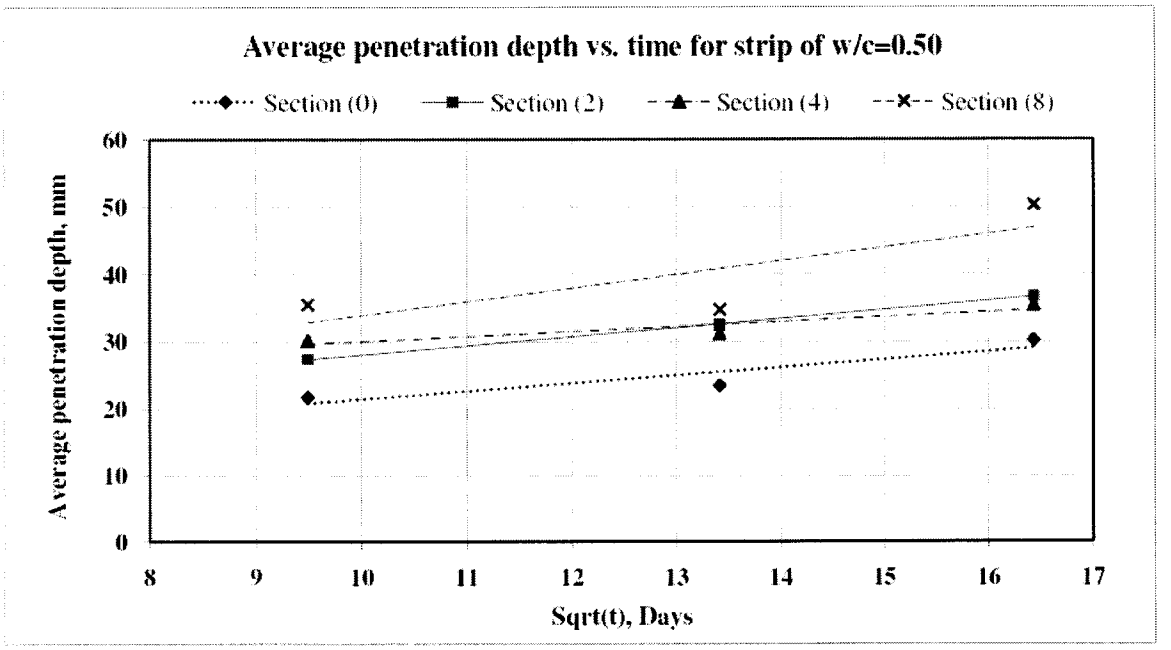

Figure 5.46: Average penetration depth X_d versus time for the RC strip of w/c = 0.50.

5.5. Chloride diffusivity as a function of w/c

The diffusivity of chloride ions in concrete depends on the composition of the concrete. The water-to-cement ratio, or w/c, is one of the decisive parameters, as it affects the resulting capillary porosity of the hydrated cement matrix. Another parameter is the ability of the cement matrix to bind chloride ions. In this section, the chloride diffusivity data obtained in Section 5.2.1 is analyzed as a function of the three w/c of the RC slab. Since the three strips in the RC slab were made with the same type and amount of cement, the effect of the binding capacity of the cement matrix cannot be evaluated here.

Figures 5.47, 5.48 and 5.49 respectively plot the chloride diffusion coefficients against the w/c for each individual section after each wet/dry cycle. With the exception of sections 7 and 8, the value of the chloride diffusion coefficient increases with the increase of w/c as expected (Hobbs, 1999). Concretes with a higher w/c have a higher degree of porosity at a given maturity age. In section 7, where the concrete cover is cracked as a result of the applied load, the rate of chloride ingress is mainly governed by the crack characteristics (width, depth, tortuosity) rather than by the concrete quality as given by the w/c.

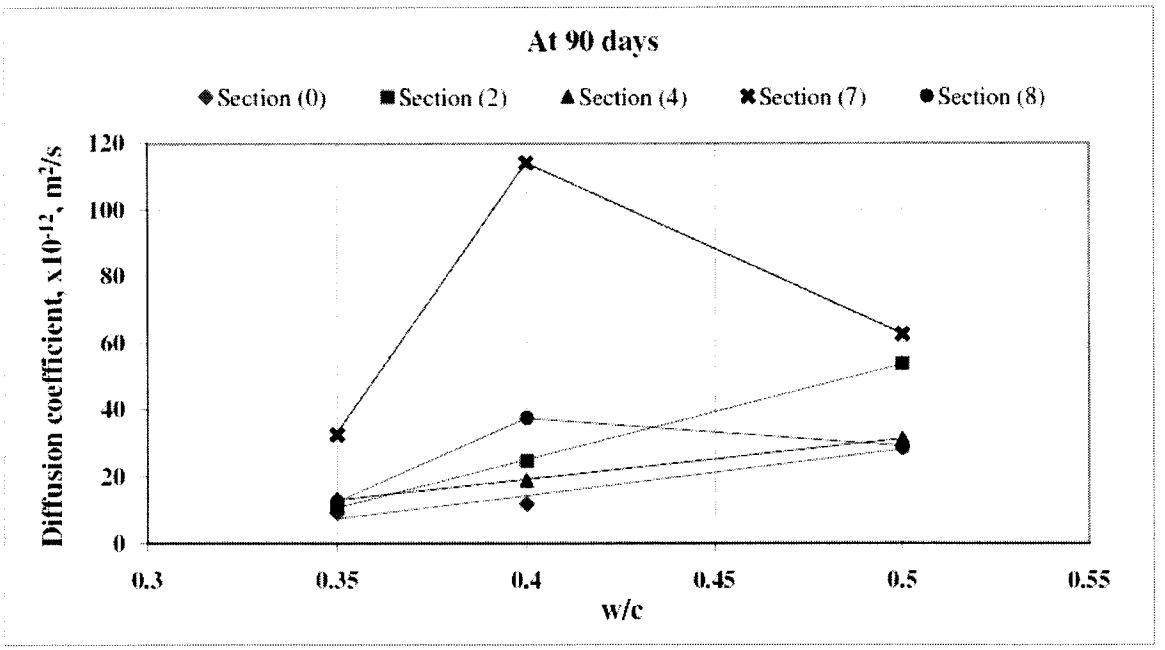

Figure 5.47: Diffusion coefficient versus w/c ratio after 90 days of exposure.

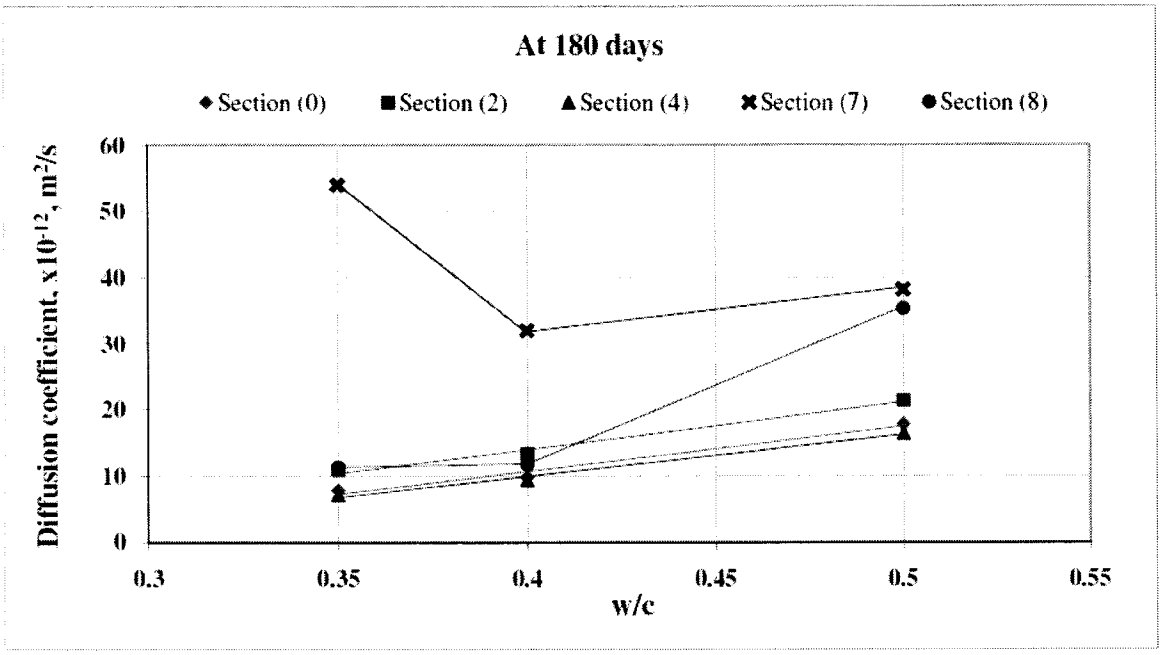

Figure 5.48: Diffusion coefficient versus w/c ratio after 180 days of exposure.

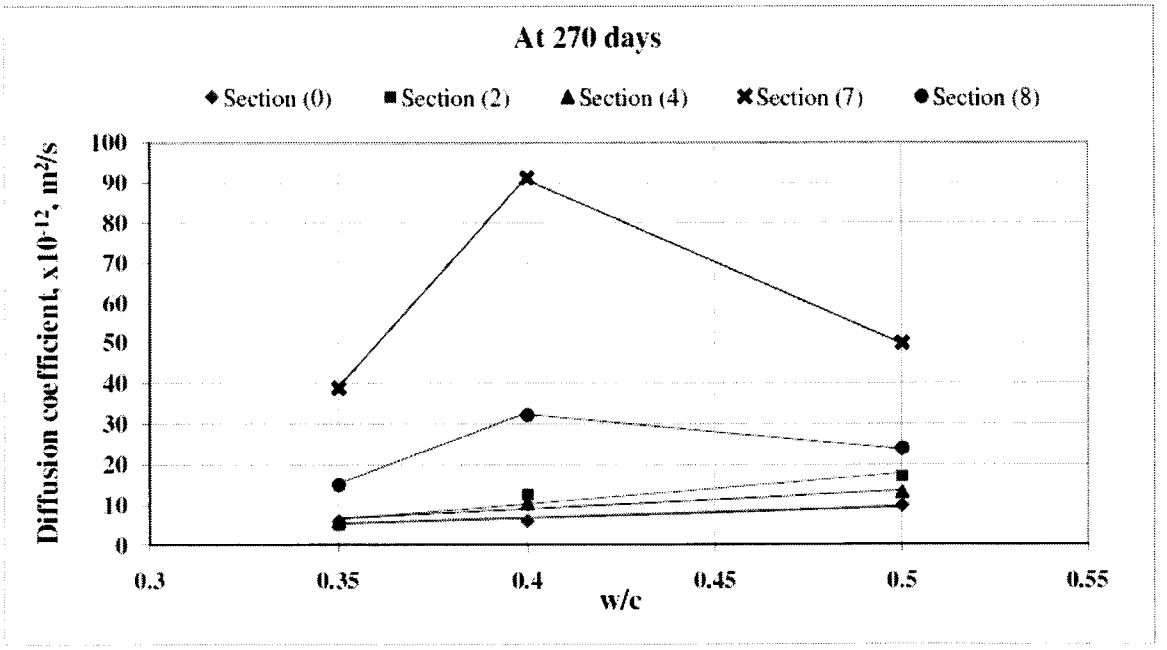

Figure 5.49: Diffusion coefficient versus w/c ratio after 270 days of exposure.

The dependence of the diffusion coefficient on the w/c for uncracked concrete can be expressed as:

$$D = \left[\alpha\left(w/c\right) + \beta\right] \times 10^{-12} \tag{5.5}$$

where D is the diffusion coefficient (m^2/s), w/c is the water-to-cement ratio, and α and β are constants. The values of α and β have been determined for sections 0, 2, and 4 and are given in Table 5.9 along with the corresponding coefficients of determination R^2. A linear relationship as described by Eq. (5.5) gives a good description of the change in D with w/c.

Table 5.9: Constants and correlation factors in Eq. (5.5).

Time	Section	α	β	R^2
1st cycle	0	136.6	-40.20	0.96
	2	284.0	-88.50	1.00
	4	119.9	-28.70	1.00
2nd cycle	0	68.2	-16.60	0.98
	2	71.8	-14.80	0.99
	4	63.1	-15.30	0.99
3rd cycle	0	27.0	-4.00	0.89
	2	78.0	-20.10	0.90
	4	45.4	-9.10	0.90

Chapter 6

Closure

6.1. Summary and conclusions

The purpose of the present work is to investigate the effect of sustained loads on the mechanisms of chloride ingress into RC. To achieve those objectives, an experimental program was established in which a 4.35-m long by 2.73-m wide RC slab was chosen as the test specimen. The slab was cast with three 0.91-m width strips of different w/c (0.35, 0.40 and 0.50), and it was designed as a one-way slab. Each RC strip was loaded by means of three threaded steel bars, and supports were located to create different loading conditions such as pure bending moments and a mix of shear and bending tensile and compressive stresses. The applied loads corresponded to 60% of the ultimate moment capacity of the slab.

Strains were measured by means of electrical strain gauges that were fixed on the top and bottom steel reinforcing bars and on the top and bottom of the concrete surface. In addition, six distributed Brillouin fibre sensors, two for each RC strip with one at the top surface and the other at the bottom surface, were continuously glued to measure the compressive and tensile strain distributions resulting from the applied load. Regular de-icing salt was spread uniformly all over the deck surface forming a layer of thickness ranging from 30 to 50 mm. During the wetting cycle, the deck was sprayed with water until it reached a depth of approximately 50-60 mm. The resulting chloride solution was in a saturated condition. Concrete cores were taken at different sections of different levels of straining. Colourimetric and potentiometric titration methods were used to detect average chloride penetration depths and profiles after three cycles of wetting and drying; each cycle of wetting and drying was 90 days.

From the analysis of the results, the following conclusions can be drawn:

1. The chloride transport into concrete in this study was assumed to be one-dimensional in a semi-infinite medium, complying with Fick's 2nd law of pure diffusion. The results obtained from the potentiometric titration method showed that the diffusion coefficient obtained by non-linear fitting of the chloride profiles is affected by the stress level and type. Also, the diffusion coefficient is affected by whether the exposed concrete surface is subjected to tension or compression. Obviously, higher diffusion coefficients were obtained for un-cracked tension zones, and much higher in cracked zones. According to the results, the diffusion in concrete containing cracks does not follow Fick's law.

2. In using the colourimetric method, an average penetration depth was chosen by drawing two parallel lines to the exposed surface, which respectively represent the minimum and maximum depths. Some useful relationships were obtained where the penetration depth was related to the square root of time for sections 0, 2 and 4. The results for sections under tensile stresses could not be correlated to such expressions.

3. The penetration rate increases with concrete micro-cracking as was shown clearly in core samples retrieved from section 8 (uncracked under tension).

4. Excluding section 7, there are good agreements between the colourimetric and titration methods. In both methods, the existence of tension at the exposed surface is obvious. Some general relationships that relate relative diffusivities in the two methods were obtained. Relative diffusivity in the colourimetric method is the square of the ratio between the chloride penetration depth of the section under consideration (subjected to loads) to that in the unloaded section, whereas the relative diffusivity in the potentiometric method is the ratio between the diffusion coefficient obtained by fitting the chloride profile of the section under consideration to that of the unloaded section. Also, both methods are in agreement regarding to the data obtained from the cracked section. Moreover, a relationship between the colourimetric and potentiometric methods was obtained in which the relative diffusivity of both methods was plotted. This relationship revealed that the colourimetric method can be practically used provided that the concrete is exposed to chloride for at least one year. In the equation $(x_i/x_o)^2 = D_i/D_o$, x_i and x_o can be obtained simply from the relations

that relate chloride penetration to the square root of time, or in case of poor correlation factors, core samples can be taken and sprayed with $AgNO_3$; D_o can be known as there are tremendous amount of literature and numerical models that can predict the diffusion coefficient for unloaded concrete. Having that, the diffusion coefficient for a particular concrete for a particular period of time can be estimated. By doing so, chloride concentration can be easily monitored and consequently the time to the onset of corrosion can be estimated assuming that the exposure conditions are similar.

5. The ratio of diffusivities between stressed and unstressed sections was related to the ratio of applied bending moment to that corresponding to cracking. Again, similar curve trends were obtained from the results of both the colourimetric and titration methods. Higher ratios were obtained for sections subjected to tensile stresses. In general, the ratios corresponding to sections subjected to shear stresses as well as compressive stresses were higher than those corresponding to sections subjected to compressive stresses alone. As previously noted, the results of the two methods converge with time.
6. Relations were obtained that relate the chloride diffusion coefficient with time and w/c. The diffusion coefficient decreases with increasing time of exposure, as observed from the results of both the colourimetric and titration methods. Furthermore, low w/c reduces the penetration of chloride ions into concrete.
7. Despite of the existence of many factors that affect the results in the present study, the results can be considered as a part of the data bank in the field of chloride ingress into concrete subjected to mechanical loading.

6.2. Recommendations for future work

According to the gained experience from the present work and the obtained results in this study, the following points are recommended:

Experimental program

Materials:

- When comparing colourimetric results with titration results, it is preferable to carry out titration to quantify free chloride ions, as these are the ones that react with the $AgNO_3$ to form the whitish precipitate.
- In doing comparison studies between different mix designs, it is preferable for the mixes to be identical except that variable which is intended to be compared. This will facilitate the interpretation of the results without the effects of other ingredients.
- Quantification of chloride contents along a crack plane as well as perpendicular to it will clarify chloride transport phenomena in cracked concrete.
- More studies are needed to know the effects of aggregate on the process of chloride ingress into concrete.
- It is recommended to study chloride penetration into masonry, as there are many masonry structures, and it is a form of construction vital in ancient structures.

Chloride exposure regime:

- It is recommended to carry out similar experiments outside the laboratory environment to evaluate real conditions.
- It is preferable for the exposure time to be at least 3 years. Although the time frame is quite lengthy, the work can be continued by subsequent researchers, instead of using accelerated tests that might increase the variables leading to more uncertainties.
- It is recommended to do further studies on chloride ingress into concrete due to splashing and runoff, as these regimes are very common in the field.

Loading:

- It would be interesting to study the chloride ingress into concrete under pure shear and compare the results with that under pure bending moment and under variable bending conditions.

- It is important to study the effect of vibrations/cyclic loads on the chloride ingress into concrete, as reinforced concrete slabs in bridge decks or parking garages are continuously subjected to the transient loading of traffic.

Data collection:

- It is important to take a minimum number of samples subjected to the same conditions to reduce the variability in the results.
- The adoption of accurate crack detection techniques will help relate chloride ingress to actual load-induced damage accumulation in concrete.
- It is recommended to further study the microstructure of the sample, as this will facilitate interpreting the results.

Theoretical aspects

- A general solution to Fick's 2nd law should be used instead of Crank's solution to account for the many processes taking place at the same time.
- Coupling fracture mechanics with the above solution in a numerical model framework will help to further the understanding of the interactions between the formation of mircro- and macro-cracks and chloride ingress.

Miscellaneous

- In the present work, core samples were taken away from reinforcing steel; however, it is recommended to study the phenomena of chloride ingress in regions where rebars are present.
- It is recommended that a data base of chloride ingress studies, either from laboratory experiments or fields investigations, be built to provide a source of data for chloride ingress models.

Bibliography

ACI Committee 222. (2001). "Protection of Metals in Concrete Against Corrosion." ACI 222R-01, American Concrete Institute.

ACI Committee 224. (2007). "Causes, Evaluation and Repair of Cracks in Concrete Structures." ACI 224.1R-07, American Concrete Institute.

Andrade, C., Sagrera, J., and Sanjuán, M. (2000).Several years study on chloride ion penetration into concrete exposed to Atlantic Ocean water. *Second international RILEM workshop on testing modeling the chloride ingress into concrete*. Edited by C. Andrade and J. Kropp. 11-12 September, Paris, France. 121-134.

ASCE. (2009). "Report Card for America's Infrastructure." <www.asce.org/reportcard> (January 18, 2010).

ASTM C 114-07. (2007). *Standard Test Methods for Chemical Analysis of Hydraulic Cement*. ASTM International, West Conshohocken, PA.

ASTM C 1152/C 1152M-04. (2004). *Standard Test Method for Acid-Soluble Chloride in Mortar and Concrete*. ASTM International, West Conshohocken, PA.

Atkins, C., Carter, M., and Scantlebury, J. (2001). "Sources of error in using silver/silver chloride electrodes to monitor chloride activity in concrete." *Cement and Concrete Research.* **31**, 1207– 1211.

Bamforth, P. B. (1998) "Spreadsheet model for reinforcement corrosion in structures exposed to chlorides." In *Concrete Under Severe Conditions 2: Environment and Loading*, Vol. 1 (Eds, Gjørv, O. E., Sakai, K. and Banthia, N.) London, pp. 64-75.

Baroghel-Bouny, V., and Maultzsch, M. (2007). "$AgNO_3$ spray tests: advantages, weaknesses, and various applications to quantify chloride ingress into concrete. Part 1: Non-steady-state diffusion tests and exposure to natural conditions." *Materials and Structures*, **40**, 759–781.

Ben Romdhane, M. R., and Ulm, F. J. (2002). "Computational mechanics of the steel-concrete interface." *International Journal for Numerical and Analytical Methods in Geomechanics*, **26**(2), 99-120.

Bentur, A., Diamond, S., and Berke, N. S. (1997). *Steel Corrosion in Concrete: Fundamentals and Civil Engineering Practice*, E & FN Spon, London, UK.

Chen, W. (1998). "Cracking damage assessment of reinforced concrete members." *Proc. Natl. Sci. Counc. ROC(A).* **22**(6). 765-774.

Claisse, P. (2005). "Transport properties of concrete." *Concrete International*, **27**(1), 43-48.

Climent, M., Viqueira, E., de Vera, G., and López-Atalaya, M. (1999). "Analysis of acid-soluble chloride in cement, mortar, and concrete by potentiometric titration without filtration steps." *Cement and Concrete Research*, **29**, 893–898.

Climent, M., de Vera, G., Viqueira, E., and López-Atalaya, M. (2004). "Generalization of the possibility of eliminating the filtration step in the determination of acid-soluble chloride content in cement and concrete by potentiometric titration." *Cement and Concrete Research*, **34**, 2291–2295.

Cousin, B., Deif, A., and Martín-Pérez, B. (2009). "Étude de l'intrusion d'ions chlorures dans des ouvrages en béton armé sous charge." XXVIIèmes Rencontres de L'Association Universitaire de Génie Civil (AUGC), 3, 4 et 5 juin, Saint-Malo, France.

Crank, J. (1975). *The Mathematics of Diffusion* (2nd ed.). London: Oxford University Press. (414 pp.)

CSA A23.1-04. (2004). *Concrete materials and methods of concrete construction.* Canadian Standards Association, Mississauga, ON, Canada.

CSA A23.3-04. (2004). *Design of concrete structures.* Canadian Standards Association, Mississauga, ON, Canada.

De Schutter, G. (1999). "Quantification of the influence of cracks in concrete structures on carbonation and chloride penetration." *Magazine of Concrete Research.* **51** (6). 427-435.

Deif, A., Martín-Pérez, B., and Cousin, B. (2008). "Experimental study of chloride penetration in a RC slab sustaining in-service loads," *8th International Conference on Creep, Shrinkage and Durability of Concrete and Concrete Structures,* Sept. 30th – Oct. 2nd, Ise-Shima, Japan.

Deif, A., Martín-Pérez, B., Cousin, B., Zhang, C., Li, W., and Bao, X. (2009). "A comparison of crack detection by optical fibers and strain gauges with theory for a loaded bridge deck subjected to chloride attack," *7th International Symposium on Non Destructive Testing in Civil Engineering*, June 30th - July 3rd, Nantes, France.

Deif, A., Martín-Pérez, B., Cousin, B., C Zhang, C., Bao, X., and Li, W. (2010). "Detection of cracks in a reinforced concrete beam using distributed Brillouin fibre sensors," *Smart Materials and Structures*, **19**(5), 055014 (7pp).

Djerbi, A., Bonnet, S., Khelidj, A., and Baroghel-bouny, V. (2008). "Influence of traversing crack on chloride diffusion into concrete." *Cement and Concrete Research*, **38**, 877-883.

Diamond, S., and Bentur, A. (1984). "On the cracking in concrete and fiber-reinforcement cements." *Application of fracture mechanics to cementitious composites*. S.P. Shah (editor). NATO-ARW, Sept. 4-7, Northwestern University, USA. 87-140.

Garces Rodriguez, O., and Hooton, R.D (2003). "Influence of cracks on chloride ingress into concrete." *ACI Materials Journal*, **100**(2), 120-126.

Gérard, B., and Marchand, J. (2000). "Influence of cracking on the diffusion properties of cement-based materials. Part I: Influence of continuous cracks on the steady-state regime." *Cement and Concrete Research.* **30**, 37–43.

Goto, Y. (1971). "Cracks formed in concrete around deformed tension bars." *ACI Journal*, **68**(4), 244-251.

Gowripalan, N., Sirivivatnanon,V., and Lim, C.(2000). "Chloride diffusivity of concrete cracked in flexure." *Cement and Concrete Research.* **30**, 725 -730.

Heideman, H., and Sundstrom, H. (1995). "The effects of stress on chloride penetration into concrete." *Concrete Under Severe Conditions: Environment and*

Loading (Volume Two), K. Sakai, N. Banthia, and O. E. Gjørv, eds., E & FN Spon , 1399-1407.

Hobbs, D. (1999). "Aggregate influence on chloride ion diffusion into concrete." *Cement and Concrete Research*, **29**, 1995–1998.

Ismail, M., Toumi, M., François, R., and Gagné, R. (2008). "Effect of crack opening on the local diffusion of chloride in cracked mortar samples." *Cement and Concrete Research*, **38**, 1106–1111.

Jacobsen, S., Marchand, J., and Boisvert, L. (1996)." Effect of cracking and healing on chloride transport in OPC concrete." *Cement and Concrete Research*, **26**(6). 869-881.

Konin, A., Franfois,R., and Arliguie, G. (1998). "Penetration of chlorides in relation to the microcracking state into reinforced ordinary and high strength concrete." *Materials and Structures*, **31**, 310-316.

Lee, N., and. Christholm, D. (2000). "Impediments to the application of marine concrete durability models in design." *Second International RILEM Workshop on Testing Modeling the Chloride Ingress Into Concrete*. Edited by C. Andrade and J. Kropp. 11-12 September, Paris, France. 383-393.

Lindquist, W. D., Darwin, D., Browning, J., and Miller, G. G. (2006). "Effect of cracking on chloride content in concrete bridge decks." *ACI Materials Journal*, **102**(6), 467-473.

Lindvall, A., Andersen, A., and Nilsson, L-O. (2000). "Chloride ingress data from Danish and Swedish road bridges exposed to splash from de-icing salt." *Second international RILEM workshop on testing modeling the chloride ingress into concrete*. Edited by C. Andrade and J. Kropp. 11-12 September, Paris, France. 85-103.

Lounis, Z., Martín-Pérez, B., and Hunaidi, O. (2001). "Decision support tools for life prediction and rehabilitation of concrete bridge decks." *NRCC/CPWA/IPWEA Seminar Series .Innovations in Urban Infrastructure*. APWA International Public Works Congress, Philadelphia, USA. 67-78.

Mangat, P. S., and Molloy, B. T. (1994). "Prediction of long term chloride concentration in concrete." *Materials and Structures*, **27**, 338-346.

Manual of 794 Basic Titrino. "Instruction for use – 8.794.1003." Metrohm Ltd.

Marsavina, L., Audenaert, K., De Schutter, G., Faur, N., and Marsavina, D. (2009). "Experimental and numerical determination of the chloride penetration in cracked concrete." *Construction and Building Materials*, **23**(1), 264-274.

Martín-Pérez, B. (1999). "Service Life Modelling of R.C. Highway Structures Exposed to Chlorides," Ph.D. thesis, Civil Engineering, University of Toronto, Toronto, 168 pp.

Maruyama, I., Tanaka, K., and Sato, R. (2006). "Distribution of chloride ion in cracked reinforced concrete prism transported by cyclic rain with chloride ion." *Proceedings of International Seminar on Durability and Lifecycle Evaluation of Concrete Structures*. Edited by Sato. et. al, Higashi Hiroshima. 61- 68.

Meck, E., Sirivivatnanon, V. (2003). "Field indicator of chloride penetration depth." *Cement and Concrete Research*, **33**, 1113–1117.

Nilson, L-O., Sandberg, P., Poulsen, E., Tang, L., Andersen, A., and Frederiksen, J. (1996). *HETEK, A system of estimation of chloride ingress into concrete, theoretical background.* Report No. 83:1997. The Danish Road Directorate. Copenhagen, Denmark.

Nokken, M., Boddy, A., Hooton, R., and Thomas, M. (2006). "Time dependent diffusion in concrete three laboratory studies." *Cement and Concrete Research*, **36**, 200–207.

Otsuki, N., Nagataki, S., and Nakashita, K., (1992). "Evaluation of $AgNO_3$ solution spray method for measurement of chloride penetration into hardened cementitious matrix materials." *ACI Materials Journal*, **89**(6), 587-592.

Poulsen, E., and Mejlbro, L. (2006). *Diffusion of Chloride in Concrete–Theory and Applications* (1st ed.). Taylor & Francis. (442 pp.)

RILEM Recommendation CPC-18. (1984). "Measurement of hardened concrete carbonation depth." *Material and Structures*, **102**, 453-455.

Rosenberg, A., Hansson, C., and Andrade, C. (1989). Mechanisms of corrosion of steel in concrete. In J. Skalny (Ed.), Materials Science of Concrete I (pp. 285–313). Westerville, OH: The American Ceramic Society, Inc.

Rostam, S. (2005). "Service life design of concrete structures - a challenge to designers as well as to owners." *Asian Journal of Civil Engineering (Building and Housing)*, **6**(5), 423-445.

Selvarajah, S. and Johnston, A. (1995). "Water permeation through cracked single skin masonry." *Building and Environment,* **30**(1), 19-28.

Takewaka, K., and Mastumoto, S. (1988). "Quality and cover thickness ofconcrete based on the estimation ofchloride penetration in marine environments." *ACI SP 109-17.* American Concrete Institute, Detroit, USA.

Tritthart, J., and Cavlek, K. (2000). "Determination of total and free chloride in cement paste and concrete." *Second International RILEM Workshop on Testing and Modelling the Chloride Ingress into Concrete.* Edited by C. Andrade and J. Kropp. 11-12 September, Paris, France, 429-437.

Tuutti, K. (1982). *Corrosion of Steel in Concrete* (Tech. Rep.). Stockholm: Swedish Cement and Concrete Research Institute. (469 pp.)

Wall, H., and Nilsson, L-O. (2006). "Chloride profiling in concrete harbour structures – a study of extensive variations." *2nd International Symposium on Advances in Concrete through Science and Engineering*, 11-13 September, Quebec City, Canada.

Win, P., Watanabe, M., and Machida, A. (2004). "Penetration profile of chloride ion in cracked reinforced concrete." *Cement and Concrete Research*, **34**, 1073–1079.

Zhang, C., Bao, X., Li, W., Chen, L., Deif, A., Cousin, B., and Martín-Perez, B. (2008). "Crack detection in reinforced concrete beam by using of distributed Brillouin fiber sensor," *19th International Conference on Optical Fiber Sensors*, April 14-18, Perth, Australia.

Appendix A

Concrete Stress-Strain Results

Table A.1 to Table A.4 tabulate the stress-strain results for four cylinder samples of w/c = 0.35 for an applied load less or equal than 50% of the ultimate compressive strength f'_c. Figure A.1 plots the stress-strain relationship for the 0.35 w/c concrete, and Figure A.2 shows the failure patterns for the cylinder when it reached the ultimate compressive strength f'_c.

Table A.1: Stress-strain relationship, 1st cylinder sample, w/c = 0.35 ($\sigma \leq 50\%$ of f'_c).

P (kN)	Δ (mm)	σ (kPa)	Micro-strain
10.12	0.0025	1205	8
60.72	0.0279	7231	84
101.44	0.0813	12080	244
151.2	0.1270	18005	381
207.92	0.1778	24759	534
256.36	0.2235	30528	671
301.96	0.2591	35958	778
351.56	0.3099	41864	931
400.84	0.3683	47733	1106

Table A.2: Stress-strain relationship, 2nd cylinder sample, w/c = 0.35 ($\sigma \leq 50\%$ of f'_c).

P(kN)	Δ (mm)	σ (kPa)	Micro-strain
12.00	0.0051	1429	15
63.20	0.0508	7526	153
103.32	0.0787	12303	237
153.28	0.1270	18253	381
209.96	0.1803	25002	542
256.36	0.2286	30528	687
302.92	0.2794	36072	839
351.72	0.3302	41883	992
402.72	0.3861	47956	1160

Table A.3: Stress-strain relationship, 3rd cylinder sample, w/c = 0.35 ($\sigma \leq 50\%$ of f'_c).

P(kN)	Δ (mm)	σ (kPa)	Micro-strain
11.60	0.0127	1381	38
62.36	0.0533	7426	160
103.24	0.0965	12294	290
153.68	0.1473	18300	443
210.80	0.1981	25102	595
256.04	0.2413	30490	725
303.00	0.2921	36082	877
363.40	0.3505	43274	1053
405.24	0.3937	48256	1183

Table A.4: Stress-strain relationship, 4th cylinder sample, w/c = 0.35 ($\sigma \leq 50\%$ of f'_c).

P(kN)	Δ (mm)	σ (kPa)	Micro-strain
11.88	0.0051	1415	15
64.64	0.0483	7697	145
104.16	0.0787	12404	237
155.60	0.1270	18529	381
211.76	0.1778	25217	534
255.80	0.2261	30461	679
304.36	0.2794	36244	839
363.04	0.3302	43231	992
408.20	0.3810	48609	1144

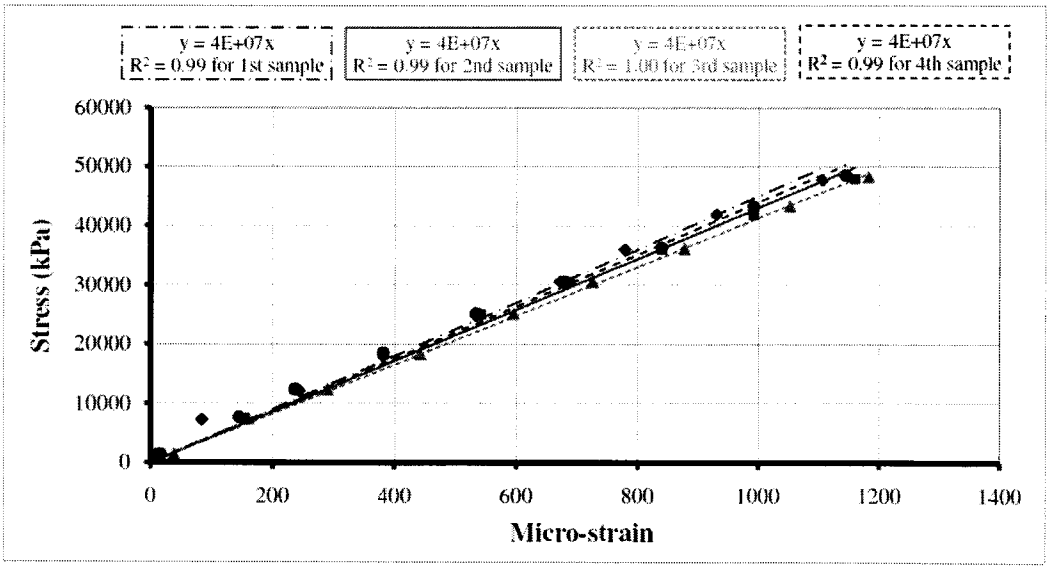

Figure A.1: Stress-strain relationship for w/c = 0.35, applied load ≤ 50% of f'_c.

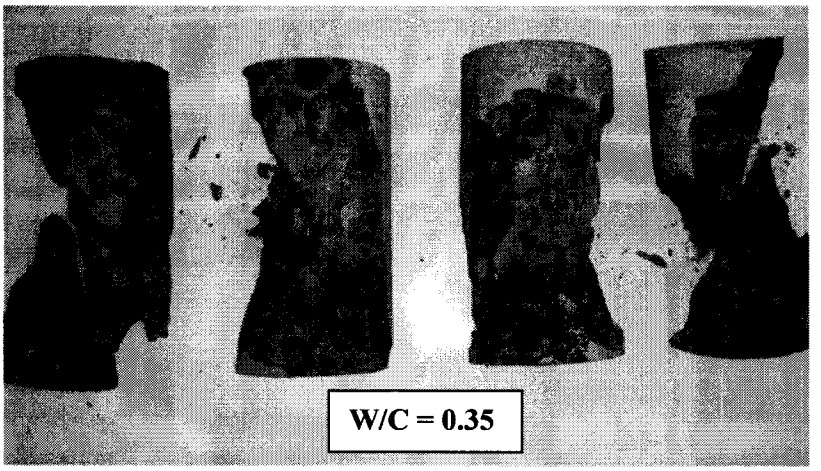

Figure A.2: Failure patterns for the cylinder with w/c = 0.35 when it reached f'_c.

Table A.5 to Table A.8 tabulate the stress-strain results for four cylinder samples of w/c = 0.40 for an applied load ≤ 50% of the ultimate compressive strength f'_c. Figure A.3 plots the stress-strain relationship for the 0.40 w/c concrete, and Figure A.4 shows the failure patterns for the cylinder when it reached the ultimate compressive strength f'_c.

Table A.5: Stress-strain relationship, 1st cylinder sample, w/c = 0.40 ($\sigma \leq 50\%$ of f'_c).

P(kN)	Δ (mm)	σ (kPa)	Micro-strain
10.20	0.0051	1215	15
51.32	0.0457	6111	137
102.80	0.0889	12242	267
150.80	0.1295	17957	389
200.71	0.1803	23901	542
250.80	0.2337	29866	702
300.96	0.2819	35839	847
348.56	0.3353	41507	1007
350.72	0.3556	41764	1068

Table A.6: Stress-strain relationship, 2nd cylinder sample, w/c = 0.40 ($\sigma \leq 50\%$ of f'_c).

P(kN)	Δ (mm)	σ (kPa)	Micro-strain
10.36	0.0076	1234	23
50.76	0.0508	6045	153
101.12	0.0889	12041	267
150.88	0.1321	17967	397
200.84	0.1905	23916	572
234.68	0.2261	27946	679
264.00	0.2540	31437	763
290.52	0.2565	34595	771
321.40	0.3200	38273	961

Table A.7: Stress-strain relationship, 3rd cylinder sample, w/c = 0.40 ($\sigma \leq 50\%$ of f'_c).

P(kN)	Δ (mm)	σ (kPa)	Micro-strain
10.48	0.0127	1248	38
51.28	0.0508	6106	153
102.76	0.1016	12237	305
151.32	0.1499	18019	450
200.80	0.2007	23912	603
230.76	0.2286	27479	687
260.84	0.2565	31061	771
290.84	0.2921	34634	877
321.16	0.3277	38244	984

Table A.8: Stress-strain relationship, 4th cylinder sample, w/c = 0.40 ($\sigma \leq 50\%$ of f'_c).

P(kN)	Δ (mm)	σ (kPa)	Micro-strain
10.28	0.0102	1224	31
50.96	0.0457	6068	137
100.96	0.0864	12022	259
151.08	0.1321	17991	397
201.04	0.1803	23940	542
231.48	0.2108	27565	633
261.44	0.2489	31133	748
290.88	0.2794	34638	839
320.40	0.3099	38154	931

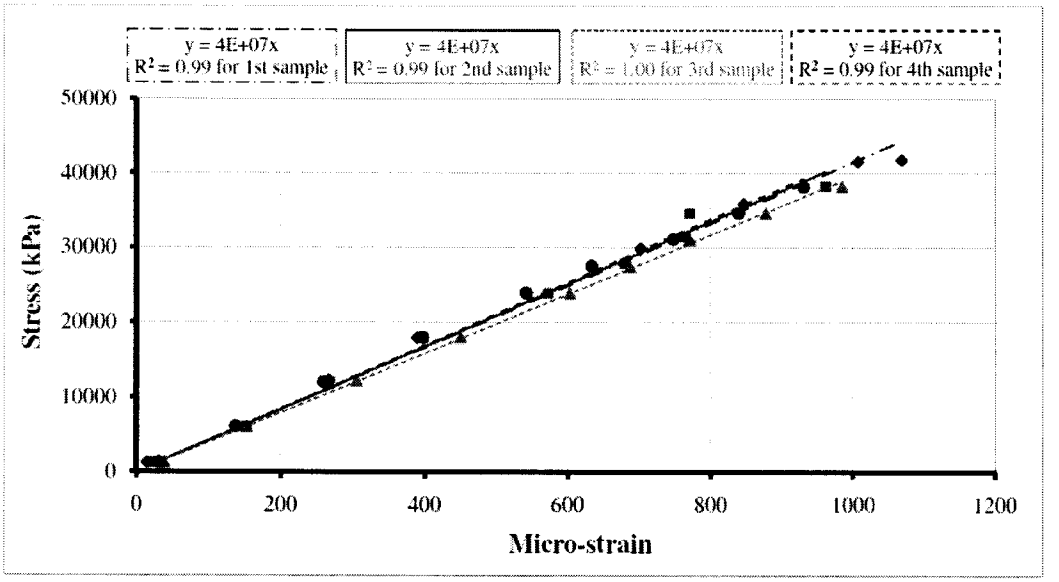

Figure A.3: Stress-strain relationship for w/c = 0.40, applied load ≤ 50% of f'_c.

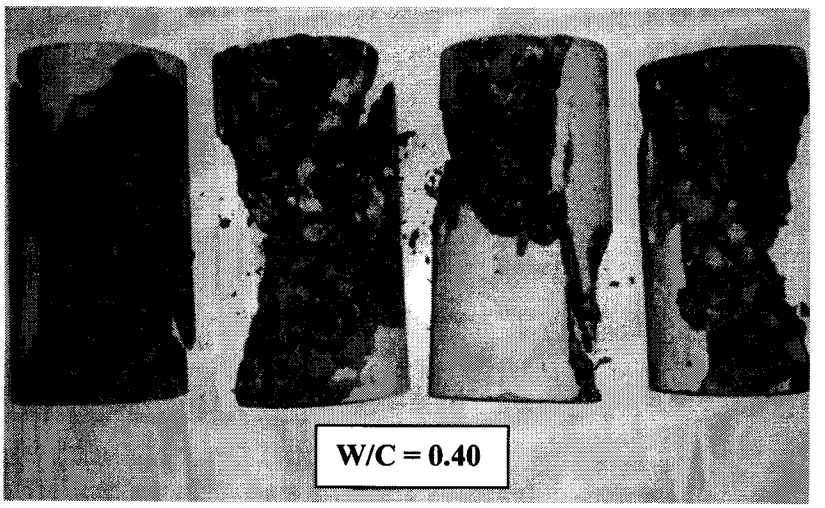

Figure A.4: Failure patterns for the cylinder with w/c = 0.40 when it reached f'_c.

Table A.9 to Table A.12 tabulate the stress-strain results for four cylinder samples of w/c = 0.50 for an applied load ≤ 50% of the ultimate compressive strength f'_c. Figure A.5 plots the stress-strain relationship for the 0.50 w/c concrete, and Figure A.6 shows the failure patterns for the cylinder when it reached to the ultimate compressive strength f'_c.

Table A.9: Stress-strain relationship, 1st cylinder sample, w/c = 0.50 ($\sigma \leq 50\%$ of f'_c).

P(kN)	Δ (mm)	σ (kPa)	Micro-strain
10.16	0.0127	1210	38
51.80	0.0508	6168	153
100.72	0.0991	11994	298
150.72	0.1473	17948	443
200.80	0.1905	23912	572
235.92	0.2286	28094	687
260.88	0.2565	31066	771
290.84	0.2921	34634	877
321.56	0.3277	38292	984

Table A.10: Stress-strain relationship, 2nd cylinder sample, w/c = 0.50 ($\sigma \leq 50\%$ of f'_c).

P(kN)	Δ (mm)	σ (kPa)	Micro-strain
10.92	0.0051	1300	15
50.60	0.0483	6026	145
101.36	0.0991	12070	298
151.04	0.1473	17986	443
200.88	0.1981	23921	595
231.20	0.2286	27532	687
260.72	0.2565	31047	771
291.48	0.2972	34710	893
324.96	0.3327	38697	999

Table A.11: Stress-strain relationship, 3rd cylinder sample, w/c = 0.50 ($\sigma \leq 50\%$ of f'_c).

P(kN)	Δ (mm)	σ (kPa)	Micro-strain
10.56	0.0051	1257	15
53.88	0.0457	6416	137
100.80	0.0864	12003	259
151.16	0.1321	18000	397
200.32	0.1803	23854	542
230.76	0.2159	27479	649
260.52	0.2515	31023	755
290.92	0.2794	34643	839
321.04	0.3073	38230	923

Table A.12: Stress-strain relationship, 4th cylinder sample, w/c = 0.50 ($\sigma \leq 50\%$ of f'_c).

P(kN)	Δ (mm)	σ (kPa)	Micro-strain
10.96	0.0025	1305	8
50.72	0.0381	6040	114
101.12	0.0813	12041	244
150.52	0.1295	17924	389
201.20	0.1778	23959	534
232.96	0.2235	27741	671
260.00	0.2540	30961	763
290.68	0.2819	34615	847
320.44	0.3175	38158	954

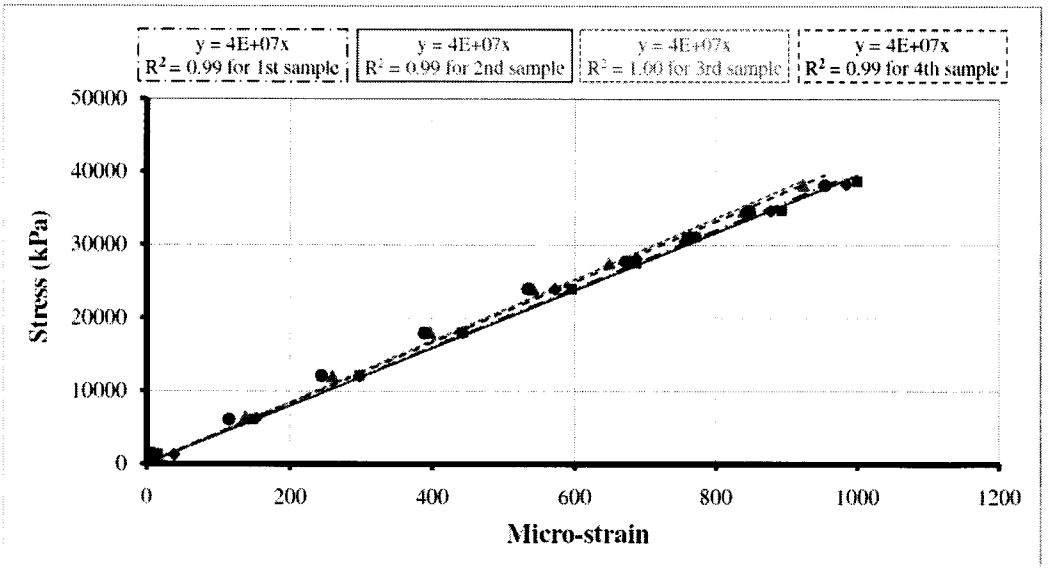

Figure A.5: Stress-strain relationship for w/c = 0.50, applied load $\leq 50\%$ of f'_c.

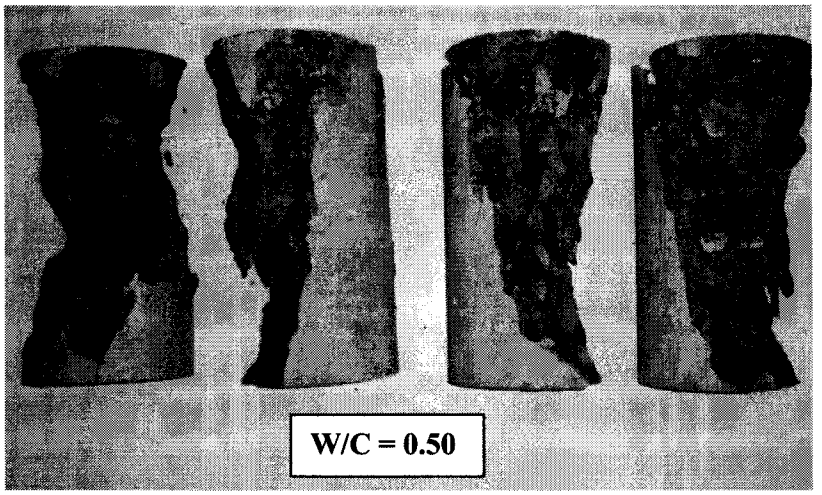

Figure A.6: Failure patterns for the cylinder with w/c = 0.50 when it reached f'_c.

Appendix B

Moment Capacity of the RC Slab

The geometry of the RC slab cross section is shown in Figure B.1.

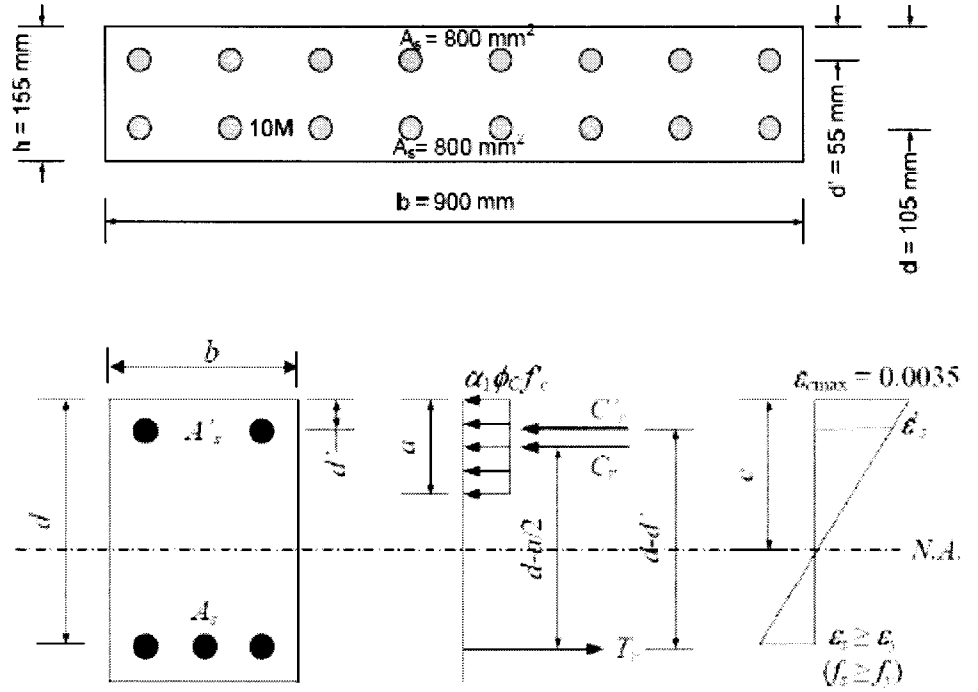

Figure B.1: Geometry of RC slab cross section.

To calculate the moment capacity of the RC slab, the following equations were used:

$$\frac{\varepsilon'_s}{c-d'} = \frac{\varepsilon_{cmax}}{c} \quad \Rightarrow \quad \varepsilon'_s = \varepsilon_{cmax}\left(1-\frac{d'}{c}\right) \tag{B.1}$$

$$C'_r = \phi_s f'_s A'_s \tag{B.2}$$

$$C_r = \alpha_1\phi_c f'_s(ab - A'_s) \approx \alpha_1\phi_c f'_c ab \tag{B.3}$$

$$T_r = \phi_s f_y A_y \tag{B.4}$$

$$\sum F = 0 \quad \Rightarrow \quad C'_r + C_r = T_r \quad \Rightarrow \quad a = \frac{T_r - C'_r}{\alpha_1\phi_c f'_c b} = \frac{f_y A_y - f'_s A'_s}{\alpha_1 f'_c b} \tag{B.5}$$

Factors ϕ_c and ϕ_s are set to 1 in Eq. B.5, since both material properties and applied load are known from the test. The moment capacity of the section is given by:

$$M_r = C_r'(d - d') + C_r\left(d - \frac{a}{2}\right) \tag{B.6}$$

The cracking moment M_{cr} of the section is calculated from:

$$M_{cr} = \frac{f_r I_g}{y_t} \tag{B.7}$$

$$f_r = 0.6\lambda\sqrt{f_c'} \tag{B.8}$$

where M_{cr} is the cracking moment (kN·m), f_r is the modulus of rupture of concrete (MPa), λ is 1, 0.85, and 0.75 for normal density concrete, semi-low density concrete, and low density concrete, respectively, I_g is the gross moment of inertia (mm^4), and y_t is the distance from the centroidal axis of the gross section to the extreme fibre in tension (mm).

Table B.1: Summary of the design

Description	Strip of w/c =0.35	Strip of w/c = 0.4	Strip of w/c = 0.5
h (mm)	155	155	155
b (mm)	900	900	900
d' (mm)	55	55	55
d (mm)	105	105	105
f_y (MPa)	400	400	400
f'_c (MPa)	81	69.4	64.5
E_s (MPa)	200,000	200,000	200,000
E_c (MPa)*	40	40	40
ε_y	0.002	0.002	0.002
ε_{cmax}	0.0035	0.0035	0.0035
n^*	5	5	5
M_r (kN.m)	47	48	48
$P_{ult.}$ (kN)	52	53	53
M_{cr} (kN.m)	19.46	18.01	17.37
30% of M (kN.m)	14.1 (uncracked)	14.4 (uncracked)	14.4 (uncracked)
60% of M (kN.m)	28.2 (cracked)	28.8 (cracked)	28.8 (cracked)

* See Appendix **A** for the results of compressive tests

Appendix C

Electrical Strain Gauges Data

Table C.1 through Table C.3 tabulate the strains measured by the electrical strain gauges for the strips of w/c = 0.35, 0.40, and 0.50, respectively, after the first wetting/drying cycle. Table C.4 through Table C.6 tabulate the strains recorded by the electrical strain gauges for the strips of w/c = 0.35, 0.40, and 0.50, respectively, after the second wetting/drying cycle. Finally, Table C.7 through Table C.9 list the strains measured by the electrical strain gauges for the strips of w/c = 0.35, 0.40, and 0.50, respectively, after the third wetting/drying cycle.

Table C.1: Strains measured by electrical strain gauges during first set for strip of w/c = 0.35.

Locations of gauges	Gauge #	Before loading (200 days since casting)	After Loading (201 days Since Casting)	A.L. (202 days S.C.)	A.L. (236 days S.C.)§	A.L. (236 days S.C.)++	A.L. (245 days S.C.)	A.L. (257 days S.C.)
Steel strain gauges on rebars	1	-2093	-2147	-2147	-2054	-2054	-2049	-2027
	3	-1508	-1112	-1108	-993	-992	-982	-931
	5	-2372	-2132	-2124	-1962	-1959	-1954	-1917
	7	-2011	-1626	-1632	-1555	-1556	-1545	-1506
	9	-2391	-2370	-2368	-2324	-2324	-2316	-2301
	11	-2139	-504	-453	-116	-113	-110	-84
	13	-1917	-1749	-1733	-1485	-1483	-1474	-1435
	2	-2082	-2013	-2010	-1953	-1953	-1948	-1941
	4	-1490	301	331	596	594	606	699
	6	-2441	-981	-941	-610	-608	-600	-505
	8	-1775	177	188	390	392	407	535
	10	-2560	-2577	-2577	-2569	-2569	-2564	-2554
	12	-1318	-954	-951	-917	-918	-917	-854
	14	-2338	-2384	-2386	-2367	-2368	-2365	-2353
Steel strain gauges on tensioned bars	27	-1650	-659	-644	-677	-672	-670	-656
	28	-1090	-230	-208	-248	-244	-241	-231
	29	-1049	535	570	563	565	568	614
	30	-1895	-4	48	40	43	47	97
	31	-1823	-1270	-1259	-1293	-1290	-1304	-1376
	32	-1242	-480	-462	-467	-465	-482	-570
Concrete strain Gauges	15	-765	-940	-947	-863	-861	-860	-855
	17	-1062	-1851	-1860	-1868	-1867	-1871	-1859
	17'	-640	-1363	-1383	-1498	-1499	-1476	-1431
	19	-882	-1545	-1552	-1529	-1529	-1523	-1527
	22	-1184	-1138	-1135	-1083	-1079	-1078	-1069
	23	-850	-848	-852	-701	-702	-709	-730
	23'	-1134	3472	3520	0.00*	0.00*	0.00*	0.00*
	16	-599	-447	-440	-407	-405	-400	-398
	18	-996	0.00*	0.00*	0.00*	0.00*	0.00*	0.00*
	20	-944	-856	-853	-830	-828	-830	-843
	21	-1006	0.00*	0.00*	0.00*	0.00*	0.00*	0.00*
	22'	-778	-793	-801	-803	-806	-803	-804
	24	-1176	-1828	-1841	-1949	-1953	-1958	-1892
	25	-944	-1510	-1522	-1654	-1656	-1666	-1658
	26	-831	-1024	-1029	-1130	-1129	-1135	-1167

Table C.1: Cont ...

Locations of gauges	Gauge #	A.L. (267 days S.C.)	A.L. (281 days S.C.)	A.L. (291 days S.C.)	A.L. (299 days S.C.)	A.L. (309 days S.C.)	A.L. (326 days S.C.)
Steel strain gauges on rebars	1	-2020	-2015	-2010	-2008	-2014	-2007
	3	-918	-913	-911	-908	-919	-917
	5	-1911	-1907	-1906	-1903	-1913	-1903
	7	-1501	-1505	-1505	-1500	-1511	-1505
	9	-2292	-2283	-2279	-2273	-2280	-2263
	11	-71	-77	-88	-87	-106	-119
	13	-1413	-1398	-1381	-1366	-1364	-1338
	2	-1941	-1936	-1932	-1928	-1934	-1928
	4	718	741	743	945	747	735
	6	-482	-460	-446	-439	-429	-412
	8	549	534	541	554	570	579
	10	-2559	-2559	-2556	-2555	-2568	-2560
	12	-846	-822	-815	-808	-725	-688
	14	-2356	-2332	-2362	-2328	-2328	-2334
Steel strain gauges on tensioned bars	27	-664	-665	-667	-672	-670	-672
	28	-238	-244	-239	-242	-238	-244
	29	598	578	567	557	597	574
	30	-79	58	47	37	77	51
	31	-1394	-1394	-1396	-1405	-1385	-1411
	32	-590	-594	-596	-608	-581	-616
Concrete strain gauges	15	-862	-871	-873	-872	-877	-866
	17	-1851	-1845	-1833	-1825	-1832	-1823
	17'	-1430	-1430	-1432	-1431	-1443	-1428
	19	-1532	-1538	-1541	-1537	-1552	-1542
	22	-1067	-1058	-1057	-1051	-1050	-1037
	23	-765	-750	-562	-594	-748	-640
	23'	0.00*	0.00*	0.00*	0.00*	0.00*	0.00*
	16	-398	-387	-381	-381	-378	-377
	18	0.00*	0.00*	0.00*	0.00*	0.00*	0.00*
	20	-866	-884	-886	-888	-891	-899
	21	0.00*	0.00*	0.00*	0.00*	0.00*	0.00*
	22'	-817	-823	-823	-824	-830	-837
	24	-1855	-1860	-1867	-1869	-1896	-1895
	25	-1647	-1589	1590	-1609	-1551	-1607
	26	-1178	-1160	-1152	-1154	-1155	-1177

Table C.2: Strains measured by electrical strain gauges during first set for strip of w/c = 0.40.

Locations of gauges	Gauge #	Before loading (200 days since casting)	After Loading (201 days Since Casting)	A.L. (202 days S.C.)	A.L. (236 days S.C.)§	A.L. (236 days S.C.)++	A.L. (245 days S.C.)	A.L. (257 days S.C.)
Steel strain Gauges on rebars	1	-2393	-2426	-2426	-2399	-2398	-2388	-2316
	3	-1705	-1390	-1378	-1315	-1315	-1296	-1199
	5	-2416	-1959	-1963	-1976	-1976	-1951	-1849
	7	-2553	-2170	-2157	-2103	-2103	-2083	-1972
	9	-1424	-1415	-1418	-1330	-1329	-1317	-1244
	11	-2563	-562	-585	-280	-275	-273	-594
	13	-1723	-1611	-1503	-1185	-1182	-1152	-1020
	2	-2555	-2506	-2503	-2451	-2451	-2448	-2442
	4	-2447	-1185	-1133	-903	-902	-893	-801
	6	-2376	-384	-355	-212	-209	-203	-80
	8	-2809	-1136	-1086	-918	-918	-902	-767
	10	-2531	-2532	-2532	-2515	-2515	-2509	-2488
	12	-2242	-1613	-1630	-1610	-1610	-1602	-1546
	14	-2550	-2596	-2589	-2555	-2556	-2552	-2481
Steel strain gauges on tensioned bars	27	-1295	-198	-225	-210	-209	-206	-171
	28	-1254	-525	-557	-541	-544	-536	-503
	29	-1236	437	462	426	434	438	500
	30	-1320	625	648	653	657	661	730
	31	-1677	-994	-1001	-963	-959	-975	-1016
	32	-1407	-630	-626	-571	-574	-589	-635
Concrete strain gauges	15	-1007	-1095	-1096	-1117	-1116	-1115	-1102
	17	-1154	-1787	-1809	-1808	-1810	-1808	-1850
	17'	-1110	-1567	-1583	-1659	-1658	-1629	-1570
	19	-884	-1648	-1672	-1729	-1727	-1725	-1767
	22	-406	-358	-363	-199	-196	-192	-187
	23	-1020	-1045	-1046	-984	-982	-1023	0.00*
	23'	-753	-350	-351	-204	-203	-188	-75
	16	-946	-847	-841	-798	-800	-797	-817
	18	-1033	-971	-972	-981	-982	-977	-979
	20	-1030	-957	-958	-970	-968	-964	-968
	21	-812	-813	-814	-813	-813	-813	-849
	22'	-1021	-1046	-1046	-1073	-1074	-1069	-1058
	24	-704	-1295	-1286	-1403	-1408	-1414	-1375
	25	-908	-1499	-1489	-1621	-1625	-1628	-1580
	26	-626	-771	-838	-937	-936	-940	-928

Table C.2: Cont ...

Locations of gauges	Gauge #	A.L. (267 days S.C.)	A.L. (281 days S.C.)	A.L. (291 days S.C.)	A.L. (299 days S.C.)	A.L. (309 days S.C.)	A.L. (326 days S.C.)
Steel strain Gauges on rebars	1	-2295	-2278	-2268	-2261	-2269	-2253
	3	-1174	-1161	-1150	-1146	-1153	-1142
	5	-1838	-1831	-1830	-1826	-1840	-1826
	7	-1950	-1934	-1926	-1921	-1930	-1913
	9	-1218	-1193	-1179	-1170	-1167	-1158
	11	-335	-543	-515	-387	-513	-390
	13	-976	-942	-921	-907	-905	-876
	2	-2441	-2434	-2427	-2424	-2426	-2419
	4	-775	-750	-736	-725	-722	-706
	6	-63	-52	-53	-47	-60	-45
	8	-760	-755	-759	-754	-766	-744
	10	-2487	-2483	-2478	-2474	-2484	-2484
	12	-1532	-1531	-1510	-1510	-1512	-1520
	14	-2467	-2428	-2419	-2417	-2397	-2409
Steel strain gauges on tensioned bars	27	-167	-169	-170	-175	-173	-179
	28	-503	-503	-505	-506	-508	-511
	29	506	506	503	497	500	483
	30	737	737	733	728	732	712
	31	-1008	-1013	-1015	-1018	-1009	-1022
	32	-626	-632	-633	-637	-625	-641
Concrete strain gauges	15	-1102	-1091	-1088	-1085	-1086	-1070
	17	-1855	-1863	-1861	-1860	-1882	-1888
	17'	-1561	-1561	-1547	-1544	-1554	-1542
	19	-1786	-1805	-1810	-1812	-1821	-1808
	22	-183	-171	-174	-171	-166	-150
	23	0.00*	-780	-757	-625	-767	-567
	23'	-42	37	101	157	180	300
	16	-837	-848	-849	-849	-853	-854
	18	-994	-1010	-1008	-1008	-1011	-1017
	20	-982	-1004	-995	-996	-999	-1008
	21	-863	-888	-871	-871	-874	-891
	22'	-1072	-1079	-1083	-1081	-1091	-1094
	24	-1371	-1362	-1366	-1372	-1396	-1403
	25	-1570	-1528	-1528	-1537	-1512	-1543
	26	-928	-887	-884	-889	-847	-875

Table C.3: Strains measured by electrical strain gauges during first set for strip of w/c = 0.50.

Locations of gauges	Gauge #	Before loading (200 days since casting)	After Loading (201 days Since Casting)	A.L. (202 days S.C.)	A.L. (236 days S.C.)§	A.L. (236 days S.C.)++	A.L. (245 days S.C.)	A.L. (257 days S.C.)
Steel strain gauges on rebars	1	-2802	-2848	-2849	-2790	-2791	-2786	-2759
	3	-1981	-1771	-1767	-1648	-1649	-1637	-1592
	5	-2384	-2133	-2127	-2008	-2008	-1996	-1957
	7	-2212	-2004	-1992	-1830	-1830	-1820	-1770
	9	-2060	-2056	-2052	-1924	-1923	-1918	-1879
	11	-2547	-492	-407	59	63	69	132
	13	-2413	-2356	-2348	-2018	-2018	-2000	-1702
	2	-1525	-1525	-1514	-1483	-1483	-1480	-1475
	4	-1966	-544	-496	-165	-163	-147	-81
	6	-1504	-222	-163	265	267	277	373
	8	-2414	-1296	-1257	-962	-961	-948	-866
	10	-1841	-1882	-1884	-1870	-1871	-1867	-1857
	12	-2211	-1723	-1726	-1664	-1665	-1661	-1568
	14	-1790	-1844	-1845	-1814	-1815	-1812	-1780
Steel strain gauges on tensioned bars	27	-1496	-577	-556	-526	-521	-518	-503
	28	-1178	-307	-285	-250	-248	-243	-231
	29	-1361	379	362	430	429	439	481
	30	-1721	101	84	164	166	177	225
	31	-1979	-1329	-1328	-1310	-1307	-1324	-1380
	32	-1577	-812	-807	-787	-786	-803	-863
Concrete strain gauges	15	-1088	-1175	-1181	-1080	-1082	-1081	-1072
	17	-795	-1583	-1609	-1658	-1659	-1656	-1644
	17'	-536	-1056	-1082	-1198	-1200	-1176	-1149
	19	-748	-1456	-1481	-1546	-1546	-1537	-1587
	22	-430	0.00*	0.00*	0.00*	0.00*	0.00*	0.00*
	23	-1331	-1303	-1309	-1080	-1077	-1079	-1072
	23'	-950	60	83	425	431	426	523
	16	-1173	-1118	-1113	-1097	-1096	-1095	-1111
	18	-788	0.00*	0.00*	0.00*	0.00*	0.00*	0.00*
	20	-448	-438	-435	-466	-464	-462	-436
	21	-1075	5121	5273	6486	6490	6562	6900
	22'	-1439	-1486	-1499	-1533	-1534	-1533	-1545
	24	-1005	-1599	-1623	-1761	-1761	-1765	-1746
	25	-1146	-1672	-1692	-1830	-1832	-1839	-1801
	26	-960	-1102	-1116	-1314	-1315	-1321	-1345

Table C.3: Cont ...

Locations of gauges	Gauge #	A.L. (267 days S.C.)	A.L. (281 days S.C.)	A.L. (291 days S.C.)	A.L. (299 days S.C.)	A.L. (309 days S.C.)	A.L. (326 days S.C.)
Steel strain gauges on rebars	1	-2748	-2730	-2720	-2712	-2717	-2696
	3	-1585	-1577	-1574	-1571	-1580	-1566
	5	-1939	-1929	-1923	-1915	-1908	-1812
	7	-1755	-1742	-1733	-1726	-1734	-1712
	9	-1854	-1826	-1809	-1795	-1786	-1745
	11	38	-56	-123	-130	-134	-123
	13	-1632	-1585	-1548	-1528	-1521	-1468
	2	-1480	-1479	-1475	-1472	-1476	-1469
	4	-69	-53	-45	-38	-32	-14
	6	430	286	261	154	349	404
	8	-842	-822	-805	-793	-786	-757
	10	-1863	-1861	-1855	-1851	-1856	-1845
	12	-1547	-1504	-1467	-1450	-1436	-1396
	14	-1772	-1723	-1707	-1705	-1700	-1698
Steel strain gauges on tensioned bars	27	-511	-516	-518	-524	-516	-528
	28	-235	-241	-245	-248	-241	-255
	29	477	468	463	456	477	452
	30	220	215	209	202	222	194
	31	-1386	-1380	-1382	-1393	-1386	-1402
	32	-865	-861	-862	-877	-861	-886
Concrete strain gauges	15	-1078	-1076	-1060	-1051	-1051	-1032
	17	-1649	-1654	-1652	-1651	-1669	-1672
	17'	-1152	-1155	-1152	-1152	-1162	-1152
	19	-1606	-1611	-1608	-1604	-1617	-1603
	22	0.00*	0.00*	0.00*	0.00*	0.00*	0.00*
	23	-1055	-1032	-1006	-987	-976	-930
	23'	584	648	685	717	773	861
	16	-1119	-1130	-1133	-1133	-1136	-1137
	18	0.00*	0.00*	0.00*	0.00*	0.00*	0.00*
	20	-315	-305	-318	-331	-363	-391
	21	6971	7055	7098	7125	7226	7336
	22'	-1567	-1580	-1584	-1577	-1589	-1591
	24	-1720	-1699	-1662	-1657	-1669	-1672
	25	-1785	-1725	-1720	-1726	-1717	-1719
	26	-1335	-1303	-1285	-1288	-1286	-1319

Table C.4: Strains measured by electrical strain gauges during second set for strip of w/c = 0.35.

Locations of gauges	Gauge #	A.L. (326 days S.C.)	A.L. (336 days S.C.)	A.L. (343 days S.C.)	A.L. (352 days S.C.)	A.L. (357 days S.C.)	A.L. (366 days S.C.)	A.L. (373 days S.C.)
Steel strain gauges on rebars	1	-2044	-2030	-2027	-2028	-2020	-2021	-2020
	3	-984	-961	-957	-961	-955	-962	-964
	5	-1903	-1936	-1935	-1938	-1931	-1935	-1936
	7	-1559	-1542	-1534	-1535	-1530	-1537	-1534
	9	-2270	-2253	-2247	-2245	-2243	-2247	-2245
	11	-159	-161	-156	-154	-160	-173	0.00*
	13	-1344	-1316	-1312	-1307	-1303	-1296	-1286
	2	-1940	-1928	-1926	-1926	-1921	-1928	-1921
	4	686	721	724	723	728	725	725
	6	-431	-396	-389	-386	-375	-373	-370
	8	507	555	563	574	581	583	581
	10	-2581	-2569	-2567	-2569	-2566	-2571	-2563
	12	-658	-649	-633	-596	-590	-583	-545
	14	-2350	-2336	-2328	-2329	-2333	-2330	-2317
Steel strain gauges on tensioned bars	27	-697	-691	-687	-688	-692	-693	-688
	28	-269	-262	-259	-261	-261	-263	-260
	29	518	539	544	544	538	528	536
	30	-12	16	22	22	17	3	14
	31	-1362	-1383	-1372	-1377	-1385	-1395	-1371
	32	-554	-581	-571	-575	-583	-597	-570
Concrete strain gauges	15	-886	-899	-909	-913	-913	-915	-919
	17	-1837	-1860	-1859	-1869	-1869	-1875	-1876
	17'	-1545	-1553	-1551	-1547	-1553	-1550	-1545
	19	-1584	-1588	-1589	-1593	-1595	-1602	-1600
	22	-1018	-1010	-1005	-1005	-1007	-1015	-1017
	23	-313	0.00*	0.00*	0.00*	0.00*	0.00*	0.00*
	23'	0.00*	0.00*	0.00*	0.00*	0.00*	0.00*	0.00*
	16	-362	-352	-352	-354	-350	-355	-343
	18	0.00*	0.00*	0.00*	0.00*	0.00*	0.00*	0.00*
	20	-904	-896	-895	-898	-900	-904	-893
	21	0.00*	0.00*	0.00*	0.00*	0.00*	0.00*	0.00*
	22'	-860	-856	-858	-857	-857	-861	-853
	24	-1975	-1940	-1918	-1901	-1901	-1903	-1891
	25	-1668	-1678	-1675	-1665	-1674	-1685	-1673
	26	-1203	-1210	-1200	-1195	-1199	-1204	-1190

Table C.4: Cont ...

Locations of gauges	Gauge #	A.L. (378 days S.C.)	A.L. (385 days S.C.)	A.L. (394 days S.C.)	A.L. (400 days S.C.)	A.L. (416 days S.C.)
Steel strain gauges on rebars	1	-2018	-2023	-2026	-2035	-2034
	3	-661	-974	-977	-984	-992
	5	-1932	-1944	-1944	-1952	-1955
	7	-1532	-1541	-1543	-1552	-1562
	9	-2237	-2246	-2244	-2243	-2240
	11	0.00*	0.00*	0.00*	0.00*	0.00*
	13	-1279	-1283	-1277	-1275	-1260
	2	-1917	-1922	-1922	-1922	-1922
	4	724	716	716	712	706
	6	-366	-379	-373	-379	-386
	8	581	576	576	558	535
	10	-2557	-2566	-2566	-2572	-2572
	12	-536	-522	-515	-484	-460
	14	-2318	-2328	-2336	-2261	-2200
Steel strain gauges on tensioned bars	27	-688	-694	-701	-692	-687
	28	-260	-264	-272	-261	-257
	29	532	525	508	527	537
	30	6	-5	-21	2	17
	31	-1379	-1384	-1404	-1365	-1342
	32	-581	-589	-610	-562	-533
Concrete strain gauges	15	-924	-947	-925	-924	-913
	17	-1876	-1885	-1886	-1893	-1891
	17'	-1540	-1554	-1551	-1560	-1552
	19	-1602	-1614	-1618	-1622	-1614
	22	-1021	-1026	-1018	-1008	-987
	23	0.00*	0.00*	0.00*	0.00*	0.00*
	23'	0.00*	0.00*	0.00*	0.00*	0.00*
	16	-342	-342	-338	-334	-316
	18	0.00*	0.00*	0.00*	0.00*	0.00*
	20	-890	-894	-892	-891	-874
	21	0.00*	0.00*	0.00*	0.00*	0.00*
	22'	-848	-849	-848	-857	-845
	24	-1884	-1895	-1919	-1957	-1983
	25	-1673	-1684	-1707	-1605	-1546
	26	-1193	-1201	-1212	-1157	-1002

Table C.5: Strains measured by electrical strain gauges during second set for strip of w/c = 0.40.

Locations of gauges	Gauge #	A.L. (326 days S.C.)	A.L. (336 days S.C.)	A.L. (343 days S.C.)	A.L. (352 days S.C.)	A.L. (357 days S.C.)	A.L. (366 days S.C.)	A.L. (373 days S.C.)
Steel strain gauges on rebars	1	-2292	-2271	-2268	-2270	-2267	-2267	-2260
	3	-1217	-1189	-1175	-1163	-1155	-1156	-1152
	5	-1953	-1925	-1924	-1922	-1924	-1924	-1926
	7	-1984	-1961	-1957	-1947	-1940	-1938	-1934
	9	-1158	-1131	-1124	-1128	-1130	-1125	-1126
	11	0.00*	0.00*	0.00*	0.00*	0.00*	0.00*	0.00*
	13	-902	-848	-834	-832	-824	-813	-820
	2	-2426	-2412	-2408	-2410	-2410	-2411	-2403
	4	-725	-697	-686	-678	-668	-664	-661
	6	-100	-65	-63	-64	-56	-60	-71
	8	-816	-778	-783	-765	-753	-747	-751
	10	-2488	-2475	-2473	-2478	-2479	-2478	-2475
	12	-1380	0.00*	0.00*	0.00*	0.00*	0.00*	-1601
	14	-2409	-2375	-2351	-2334	-2322	-2305	-2284
Steel strain gauges on tensioned bars	27	-215	-200	-197	-195	-195	-205	-196
	28	-550	-533	-531	-528	-529	-533	-532
	29	425	442	447	447	445	436	439
	30	650	669	675	675	674	665	665
	31	-987	-1012	-1005	-1009	-1016	-1026	-1014
	32	-601	-631	-623	-627	-633	-645	-628
Concrete strain gauges	15	-1054	-1060	-1063	-1065	-1061	-1063	-1061
	17	-1915	-1940	-1944	-1951	-1954	-1954	-1947
	17'	-1623	-1595	-1588	-1584	-1587	-1576	-1586
	19	-1806	-1809	-1804	-1806	-1811	-1812	-1809
	22	-120	-112	-111	-125	-123	-123	-129
	23	0.00*	0.00*	0.00*	0.00*	0.00*	0.00*	0.00*
	23'	333	800	874	866	870	800	0.00*
	16	-847	-840	-838	-841	-843	-842	-833
	18	-1029	-1013	-1012	-1013	-1018	-1019	-1009
	20	-1020	-1005	-1006	-1006	-1013	-1012	-1001
	21	-918	-905	-901	-908	-925	-933	-920
	22'	-1108	-1104	-1104	-1112	-1112	-1115	-1107
	24	-1484	-1481	-1486	-1495	-1494	-1501	-1487
	25	-1589	-1566	-1544	-1534	-1527	-1527	-1520
	26	-871	-880	-892	-911	-921	-929	-920

Table C.5: Cont ...

Locations of gauges	Gauge #	A.L. (378 days S.C.)	A.L. (385 days S.C.)	A.L. (394 days S.C.)	A.L. (400 days S.C.)	A.L. (416 days S.C.)
Steel strain gauges on rebars	1	-2253	-2260	-2252	-2251	-2244
	3	-1147	-1158	-1161	-1161	-1160
	5	-1917	-1932	-1932	-1936	-1932
	7	-1927	-1935	-1937	-1939	-1940
	9	-1119	-1131	-1122	-1122	-1108
	11	0.00*	0.00*	0.00*	0.00*	0.00*
	13	-815	-812	-775	-800	-865
	2	-2397	-2403	-2409	-2406	-2395
	4	-656	-661	-659	-659	-653
	6	-66	-76	-77	-86	-88
	8	-744	-749	-746	-753	-751
	10	-2469	-2482	-2478	-2482	-2470
	12	0.00*	0.00*	0.00*	0.00*	0.00*
	14	-2274	-2243	-2222	-2159	-2013
Steel strain gauges on tensioned bars	27	-197	-199	-207	-202	-201
	28	-532	-534	-541	-537	-536
	29	435	422	420	430	434
	30	662	657	645	653	660
	31	-1018	-1019	-1023	-998	-982
	32	-640	-640	-647	-618	-598
Concrete strain gauges	15	-1059	-1056	-1056	-1054	-1035
	17	-1951	-1979	-1980	-1991	-1983
	17'	-1584	-1607	-1600	-1606	-1596
	19	-1808	-1824	-1821	-1824	-1812
	22	-134	-147	-139	-138	-123
	23	0.00*	0.00*	0.00*	0.00*	0.00*
	23'	0.00*	-300	-770	0.00*	0.00*
	16	-833	-840	-837	-838	-820
	18	-1007	-1021	-1014	-1011	-999
	20	-1002	-1009	-1006	-1007	-991
	21	-921	-922	-936	-929	-916
	22'	-1105	-1108	-1108	-1111	-1098
	24	-1491	-1499	-1514	-1524	-1535
	25	-1518	-1527	-1537	-1521	-1490
	26	-927	-945	-970	-875	-782

Table C.6: Strains measured by electrical strain gauges during second set for strip of w/c = 0.50.

Locations of gauges	Gauge #	A.L. (326 days S.C.)	A.L. (336 days S.C.)	A.L. (343 days S.C.)	A.L. (352 days S.C.)	A.L. (357 days S.C.)	A.L. (366 days S.C.)	A.L. (373 days S.C.)
Steel strain gauges on rebars	1	-2717	-2694	-2683	-2675	-2674	-2673	-2669
	3	-1610	-1588	-1587	-1587	-1588	-1588	-1590
	5	-1744	-1720	-1715	-1709	-1706	-1701	-1698
	7	-1735	-1710	-1702	-1694	-1697	-1688	-1687
	9	-1712	-1691	-1680	-1667	-1661	-1650	-1633
	11	0.00*	0.00*	0.00*	0.00*	0.00*	0.00*	0.00*
	13	-1426	-1391	-1374	-1361	-1350	-1331	-1314
	2	-1480	-1477	-1475	-1473	-1475	-1477	-1471
	4	-29	3	3	-2	1	3	-8
	6	0.00*	0.00*	0.00*	0.00*	0.00*	0.00*	185
	8	-766	-718	-707	-696	-693	-681	-675
	10	-1863	-1849	-1850	-1853	-1854	-1852	-1845
	12	-1293	-1274	-1270	-1289	-1293	-1340	-1383
	14	-1671	-1663	-1660	-1658	-1661	-1662	-1655
Steel strain gauges on tensioned bars	27	-540	-532	-536	-533	-537	-544	-538
	28	-269	-260	-260	-261	-265	-273	-268
	29	413	421	418	417	412	407	411
	30	152	161	161	156	150	147	148
	31	-1362	-1393	-1393	-1393	-1398	-1407	-1392
	32	-844	875	-873	-877	-885	-893	-880
Concrete strain gauges	15	-1057	-1065	-1041	-1029	-1024	-1032	-1018
	17	-1695	-1696	-1695	-1720	-1733	-1744	-1745
	17'	-1222	-1204	-1199	-1194	-1188	-1191	-1188
	19	-1605	-1612	-1612	-1625	-1634	-1632	-1638
	22	0.00*	0.00*	0.00*	0.00*	0.00*	0.00*	0.00*
	23	-841	-831	-788	-783	-742	-668	-620
	23'	918	800	874	866	870	800	0.00*
	16	-1133	-1138	-1139	-1144	-1147	-1151	-1142
	18	0.00*	0.00*	0.00*	0.00*	0.00*	0.00*	0.00*
	20	-450	-451	-459	-473	-483	-491	-483
	21	7348	7546	7579	7618	7662	7691	7661
	22'	-1602	-1605	-1601	-1603	-1607	-1610	-1595
	24	-1746	-1755	-1758	-1763	-1767	-1771	-1762
	25	-1739	-1748	-1735	-1736	-1740	-1740	-1733
	26	-1355	-1355	-1346	-1341	-1351	-1359	-1351

Table C.6: Cont ...

Locations of gauges	Gauge #	A.L. (378 days S.C.)	A.L. (385 days S.C.)	A.L. (394 days S.C.)	A.L. (400 days S.C.)	A.L. (416 days S.C.)
Steel strain gauges on rebars	1	-2663	-2671	-2672	-2675	-2669
	3	-1588	-1602	-1603	-1609	-1605
	5	-1690	-1694	-1683	-1685	-1669
	7	-1682	-1689	-1684	-1687	-1679
	9	-1620	-1608	-1586	-1573	-1546
	11	0.00*	0.00*	0.00*	0.00*	0.00*
	13	-1292	-1286	-1254	-1270	-1250
	2	-1466	-1470	-1472	-1472	-1456
	4	-6	-16	-14	-14	-4
	6	250	300	380	382	429
	8	-663	-668	-648	-655	-642
	10	-1838	-1844	-1844	-1846	-1836
	12	-1400	-1450	-1463	-1470	-1475
	14	-1652	-1670	-1673	-1597	-1545
Steel strain gauges on tensioned bars	27	-542	-550	-553	-545	-543
	28	-268	-274	-282	-269	-264
	29	403	400	392	410	421
	30	141	139	131	149	162
	31	-1398	-1400	-1409	-1375	-1357
	32	-882	-886	-897	-871	-856
Concrete strain gauges	15	-1003	-1001	-980	-985	-968
	17	-1745	-1758	-1760	-1761	-1758
	17'	-1179	-1191	-1180	-1180	-1165
	19	-1631	-1646	-1647	-1648	-1638
	22	0.00*	0.00*	0.00*	0.00*	0.00*
	23	-571	-496	-460	-374	-374
	23'	0.00*	0.00*	300	0.00*	0.00*
	16	-1140	-1142	-1142	-1138	-1123
	18	0.00*	0.00*	0.00*	0.00*	0.00*
	20	-487	-492	-499	-497	-481
	21	7691	7687	7750	7707	7737
	22'	-1595	-1589	-1593	-1599	-1585
	24	-1763	-1766	-1782	-1794	-1802
	25	-1729	-1747	-1759	-1724	-1609
	26	-1355	-1377	-1401	-1313	-1230

Table C.7: Strains measured by electrical strain gauges during third set for strip of w/c = 0.35.

Locations of gauges	Gauge #	A.L. (415 days S.C.)	A.L. (417 days S.C.)	A.L. (421 days S.C.)	A.L. (422 days S.C.)	A.L. (458 days S.C.)	A.L. (469 days S.C.)	A.L. (473 days S.C.)
Steel strain gauges on rebars	1	-2050	-2037	-2026	-2036	-2063	-1978	-1961
	3	-1018	-1061	-1007	-995	-1024	-1003	-1000
	5	-1970	-2001	-1971	-1948	-1921	-1875	-1931
	7	-15575	-1561	-1542	-1549	-1463	-1513	-1504
	9	-2224	-2192	-2236	-2266	-2384	-2210	-2262
	11	0.00*	0.00*	0.00*	0.00*	0.00*	0.00*	0.00*
	13	-1218	-1211	-1193	-1209	-1100	-1089	-1160
	2	-1910	-1905	-1911	-1901	-1882	-1850	-1844
	4	672	679	680	662	659	715	707
	6	-391	-372	-387	-384	-390	-392	-360
	8	506	501	532	527	606	599	532
	10	-2554	-2555	-2548	-2546	-2513	-2510	-2517
	12	-420	-400	-380	-379	-301	-290	-305
	14	-2159	-2172	-2091	-2191	-1877	-1877	-1863
Steel strain gauges on tensioned bars	27	-694	-698	-695	-717	-834	-697	-694
	28	-260	-271	-265	-267	-283	-255	-267
	29	524	515	529	517	505	517	513
	30	13	-4	6	11	-90	65	1
	31	-1293	-1325	-1314	-1313	-1307	-1292	-1325
	32	-474	-509	-503	-516	-480	-534	-515
Concrete strain gauges	15	-923	-963	-953	-958	-1009	-946	-947
	17	-1888	-1913	-1900	-1904	-1902	-1902	-1872
	17'	-1636	0.00*	0.00*	0.00*	0.00*	0.00*	0.00*
	19	-1625	-1644	-1649	-1642	-1641	-1616	-1509
	22	-987	-1015	-1001	-1023	-1006	-970	-982
	23	0.00*	0.00*	0.00*	0.00*	0.00*	0.00*	0.00*
	23'	0.00*	0.00*	0.00*	0.00*	0.00*	0.00*	0.00*
	16	-291	-299	-292	-295	-294	-261	-262
	18	0.00*	0.00*	0.00*	0.00*	0.00*	0.00*	0.00*
	20	-854	-859	-836	-864	-780	-672	-801
	21	0.00*	0.00*	0.00*	0.00*	0.00*	0.00*	0.00*
	22'	-828	-809	-822	-848	-809	-786	-776
	24	-1986	-2011	-1992	-2035	-1959	-1951	-1957
	25	-1372	-1305	-1287	-1255	-1151	-1080	-1106
	26	-219	-215	-193	-174	-247	-260	-261

Table C.7: Cont ...

Locations of gauges	Gauge #	A.L. (477 days S.C.)	A.L. (484 days S.C.)	A.L. (487 days S.C.)	A.L. (491 days S.C.)	A.L. (506 days S.C.)
Steel strain gauges on rebars	1	-1946	-1956	-1942	-1954	-1955
	3	-990	-987	-955	-998	-998
	5	-1923	-1935	-1965	-1946	-1906
	7	-1483	-1482	-1493	-1472	-1463
	9	-2192	-2266	-2215	-2195	-2173
	11	0.00*	0.00*	0.00*	0.00*	0.00*
	13	-1093	-1085	-1068	-1072	-1077
	2	-1844	-1852	-1847	-1849	-1844
	4	696	671	693	694	711
	6	-344	-350	-340	-356	-325
	8	593	590	580	583	634
	10	-2565	-2508	-2523	-2484	-2487
	12	-325	-294	-313	-310	-270
	14	-1750	-1860	-1788	-1846	-1814
Steel strain gauges on tensioned bars	27	-719	-693	-687	-688	-661
	28	-267	-267	-260	-270	-238
	29	511	511	517	516	548
	30	-4	-14	-5	-24	47
	31	-1324	-1335	-1331	-1331	-1290
	32	-605	-525	-533	-523	-494
Concrete strain gauges	15	-942	-908	-938	-946	-919
	17	-1891	-1850	-1869	-1872	-1563
	17'	0.00*	0.00*	0.00*	0.00*	-2898
	19	-1631	-1786	-1628	-1752	-1282
	22	-982	-971	-1051	-957	-660
	23	0.00*	0.00*	0.00*	0.00*	0.00*
	23'	0.00*	0.00*	0.00*	0.00*	0.00*
	16	-260	-249	-255	-225	-145
	18	0.00*	0.00*	0.00*	0.00*	0.00*
	20	-677	-825	-823	-892	-731
	21	0.00*	0.00*	0.00*	0.00*	0.00*
	22'	-777	-748	-781	-769	-592
	24	-1993	-1935	-1955	-1922	-1560
	25	-1061	-1043	-1056	-1029	-620
	26	-242	-252	-215	-231	-170

Table C.8: Strains measured by electrical strain gauges during third set for strip of w/c = 0.40.

Locations of gauges	Gauge #	A.L. (415 days S.C.)	A.L. (417 days S.C.)	A.L. (421 days S.C.)	A.L. (422 days S.C.)	A.L. (458 days S.C.)	A.L. (469 days S.C.)	A.L. (473 days S.C.)
Steel strain gauges on rebars	1	-2250	-2234	-2211	-2229	-2149	-2120	-2065
	3	-1188	-1159	-1151	-1153	-1127	-1106	-1097
	5	-1998	-2033	-2081	-2019	-2003	-1952	-2094
	7	-1981	-1959	-1993	-1930	-1906	-1783	-1901
	9	-1097	-1075	-1057	-1069	-1014	-1017	-998
	11	0.00*	0.00*	0.00*	0.00*	0.00*	0.00*	0.00*
	13	-770	-900	-1267	-1250	-940	0.00*	0.00*
	2	-2378	-2380	-2416	-2362	-2357	-2345	-2330
	4	-677	-661	-623	-631	-590	-574	-566
	6	-146	-128	-126	-126	-114	-113	-103
	8	-820	-811	-803	-807	-780	-717	-757
	10	-2472	-2465	-2460	-2462	-2447	-2440	-2423
	12	0.00*	0.00*	0.00*	0.00*	0.00*	0.00*	0.00*
	14	-1753	-1694	-1617	-1618	-1427	-1434	-1402
Steel strain gauges on tensioned bars	27	-208	-216	-216	-200	-216	-214	-210
	28	-549	-564	-557	-568	-599	-550	-553
	29	431	409	432	408	406	407	430
	30	652	636	680	700	647	623	644
	31	-949	-982	-987	-983	-993	-981	-985
	32	-560	-595	-582	-549	-528	-593	-557
Concrete strain gauges	15	-1050	-1067	-1071	-1071	-1148	-1088	-1103
	17	-2008	-1998	-2005	-1995	-1990	-1967	-1939
	17'	-1646	-1641	-1651	-1633	-1625	-1579	-1600
	19	-1828	-1846	-1838	-1866	-1835	-1858	-1842
	22	-134	-156	-156	-158	-180	-158	-133
	23	0.00*	0.00*	0.00*	0.00*	0.00*	0.00*	0.00*
	23'	333	800	874	866	870	800	0.00*
	16	-795	-798	-790	-792	-759	-756	-758
	18	-986	-983	-1012	-974	-958	-944	-924
	20	-971	-975	-982	-1030	-972	-967	-970
	21	-882	-879	-870	-868	-871	-845	-875
	22'	-1077	-1105	-1052	-1034	-1068	-1054	-1056
	24	-1553	-1528	-1479	-1499	-1516	-1500	-1503
	25	-1185	-1005	-865	-800	-601	-550	-615
	26	-663	-768	-780	-760	-770	-800	-776

Table C.8: Cont ...

Locations of gauges	Gauge #	A.L. (477 days S.C.)	A.L. (484 days S.C.)	A.L. (487 days S.C.)	A.L. (491 days S.C.)	A.L. (506 days S.C.)
Steel strain gauges on rebars	1	-2094	-2116	-2106	-2103	-2062
	3	-1119	-1090	-1084	-1092	-1040
	5	-1988	-1990	-1990	-2008	-1936
	7	-1878	-1864	-1869	-1867	-1809
	9	-980	-1003	-990	-1006	-870
	11	0.00*	0.00*	0.00*	0.00*	0.00*
	13	0.00*	0.00*	0.00*	0.00*	0.00*
	2	-2341	-2336	-2340	-2336	-2312
	4	-570	-569	-573	-583	-518
	6	-86	-107	-82	-94	-25
	8	-750	-755	-755	-738	-722
	10	-2443	-2430	-2447	-2440	-2190
	12	0.00*	0.00*	0.00*	0.00*	0.00*
	14	-1391	-1380	-1375	-1360	-1150
Steel strain gauges on tensioned bars	27	-235	-202	-189	-162	-153
	28	-553	-555	-543	-542	-495
	29	421	454	459	435	472
	30	644	649	648	646	689
	31	-1092	-1013	-982	-983	-897
	32	-580	-600	-572	-626	-526
Concrete strain gauges	15	-1059	-1078	-1047	-1083	-975
	17	-1990	-1965	-1963	-1929	-1627
	17'	-1600	-1648	-1590	-1591	-1633
	19	-1875	-1857	-1853	-1879	-1345
	22	-145	-152	-150	-149	-227
	23	0.00*	0.00*	0.00*	0.00*	0.00*
	23'	0.00*	-300	-770	0.00*	0.00*
	16	-716	-642	-755	-655	-581
	18	-973	-960	-951	-943	-975
	20	-966	-950	-966	-967	-984
	21	-869	-863	-858	-872	-539
	22'	-1040	-1055	-1080	-1037	-1064
	24	-1501	-1496	-1497	-1505	-1403
	25	-481	0.00*	0.00*	0.00*	0.00*
	26	-740	0.00*	0.00*	0.00*	0.00*

Table C.9: Strains measured by electrical strain gauges during third set for strip of w/c = 0.50.

Locations of gauges	Gauge #	A.L. (415 days S.C.)	A.L. (417 days S.C.)	A.L. (421 days S.C.)	A.L. (422 days S.C.)	A.L. (458 days S.C.)	A.L. (469 days S.C.)	A.L. (473 days S.C.)
Steel strain gauges on rebars	1	-2693	-2687	-2679	-2686	-2676	-2657	-2700
	3	-1640	-1623	-1581	-1617	-1676	-1566	-1587
	5	-1682	-1688	-1693	-1738	-1676	-1590	-1588
	7	-1703	-1680	-1670	-1730	-1685	-1669	-1624
	9	-1524	-1514	-1506	-1502	-1425	-1385	-1382
	11	0.00*	0.00*	0.00*	0.00*	0.00*	0.00*	0.00*
	13	-1219	-1225	-1209	-1215	-1230	0.00*	0.00*
	2	-1453	-1448	-1440	-1444	-1424	-1397	-1407
	4	-35	-20	-14	-14	-14	10	-12
	6	422	417	417	404	429	460	472
	8	-655	-634	-622	-620	-551	-550	-550
	10	-1828	-1830	-1822	-1844	-1797	-1800	-1788
	12	-1480	0.00*	0.00*	-1400	-1300	0.00*	0.00*
	14	-1360	-925	-1310	-1304	-1210	-1177	-1158
Steel strain gauges on tensioned bars	27	-558	-559	-546	-558	-685	-547	-586
	28	-271	-286	-273	-284	-291	-291	-292
	29	410	394	400	389	357	384	357
	30	147	134	136	180	116	101	120
	31	-1277	-1000	-1593	-1300	-1420	-1373	-1350
	32	-842	-862	-869	-1210	-870	-858	-864
Concrete strain gauges	15	-993	-970	-945	-951	0.00*	0.00*	0.00*
	17	-1771	-1761	-1746	-1761	-1705	-1728	-1733
	17'	-1192	-1206	-1288	-1190	0.00*	0.00*	0.00*
	19	-1660	0.00*	0.00*	0.00*	-1751	-1900	-2040
	22	0.00*	0.00*	0.00*	0.00*	0.00*	0.00*	0.00*
	23	-347	0.00*	0.00*	0.00*	0.00*	0.00*	291
	23'	0.00*	0.00*	0.00*	0.00*	0.00*	0.00*	0.00*
	16	-1093	-1152	-1083	-1093	-1109	-1073	-1012
	18	0.00*	0.00*	0.00*	0.00*	0.00*	0.00*	0.00*
	20	-447	-460	-444	-444	-445	-415	-436
	21	7558	7602	7602	7620	7592	7715	7759
	22'	-1563	-1562	-1548	-1554	-1508	-1508	-1480
	24	-1793	-1760	-1728	-1729	-1631	-1880	-1740
	25	-1375	-1086	-1031	-1001	-515	-530	-635
	26	-1060	-982	-909	-894	-670	-613	-600

Table C.9: Cont ...

Locations of gauges	Gauge #	A.L. (477 days S.C.)	A.L. (484 days S.C.)	A.L. (487 days S.C.)	A.L. (491 days S.C.)	A.L. (506 days S.C.)
Steel strain gauges on rebars	1	-2642	-2652	-2656	-2653	-2587
	3	-1551	-1538	-1528	-1522	-1439
	5	-1593	-1602	-1591	-1601	-1403
	7	-1567	-1613	-1614	-1609	-1550
	9	-1388	-1357	-1349	-1350	-1216
	11	0.00*	0.00*	0.00*	0.00*	0.00*
	13	0.00*	0.00*	0.00*	0.00*	-1800
	2	-1404	-1413	-1402	-1401	-1361
	4	41	24	15	10	13
	6	467	473	482	474	615
	8	-555	-541	-532	-547	-444
	10	-1783	-1795	-1788	-1784	-1678
	12	0	-963	-970	-988	-810
	14	-1145	-1132	-1114	-1101	-1023
Steel strain gauges on tensioned bars	27	-502	-565	-526	-558	-434
	28	-296	-294	-291	-295	-207
	29	371	420	432	369	377
	30	101	109	111	101	282
	31	-1341	-1345	-1359	-1360	-1300
	32	-854	-865	-846	-839	-801
Concrete strain gauges	15	0.00*	0.00*	0.00*	0.00*	-870
	17	-1650	-1735	-1739	-1746	-1440
	17'	0.00*	0.00*	0.00*	0.00*	-701
	19	-2055	-2000	-2033	-2083	-1427
	22	0.00*	0.00*	0.00*	0.00*	0.00*
	23	283	480	551	722	1261
	23'	0.00*	0.00*	0.00*	0.00*	997
	16	-1070	-1052	-1019	-1132	-921
	18	0.00*	0.00*	0.00*	0.00*	0.00*
	20	-422	-463	-488	-454	-211
	21	7762	7756	7769	7756	8599
	22'	-1500	-1499	-1536	-1478	-1414
	24	-1636	-1610	-1596	-1594	-1693
	25	-641	0.00*	-566	0.00*	-309
	26	-698	-563	-566	-560	-555

§ Measurements taken after applying Cl^- only.

‡ Measurements taken after applying Cl^- and H_2O.

- Compression.

* No data at this particular reading as the gauge malfunctioned.

Appendix D

Strains Results by Optical Fibres Technique

Strain data obtained from the optical fibres data acquisition system are given in Table D.1 for the three strips right after the load was applied and before exposure to chlorides.

Table D.1: Micro-strains measured by optical fiber technique.

Distance from left threaded bar	w/c = 0.35		w/c = 0.40		w/c = 0.50	
	Bottom	Top	Bottom	Top	Bottom	Top
0	152	0	130	30	113	57
0.1	65	-82	224	32	55	48
0.2	-191	-8	318	35	107	39
0.3	-114	-18	316	30	48	25
0.4	-38	46	315	26	172	11
0.5	72	26	325	9	87	81
0.6	62	16	46	-8	-128	-17
0.7	148	6	54	67	-140	-15
0.8	-18	-82	-22	-27	-43	-13
0.9	-197	-3	-19	-21	-161	-27
1	-291	80	-16	-15	-135	-41
1.1	25	-6	-16	-14	-121	-53
1.2	-79	-30	-16	-13	-69	-55
1.3	-425	-54	-34	-29	-46	-57
1.4	-99	-43	-52	-297	-55	-39
1.5	65	-116	-63	-892	3	62
1.6	61	-14	-75	-897	65	-13
1.7	228	1603	-387	-978	-119	-4
1.8	226	1519	-27	-807	131	-11
1.9	202	2024	-25	-718	147	-18
2	178	2441	-191	-628	82	-268
2.1	189	2607	2842	-982	13	-687
2.2	621	2683	3183	-998	2539	-606
2.3	1312	-1028	3530	-767	2112	-777
2.4	2256	-581	3960	-529	2766	-841
2.5	3266	-675	3812	-710	2145	-736
2.6	3686	-673	3580	-719	2123	-812
2.7	3178	-671	3590	-631	2283	-888
2.8	3428	-765	3011	-368	2387	-643
2.9	3588	-775	3346	-356	2176	-736
3	2739	-796	2166	-279	188	-754

Table D.1: Cont ...

Distance from left threaded bar	w/c = 0.35		w/c = 0.40		w/c = 0.50	
	Bottom	Top	Bottom	Top	Bottom	Top
3.1	3017	-984	2092	-377	282	-689
3.2	2923	-826	1224	-221	277	-781
3.3	316	-1004	390	-312	182	-621
3.4	318	-756	398	-467	181	-510
3.5	308	-760	233	-460	107	-484
3.6	130	-930	152	-460	41	-473
3.7	110	-343	152	-360	60	-547
3.8	89	-451	236	-420	256	-120
3.9	164	-391	50	-318	128	-30
4	238	-211	32	-396	311	45
4.1	150	-200	105	-298	222	36
4.2	145	-182	10	-282	291	-124
4.3	228	-248	-51	-265	280	-116

Appendix E

Titration Results

Table E.1: Potentiometric results of total chloride contents for first set of samples.

w/c	Depth, mm	Section (0)			Section (2)		
		Wt, gm	V_2, ml	Cl, %	Wt, gm	V_2, ml	Cl, %
0.35	2.5	7.4969	40.896	0.920	7.4931	32.222	0.715
	7.5	7.4763	27.014	0.593	7.4745	25.694	0.562
	12.5	8.5636	17.721	0.325	8.5672	17.134	0.313
	17.5	8.5896	9.668	0.158	8.5806	8.158	0.127
	22.5	8.5602	4.888	0.060	8.5641	4.084	0.043
	27.5	9.5519	3.812	0.034	9.5775	4.086	0.039
	32.5	9.5845	3.624	0.030	9.5861	3.724	0.032
0.40	2.5	7.5886	35.621	0.785	7.5832	35.352	0.780
	7.5	7.5383	26.108	0.567	7.5326	33.272	0.736
	12.5	8.0851	17.374	0.337	8.0871	27.091	0.550
	17.5	8.0411	10.991	0.198	8.0822	16.734	0.323
	22.5	8.0528	4.724	0.060	8.0704	7.894	0.129
	27.5	8.5626	2.974	0.020	6.0502	9.611	0.223
	32.5	6.0874	2.798	0.023	8.5669	5.296	0.068
0.50	2.5	6.5499	32.228	0.818	6.5345	25.526	0.638
	7.5	6.5367	28.592	0.721	6.5572	31.166	0.788
	12.5	7.5241	26.286	0.572	7.5241	26.251	0.571
	17.5	7.5403	19.931	0.422	7.5622	22.564	0.482
	22.5	8.5284	16.258	0.296	8.5395	21.922	0.414
	27.5	8.5763	8.738	0.139	8.5673	13.251	0.233
	32.5	8.5335	5.056	0.063	8.4746	8.441	0.135

Table E.1: Contd ...

w/c	Depth, mm	Section (4)			Section (8)		
		Wt, gm	V_2, ml	Cl, %	Wt, gm	V_2, ml	Cl, %
0.35	2.5	7.4588	30.151	0.669	7.4322	34.226	0.769
	7.5	7.4222	29.894	0.666	7.4068	21.272	0.461
	12.5	8.5431	19.742	0.368	8.5506	17.286	0.317
	17.5	8.5539	9.461	0.155	8.5548	11.172	0.190
	22.5	8.5637	3.344	0.028	8.5532	7.301	0.110
	27.5	9.5351	3.821	0.034	9.5564	5.548	0.066
	32.5	9.5815	3.521	0.028	9.5432	3.918	0.036
0.40	2.5	7.5271	37.784	0.843	7.5261	41.572	0.932
	7.5	7.5367	31.214	0.687	7.5735	30.566	0.669
	12.5	8.0791	27.118	0.551	8.0687	26.986	0.549
	17.5	8.0168	15.142	0.291	8.0672	23.192	0.466
	22.5	6.5219	8.466	0.176	8.0431	18.296	0.359
	27.5	6.5202	4.151	0.058	8.0091	11.958	0.220
	32.5	7.5921	3.252	0.029	8.0917	11.366	0.205
0.50	2.5	6.5243	32.004	0.815	6.5551	33.531	0.853
	7.5	6.5716	32.016	0.810	6.5317	31.104	0.790
	12.5	7.5669	30.084	0.658	7.5348	28.476	0.623
	17.5	7.5893	22.186	0.471	7.5564	17.424	0.362
	22.5	8.5276	15.818	0.287	8.5663	14.898	0.267
	27.5	8.5704	11.012	0.186	8.5832	11.488	0.196
	32.5	8.5235	4.462	0.051	8.5533	7.114	0.106

Table E.1: Contd ...

w/c	Depth, mm	Section (7)		
		Wt,(gm)	V_2, ml	Cl %
0.35 (7')	2.5	6.5134	35.631	3.15
	7.5	6.5188	25.544	2.26
	12.5	7.5132	20.216	1.54
	17.5	7.5086	18.084	1.37
	22.5	7.5175	14.552	1.11
	27.5	8.5069	11.876	0.76
	32.5	8.5154	9.858	0.65
0.40 (7')	2.5	6.5035	42.741	3.57
	7.5	6.5065	33.372	2.95
	12.5	6.5091	26.924	2.38
	17.5	7.5031	23.954	1.82
	22.5	7.5081	18.154	1.33
	27.5	7.5055	32.592	2.48
	32.5	7.5078	22.094	1.69
0.50 (7'')	2.5	6.5068	56.794	5.05
	7.5	6.5087	34.102	3.01
	12.5	6.5074	28.638	2.51
	17.5	7.5022	33.452	2.56
	22.5	7.5038	30.238	2.32
	27.5	7.5079	26.682	2.03
	32.5	7.5041	18.438	1.42

Table E.2: Potentiometric results of total chloride contents for second set of samples.

w/c	Depth, Mm	Section (0)			Section (2)		
		Wt, gm	V_2, ml	Cl, %	Wt, gm	V_2, ml	Cl, %
0.35	2.5	6.5067	32.864	0.841	6.5199	32.506	0.829
	7.5	6.5164	26.212	0.659	6.5111	28.474	0.721
	12.5	7.5257	21.984	0.471	7.5037	26.058	0.568
	17.5	7.5281	13.281	0.266	7.5152	17.316	0.361
	22.5	7.5457	6.874	0.114	7.5137	9.854	0.185
	27.5	8.5088	3.778	0.037	8.5179	6.016	0.084
	32.5	8.5044	3.646	0.034	8.5063	3.751	0.036
0.40	2.5	6.5447	33.021	0.840	6.5461	31.132	0.789
	7.5	6.5516	25.286	0.630	6.5674	30.631	0.773
	12.5	7.5351	24.262	0.524	6.5231	27.001	0.679
	17.5	7.5561	15.521	0.317	7.5523	19.376	0.408
	22.5	7.5456	9.224	0.170	7.5455	11.872	0.232
	27.5	8.5519	5.514	0.073	8.5306	6.841	0.101
	32.5	8.5625	4.312	0.048	8.5205	3.904	0.040
0.50	2.5	6.5681	34.452	0.876	6.5646	38.208	0.978
	7.5	6.5502	32.398	0.823	6.5592	33.396	0.848
	12.5	7.5525	28.502	0.622	7.5721	31.986	0.702
	17.5	7.5504	24.096	0.519	7.5748	25.912	0.560
	22.5	7.5638	17.704	0.368	7.5537	22.548	0.482
	27.5	8.5736	12.468	0.216	8.5646	17.356	0.318
	32.5	8.5659	7.016	0.104	8.5835	8.291	0.130

Table E.2: Contd ...

w/c	Depth, Mm	Section (4)			Section (8)		
		Wt, gm	V_2, ml	Cl, %	Wt, gm	V_2, ml	Cl, %
0.35	2.5	6.5244	34.094	0.872	6.4316	25.217	0.640
	7.5	6.5165	26.858	0.676	6.5264	24.524	0.612
	12.5	7.5152	20.718	0.441	7.5537	22.784	0.488
	17.5	7.5196	12.588	0.250	7.5114	13.914	0.281
	22.5	7.5131	6.046	0.095	7.5201	8.326	0.149
	27.5	8.5246	4.438	0.051	8.5602	5.004	0.062
	32.5	8.5165	3.601	0.033	8.5686	3.754	0.036
0.40	2.5	6.5761	34.192	0.868	6.5737	35.511	0.904
	7.5	6.5491	27.894	0.701	6.5649	27.702	0.694
	12.5	7.5401	21.594	0.461	7.5477	25.636	0.555
	17.5	7.5528	15.144	0.308	7.5243	18.378	0.386
	22.5	7.5766	10.621	0.202	7.5425	12.476	0.246
	27.5	8.5841	5.996	0.083	8.5662	8.372	0.132
	32.5	8.5689	4.382	0.049	8.5517	4.892	0.060
0.50	2.5	6.5656	37.722	0.964	6.5831	32.012	0.808
	7.5	6.5721	32.171	0.814	6.5701	29.518	0.742
	12.5	7.5674	31.518	0.691	7.5714	32.948	0.725
	17.5	7.5703	22.191	0.473	7.5709	31.236	0.684
	22.5	7.5762	16.756	0.345	7.5891	20.058	0.422
	27.5	8.5418	13.918	0.247	8.5581	19.031	0.353
	32.5	8.5663	7.881	0.122	8.5548	13.521	0.239

Table E.2: Contd ...

w/c	Depth, mm	Section (7)		
		Wt (gm)	V_2, ml	Cl %
0.35 (7')	2.5	6.5095	30.906	2.72
	7.5	6.5184	25.432	2.26
	12.5	7.5054	29.668	2.18
	17.5	7.5178	23.991	1.82
	22.5	7.5108	19.982	1.52
	27.5	8.5023	20.116	1.35
	32.5	8.5161	19.558	1.31
0.40 (7')	2.5	6.5068	34.474	3.05
	7.5	6.5089	28.726	2.52
	12.5	6.5067	24.562	2.17
	17.5	7.5078	22.318	1.54
	22.5	7.5054	19.331	1.47
	27.5	7.5061	16.322	1.23
	32.5	7.5069	15.202	1.14
0.50 (7)	2.5	6.5032	32.751	2.88
	7.5	6.5089	33.251	2.92
	12.5	6.5093	30.208	2.67
	17.5	7.5085	28.171	2.14
	22.5	7.5093	23.238	1.81
	27.5	7.5022	16.924	1.27
	32.5	7.5018	13.502	1.03

Table E.3: Potentiometric results of total chloride contents for third set of samples.

w/c	Depth, mm	Section (0)			Section (2)		
		Wt, gm	V_2, ml	Cl, %	Wt, gm	V_2, ml	Cl, %
0.35	2.5	6.5718	35.421	0.901	6.5745	34.631	0.880
	7.5	6.5719	27.258	0.681	6.5683	24.602	0.610
	12.5	7.5771	23.254	0.497	7.5711	21.326	0.452
	17.5	7.5744	14.896	0.302	7.5891	13.601	0.271
	22.5	7.5697	8.908	0.162	7.5828	7.224	0.122
	27.5	8.5706	7.186	0.107	8.5845	3.602	0.033
	32.5	8.5789	4.178	0.045	8.5713	3.586	0.033
0.40	2.5	6.5856	35.994	0.915	6.5844	34.961	0.887
	7.5	6.5869	25.051	0.620	6.5824	24.794	0.614
	12.5	7.5889	21.881	0.464	7.5872	30.008	0.654
	17.5	7.5878	15.752	0.321	7.5854	21.974	0.467
	22.5	7.5835	10.921	0.209	7.5864	17.021	0.351
	27.5	8.5839	6.178	0.086	8.5842	13.008	0.227
	32.5	8.5858	2.914	0.019	8.5853	7.602	0.116
0.50	2.5	6.5841	38.678	0.987	6.5882	38.626	0.985
	7.5	6.5829	30.394	0.765	6.5854	32.592	0.823
	12.5	7.5829	27.691	0.601	7.5882	36.281	0.801
	17.5	7.5895	22.654	0.482	7.5881	29.331	0.638
	22.5	7.5855	16.386	0.336	7.5875	20.174	0.425
	27.5	8.5889	11.404	0.194	8.5855	16.508	0.300
	32.5	8.5891	7.322	0.110	8.5836	15.654	0.282

Table E.3: Contd ...

w/c	Depth, mm	Section (4)			Section (8)		
		Wt, gm	V_2, ml	Cl, %	Wt, gm	V_2, ml	Cl, %
0.35	2.5	6.5797	35.584	0.905	6.5808	34.132	0.865
	7.5	6.5623	31.458	0.796	6.5683	29.041	0.730
	12.5	7.5884	23.058	0.492	7.5783	30.022	0.655
	17.5	7.5875	15.602	0.318	7.5763	21.988	0.468
	22.5	7.5857	9.684	0.180	7.5835	17.348	0.359
	27.5	8.5865	5.786	0.078	8.5783	16.411	0.298
	32.5	8.5835	3.214	0.025	8.5758	11.348	0.193
0.40	2.5	6.5894	36.886	0.938	6.5878	42.381	1.086
	7.5	6.5902	32.056	0.808	6.5837	34.768	0.882
	12.5	7.5915	27.594	0.598	7.5879	33.748	0.742
	17.5	7.5888	20.732	0.438	7.5852	28.866	0.628
	22.5	7.5836	15.588	0.318	7.5865	29.872	0.651
	27.5	8.5925	13.484	0.237	8.5834	28.354	0.544
	32.5	8.5854	8.332	0.131	8.5881	23.346	0.441
0.50	2.5	6.5866	38.222	0.975	6.5889	39.604	1.012
	7.5	6.5853	28.032	0.701	6.5844	37.964	0.968
	12.5	7.5878	26.858	0.581	7.5875	37.894	0.839
	17.5	7.5873	23.942	0.513	7.5831	34.584	0.762
	22.5	7.5874	22.086	0.469	7.5819	27.438	0.595
	27.5	8.5822	13.682	0.241	8.5867	23.914	0.452
	32.5	8.5842	8.861	0.142	8.5878	16.882	0.307

Table E.3: Contd ...

w/c	Depth, mm	Section (7)		
		wt (gm)	V_2, ml	Cl %
0.35 (7)	2.5	6.5278	36.555	3.23
	7.5	6.5014	33.694	2.99
	12.5	7.5192	34.726	2.64
	17.5	7.5173	35.946	2.75
	22.5	7.5101	30.441	2.32
	27.5	7.5044	16.338	1.21
	32.5	7.5094	22.991	1.72
0.40 (7)	2.5	6.5071	42.071	3.72
	7.5	6.5073	34.921	3.08
	12.5	6.5015	38.084	3.37
	17.5	7.5082	37.521	2.86
	22.5	7.5092	33.204	2.54
	27.5	7.5079	31.364	2.41
	32.5	7.5084	31.824	2.44
0.50 (7')	2.5	6.5056	56.852	5.06
	7.5	6.5091	42.888	3.61
	12.5	6.5046	34.964	3.08
	17.5	7.5097	41.044	3.59
	22.5	7.5065	32.874	2.51
	27.5	7.5057	37.022	2.85
	32.5	7.5087	33.588	2.57